THE SKIN FRICTION OF A HYDROFOIL NEAR A FREE SURFACE

by

John C. Gebhardt

This research was carried out under the
Naval Ship Systems Command
General Hydromechanics Research Program
Subproject SR 009 01 01, administered by the
Naval Ship Research and Development Center
Contract Number N00014-67-A0181-0002

. . . And when the resistance of bodies in nonelastic fluids is once known, we may then augment this resistance a little in elastic fluids, as our air; and in the surfaces of stagnating fluids, as lakes and seas.

Sir Isaac Newton, 1642-1727

ABSTRACT

The effect of the free surface on the viscous boundary-layer around a two-dimensional hydrofoil is investigated both theoretically and experimentally.

The methods of Giesing and Smith are used to calculate the potential flow for a hydrofoil moving near a free surface. This potential flow is then used as a basis for calculating the laminar boundary layer, transition and the turbulent layer.

The calculations indicate that while the free surface affects the laminar skin friction near the nose of the foil strongly, the effect of Froude number and depth on the average skin friction coefficient is negligible, even for small depths and large Froude numbers.

Experiments to measure the pressure distribution on both top and bottom surfaces of the foil, together with the wave patterns at several depths and Froude numbers are described. Using the experimental pressure distributions instead of the potential flow calculations, the boundary layer calculations predict essentially the same variations of the skin friction with depth and Froude number. The wave profile measurements confirm and extend Salvesen's previous work.

Local skin-friction measurements on the foil using specially built flush-mounted hot-film probes are also described.

Because of data scatter, only an average skin-friction

coefficient could be measured. The value obtained compares reasonably with the value obtained from the boundary-layer calculations and the value obtained from Schoenherr's flat-plate friction line.

ACKNOWLEDGMENTS

I would like to thank Professors Finn C. Michelsen, T. F. Ogilvie, Horst Nowacki, Hun Chol Kim, and Walter Debler for their able assistance in this work. Jim Moss and the rest of the staff of Ship Hydrodynamics Laboratory also gave freely of their time and talent.

In particular, Miss Kathie Blanck and Kazuo Kubo deserve a special note of thanks for their skillful work in typing the manuscript and preparing the figures.

CONTENTS

LIST OF FIGURES

LIST OF FIGURES (cont.)

NOMENCLATURE

c	chord length of foil, eigenvalue
C_f	skin friction coefficient $\tau_w/\frac{1}{2}\rho U_\infty^2$
$\bar{C}_f$	$(C_f)_{ave}/(C_f)_{\text{deeply submerged}}$
C_t	total resistance coefficient, $R_t/\frac{1}{2}\rho U_\infty^2 A$
C_v	viscous resistance coefficient, $R_v/\frac{1}{2}\rho U_\infty^2 A$
C_w	wave resistance coefficient of foil $R_w/\frac{1}{2}\rho U_\infty^2 c$
d	nondimensional foil depth
F	chord Froude number, function in boundary-layer analysis, defining function for free surface
F_d	Froude number based on d
F_y	Froude number based on y
H	shape factor δ^*/θ
i	imaginary unity, subscript
j	subscript
k	summation subscript
K	$Z\frac{dU}{ds}$
ln	natural logarithm
n_i	i^{th} component of unit normal
p	pressure
p_a	atmospheric pressure
R	Reynold's number, $U_\infty c/\nu$

NOMENCLATURE (cont.)

R_δ	δ x R
R_θ	θ x R
s, n	nondimensional coordinates tangential and normal to body surface
S	defining function for body surface
S_1	defining function for two-dimensional body surface
t	time
T	entrainment function
u, v	nondimensional velocity components in x and y directions
$\bar{u}$, $\bar{v}$	nondimensional velocities in the s and n system
U_i	i^{th} component of velocity
U	nondimensional velocity outside boundary layer
U_∞	speed of body; also speed of uniform stream
x, y	nondimensional length coordinates
Z	$R\theta^2$
α	wave amplitude far downstream
γ	weight per unit volume of fluid
δ	boundary layer thickness (nondimensional)
δ^*	nondimensional displacement thickness
Δ	function of laminar skin friction on foil
ε	perturbation parameter
η	nondimensional elevation of free surface, nondimensional boundary-layer coordinate

NOMENCLATURE (cont.)

θ	nondimensional momentum thickness
Λ	a shape factor, $R\delta^2\frac{dU}{ds}$
μ	dynamic viscosity
ν	kinematic viscosity
ρ	mass density of fluid
τ_w	wall shear stress
ϕ	disturbance potential
Φ	complete velocity potential
χ	$p/\rho U_\infty^2 + \frac{1}{F_y^2}$
∇	gradient

I. Introduction

The forces on a stationary body in a uniform stream of real incompressible fluid near a free surface arise from essentially two basic physical phenomena. First, the presence of the body causes a disturbance of the free surface downstream from the body. The result is a loss of momentum downstream relative to the momentum of the uniform stream, which manifests itself as a drag force on the body. If the body has a shape which can support a circulatory flow (a sharp trailing edge, for example) the disturbance due to the free surface could induce such a flow and thereby cause a lift force on the body perpendicular to the stream. Second, since all real fluids are viscous, the velocity at the wall must be zero. This causes velocity gradients close to the body and thus shear stresses. The velocity gradients result in a further decrease of the momentum behind the body relative to the free stream, which results in an additional force on the body in the direction of motion of the stream. If the vertical component of the shear stress on the body is integrated over the body surface, the resulting viscous lift force could be nonzero due to the assymettry of the flow caused by the free surface.

Even if the body position and the uniform stream are invarient with time, the presence of viscosity precludes the possibility of steady flow except for special cases such as very slow flows and stable laminar flows. Therefore, to be

complete the governing Navier-Stokes equations for the general problem must be written in their time-dependent form:

$$\frac{\partial u_i}{\partial t} + u_j \frac{\partial u_i}{\partial x_j} = - \frac{1}{\rho} \frac{\partial (p + \gamma x_2)}{\partial x_i} + \nu \frac{\partial^2 u_j}{\partial x^2_j}. \tag{1}$$

The continuity condition

$$\frac{\partial u_i}{\partial x_i} = 0 \tag{2}$$

must also be satisfied throughout the fluid, together with appropriate boundary conditions. At the body surface defined by

$$S(x_1, x_2, x_3) = 0 \tag{3}$$

the velocity relative to the surface must be zero.

$$u_i = 0 \qquad i = 1, 2, 3 \tag{4}$$

is sufficient to insure this conditon. At the free surface two conditions must be met. First, a particle of fluid on the free surface must remain on the surface, i.e.,

$$\frac{DF}{Dt} = 0 \text{ on } F = \eta(x_1, x_3, t) - x_2 = 0, \tag{5}$$

where $F(x_1, x_2, x_3, t)$ is the equation of the free surface and

$$\frac{D}{Dt} = \frac{\partial}{\partial t} + u_i \frac{\partial}{\partial x_i}.$$

In addition, the dynamic condition that the stress be continuous across the free surface requires that

$$\mu\left(\frac{\partial u_i}{\partial x_k} + \frac{\partial u_k}{\partial x_i}\right) n_k - p n_i = -p_a n_i \text{ on } F, \tag{6}$$

where n_i is the i^{th} component of the unit normal to the free surface. In equations 1 to 6 index notation is used. A repeated subscript implies summation. Because this mixed boundary value problem is an extremely difficult one to treat even for the simplest of body shapes, the progress which has been made in solving problems of this kind is limited. Welsh et al has solved the two-dimensional Navier-Stokes equations by a finite-difference method with various boundary conditions and has produced many results including examples of separated flows. Dugan has applied an integral equation technique, based on Oseen's linearized form of the steady-state Navier-Stokes equations to the two-dimensional flow about a flat plate moving far beneath a free surface at small Froude and Reynolds numbers.[2]

In this paper the problem of a hydrofoil moving near a free surface in a viscous fluid will be investigated both theoretically and experimentally. The principle aim of the

investigation is to find out what effect, if any, the free surface has on the skin friction of the foil. The foil section studied has a thickness to chord ratio of approximately 1:3 and a chord length of approximately one foot. It is described completely elsewhere in this work.

The motivation for examining this problem is the difficulty experienced by researchers who attempt to determine the resistance of ships. The classical idea of Froude that the wavemaking drag and viscous effects are separable and independent has been extremely useful for predicting the drag of full-size ships from model tests. However, with the advent of the bulbous bow and other devices which greatly alter their performance, anomalous results have appeared when Froude's hypothesis is applied. A good example can be found in a paper by Couch and Moss where they cite model tests of a ship with a bulbous bow which show that at some speeds the total resistance coefficient, C_t, is less than the assumed viscous resistance coefficient, C_v.[3] This indicates that local viscous effects caused by the bulb itself or changes in the pressure gradients around the hull due to changes in wavemaking caused by the bulb result in a significant decrease in the viscous resistance.

The effects of the free surface on the boundary layer around a submerged simple two-dimensional body obviously will not parallel those corresponding to ship-shaped bodies since

the flow around ships is three-dimensional and they pierce the free surface. However, hopefully by showing that the viscous flow is significantly affected by a free surface disturbance in a simple case using well established concepts and methods as well as by direct measurement, the ship problem may at least be more fully appreciated. Wu formulated the problem of a vertical surface piercing strut in much the same fashion as done here, but because of the observed complicated three-dimensional character of the boundary layers around such a strut caused by the influence of the free surface, much truth about the actual phenomena is obscured by using two-dimensional methods for the viscous problem.[4]

By studying a two-dimensional horizontal body much of this difficulty is avoided. Two-dimensional laminar boundary layers are truly two-dimensional and the only possibilities for error lie in assuming that transition and turbulence of a two-dimensional boundary layer are completely two-dimensional phenomena. The saving grace is that there are well-established and tested methods for the analysis of turbulent two-dimensional boundary layers, while little is known about the general three-dimensional case.

The techniques used in this analysis require that the body is "thin" enough so that separation does not occur, and to assume that the viscosity is small enough so that only in the region very close to the body, the "boundary layer", is

the flow influenced by viscous effects, and that the remainder of the flow obeys the equations of motion of an ideal fluid.

This approach presupposes that outside the thin boundary layer close to the body, large velocity gradients do not exist and thus the resulting shear stresses are very small. If the velocity gradients are indeed small outside the boundary layer, then the boundary condition, equation 6, can be simplified to

$$p = p_a \text{ on } F.$$

Within the restrictions of the assumption of two distinct flow regions, one viscous and the other nonviscous, an "exact" solution for the total flow can be obtained by applying an iterative technique. As a first approximation the entire flow is assumed to be inviscid, the nonslip condition on the body is relaxed and the velocities and pressures are calculated using potential flow methods. The second approximation is then obtained by using the first approximation to obtain the characteristics of the boundary layer. From this second approximation the extent of and the flow characteristics within the viscous region are determined. The next step in the iterative process is to formulate and solve a new inviscid problem with the outer edge of the viscous region as the new body boundary, $S_1(x_1, x_2) = 0$, and with the boundary condition

on S_1 that the normal velocity on S_1 be the same as given by the second approximation.

Next, the second inviscid solution is used to obtain a new viscous solution and the procedure is repeated until no change is observed in either the inviscid solution or the viscous solution. Intuitively, this procedure should converge very rapidly to a unique solution for the entire flow region with the velocities continuous across the interface between the inviscid and viscous regions. But to assume that this solution would resemble the observed flow even for a thin body is highly presumptuous. For even if the inviscid and viscous solutions could be obtained very accurately, implicit in this method is the assumption that the value of ν at the interface is discontinuous.

However, the interface cannot be precisely defined and the flow must necessarily change gradually from viscous to inviscid behavior. Also, since in this model the potential flow is assumed to exist everywhere except very close to the body, the viscous wake is neglected. Therefore, in light of these basic shortcomings of such an approach, more accurate results are not assured by carrying this iterative scheme to convergence by computing higher order iterations.

However, if it is desired to study the interactions between the viscous and potential regions, as is the case here, a wealth of useful information can be obtained by carrying

out only the first three approximations. From the second approximation information can be derived regarding the effects of the potential flow on the boundary layer, while the third will indicate how the boundary layer affects the external potential flow.

First, the method for solving the potential problem is discussed briefly. It has been treated extensively elsewhere by Salvesen[5] and Giesing and Smith.[6] Next, methods for dealing with the viscous problem are discussed and theoretical results are presented. Finally, the experiments are described and the results compared with the theory.

II. The First Approximation (The Inviscid Problem)

By ignoring for the present the influence of viscosity and restricting the problem to steady two-dimensional flows, the formulation of the hydrofoil problem naturally becomes simpler. Let

$$x = \frac{x_1}{c};\ y = \frac{x_2}{c};\ u = \frac{u_1}{U_\infty};\ v = \frac{u_2}{U_\infty},$$

so that the equations of motion, equation 1, becomes

$$u\frac{\partial u}{\partial x} + v\frac{\partial u}{\partial y} = -\frac{\partial\left(p + \frac{1}{F_y^2}\right)}{\partial x} \tag{7}$$

and

$$u\frac{\partial v}{\partial x} + v\frac{\partial v}{\partial y} = -\frac{\partial\left(p + \frac{1}{F_y^2}\right)}{\partial y}. \tag{8}$$

The continuity equation can be written

$$\frac{\partial u}{\partial x} + \frac{\partial v}{\partial y} = 0 \tag{9}$$

and the boundary conditions become

$$un_x + vn_y = 0 \text{ on } S_1(x, y) = 0 \tag{10}$$

$$p = p_a \text{ and} \tag{11}$$

$$u\frac{\partial \eta}{\partial x} - v = 0 \text{ on } y = \eta(x). \tag{12}$$

Henceforth, unless specifically noted all lengths are nondimensionalized with respect to c and all velocities with respect to U_∞. For a body with a sharp trailing edge such as is being considered here, the Kutta condition must be satisfied at the trailing edge. Figure 1 illustrates the flow region and coordinate system. Since the flow is inviscid and is uniform far upstream, it is irrotational everywhere and the velocity may be written as the gradient of a potential, Φ, so that

$$u = \frac{\partial \Phi}{\partial x}, \quad v = \frac{\partial \Phi}{\partial y} \tag{13}$$

Equations 7 and 8 can now be integrated to yield Bernoulli's equation and equation 9 yields the familiar Laplace equation. Thus the inviscid flow is governed by these two equations:

$$\nabla^2 \Phi = 0 \tag{14}$$

$$p + 1/2(u^2 + v^2 - 1) + \frac{1}{F_y^{\,2}} = p_\infty \tag{15}$$

By defining a disturbance potential

$$\Phi = \phi + x \tag{16}$$

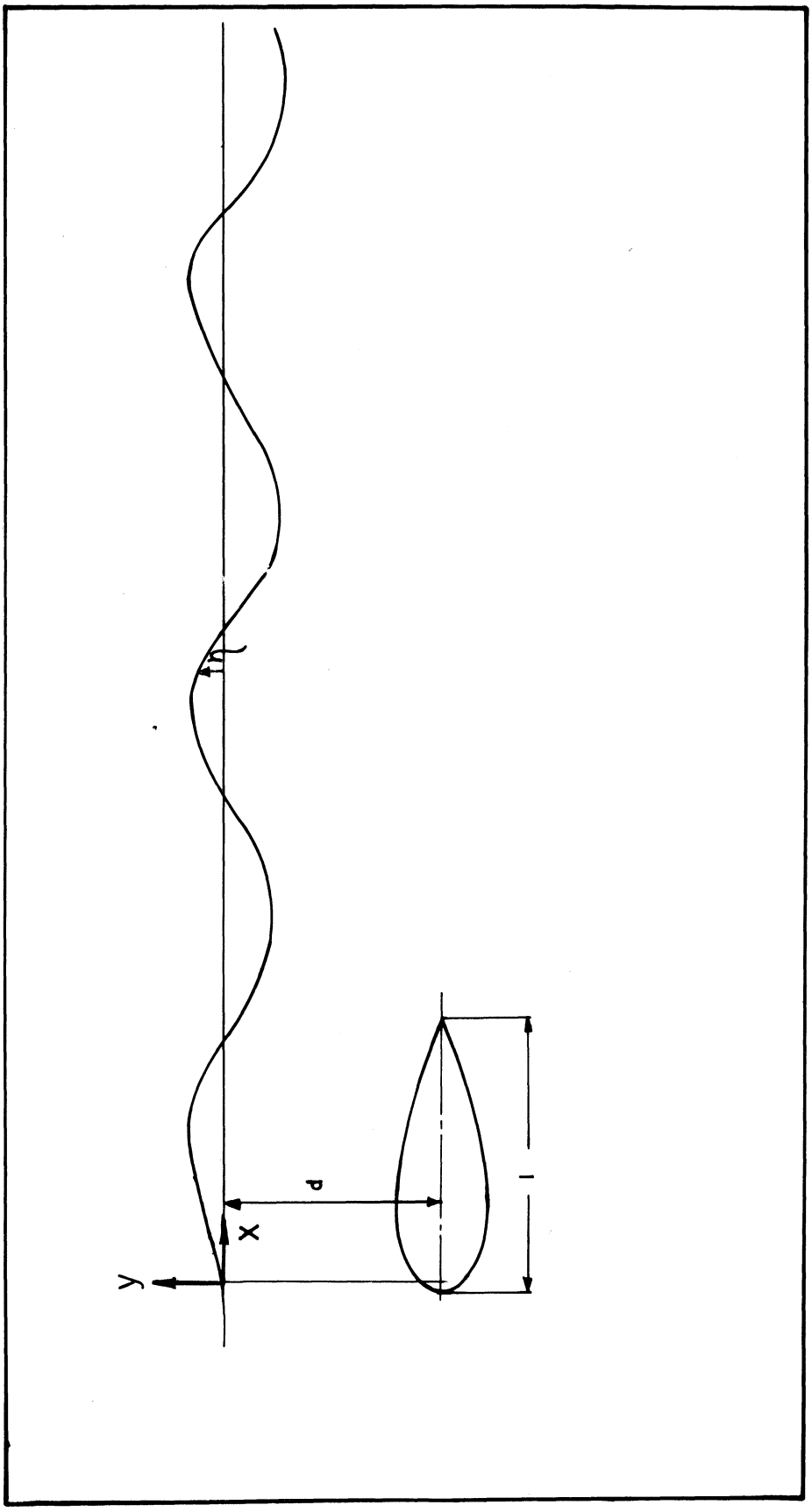

FIGURE 1 COORDINATE SYSTEM

and using Benoulli's equation, the free surface conditions (equations 11 and 12) can be combined and become

$$[1 + \frac{\partial \phi}{\partial x}][\frac{\partial^2 \phi}{\partial x^2}(1 + \frac{\partial \phi}{\partial x}) + \frac{\partial \phi}{\partial y}\frac{\partial^2 \phi}{\partial x \partial y}] + \frac{1}{F^2}\frac{\partial \phi}{\partial y} = 0$$

$$\text{on } y = \eta(x). \tag{17}$$

In addition to the boundary surface conditions and the free surface condition, the disturbance velocities must vanish far upstream and below the body, thus

$$\frac{\partial \phi}{\partial x} \to 0 \text{ and } \frac{\partial \phi}{\partial y} \to 0 \text{ for } x \to -\infty \text{ and } y \to -\infty. \tag{18}$$

While much simpler than the original viscous problem, the nonlinear boundary condition, (equation 17), which must be applied on a yet to be determined surface $y = \eta(x)$, makes even the inviscid problem untractable. If the depth of submergence is great enough so that the disturbance velocities near the free surface and the free surface elevation are small, then ϕ and η can be expanded in the form

$$\phi = \varepsilon\phi_0 + \varepsilon^2\phi_1 + \varepsilon^3\phi_2 + \ldots \tag{19}$$

and

$$\eta = \varepsilon\eta_0 + \varepsilon^2\eta_1 + \varepsilon^3\eta_2 + \ldots \tag{20}$$

where ε is some small parameter.

Substituting equation 19 into equation 17 and collecting like powers of ε, 17 becomes:

$$\left(\frac{\partial^2 \phi_o}{\partial x^2} + \frac{1}{F^2}\frac{\partial \phi_o}{\partial y}\right)\varepsilon + O(\varepsilon^2) = 0 \text{ on } y = \eta(x).$$

If we ignore the higher order terms, useful results can be obtained by imposing the linear boundary condition

$$\frac{\partial^2 \phi}{\partial x^2} + \frac{1}{F^2}\frac{\partial \phi}{\partial y} = 0 \tag{21}$$

on the line $y = 0$ as long as conditions are such that equations 19 and 20 are valid. In addition, the equation of the free surface becomes:

$$\eta = -F^2 \frac{\partial \phi}{\partial x}(x, 0) \tag{22}$$

Solutions to this linear problem have been obtained by several authors using various techniques, and to varying degrees of accuracy.

Salvesen has thoroughly investigated the influence of the various boundary conditions on the wave profiles for the same body shape being investigated here by a perturbation method and has concluded that satisfying the body boundary condition affects the resistance less compared with satisfying

the higher order terms in the free surface condition (equation 21) and satisfying the Kutta condition.[5,7] The body shape we investigated was the same thick hydrofoil used in this work at a zero angle of attack with respect to the uniform stream. His criterion for making a comparison was the degree to which the various models predicted the wave profile and the resulting wave resistance coefficient, which he shows to be

$$C_W = 1/8\ F^2\alpha^2, \tag{23}$$

accurate to the third order, where α is the wave amplitude far downstream.

Giesing and Smith have developed a method, also based on a perturbation scheme, in which the free-surface condition is satisfied only linearly but the body condition and the Kutta condition are exactly satisfied, at least in a numerical sense.[6] An added feature is that the velocity field everywhere is easily computed.

Briefly, the procedure of Giesing and Smith is to first find two elementary solutions to the Laplace equation which satisfy the free surface condition (equation 21) and the far field conditions (equation 18). The first is of the form

$$G(P, Q) = \ln[r(P, Q)] + K(P, Q). \tag{24}$$

G(P, Q) represents the potential at the point P due to a unit source at Q plus a function, K, nonsingular in the field of interest, that forces G to satisfy the boundary conditions (21) and (18).

The second is of the form

$$H(P, Q) = \mathrm{Re}\{\frac{i}{2\pi} \ln[r(P, Q)] + L(P, Q)\} \tag{25}$$

where H represents the potential at P of a unit line vortex at Q plus a function, also nonsingular in the field of interest, which forces H to satisfy the same boundary conditions as G.

After the elementary solutions are found, the potential for any given body, including those that can support a circulatory flow, can be written as:

$$\phi(P) = \frac{1}{2\pi} \int_{S_1} \sigma(q)\ G(P, q)ds + \Gamma H(P, \bar{q}), \tag{26}$$

where q is a point on the body surface S_1 and $\bar{q}$ is some point inside of S_1. $\sigma(q)$ is the "strength" of the singularity distribution as a function of the position on S. Having an expression for ϕ, expressions for the unknown strengths σ and Γ can be obtained from the body boundary conditions:

$$\frac{\partial\phi(p)}{\partial n} = -i\cdot\vec{n}(p) = \lim_{P\to p}[\frac{1}{2\pi}\int_{S_1} \sigma(q)\nabla G(P, q)\cdot\vec{n}(P)ds + \Gamma H(P, \bar{q})\cdot\vec{n}(p)] \tag{27}$$

and

$$|\vec{V}_t(+)| = |\vec{V}_t(-)| \tag{28}$$

Equation 28 is a statement of the Kutta condition, where $V_t(+)$ and $V_t(-)$ are the tangential velocities at the trailing edge on the upper and lower surfaces, respectively.

The most convenient technique for solving for the unknown source distribution $\sigma(q)$ and the unknown cyclic constant Γ is to do the computation in several steps.

First, the integral equation 27 is solved assuming $\Gamma = 0$. The resulting $\sigma(q)$ represents a nonlifting flow about the body with the Kutta condition left unsatisfied. Next, Γ is determined such that equation 28 is satisfied. With Γ now non-zero equation 26 is no longer satisfied and an additional source distribution denoted by $\sigma_\Gamma(q)$ is needed to cancel the normal flow across S_1 caused by the circulatory flow. σ_Γ can be found from

$$\lim_{P\to p}[\Gamma\nabla H(P, \bar{q})\cdot\vec{n}(P) + \frac{1}{2\pi}\int_{S_1}\sigma_\Gamma(q)\nabla G(P, q)\cdot\vec{n}(P)ds] = 0. \tag{29}$$

To be sure that ϕ satisfies both the no cross-flow condition and the Kutta condition the above process should be repeated until equations 27 and 28 are satisfied simultaneously. Apparently, Giesing has found one iteration sufficient for good

accuracy.

G can be written in terms of the complex potential J, (see Kochin et al[8]), where

$$G(z,c)=\mathrm{Re}[J(z,c)]=\mathrm{Re}\left[\ln(z-c)+\ln(z-\bar{c})-2F^2\,\mathrm{P.V.}\int_{-\infty}^{z}\frac{e^{ik(z-\bar{c})}}{F^2k-1}\,dk\right.$$
$$\left.-2\pi\, i\, e^{\frac{-i}{F^2}(2-\bar{c})}\right]. \qquad (30)$$

Similarly, H can be written in terms of the complex potential I (see Giesing and Smith[6]), where

$$H=\mathrm{Re}[I(z,c)]=\mathrm{Re}\left\{\frac{i}{2\pi}\left[\ln(z-\bar{c})-2F^2\,\mathrm{P.V.}\int_{0}^{\infty}\frac{e^{ik(z-\bar{c})}}{F^2k-1}\,dk\right.\right.$$
$$\left.\left.+2\pi\, i\, e^{\frac{-i}{F^2}(2-\bar{c})}\right]\right\} \qquad (31)$$

and z and c are the complex coordinates of P and Q respectively. Equations 30 and 31 can be used with equations 27, 28 and 29 to solve for $\sigma(q)$ and $\sigma_\Gamma(q)$ by approximating the surface S by N short, straight line segments, and assuming that σ and σ_Γ are constant over each segment. The problem now becomes one of solving two systems of N simultaneous equations in N unknowns. One system yields the source strengths for the segments $\sigma_1, \sigma_2, \ldots \sigma_N$ while the other yields the corresponding σ_Γ's. See Giesing and Smith again for details.

The total velocity anywhere in the fluid can now be determined by recalling that

$$\vec{V}(P)=u(P)i+v(P)j=\nabla\Phi=i+\int_{S_1}(\sigma+\sigma_\Gamma)\nabla G(P,q)ds+\Gamma\nabla H(P,\bar{q}). \qquad (32)$$

In particular, the speed on the surface of the body is required to determine the characteristics of the boundary layer and is given by

$$U(q) = |\vec{V}(q)|,$$

where, remember, q is a point on S and $\vec{V}$ is the velocity of the fluid. Also of interest is the wave elevation which can be determined from equation 22. The wave resistance can then be determined from equation 23.

A simpler but more approximate solution is possible if neither the body boundary condition nor the Kutta condition is satisfied exactly. The velocity potential given body near a free surface may be approximated by the potential due to a finite number of singularities of the form given by equation 30 each with an appropriate strength.

The body shape under consideration in the present work is identical to the shape chosen by Salvesen and is approximated very closely by the dividing streamline generated by 11 simple sources equally spaced on the x axis between x = 0 and x = 1.0 in an infinite, uniform stream (see Figure 2). The strengths of the 11 sources are given by

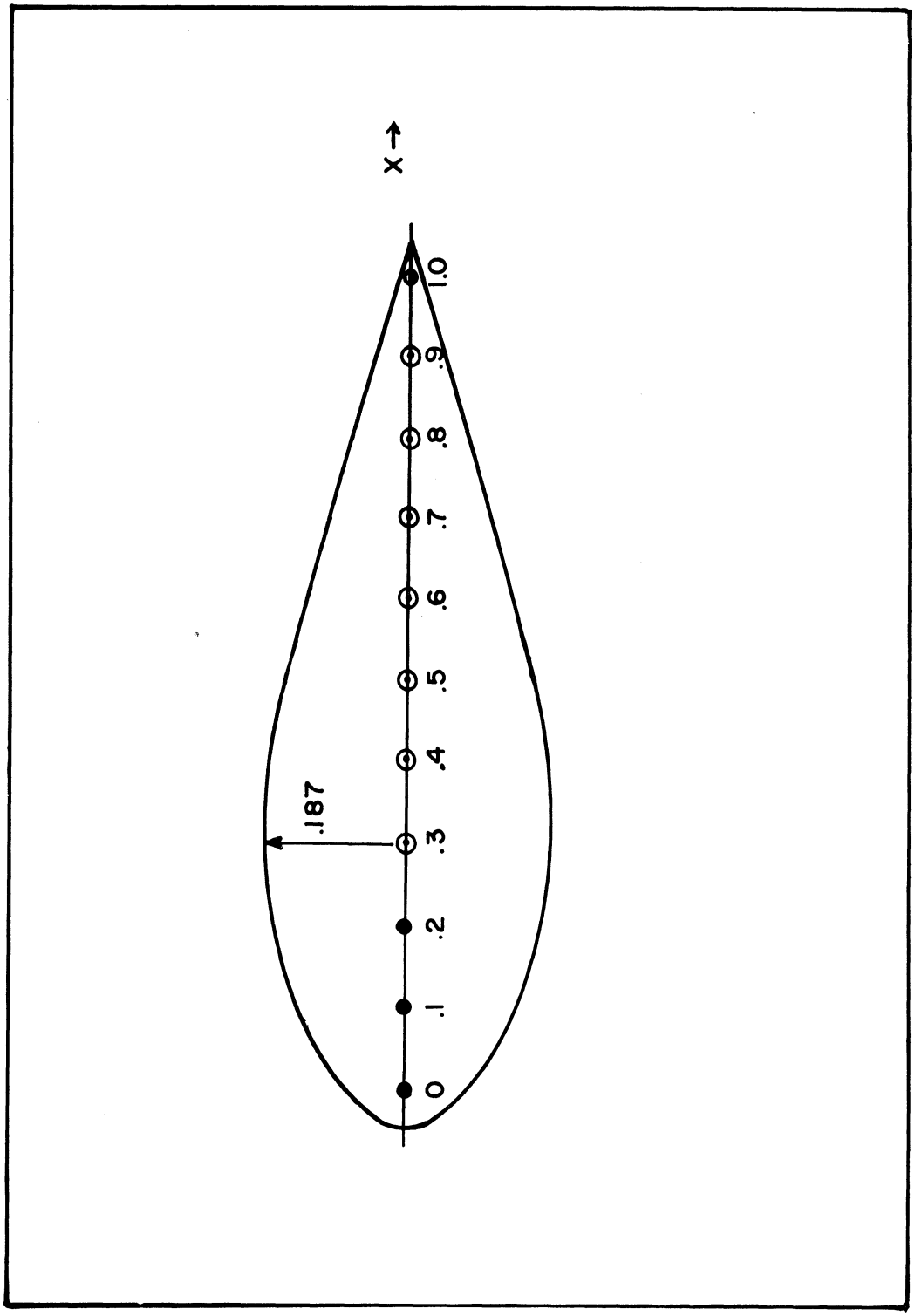

FIGURE 2 BODY SHAPE AND SINGULARITY LOCATION

$$\sigma_j = .04 \text{ for } 0 \leq j \leq 2$$

$$\sigma_j = \frac{.04}{168}(115-8j)3 \leq j \leq 10,$$

where x = j/10 and the equation of the body is given by

$$y = \pm \sum_{j=0}^{10} \sigma_j \tan^{-1}\left(\frac{y}{x-\frac{j}{10}}\right). \tag{33}$$

The body shape used in the calculations and experiments has a chord length of 1.09 and a sharp trailing edge unlike the round trailing edge of the body given by equation 33. Otherwise it is identical.

An approximation to the free surface flow can be obtained by placing eleven equally spaced singularities of the form given by equation 30 with strengths just given at a distance d below the undisturbed free surface. The potential ϕ_1 can then be written:

$$\phi_1(z) = \sum_{j=0}^{10} \sigma_j G(z,c_j), \tag{34}$$

where c_j is the location of the j^{th} singularity.

Salvesen has shown that the resulting flow does not produce a closed body, but one in which fluid enters in the vicinity of the nose and exits near the trailing edge, with the result that there is no true body surface on which to evaluate the tangential velocity for use in the boundary layer

calculations.

For this reason the solution given by equation 34 is unsuitable for this study. However, because of the relative ease of calculating the downstream wave elevation,

$$\alpha^2=16\pi^2 e^{-\frac{2}{F_d^2}}\left[\left\{\sum_{i=0}^{10}\sigma_i \sin\left(\frac{x_i}{F^2}\right)\right\}^2+\left\{\sum_{i=0}^{10}\sigma_i \cos\left(\frac{x_i}{F^2}\right)\right\}^2\right], \qquad (35)$$

it is convenient and, therefore, interesting to compare the wave resistance as predicted by the two methods. Figure 3 shows the wave resistance coefficient plotted against depth Froude number for various depths. The agreement between the two results is not too good, with the circulation and, to a much lesser degree, the improved body boundary condition effectively decreasing the wave resistance and moving the peak values toward lower depth Froude numbers. The consistent linear theory, but with the Kutta condition relaxed, shows close agreement with the simple theory.

The wave resistance is very sensitive to the circulation around the foil and if this could be predicted correctly, the wave resistance and therefore, hopefully, the wave profile and the velocities near the foil would be correct also. Unfortunately, correctly predicting the circulation about a foil or wing shaped body, even in an infinite fluid, is not an easy thing to do. Most of the uncertainty stems from the fact that in a real fluid the Kutta condition is never satisfied

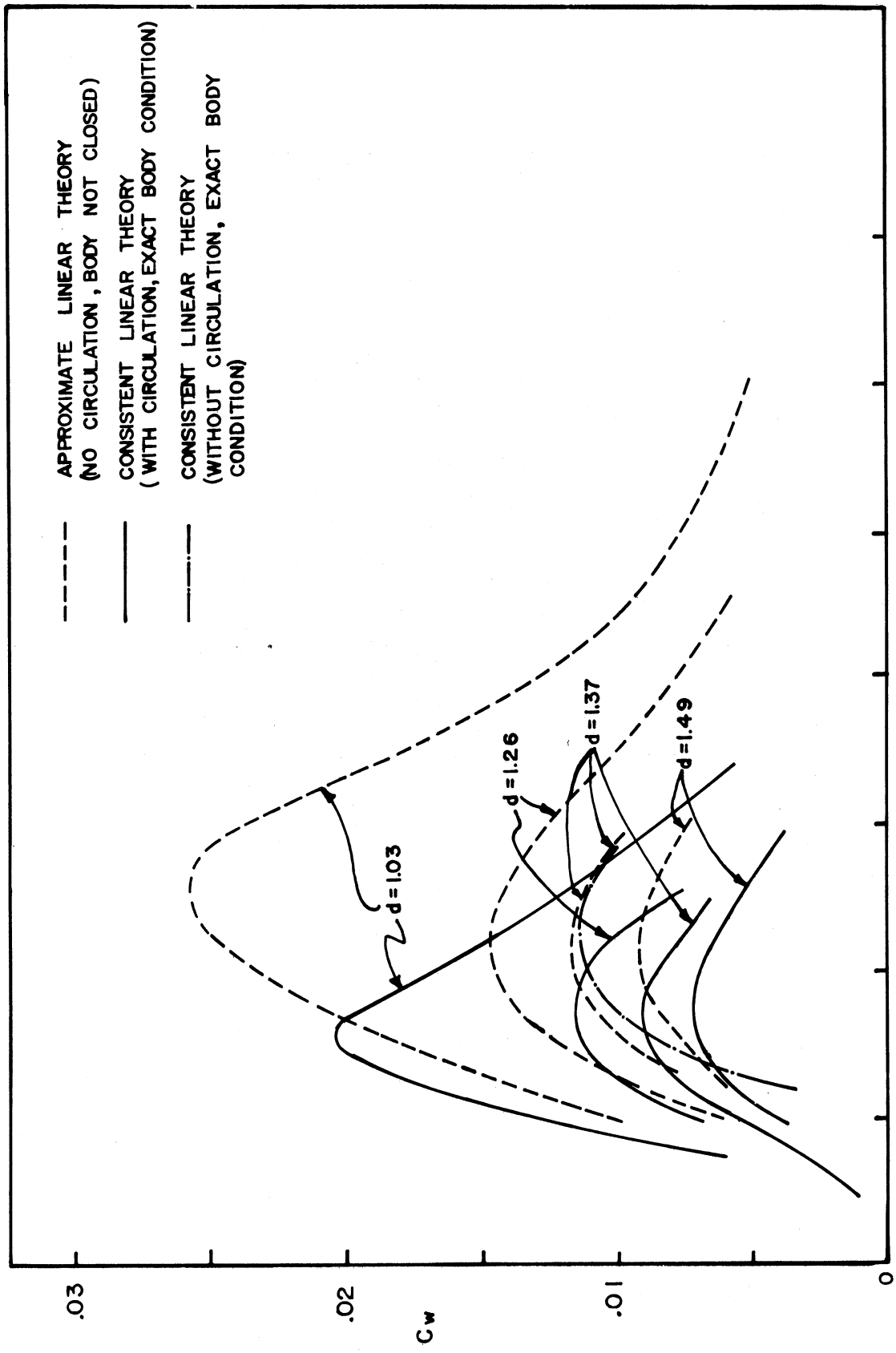

FIGURE 3 Cw vs Fd A COMPARISON OF TWO THEORIES

exactly because the thick boundary layer and wake near the trailing edge obscure the sharp trailing edge to the outside inviscid flow. Also, the existence of the boundary layer changes the effective shape of the foil, changing the circulation. Preston has analyzed these various effects, attempting to better predict the lift of airfoils and concluded that by correctly accounting for the change in effective angle of attack due to the boundary layer much of the discrepancy between the calculated and measured lift can be accounted for.[9] Even if the Kutta condition was satisfied exactly and the boundary layer had no effect on the circulation, any numerical method such as Giesing's, previously described, suffers from insufficient resolution because the boundary is assumed to be made up of a finite number of line segments. This lack of resolution is particularly troublesome at the trailing edge, for it causes an uncertainty of, at most, a segment length in the position of the stagnation point, thus causing an uncertainty in the circulation. At small depths or large speeds when the circulation is large this error is minimized. Figure 4 shows this effect quite clearly. The lift coefficient $L/\frac{1}{2}\rho U_\infty{}^2 c$ is plotted in the same fashion as C_W. The uncertainty in the circulation can be seen in the nonsystematic behavior of C_L at large depths and low values of F_d, where the free surface effect is small. All calculations reported here were done at The University of Michigan Computing Center

FIGURE 4
LIFT COEFFICIENT VERSUS DEPTH FROUDE NO.
FOR VARIOUS VALUES OF d/c
(LINEAR THEORY, WITH CIRCULATION)

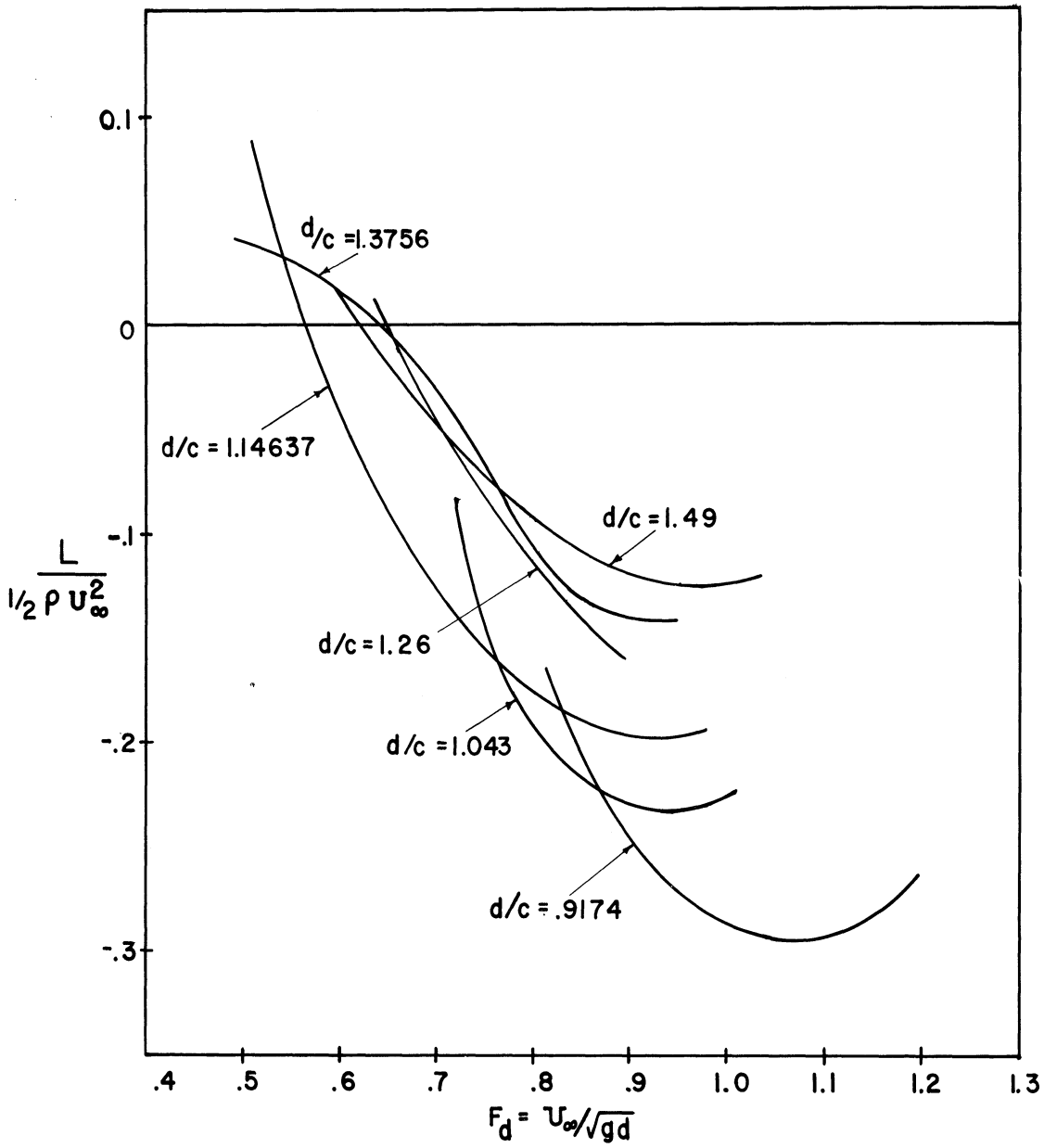

on either an IBM 7090 or IBM 360/67 computer. All potential flow calculations using the method of Giesing and Smith were made using a program written by them and adapted by the author for use on The University of Michigan Executive System.

In spite of the fact that the measured wave resistance does not agree with the calculated results (see Figure 23), the method of Giesing and Smith provides the only method of calculation known to the author which could give the velocity at the body surface accurately. For this reason it has been used to calculate the results needed in the subsequent boundary layer analysis.

III. The Second Approximation (Boundary Layer Flow)

III. 1. The Laminar Boundary Layer

Observation of the flow about two-dimensional bodies at large Reynolds numbers reveals a thin layer of retarded flow, the boundary layer, near the surface beginning at the stagnation point and becoming thicker as it progresses toward the trailing edge. Assuming that the flow in the boundary layer is steady and two-dimensional, equation 1 becomes

$$u\frac{\partial u}{\partial x} + v\frac{\partial u}{\partial y} = -\frac{\partial \chi}{\partial x} + \frac{1}{R}\left(\frac{\partial^2 u}{\partial x^2} + \frac{\partial^2 v}{\partial y^2}\right) \qquad 1a$$

and

$$u\frac{\partial v}{\partial x} + v\frac{\partial v}{\partial y} = -\frac{\partial \chi}{\partial y} + \frac{1}{R}\left(\frac{\partial^2 u}{\partial x^2} + \frac{\partial^2 u}{\partial y^2}\right) \qquad 1b$$

where all quantities are nondimensional and $R = \frac{U_\infty c}{\nu}$. If R is assumed large, the nondimensional boundary-layer thickness δ is much less than 1, and further, if the radius of curvature of the body surface is everywhere much smaller than δ, than 1a and 1b can be simpified to:

$$\bar{u}\frac{\partial \bar{u}}{\partial s} + \bar{v}\frac{\partial \bar{u}}{\partial n} = -\frac{\partial p}{\partial s} + \frac{1}{R}\frac{\partial^2 \bar{u}}{\partial n^2} \qquad (36)$$

$$\frac{\partial p}{\partial n} = 0 \qquad (37)$$

See Schlichting pp. 108-109 for details.[10] The continuity equation (2) takes the form

$$\frac{\partial \bar{u}}{\partial s} + \frac{\partial \bar{v}}{\partial y} = 0, \qquad 2a$$

where $\bar{u}$, $\bar{v}$, s, and n are the velocities and coordinates associated with a curvilinear coordinate system with s measured tangent to the body surface S_1, n measured normal to S_1. The origin of this coordinate system is taken as the stagnation point with s increasing toward the trailing edge. It will be assumed that the boundary layers on the upper and lower surfaces are completely independent and, therefore, may be treated separately. Many methods are available for solving equations 35, 36 and 2a with the boundary conditions

$$\bar{u} = \bar{v} = 0 \text{ at } n = 0$$

and

$$\bar{u} = U \text{ at } n = \delta.$$

For this work, the method of Pohlhausen as modified by Holstein and Bohlen was selected for the analysis. This method is based on the momentum integral equation,

$$RU\theta\frac{d\theta}{ds} + (2 + \frac{\delta^*}{\theta})\theta^2\frac{dU}{ds} = \frac{RC_f\theta}{2U}. \qquad (38)$$

Equation 38 is obtained by integrating equation 36 and 37 across the boundary layer. By assuming that a one-parameter family of velocity profiles exists in the form

$$\frac{\bar{u}}{U} = f(\eta) = a\eta + b\eta^2 + c\eta^3 + d\eta^4, \tag{39}$$

equation 38 can be reduced to the form

$$\frac{dZ}{ds} = \frac{F(K)}{U} \tag{40}$$

where $Z = R\theta^2$, $K = Z\frac{dU}{ds}$, and F(K) is a function which is independent of the body shape (see Appendix A). F(K) is plotted in Figure 5.

With the initial values of Z and $\frac{dZ}{ds}$ (see Appendix A again), and a given function U(s), Z can be calculated as a function of s. In the present work a fourth-order Funge-Kutta method was used to integrate Equation 40. When Z and, hence, θ is known, K can be determined since by definition $K = Z\frac{dU}{ds}$. Once Λ is calculated, the other parameter δ, δ^*, C_f, and H can be calculated by applying the appropriate relations in Appendix A. In the present work it was found convenient to represent U(s) for each Froude number and depth as a polynomial of the form

$$U(s)=a_o+a_1s+a_2s^2+ \ . \ . \ . \ +a_ks^k. \tag{41}$$

FIGURE 5 F(K) vs K USED IN LAMINAR BOUNDARY LAYER CALCULATIONS

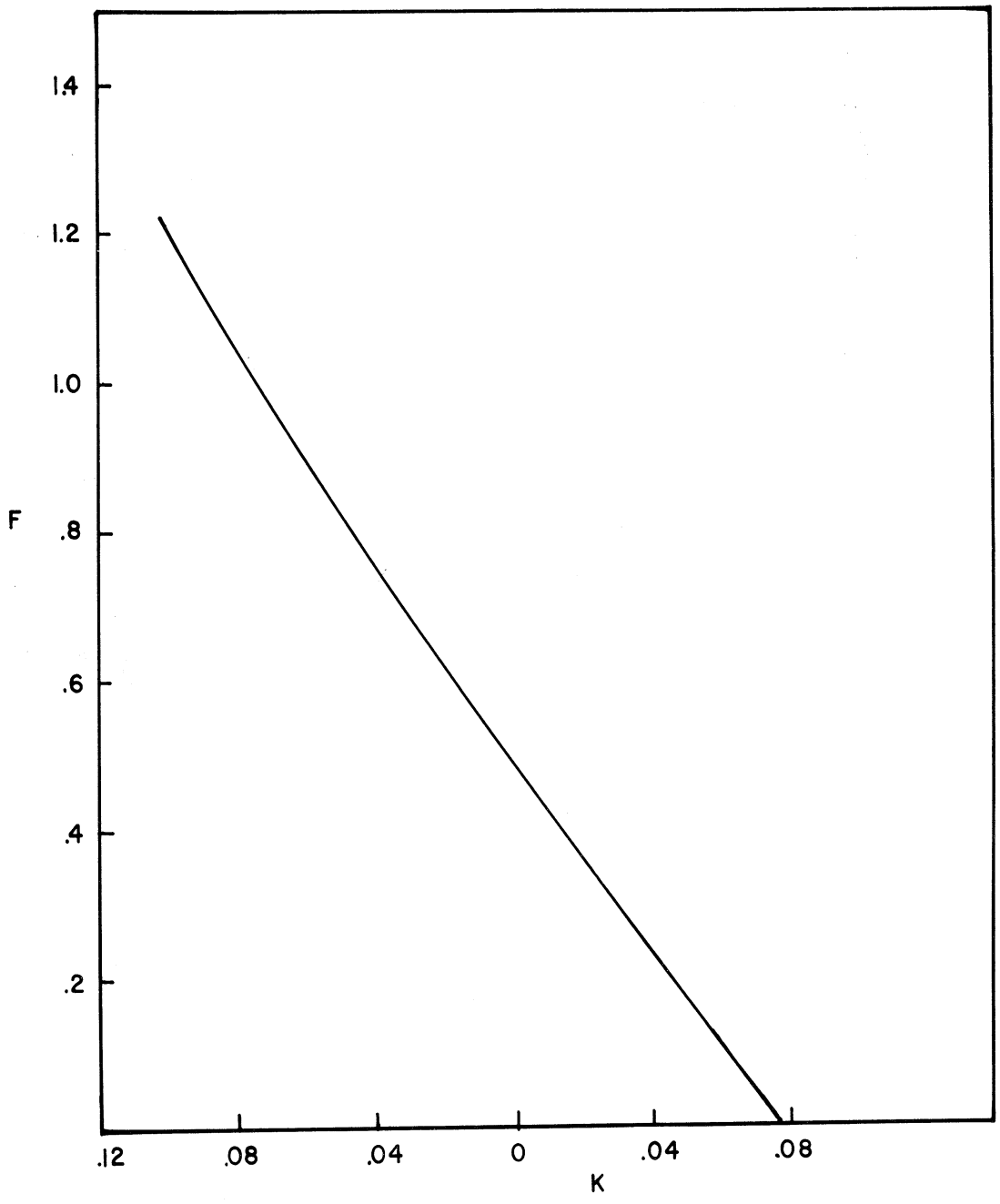

The coefficients a_o, a_1 . . . a_k and k were selected so that U(s) "best" represented the results obtained from the potential flow calculations, which yielded about 70 discrete values for the velocity at 70 values of s spaced about equally from the stagnation point to the trailing edge of the foil.

For each value of depth Froude number and depth investigated, different values of k starting with k = 2 and increasing to a maximum of k = 20 were tried. With a fixed k the coefficients of the resulting polynomial were found such that the quantity

$$E = \sum_{p=1}^{N} [\tilde{U}_p - U(s_p)]^2 \tag{42}$$

was a minimum. Here $\tilde{U}_p$ is the p^{th} discrete value, s_p is the s coordinate of the p^{th} value and N is the number of values. This is the usual least squares criterion.

The degree of the best polynomial was then selected as the smallest value of k for which E(k) exhibited a local minimum. Using this technique it was found that in most cases, polynomials of degree 5 or 6 were best and for these the maximum error between the theoretical values and the computed polynomial, $\sqrt{E}$, was only a few percent. A typical polynomial and the values it approximates are shown in Figure 6. The figure shows the top surface of the foil at a depth Froude number of .649 and a depth of 1.26.

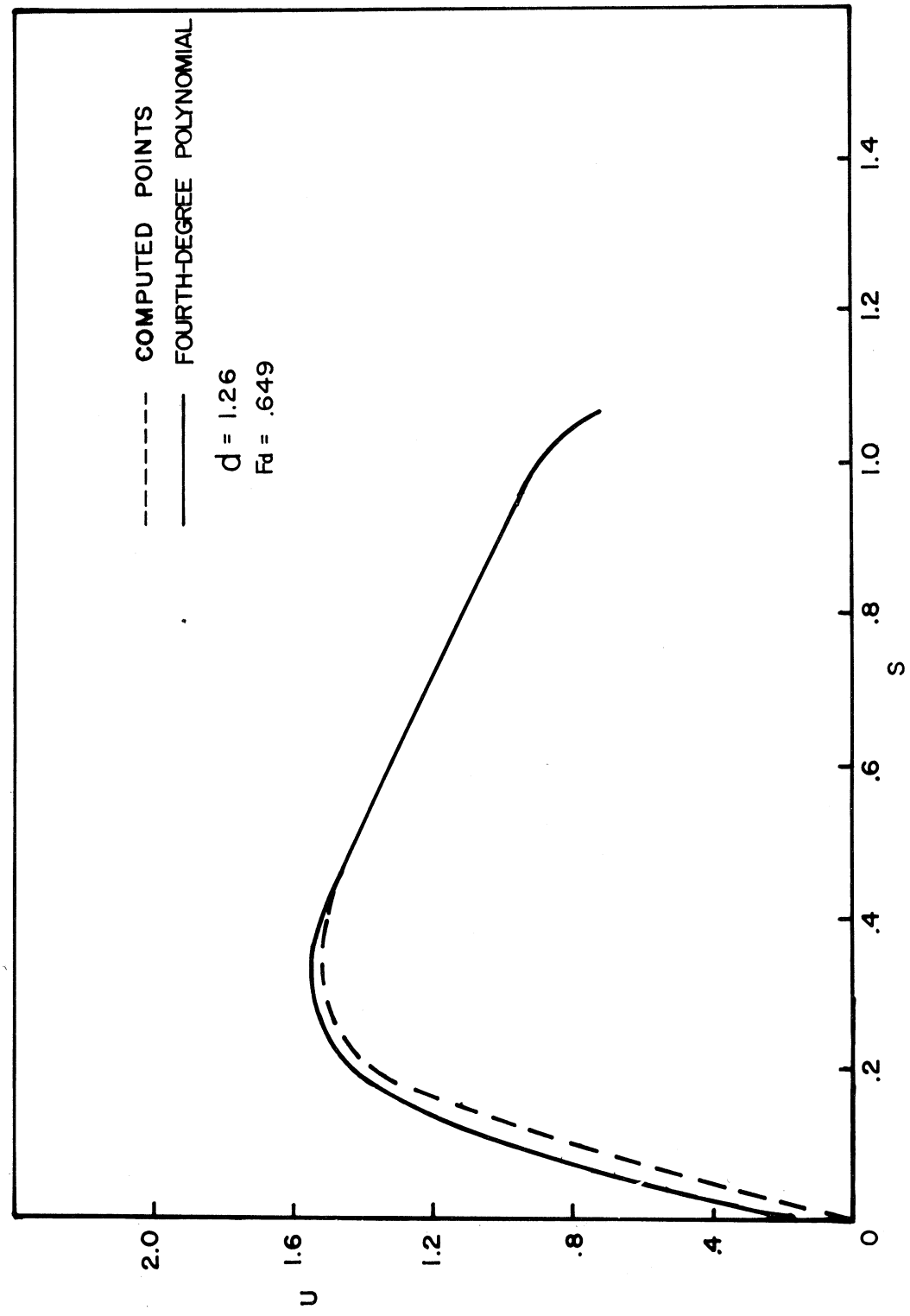

FIGURE 6 COMPARISON OF POLYNOMIAL AND COMPUTED VELOCITY DISTRIBUTION

In Figure 7 the parameter Δ, defined as the difference between the peak laminar skin friction coefficient on the bottom surface and the peak coefficient on the top surface, divided by the peak coefficient on the bottom surface, is plotted against depth Froude number for various depths. This is one of the important results of this work and shows that there is a significant local effect of the free surface on the skin friction of the foil. In an infinite fluid, of course, $\Delta = 0$ but due to the free surface the maximum laminar skin friction on the top surface is reduced compared to the bottom surface. In fact, Figure 7 resembles very closely the appearance of Figure 3, which shows the wave resistance coefficient plotted in the same manner.

III. 2. Transition of the Laminar Boundary Layer

The phenomenon of transition or the appearance of a time dependent flow component in the boundary layer obviously cannot be predicted by any theory in which steady flow is assumed. All that can be said about the possibility of the laminar boundary layer becoming turbulent from such an analysis as the Pohlhausen method is that at some point along the body laminar separation may occur.

Laminar separation occurs when $\frac{d\bar{u}}{dn}\Big|_{n=0} \leq 0$. In the Pohlhausen method inspection of the velocity profiles show this condition to occur for $\Lambda = -12$. Beyond this point boundary layer flow

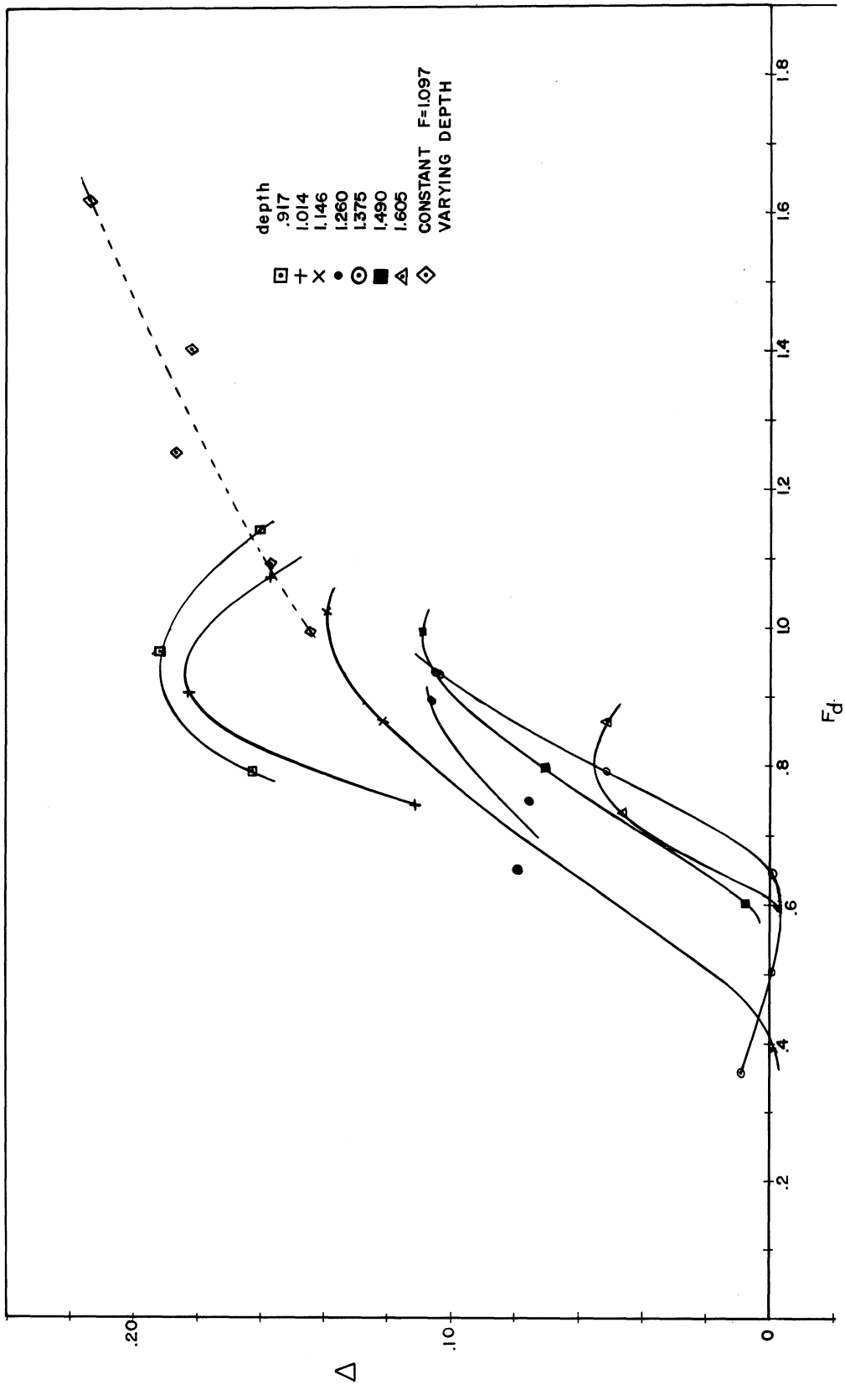

FIGURE 7 Δ vs Fd FOR VARIOUS VALUES OF DEPTH
THEORETICAL PRESSURE DISTRIBUTIONS

in the usual sense no longer exists and is replaced by a flow in which large scale "turbulence" and eddies become dominant features.

In most boundary layer type flows, if the Reynolds number is large enough, the laminar flow may become unstable at some point before the separation point. Immediately downstream from the point of instability is a region in which the flow is time dependent, but not yet full turbulent, termed the transition region. The details of transition are unclear even for simple flows and, hence, no analysis of this type of flow as it occurs in the present problem will be considered. It will be assumed, as others have done for lack of anything better, that the laminar boundary layer remains strictly laminar up to the point of instability, to be defined more clearly shortly, at which point the boundary layer becomes suddenly fully turbulent. For the purposes of this work the results of Lin, based on the method of small disturbances will be used to determine the point of instability of the laminar boundary layer.[11]

In the theory of small disturbances it is assumed that velocities and pressure in the boundary layer can be written in the form

$$\bar{u} = \tilde{u}(\eta) + u'(s,\eta,t) \tag{43}$$

$$\bar{v} = \tilde{v}(s,\eta) + v'(s,\eta,t) \tag{44}$$

$$p = \tilde{p}(s,\eta) + p'(s,\eta,t) \tag{45}$$

where the quantities with a tilda denote the mean flow and the primed quantities are assumed to be small compared with the mean flow and contain all of the time dependency.

Substituting equations 43, 44 and 45 into the Navier-Stokes equations and then assuming that a complex stream function Ψ exists of the form

$$\Psi'(s,\eta,t) = \bar{\Psi}(\eta)e^{i(\alpha s - \beta t)}$$

leads to the familiar Orr-Sommerfeld equation

$$(\tilde{u}-c)(\bar{\Psi}''-\alpha^2\bar{\Psi})-\tilde{u}''\bar{\Psi} = -\frac{i}{\alpha R_\delta}(\bar{\Psi}''''-2\alpha^2\bar{\Psi}''+\alpha^4\bar{\Psi}) \tag{46}$$

where $\bar{\Psi}$ is real and

$$c = \beta/\alpha = c_r + ic_i.$$

The necessary boundary conditions require that at $\eta = 0$ and at $\eta = \infty$ the disturbance must vanish, that is,

$$u' = v' = \bar{\Psi} = \bar{\Psi}' = 0 \text{ at } \eta=0 \text{ and } \eta=\infty \tag{47}$$

The problem is now to find for a given mean boundary layer profile $\tilde{u}(\eta)$, a value of c for each pair of α and $R_{\delta*}$. This accomplished, the curve of neutral stability, that is, those pairs of values of α and $R_{\delta*}$ for which $c_i = 0$ may be plotted. For $c_i \leq 0$, the amplitude of Ψ does not grow with time, and the disturbance is stable, while if $c_i > 0$ the disturbance is unstable and will grow with time. A typical stability curve for a laminar boundary layer is shown in Figure 8.

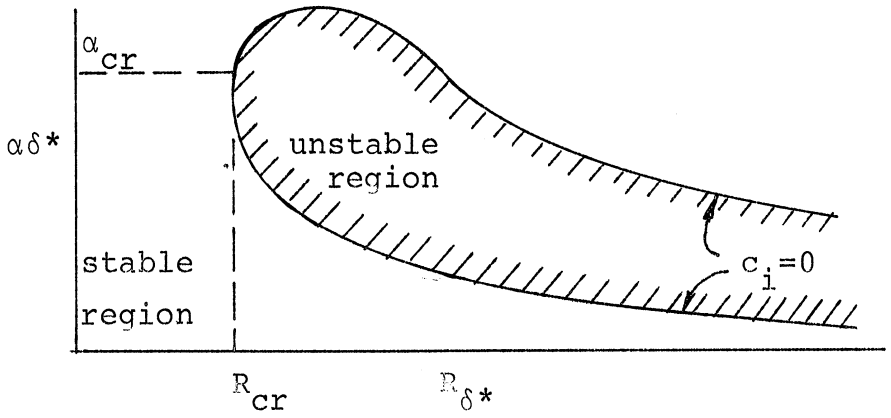

Figure 8. Typical Boundary Layer Stability Curve

R_{cr} is the Reynold's number below which disturbances of any wave length are stable.

Lin has given a simple approximate method for finding the critical Reynold's number for boundary layer flows.[11] First, the real part of c is computed as a solution to

$$\pi\tilde{u}'|_{\eta=0}(\tilde{u}\tilde{u}''/\tilde{u}'^3)_c = 0.58, \qquad (48)$$

where primes denote differentiation with respect to η, and the subscript c denotes the point whre $\tilde{u} = c$. After equation 48 is solved numerically, α_{cr} and R_{cr} can be found from the relations

$$\left.\begin{aligned} \alpha_{cr} &= \tilde{u}_w' C \\ R_{cr} &= 25\tilde{u}_w'/C^4 \end{aligned}\right\} \tag{49}$$

Hahnemann[12] carried out the above calculations for a one parameter family of profiles based on $\Lambda = R\delta^2\frac{dU}{ds}$. However, instead of a fourth-order polynomial in η, as is the case in the Pohlhausen method, for the stability calculations a sixth-order polynomial is better suited since it gives the higher order derivitives more accurately. The sixth-degree polynomial can be written in the same form as equation A6 (see Appendix A) with the A and B functions sixth-degree polynomials in η:

$$\left.\begin{aligned} A_6(\eta) &= 2\eta - 5\eta^4 + 6\eta^5 + 2\eta^6 \\ B_6(\eta) &= \frac{1}{5}\eta - \frac{1}{2}\eta^2 + \eta^4 - \eta^5 + \frac{3}{10}\eta^6 \end{aligned}\right\} \tag{50}$$

$\frac{\bar{u}}{v} = A_6(\eta) + \Lambda B_6(\eta)$ satisfies boundary conditions similar to those imposed on equation A6 (see Appendix A), but with the additional condition that the momentum thickness is the same

as the momentum thickness calculated using the fourth-degree profiles. In order to insure that a stability criteria based on a sixth-degree family of profiles is applicable to boundary layers calculated from fourth-degree polynomials, the shape factor, $H_4(\Lambda)$, for the fourth-degree profiles must be equal to the shape factor, $H_6(\Lambda)$, for the sixth-degree profiles for each Λ. H_4 and H_6 are plotted against Λ in Figure 9. Since the two curves differ by no more than 3 percent in the range of interest, the error in predicting R_{cr} should be fairly small. Figure 10 is a plot of R_{cr} as a function of the shape factor H_6.

It is now a simple matter to find the value of s for which the laminar boundary layer becomes unstable. Starting from the stagnation point the critical Reynold's number determined from Figure 10 is compared with $R_{\delta*}$. If $R_{\delta*} < R_{cr}$, the boundary layer is stable at the value of $R_{\delta*}$ in question and the process is repeated for increasing values of s until $R_{\delta*} = R_{cr}$. This value of s, s_{cr}, is termed the point of instability. At the outset it was thought that s_{cr} would be a function of depth and Froude number but this was not found to be the case. For most speeds and depths s_{cr} varied unsystematically between .32 and .34.

During transition, the characteristics of the flow change rapidly. In particular the shape factor $H = \frac{\delta*}{\theta}$ decreases to approximately half its laminar value. This results in a jump

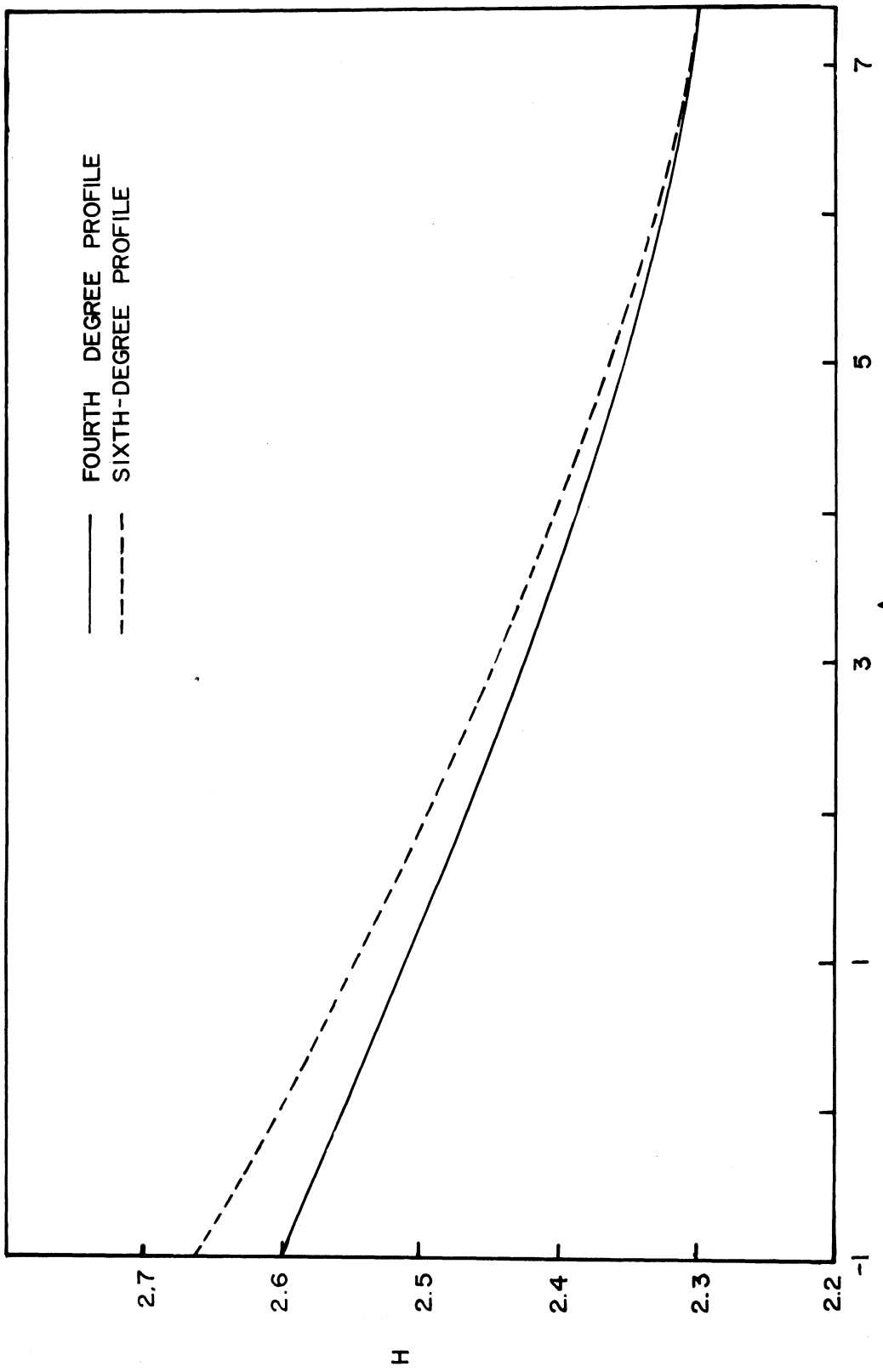

FIGURE 9 H vs Λ

FIGURE 10 CRITICAL REYNOLDS NUMBER vs H

(SIXTH-DEGREE PROFILE)

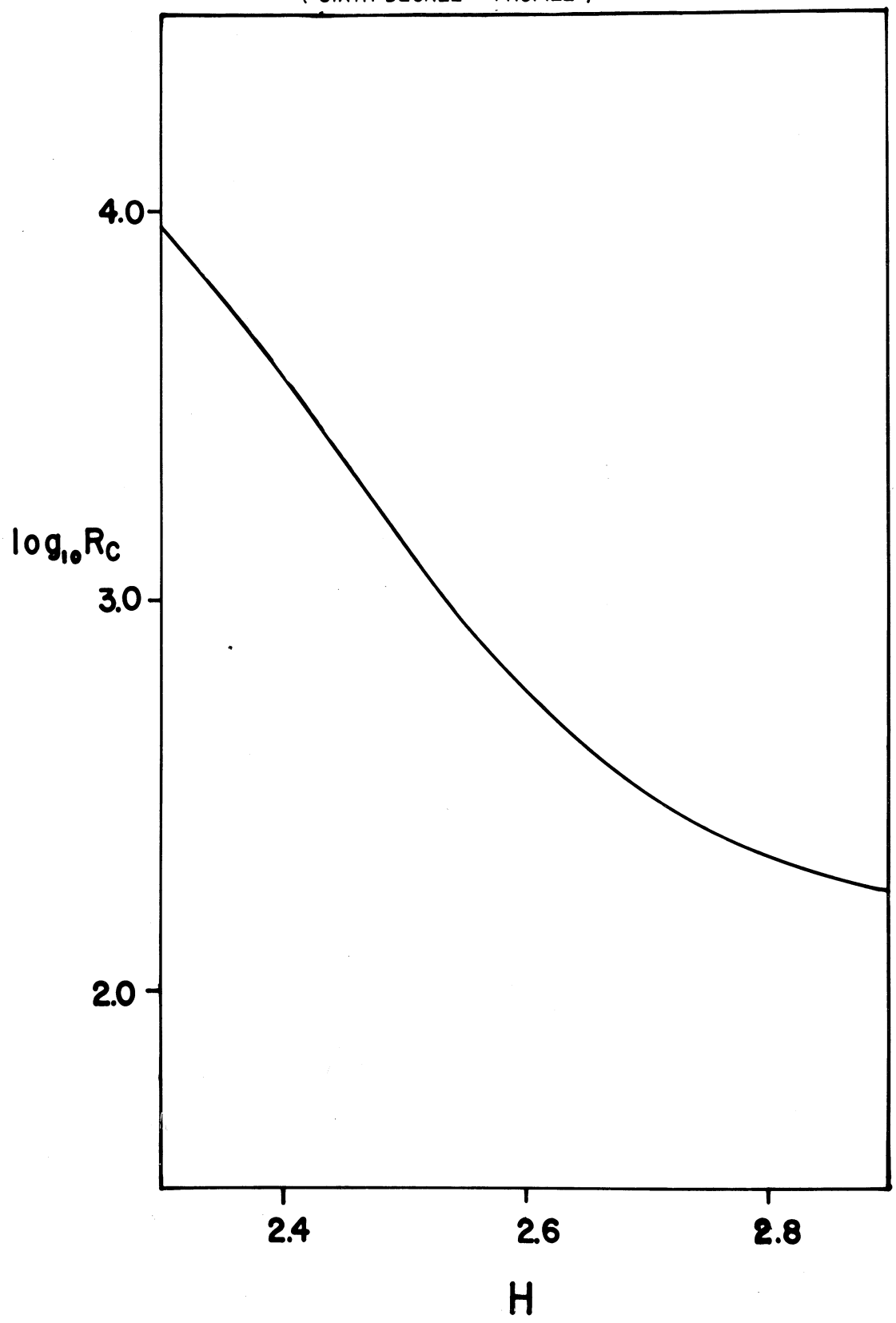

in the skin friction and changes in all the boundary layer thicknesses except θ which must be continuous across the point of transition due to momentum considerations.

III. 3. The Turbulent Boundary Layer

As mentioned before, aft of the point of instability, the boundary layer is assumed to be fully turbulent. In order to simplify the analysis of such an obviously complex flow in which there are more or less randomly fluctuating time dependent velocities, it is convenient and customary to divide the velocity components into their mean and fluctuating parts and write:

$$\bar{u} = \tilde{u}(s,n) + u'(s,n,\tau) \tag{51}$$

and

$$\bar{v} = \tilde{v}(s,n) + v'(s,n,\tau) \tag{52}$$

where τ is a nondimensional time, $\frac{tc}{U_\infty}$, and

$$\tilde{u} = \frac{1}{2T}\int_{-T}^{T}\bar{u}d\tau \text{ and } \int_{-T}^{T}u'\,d\tau = 0$$

T is some arbitrary time interval, at least an order of magnitude longer than the significant oscillations of u'. Similar expressions hold for $\tilde{v}$ and v'. Substituting expressions 51 and 52 into the Navier-Stokes equations, averaging the

time varying quantities with respect to time and making the usual boundary layer assumptions similar to those made in III. 1., the boundary layer equations for turbulent flow are obtained and can be written in the form

$$\tilde{u}\frac{\partial \tilde{u}}{\partial s} + \tilde{v}\frac{\partial \tilde{v}}{\partial n} = -\frac{\partial p}{\partial s} + \frac{1}{R}\frac{\partial^2 \tilde{u}}{\partial n^2} - \frac{\partial \overline{u'^2}}{\partial s} - \frac{\partial \overline{u'v'}}{\partial n} \tag{53}$$

$$\frac{\partial p}{\partial n} + \frac{\partial \overline{v'^2}}{\partial n} = 0 \tag{54}$$

The continuity equation

$$\frac{\partial \tilde{u}}{\partial s} + \frac{\partial \tilde{v}}{\partial n} = 0 \tag{55}$$

does not contain any time averaged quantities. In equations 53 and 54

$$\frac{\partial \overline{u'^2}}{\partial s}, \quad \frac{\partial \overline{u'v'}}{\partial n}, \text{ and } \frac{\partial \overline{v'^2}}{\partial n}$$

are unknown quantities related to the turbulent motion. The term $\frac{\partial \overline{u'^2}}{\partial s}$ is customarily neglected in equation 53 which leads, through continuity considerations, to the conclusion that the pressure can be considered to be constant across the boundary layer just as in the laminar case.

Completely analagous to the laminar analysis, equation 53 is integrated from $n = 0$ to $n = \delta$ to get as before

$$RU\theta\frac{d\theta}{ds} + (2+H)\theta^2\frac{dU}{ds} = \frac{RC_f\theta}{2U} \tag{56}$$

However, another unknown has entered the problem, namely $\overline{u'v'}$, and a simple family of boundary layer profiles cannot be determined as in the method of Pohlhausen.

There are many different methods for obtaining two extra equations so that θ, H, and C_f may be obtained as functions of s, all of which have to ultimately rely on experimental evidence. The method used in this analysis uses Head's concept of boundary layer entrainment[13] together with the Ludwig-Tillmann equation for C_f, which Moses feels is one of the most reliable approximations for adverse pressure gradients.

Following Head's arguments, if Q is the quantity of fluid flowing in the boundary layer past a plane perpendicular to the surface at a fixed s then $\frac{dQ}{ds}$ is the amount of fluid entrained by the boundary layer per unit length along the surface. He then assumes that the entrainment is a function only of the profile shape, the external velocity, and some measure of the boundary layer thickness. Instead of using $H^* = \frac{\delta-\delta^*}{\theta}$ as the profile shape parameter as Head did, the conventional shape parameter is used and the entrainment relation can be written

$$\frac{dQ}{ds} = f(H,U,\delta^*-\delta). \tag{57}$$

Now

$$Q = \int_0^{\delta} \tilde{u} dn = \int_0^{\delta} U dn - \int_0^{\delta} U\left(1 - \frac{\tilde{u}}{v}\right) dn = U(\delta - \delta^*)$$

so that

$$\frac{dQ}{ds} = \frac{d}{ds}[U(\delta - \delta^*)].$$

Finally, equation 57 may be written:

$$\frac{1}{U} \frac{d}{ds}[U(\delta - \delta^*)] = T(H). \tag{58}$$

where T(H) is the only function which need be determined from experimental data. By assuming that the profile shape can be characterized by only one parameter, H, the profile family is restricted to the form

$$\tilde{u} = \tilde{u}(H, \eta).$$

The measurements of Schubauer and Klebanoff[14], were used to determine the functional relationship described in equation 58. The results are shown in Figure 11. Considerable scatter is evident in the data but at least an approximate functional relationship is apparent which is very encouraging considering the assumptions made in deriving (58). A reasonable approximation for the function T is:

FIGURE 11 T(H) USED IN TURBULENT BOUNDARY LAYER ANALYSIS

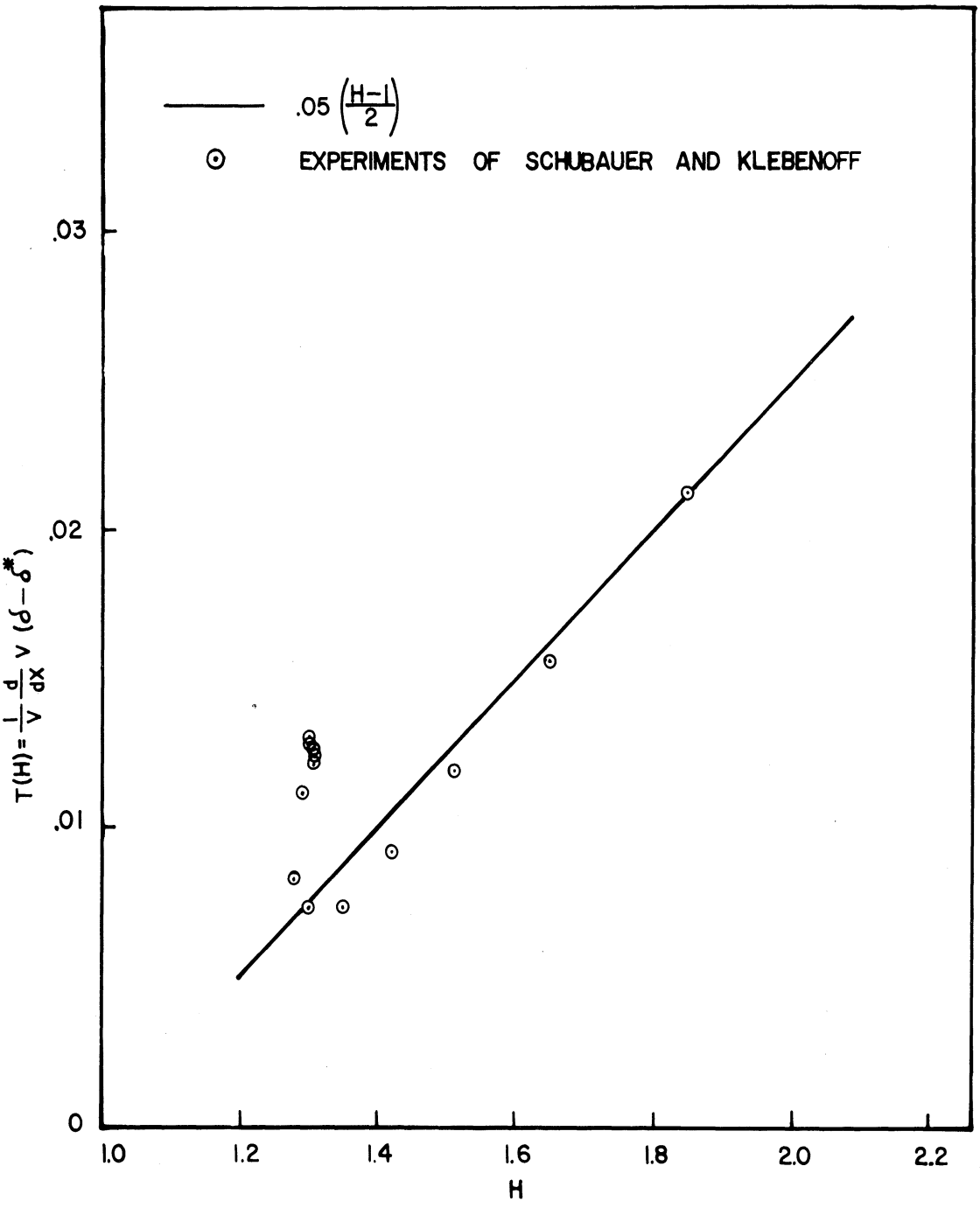

$$T(H) = .05\left(\frac{H-1}{2}\right). \tag{59}$$

The widely used and accepted Ludwig-Tillmann equation for C_f is used to relate C_f, H, and θ as follows:

$$C_f = .246\, R_\theta^{-.268} \times 10^{-.678H}. \tag{60}$$

If the velocity profiles are now assumed to obey the power law:

$$\frac{\tilde{u}}{v} = \eta^{1/k} \tag{61}$$

then from the definition of H, it can be shown that $k = \frac{2}{H-1}$. Now equation 61 can be used to eliminate δ and δ^* from (58) leaving finally three equations in the three unknowns θ, H, and C_f:

$$RU\theta\frac{d\theta}{ds} + (2+H)\theta^2\frac{dU}{ds} = \frac{RC_f\theta}{2U} \tag{56 repeated}$$

$$\frac{1}{U}\frac{d}{ds}\left[2U\theta\left(\frac{H}{H-1}\right)\right] = .05\left(\frac{H-1}{2}\right) \tag{62}$$

and

$$C_f = .246(RU\theta)^{-.268} \times 10^{-.678H} \tag{60 repeated}$$

Equation 60 can immediately be substituted into equation 56

to yield

$$RU\theta\frac{d\theta}{ds} + (2+H)\theta^2\frac{dU}{ds} = \frac{R\theta}{2U}[.246(RU\theta)^{-.268} \times 10^{-.678H}]. \qquad (63)$$

Now, defining the new variable

$$\Omega = 2U\theta\left(\frac{H}{H-1}\right)$$

Equations 62 and 63 can be written in the form

$$\frac{d\Omega}{ds} = G_1(\Omega,\theta) \qquad (64)$$

$$\frac{d\theta}{ds} = G_2(\Omega,\theta) \qquad (65)$$

and given initial values for Ω, θ, G_1, and G_2, Equations 64 and 65 can be simultaneously integrated step by step using again, a fourth-order Runge-Kutta procedure to yield $\Omega(s)$ and $\theta(s)$ from which $C_f(s)$ and $H(s)$ can immediately be obtained. The total skin friction coefficient of the foil can now be obtained by numerically evaluating the following integral:

$$(C_f)_{ave} = \frac{1}{2}\left[\frac{1}{S_T}\int_0^{S_T} C_{f_T} \cos[\gamma(s)]ds + \frac{1}{S_B}\int C_{f_B} \cos[\gamma(s)]ds\right] \qquad (66)$$

where S_T and S_B are the lengths of top and bottom surfaces, C_{f_T} and C_{f_B} are the local skin friction coefficients on the

two surfaces, and $\gamma(s)$ is the angle between the tangent to the surface and the horizontal.

Before applying the above turbulent boundary layer analysis to the foil under investigation it was checked against the experiments of Moses and was found to agree fairly well.[15] Moses investigated the turbulent boundary layer in various adverse pressure gradients. Using the same pressure gradients the above method was applied to predict the development of θ and H. These results are shown compared with Moses' experiments in Figures 12, 13, and 14. Agreement is seen to be reasonable for velocity distributions 1 and 2, which are not severe, but not as good for distributions 3, 5 and 6 which are strongly adverse. Fortunately, the distribution on the after portion of the hydrofoil under investigation is not severely adverse and the theory is therefore probably quite accurate. Figure 15 shows the boundary layer characteristics on the top surface of the foil at a depth Froude number of .751 and a depth of 1.26. Similar plots for all the conditions investigated can be found in Appendix 1. Figure 16 shows the nondimensional quantity $\overline{C_f}$ which is defined as the total skin friction of the foil divided by the calculated skin friction coefficient of the deeply submerged foil operating at the same Reynolds number. $\overline{C_f}$ is plotted against the depth Froude number with the depth as parameter.

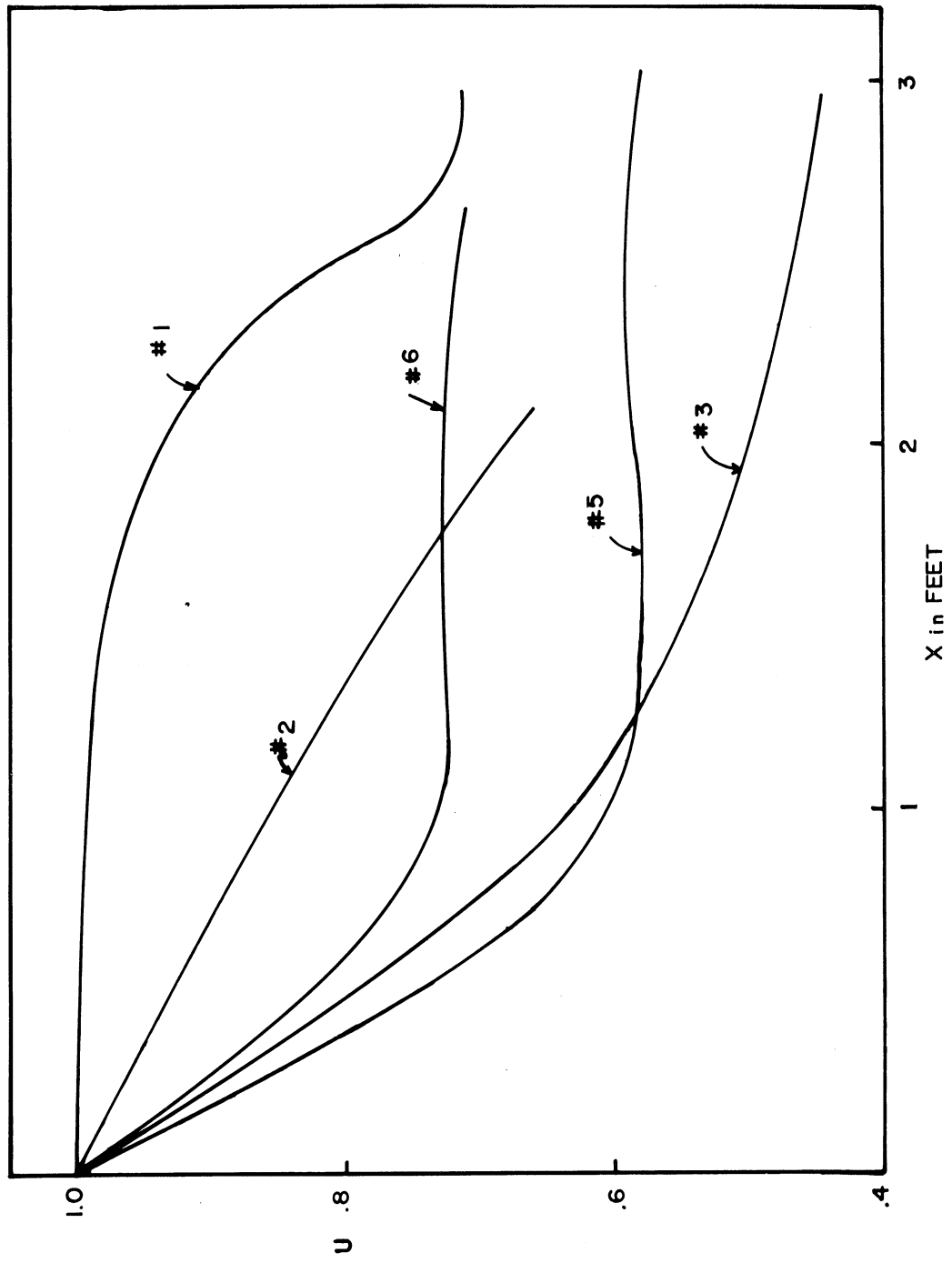

FIGURE 12 U vs X. VELOCITY DISTRIBUTIONS AFTER MOSES

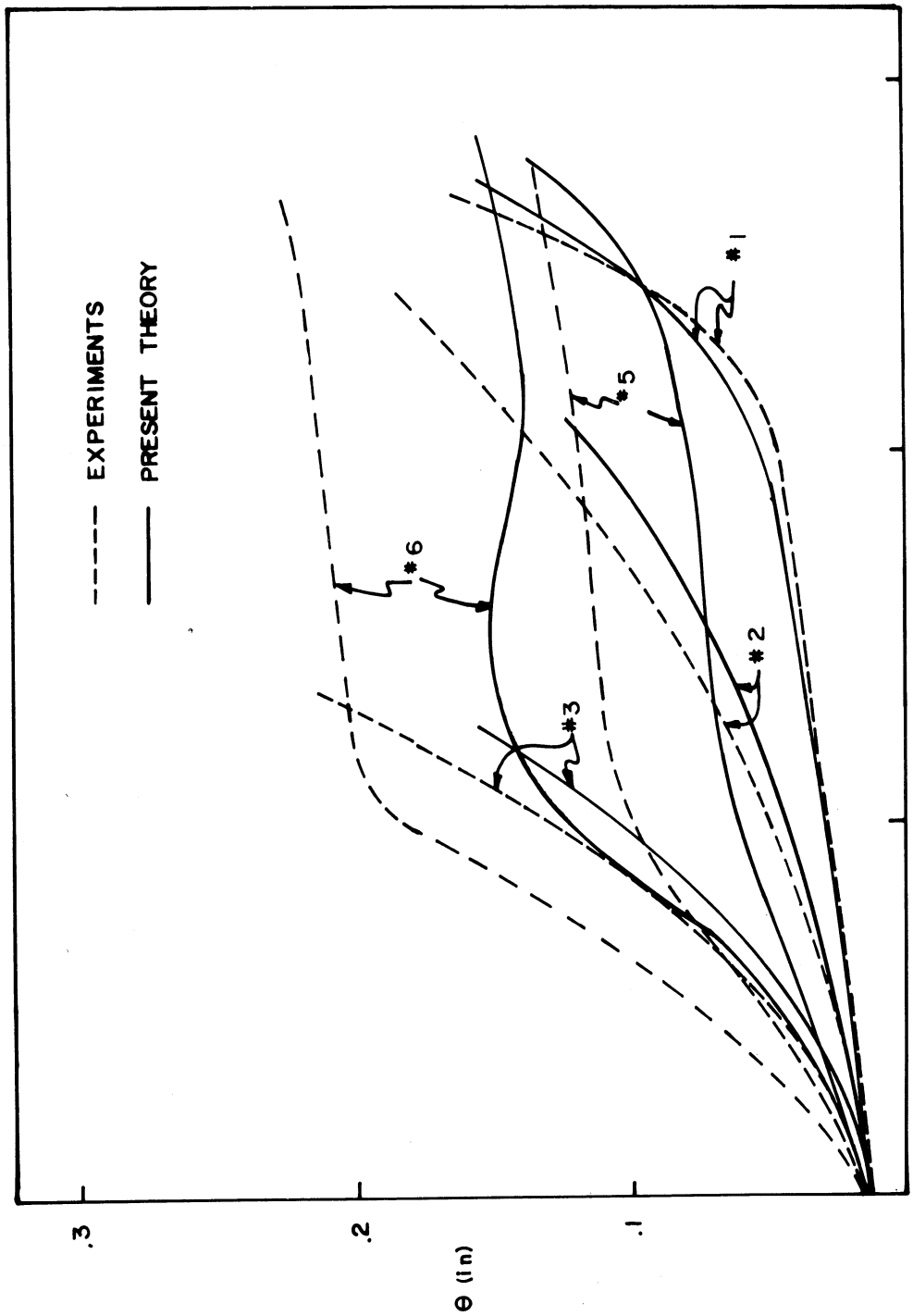

FIGURE 13 Θ vs X FOR MOSES' VELOCITY DISTRIBUTIONS

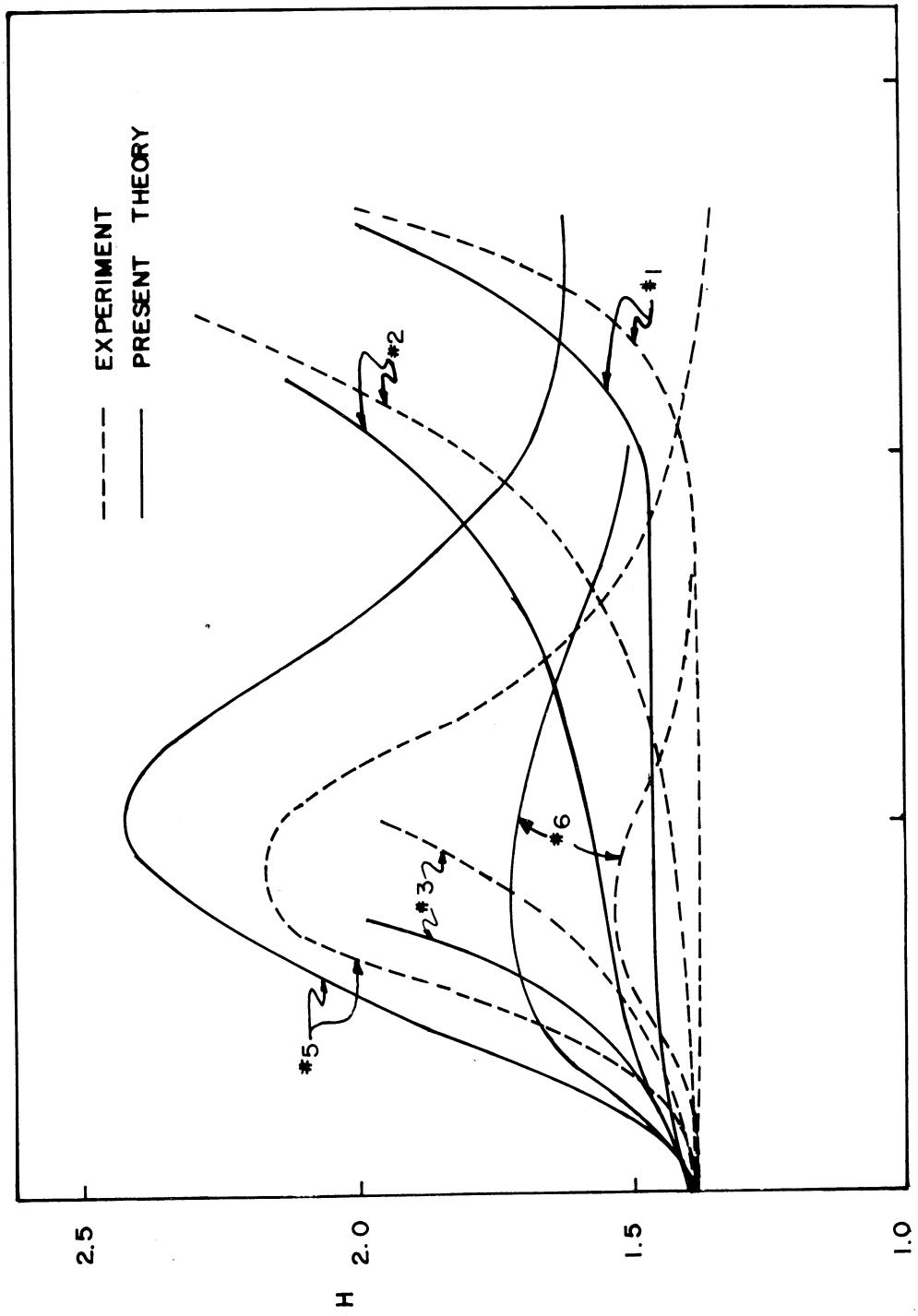

FIGURE 14 H vs X FOR MOSES' VELOCITY DISTRIBUTIONS

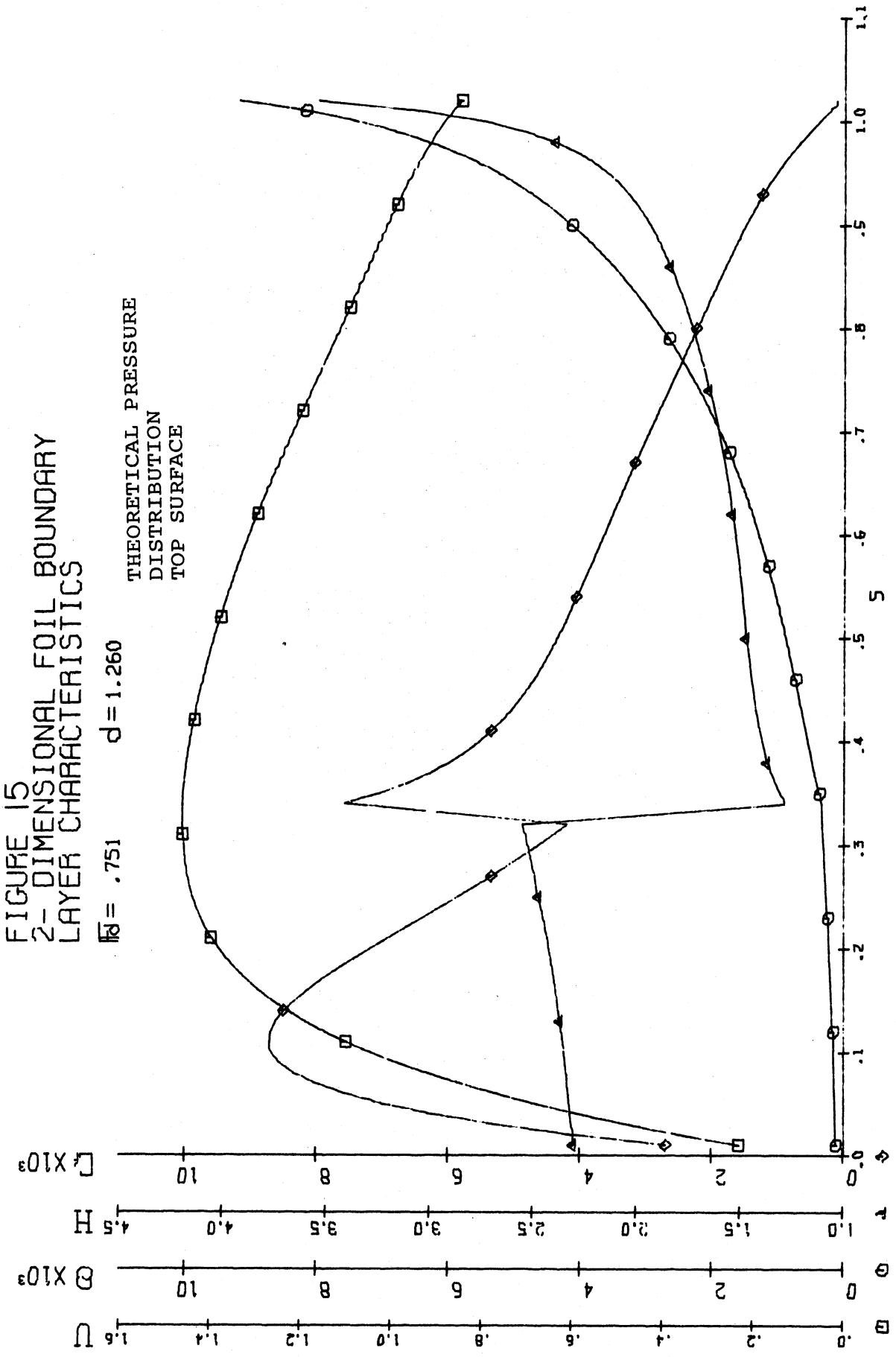
FIGURE 15
2- DIMENSIONAL FOIL BOUNDARY
LAYER CHARACTERISTICS
M = .751
d = 1.260
THEORETICAL PRESSURE
DISTRIBUTION
TOP SURFACE
U
Θ X10³
H
δ* X10³
S

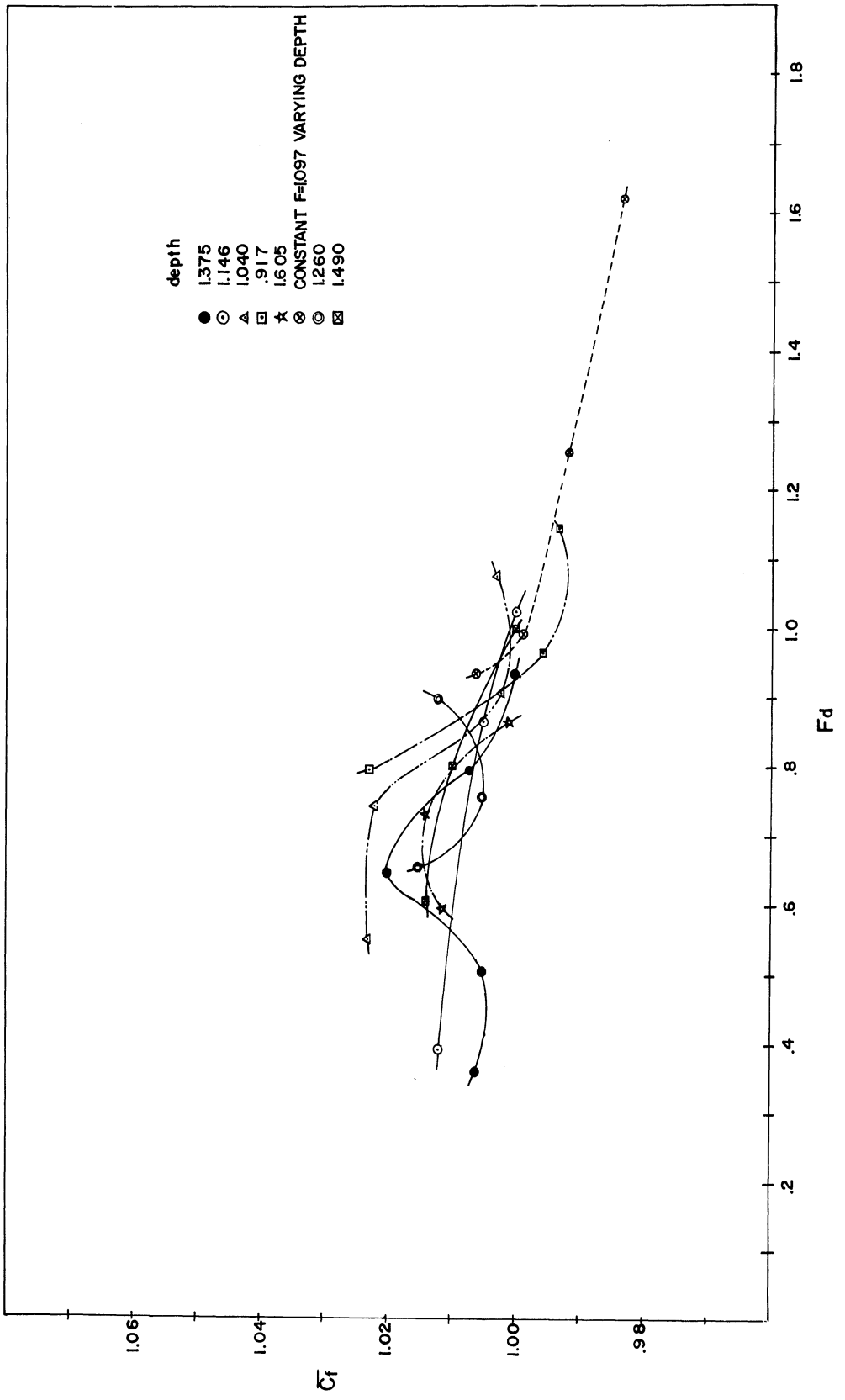

FIGURE 16 $\bar{C}_f$ vs Fd FOR VARIOUS VALUES OF DEPTH
THEORETICAL PRESSURE DISTRIBUTIONS

The dashed line is a line of constant chord Froude number, F. The interesting and somewhat surprising feature of Figure 16 is the very small influence of depth and Froude number on $\overline{C_f}$. For all depths and Froude numbers $\bar{C}_f$ lies between .98 and 1.02. In constrast Δ, plotted in the same manner in Figure 7, has a maximum value of .20. The large effect of the free surface on the laminar skin friction near the nose of the foil obviously does not have a great influence on the overall drag coefficient since the shear stress at the nose is acting largely perpendicular to the direction of motion.

Further, the distortion of the pressure distributions due to the free surface seems to be limited to the forward part of the foil since the turbulent skin friction is not affected nearly as strongly.

IV. Experimental Program

To attempt to verify the results obtained in the previous sections and to show that influences of the free surface on the boundary layer could actually be observed, a series of experiments were carried out using a foil with a span of 11 feet and a chord length of about 13 inches. The foil was constructed with a removable hollow center section (see Figure 17) fabricated out of .25 inch thick aluminum so that instrumentation could be readily installed and maintained. The foil had a section shape the same as that used in the theoretical investigation. To enhance the two dimensionality of the flow and also provide a means for supporting the foil, end plates were fitted.

These plates extended upward through the free surface and fastened to the towing carriage. The end plates were thin and the edges were faired so that the free-surface disturbances due to them were minimal. The foil was towed in the towing tank of The University of Michigan's Ship Hydrodynamics Laboratory. The tank is 360 feet long, about 22 feet wide, and 12 feet deep. The foil was attached to a lightweight auxiliary carriage which was towed behind the main carriage. The speed of the carriage could be kept constant to within about one-half percent. Three investigations were carried out, the first two simultaneously:

Figure 17. Center Section of Foil

1. Wave profiles were recorded at various depths and depth Froude numbers.
2. At each of the conditions that wave profiles were measured, the pressure distribution over the surface of the center section of the foil was measured.
3. At selected depths and depth Froude numbers attempts were made to directly measure the local skin friction as a function of s using flush mounted hot film probes.

IV. 1. Wave Profile Measurements

To determine the wave resistance experimentally by means of equation 23, the wave profiles generated by the foil at various depths and depth Froude numbers were measured. The waves were measured by using a thin enamel coated copper wire suspended at a fixed point in the tank as a variable capacitor which changed its capacitance linearly with the depth of submergence of the wire. As the foil passed the wire the accompanying wave train caused the capacitance to change, the changing capacitance was converted to a voltage proportional to the wave height by means of a capacitance bridge, and the voltage was recorded on a strip-chart recorder. Great care had to be taken to make sure the wire did not become contaminated or the linearity of the system would deteriorate considerably. Before any waves were

measured, the foil was run at a great number of depths and Froude numbers to try to determine the region of breaking waves found by Salvesen in his experiments. He states that " . . . at even smaller submergences [than one foot] the waves break down completely leaving no regular waves behind the body, but only some kind of a 'hydraulic jump'." If the foil is accelerated monotonically up to a constant speed this description of the breaking reion is essentially correct. However, it was found that at any depth there was a speed at which the breaking waves disappeared. Once this speed was reached and the wave pattern became smooth, the foil could be slowed down considerably before breaking occured again. In fact, the foil could be operated at a Froude number of .9 at any depth (see Figure 18) without breaking waves. Even when half of the foil was above the undisturbed mean water (d = 0) a smooth nonbreaking flow could be obtained if the foil was accelerated to a Froude number of $\simeq 2.0$ and then decelerated to F = .9. As the theory predicts there were no observable waves behind the foil. Figures 19 and 20 show examples of the recorded wave records plotted against the nondimensional length coordinate x/F^2. The results in Figure 19 were obtained at one depth and only the speed was varied. The results in Figure 20 were obtained by holding U_∞ constant and varying d. The amplified wave which sometimes appears near the end of the records was caused by the

FIGURE 18 WAVE STABILITY OF TWO-DIMENSIONAL HYDROFOIL

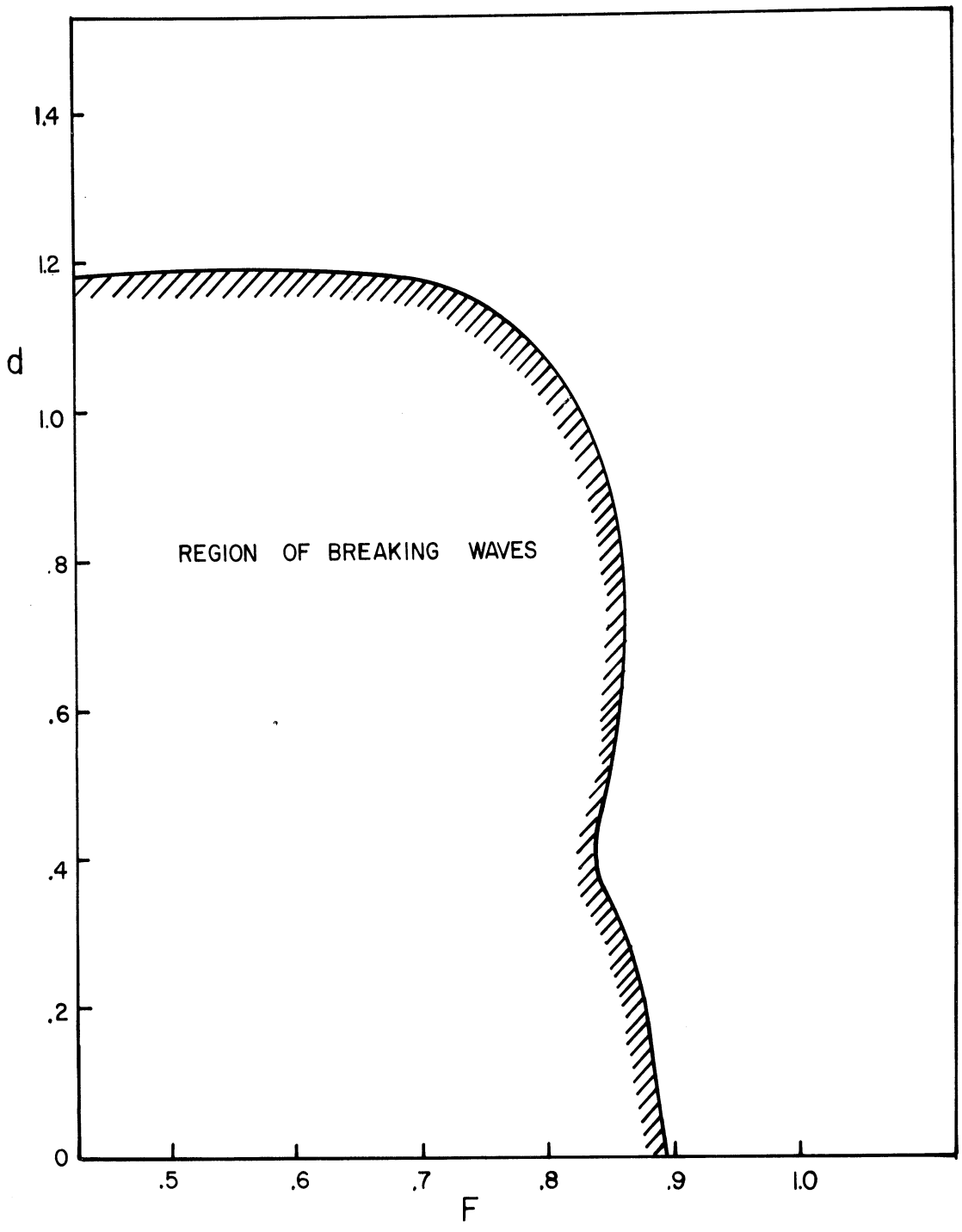

FIGURE 19
MEASURED WAVE AMPLITUDES VERSUS X/F^2 FOR VARIOUS VALUES OF DEPTH FROUDE NO.: d = 1.26

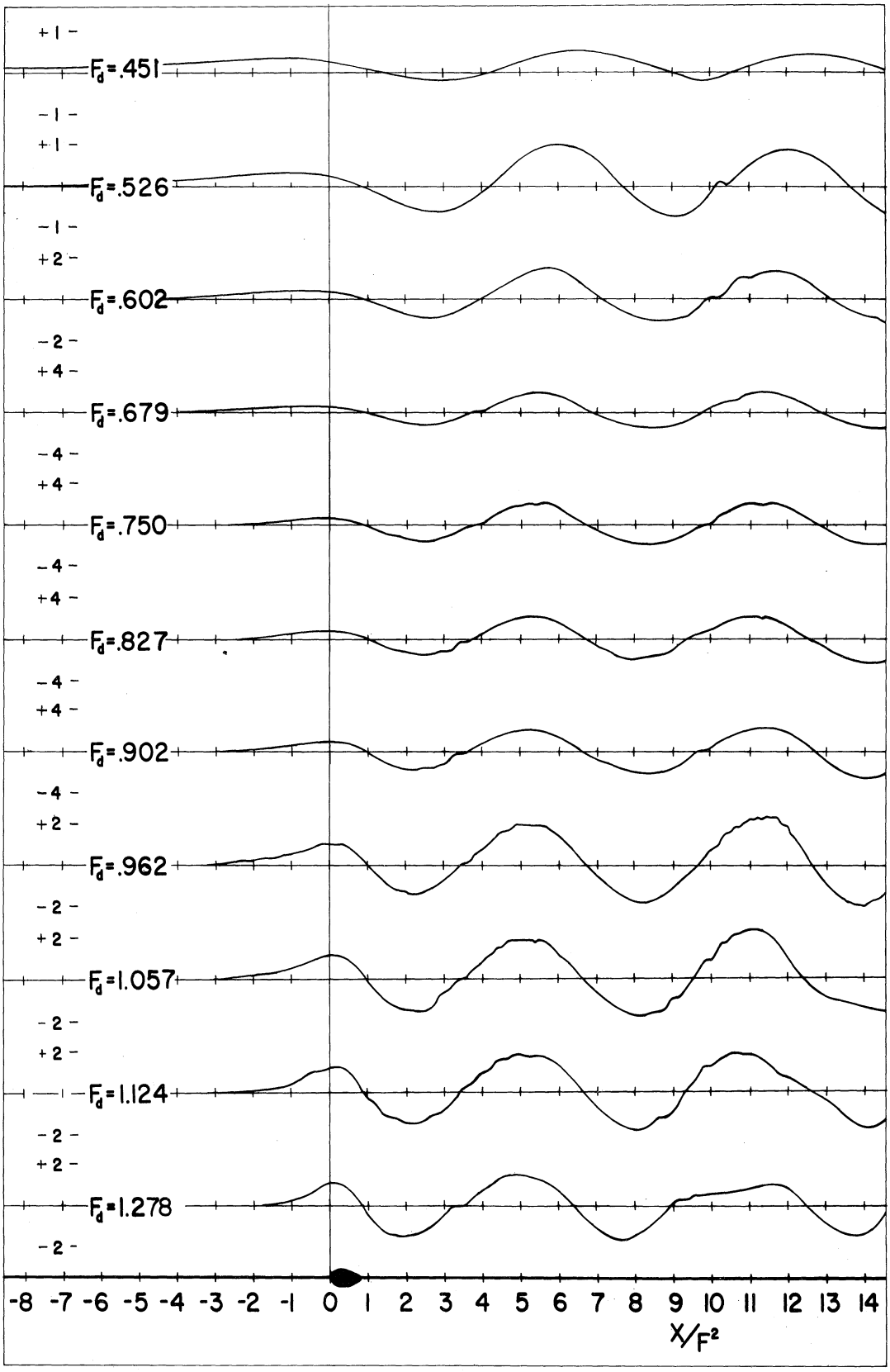

FIGURE 20
MEASURED WAVE AMPLITUDES VERSUS X/F^2 FOR VARIOUS VALUES OF DEPTH FROUDE NO.: F = 1.097

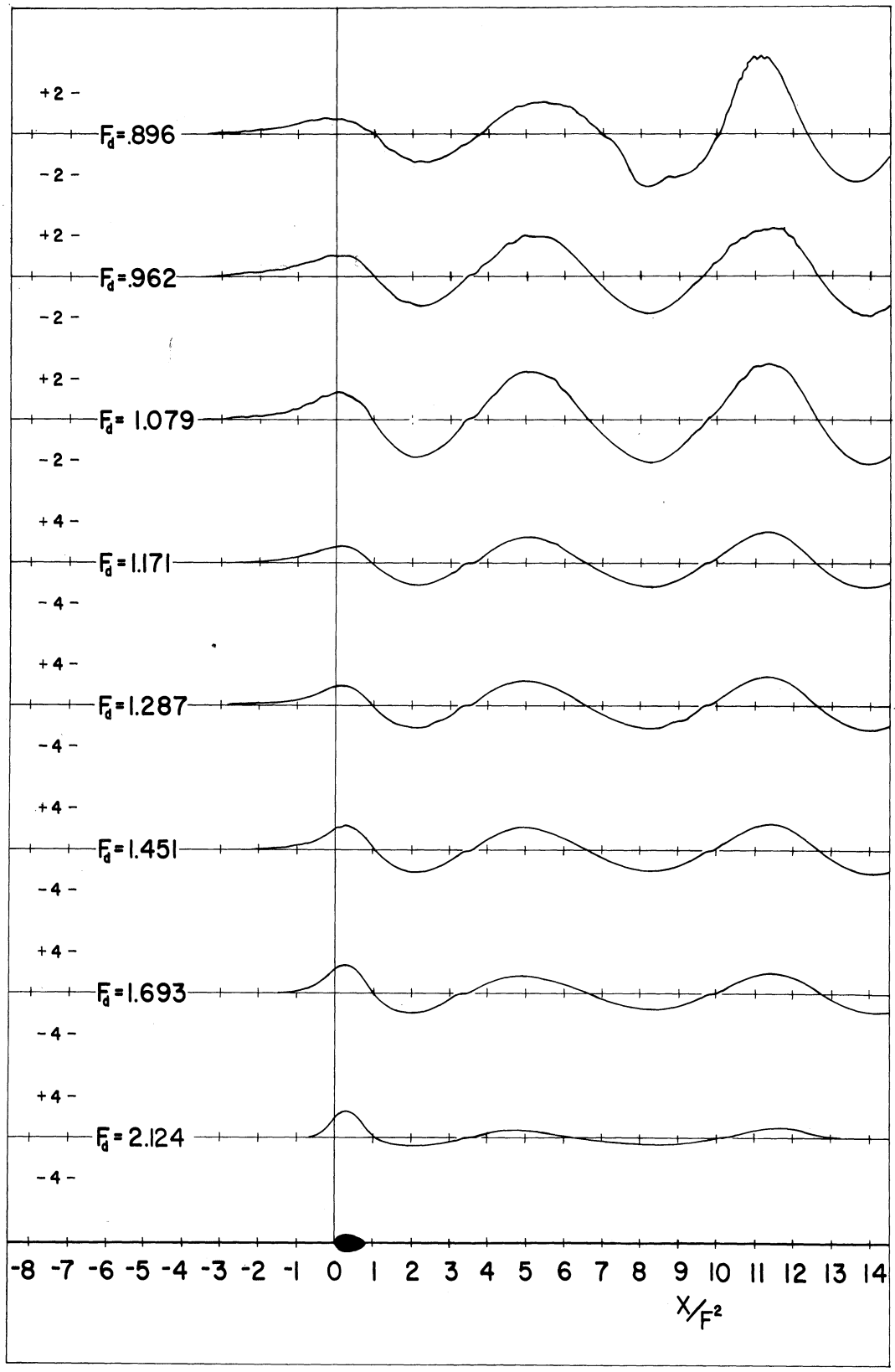

transverse waves caused by the end plates converging at the center section, where the measurements were taken, and interfering with the wave profile. Figure 21 shows a comparison between the measured profile and the computed profile for a depth of 1.26 and a depth Froude number of .750. The frequent occurrence of a flat spot in the measured profile at the undisturbed free surface is not predicted by the theory and cannot yet be explained. It may be caused by a malfunction of the capacitance wire due to contamination near the free surface but this seems unlikely since the mean vertical position of the wire was changed frequently with no effect. A more realistic hypothesis, but as yet unconfirmed, is that the orbital velocity in the wave changes sign at precisely the point where the anomaly always appeared. This change in the cross flow around the wire could conceivably cause the flat spots in the record. However, attempts to produce a similar effect under controlled conditions failed. The wire proved to be insensitive to small cross flows regardless of direction.

In Figure 22, the wave resistance computed from the measured profiles is compared with the similar experiments of Salvesen, and, in Figure 23, is compared with both the consistent linear theory of Giesing with circulation and the approximate theory with no circulation and the body boundary condition unsatisfied.

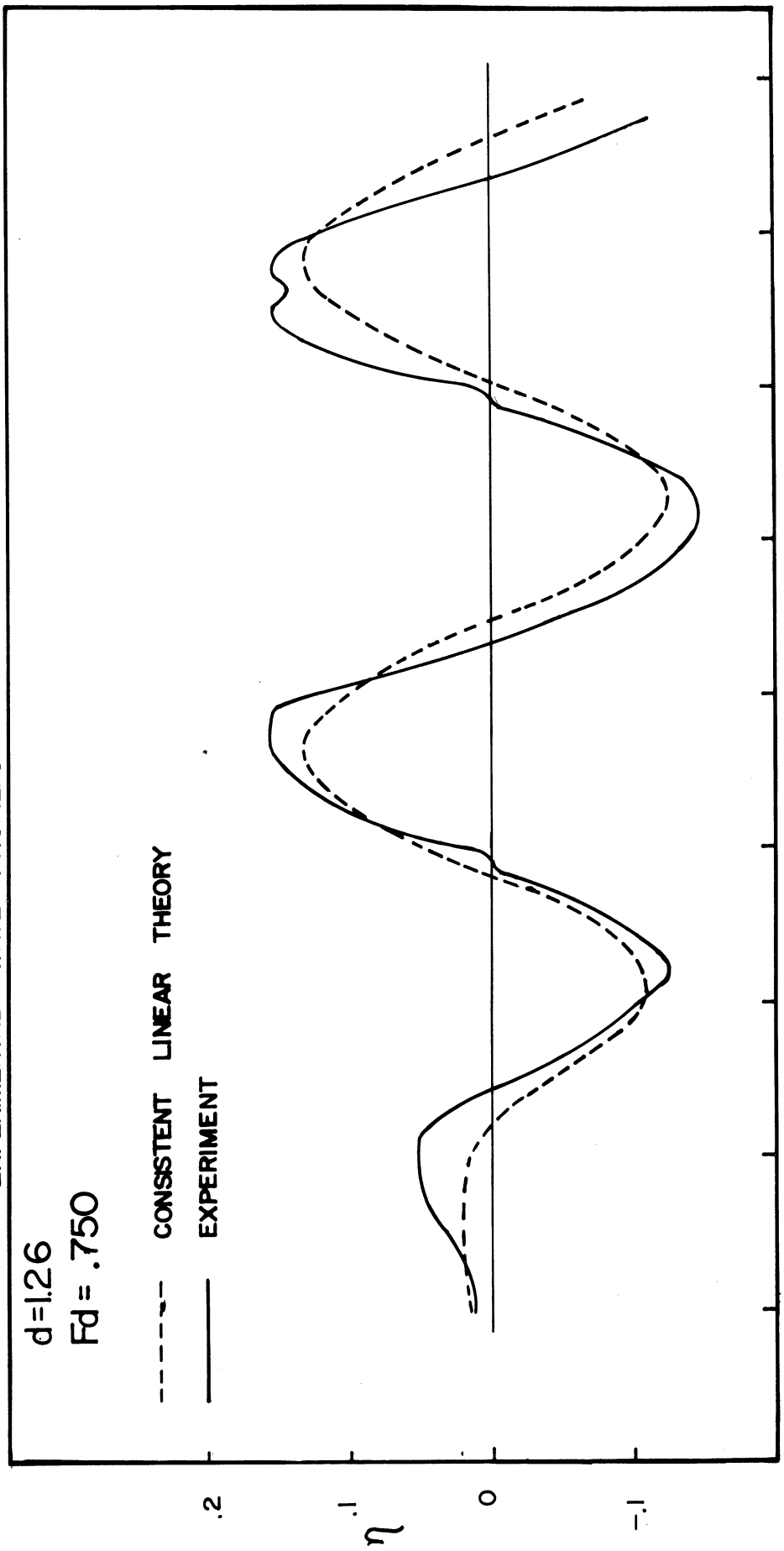

FIGURE 21 COMPARISON BETWEEN THEORETICAL AND EXPERIMENTAL WAVE PROFILES

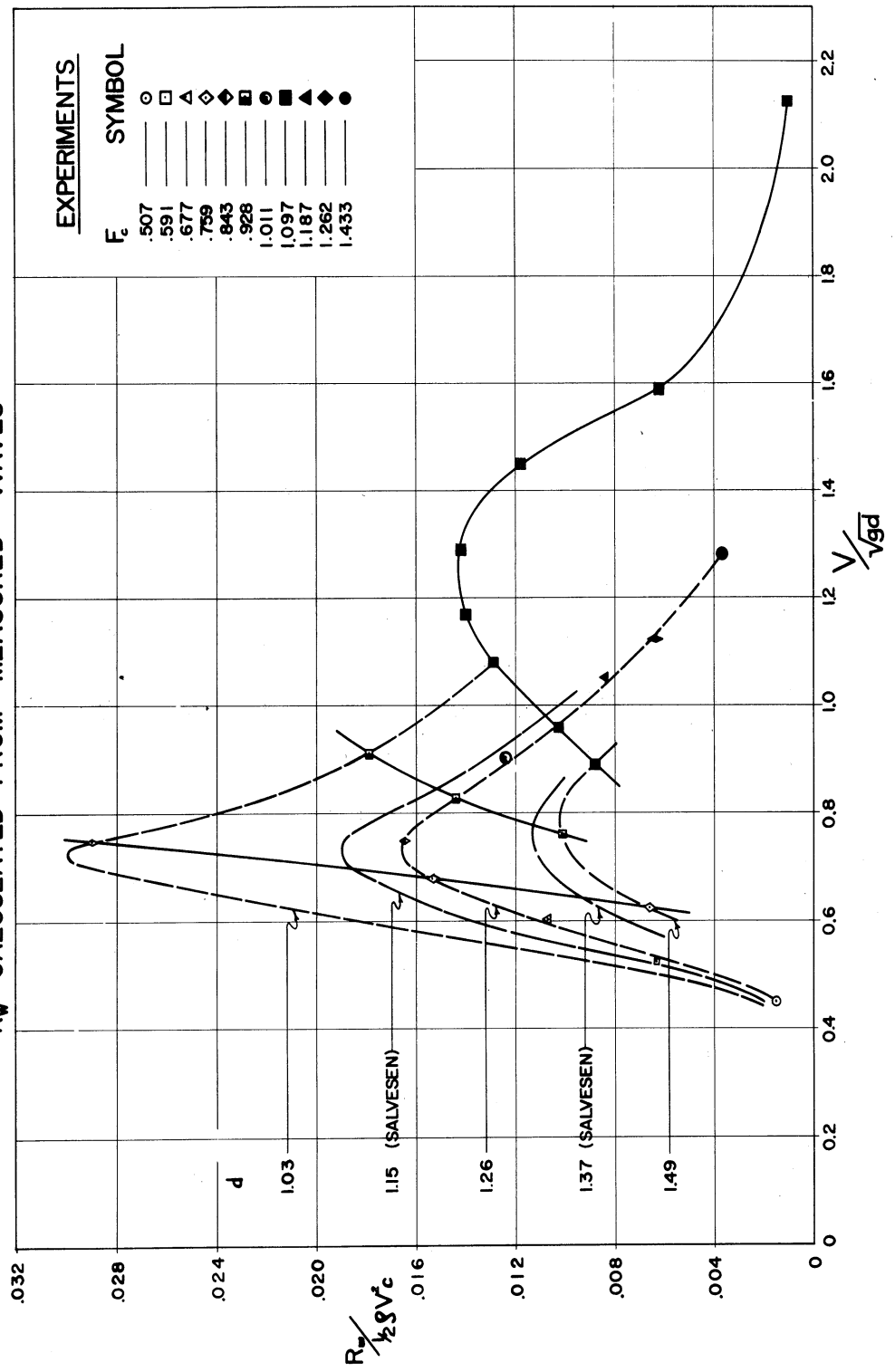

FIGURE 22
WAVE RESISTANCE VERSUS DEPTH FROUDE NO. FOR VARIOUS VALUES OF DEPTH AND FROUDE NO.
R_w CALCULATED FROM MEASURED WAVES

FIGURE 23
WAVE RESISTANCE VERSUS DEPTH FROUDE NO. FOR VARIOUS VALUES OF DEPTH. A COMPARISON OF THEORY AND EXPERIMENT

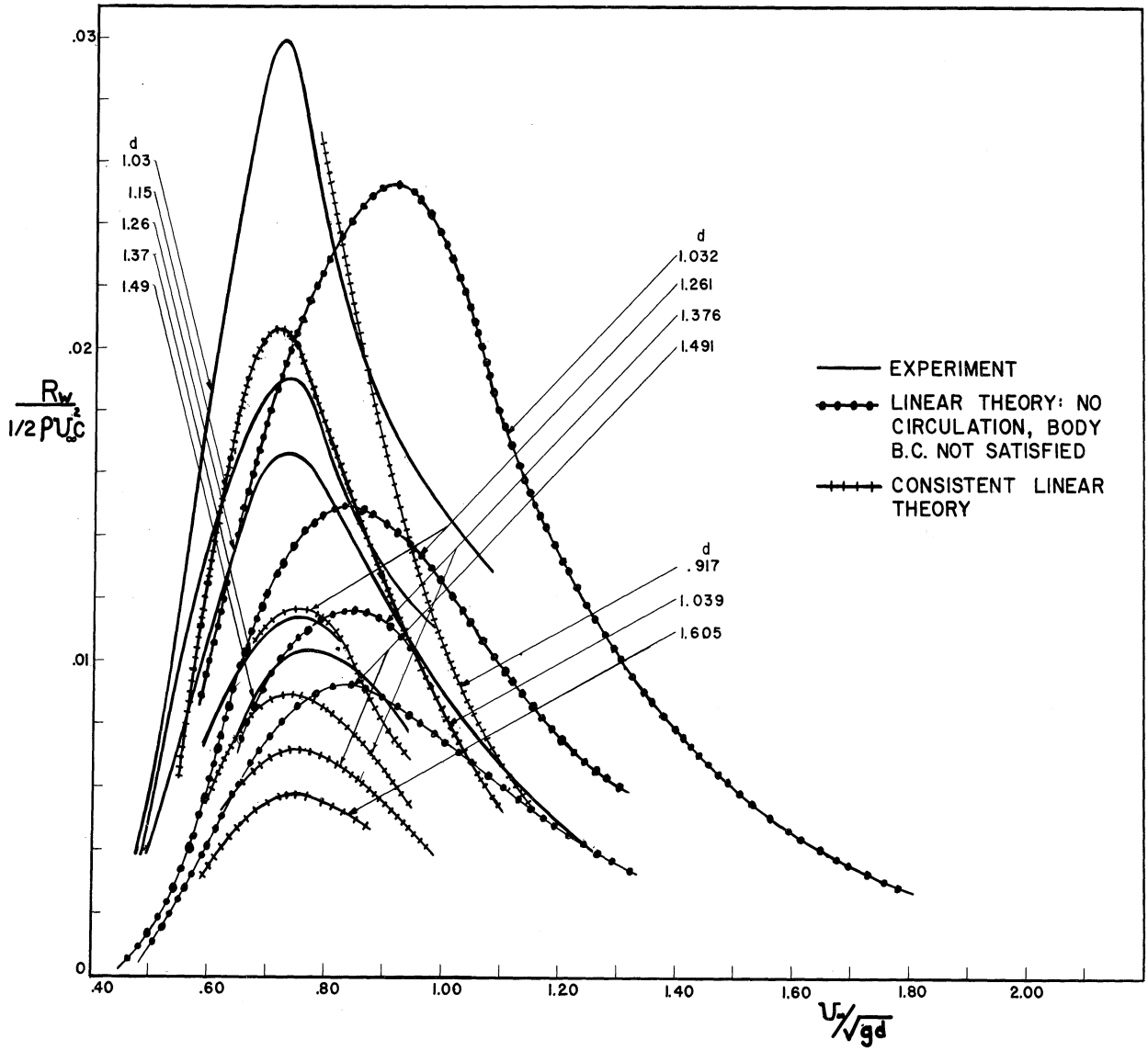

It appears that except for a shift in the peak values the simple linear theory gives surprisingly close agreement with the experiment, while the consistent linear theory with circulation predicts considerably lower wave resistance but predicts the peaks correctly.

IV. 2. Pressure Measurements

Twenty-eight equally spaced holes, .095 inches in diameter, were drilled in the aluminum center section in a diagonal pattern so that the flow to each hole would not be affected by holes farther forward. Fourteen holes were drilled on the top surface and fourteen on the bottom. Into each hole was fitted a small plastic tube. Inside the center section larger tubes were joined to the small ones and were led out the end of the foil and up to a 28 tube manometer board. The small plastic tubes were cut off flush with the outside surface of the foil. Each tube on the manometer board was connected to a common air reservoir, so that the fluid levels in the tubes could be raised to a convenient height. The response of the system was good enough so that by the end of a run down the tank the fluid levels had reached equilibrium, making a complicated shut-off value unnecessary. Data was taken by photographing the manometer board near the end of each run and then projecting the resulting negative on a large screen from which the pressure

at each hole could be read to an accuracy of ±.01 inches of water. Using Bernoulli's equation the resulting pressure distributions were converted to velocity distributions for the top and bottom surfaces. Polynomials were then fitted to the raw data in the same fashion as for the theoretical velocity distributions. Figure 24 shows a comparison between the experimental and theoretical velocity distributions on the top surface for a depth of 1.26 and a depth Froude number of .750. They are in close agreement except near the trailing edge where the turbulent boundary layer prevents total pressure recovery. It is encouraging that the experimental pressure distributions show no evidence of large scale separation, except very near the trailing edge, as might be expected on such a thick foil.

These velocity distributions were then used to calculate the boundary layers as detailed in Part III. Figure 25 is a plot of U, θ, H, and C_f as a function of s for a depth of 1.26 and a depth Froude number of .750. This figure is analogous to Figure 15, for which the theoretical velocity distribution was used to calculate the boundary layer characteristics. Similar plots for the other depths and Froude numbers can be found in Appendix 2.

Figures 26 and 27 show Δ and $\overline{C_f}$, plotted against F_d for various values of d calculated from the experimental velocity distributions. Notice that the curves are of similar

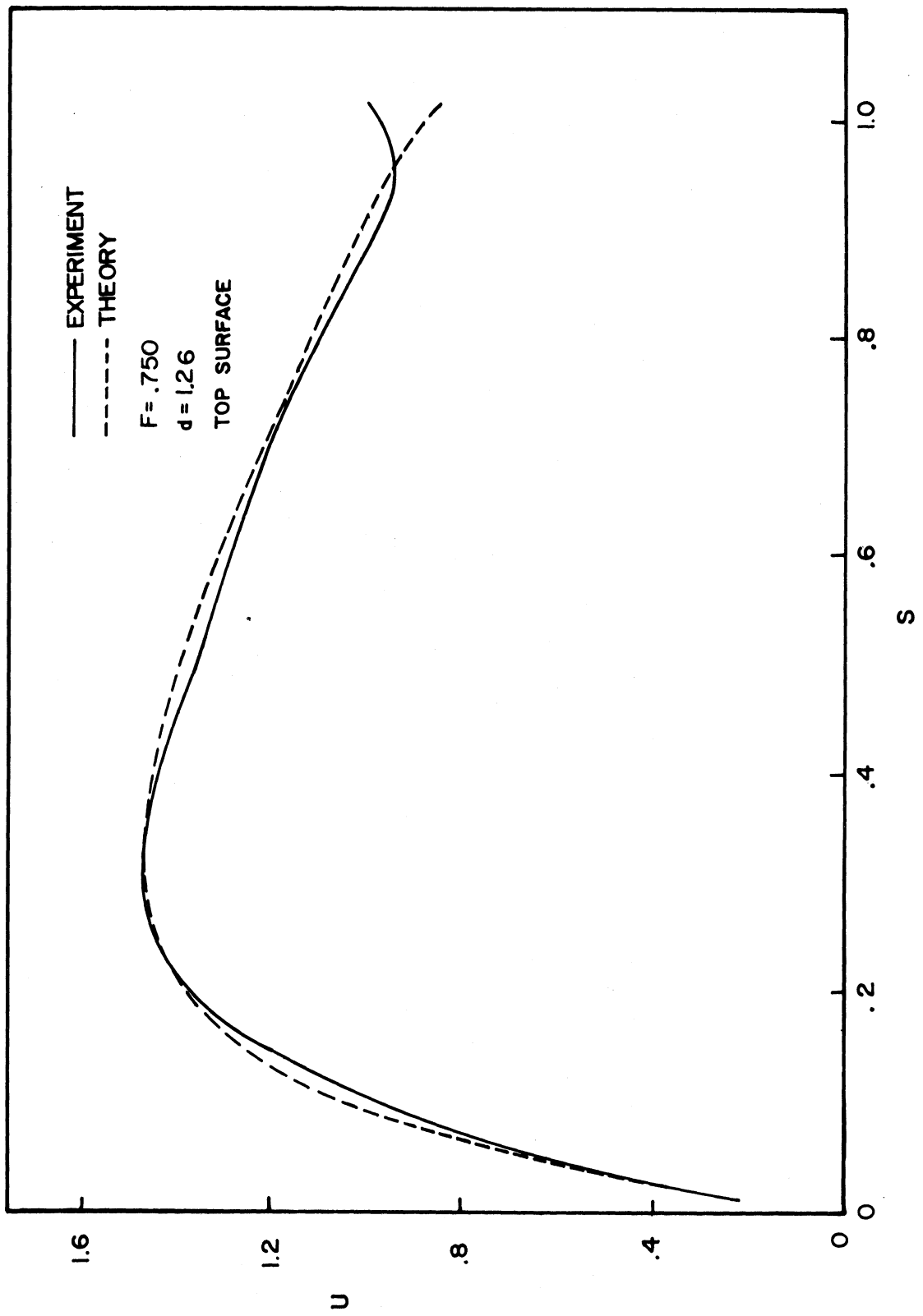

FIGURE 24 COMPARISON BETWEEN EXPERIMENTAL AND THEORETICAL PRESSURE DISTRIBUTIONS

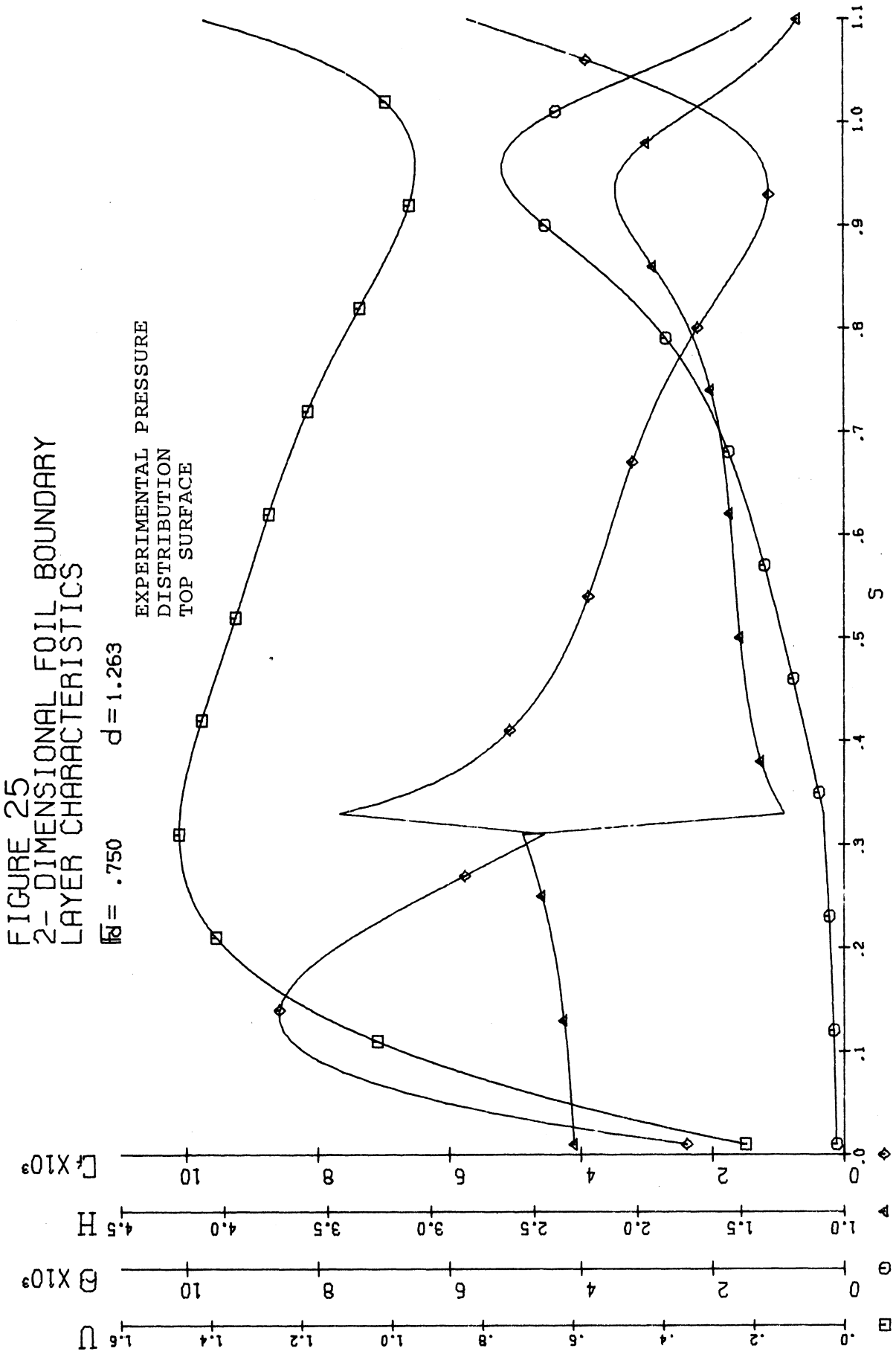
FIGURE 25
2- DIMENSIONAL FOIL BOUNDARY
LAYER CHARACTERISTICS
d = 1.263
EXPERIMENTAL PRESSURE
DISTRIBUTION
TOP SURFACE
S
U
H

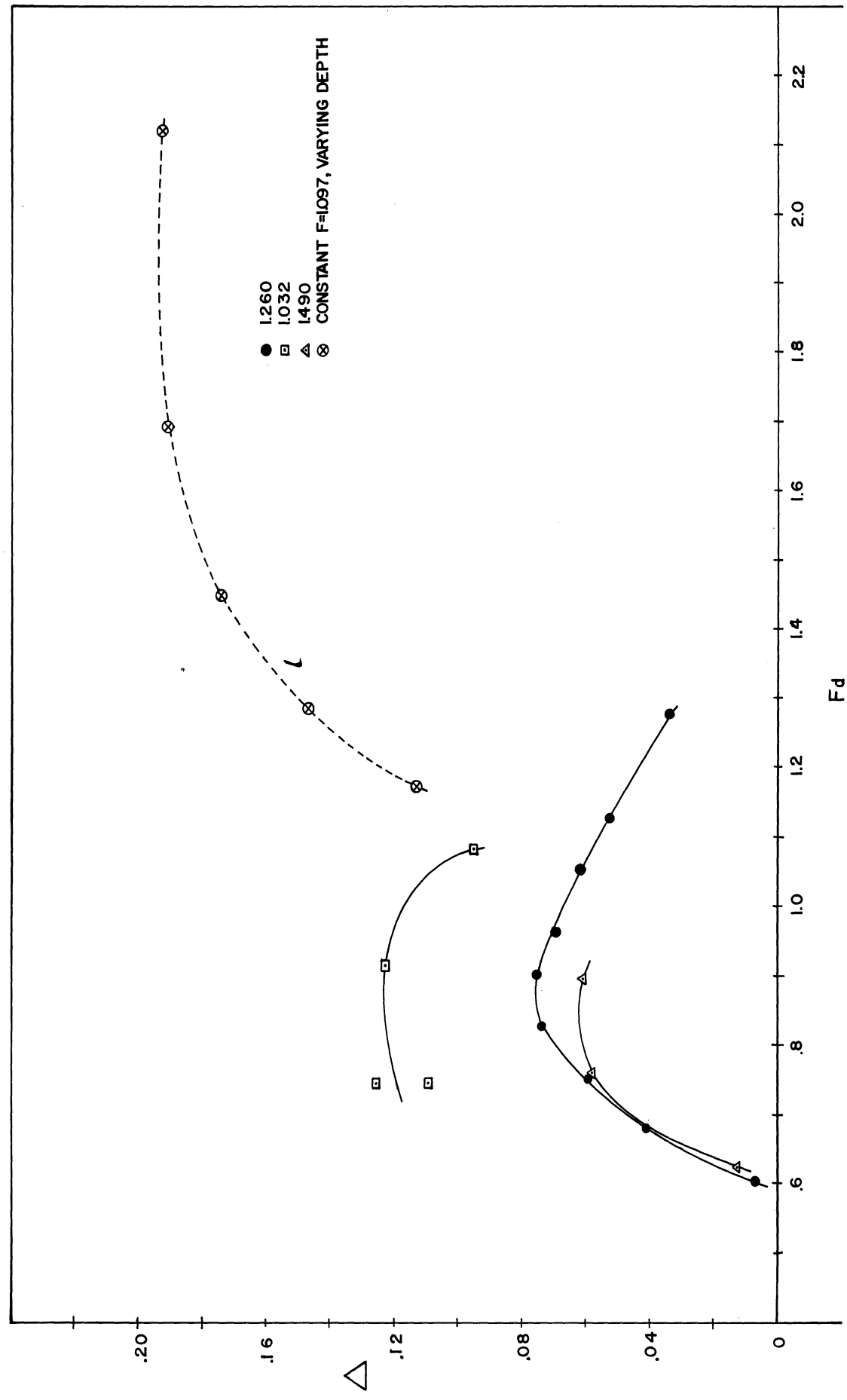

FIGURE 26 Δ vs Fd FOR VARIOUS VALUES OF DEPTH EXPERIMENTAL PRESSURE DISTRIBUTIONS

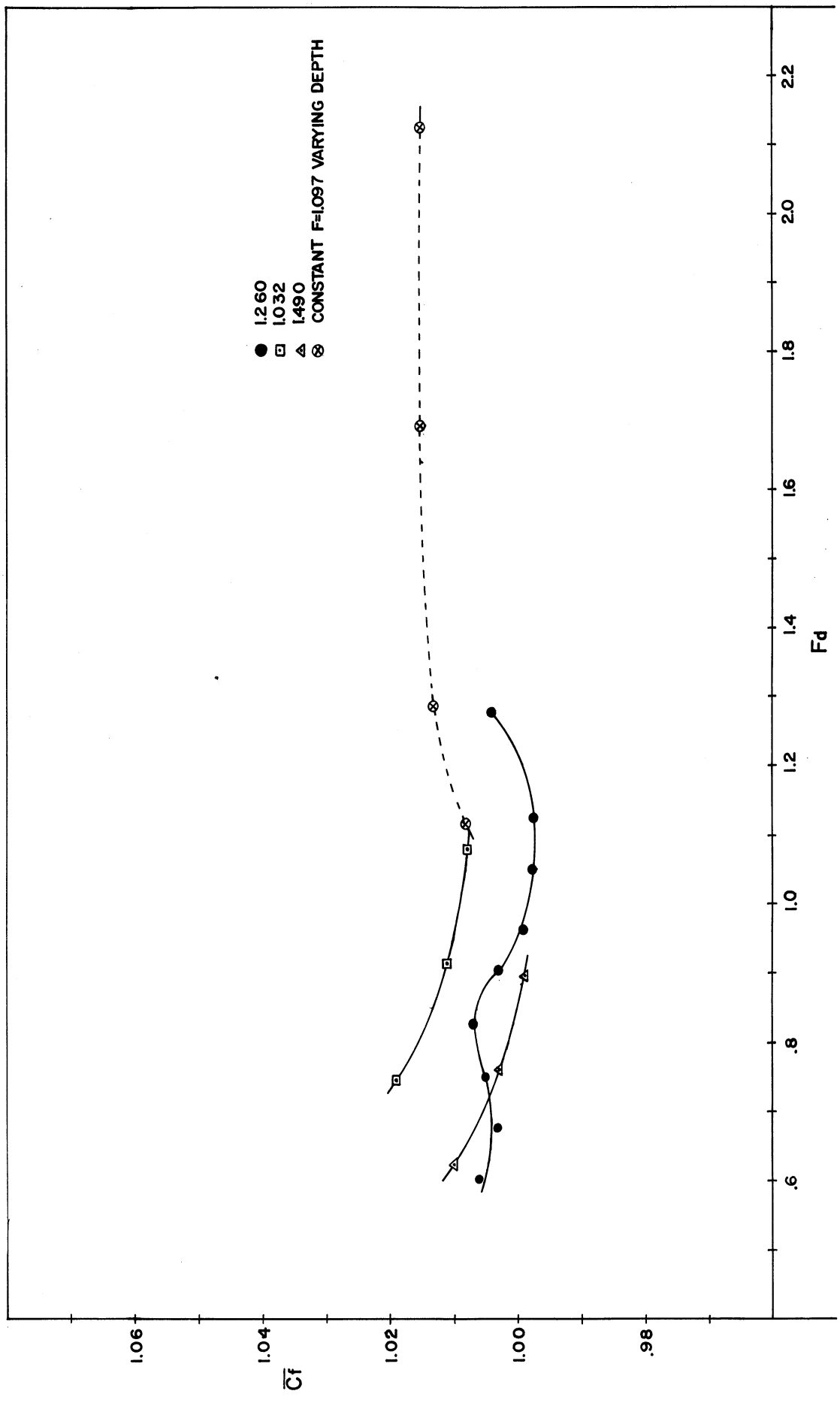

FIGURE 27 $\bar{C}f$ vs Fd FOR VARIOUS VALUES OF DEPTH EXPERIMENTAL PRESSURE DISTRBUTIONS

shape but do not agree too well numerically with Figures 7 and 16. In the case of Δ it is interesting, though perhaps not significant, that the experimental values are lower than the theoretical values while for the wave resistance just the opposite is true. The variation of Δ with Froude number and depth confirm that the free surface does exert a significant influence on the boundary layers but not on the total skin friction and that these variations can be detected using experimental methods together with boundary-layer theory.

IV. 3. Direct Measurement of the Local Skin Friction

Bellhouse and Schultz have shown that the following simple relationship exists between the rate of heat transfer, q, from a thin, heated element mounted flush with a surface across which fluid is flowing and the local skin friction:[16]

$$q=(C+D\tau_w^m)(t_e-t_f),\ m \simeq \frac{1}{3} \tag{67}$$

In Equation 67, C and D are constants dependent on the geometry of the probe and fluid properties, t_e is temperature of the element, and t_f is the ambient temperature of the fluid.

Several small flush-mounted hot-film probes were designed and built to try to measure the local shear stress over the surface of the foil. In order for such probes to be effective

and for equation 67 to hold the heated element must be small enough so that the thermal boundary layer generated by the element is much thinner than the fully developed velocity layer at the probe. Brown[17] shows that if

$$\frac{u_\tau l}{\nu} < 64 P_r \tag{68}$$

where l is the length of the probe in the flow direction, u_τ is the friction velocity, $\sqrt{\frac{\tau_w}{\rho}}$, and P_r is the Prandtl Number, then this condition is satisfied. For probes operating in water in shears less than 1 lb/ft^2, inequality 68 is satisfied for probes less than .076 inches long. The probes built for this work all satisfied 68 as they varied in length between .01 and .015 inches long. However, the effective lengths are probably two or three times greater due to conduction in the base material.

The probes were built by firing a thin platinum film on the polished end of a Pyrex rod .090 inch in diameter. The platinum film was obtained by painting Hanovia liquid bright platinum #05 on th end of the rod using a single human hair stretched between a pair of supports. A jig was built which held the rod and the supports and made it possible to paint a thin straight line across the center of the tip of the rod. After the line was painted, short tabs about 1/8 inch long were painted down the sides of the probes,

and the probe was fired at 1250°F for about ten minutes. Several coats of platinum were required in order to reduce the probe resistance to less than 40 ohms. After the probe tips were completed a strip of Hanovia platinum suspension #130-A was painted on each side of each probe over the bright platinum tabs. The probes were fired again at 1250°F. Next, the platinum strips were tinned right up to the tip and wire leads were soldered to them. To complete the construction, polyethelene tubing .120 inches in diameter was forced over the probe, cut off flush with the tip, and epoxied in place. The epoxy also served to strengthen the probe and insulate the leads from each other and the water. A view of the probes mounted in the foil surface is shown in Figure 28.

The calibration of flush-mounted hot films has received much attention, and with good reason, for the success of the probe is entirely dependent on the quality of its calibration. A very direct and simple method of obtaining a known shear stress was employed with the hope that the probes could be easily and accurately calibrated. If they could be calibrated easily, then the direct measurement of shear stresses in liquids might become more common. A plexiglas tube seven feet long and two inches in diameter, was connected to a constant head tank via a small settling tank which contained six mesh screens of varying mesh size and a faired entrance section. Two pressure taps were located 2 feet apart near

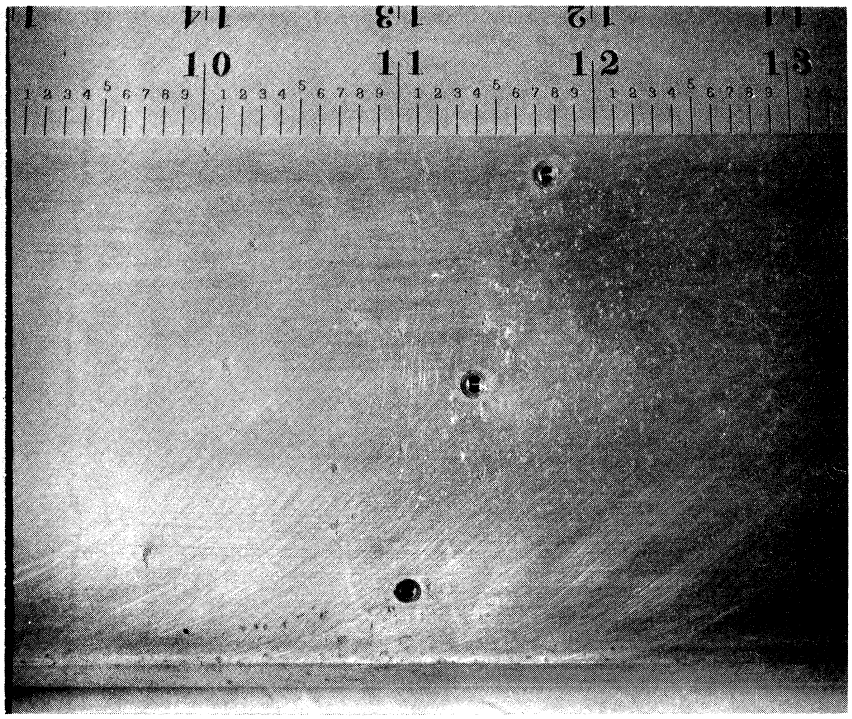

Figure 28. Hot Film Probes Mounted in Foil Surface

near the downstream end of the tube. The probes were located circumferentially about the tube midway between the pressure taps. It can easily be shown by momentum considerations that the wall shear stress and the pressure drop between the pressure taps are related as follows:

$$\tau_w = .108\Delta p, \tag{69}$$

where τ_w is in lb/ft^2 and Δp is in inches of water. Equation 69 is valid for both laminar and turbulent flows. A Pace model P7D differential pressure transducer was used to measure Δp while the probes were operated one at a time at an overheat ratio of 1.04 by a Thermo-Systems Model 1033 constant temperature anemometer. The bridge voltage was read out via a Dymec voltage to frequency converter and a Hewlett Packard counter, which averaged the output over a 10 second period. The pressure transducer was excited by a Sanborn 350-1100B carrier amplifier and the output was read out on a Leeds and Northrup potentiometric bridge. The flow was checked for uniformity by rotating the tube and measuring the output of one probe. The variations in output with circumferential position were found to be within the normal data scatter.

Seven probes were calibrated within a three day period. The results are shown in Figure 29. The square of the anemometor bridge voltage is plotted against $(\tau_w)^{1/3}$. For most

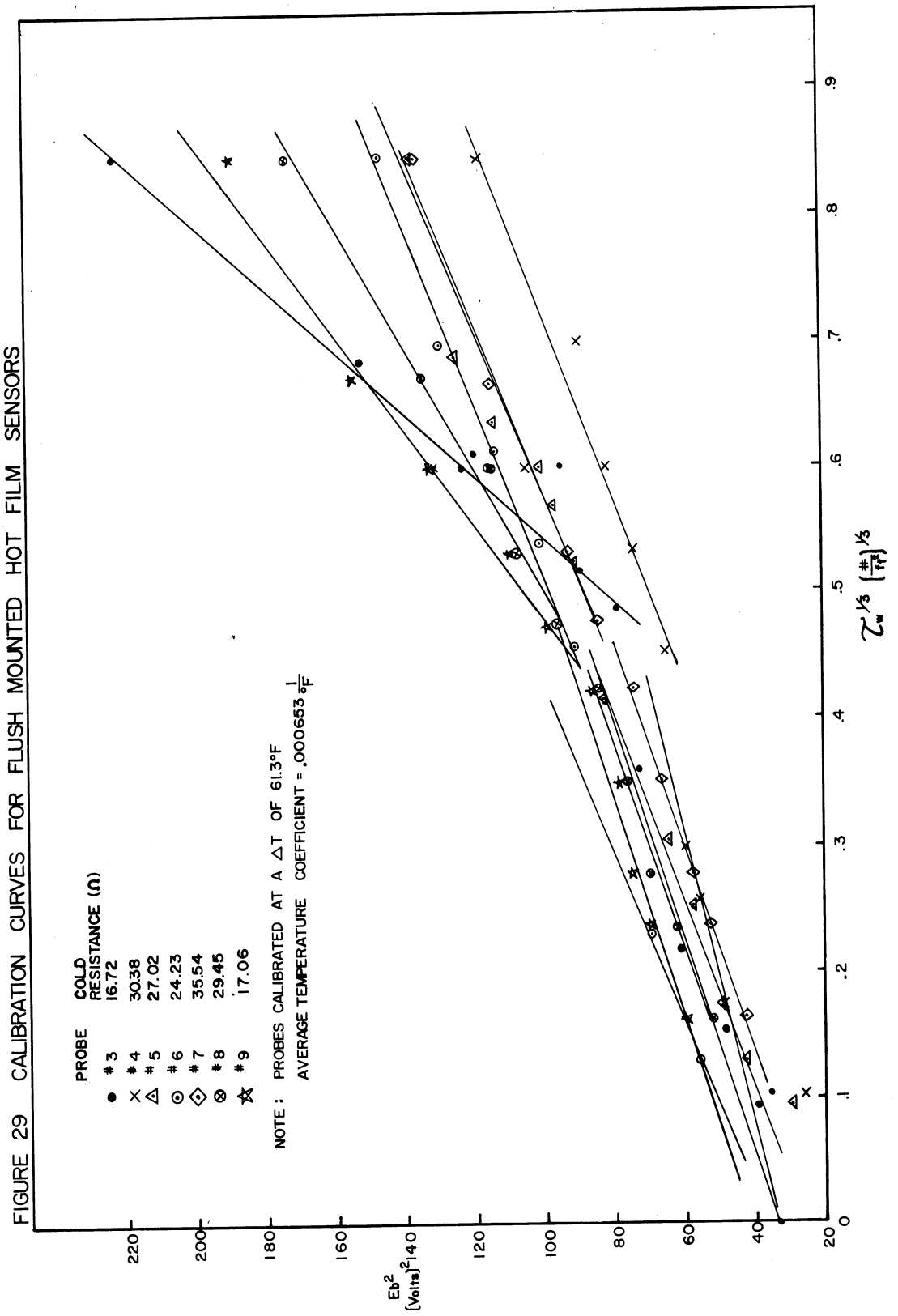

FIGURE 29 CALIBRATION CURVES FOR FLUSH MOUNTED HOT FILM SENSORS

of the probes, a single calibration line for both laminar and turbulent flow could be drawn. However, since two probes clearly exhibited different sensitivities to laminar and turbulent flow, all calibration curves were drawn as two straight lines--one for laminar flow, the other for turbulent flow. Significantly, the lower resistance probes, Numbers 3 and 9, have higher sensitivities in turbulent flow. This is probably because these two probes are also somewhat larger than the higher resistance probes and therefore do not satisfy condition 68 as well.

At the outset it was hoped that the hot films would be sensitive and precise enough to measure the local skin friction over the chord of the foil and thus confirm the theoretical predictions based on both the experimental and theoretical pressure distributions. It was also hoped that they would be sensitive enough to detect changes in the skin friction with depth and Froude number. Unfortunately, such was not the case. Some of the higher resistance probes suffered from drift, apparently due to electrolytic deposition. (see Rasmussen[18]), while the low resistance probes might have suffered from being so large that a unique calibration for both laminar and turbulent flow was not possible. Because of these difficulties some desired results were not obtained.

The entire chord length was surveyed with the hot film probes for d = .842 and F = 1.097 but the data was too

scattered to plot the chordwise variation of shear stress or to detect differences due to depth and Froude number.

However, the experiments did produce two significant results. First, from visual observations of the a-c component of the bridge voltage the transition point on both surfaces of the foil could be easily determined. On the top surface transition occured somewhere between the seventh and eighth probe position from the nose while on the bottom surface transition occurred between the sixth and seventh probe position from the nose. Or in terms of s

$$.49 < (s_t)_{top} \leq .56$$

$$.42 < (s_t)_{bottom} \leq .49$$

This compares with the predicted point of transition of $s_t = .32$ for both the top and bottom surfaces. The result is reasonable since the predicted s_t is actually the point of instability of laminar boundary layer and transition does not occur until the initial disturbances have been amplified sufficiently to cause turbulence.

The second result was obtained by merely averaging the component of the measured local shear stress in the direction of motion to obtain an average C_f. The results are summarized in the following table.

Method	C_f
Direct Shear-Stress Measurements	5.05×10^{-3}
Boundary-Layer Calculations	3.52×10^{-3}
Schoenherr Turbulent Friction Line[19]	4.767×10^{-3}

V. New Results

The new results found in this investigation are summarized in this section.

1. The free surface affects the laminar boundary layer and thus the laminar skin friction significantly (Figures 7 and 26). The variations in Δ are exactly analogous to the variations in the wave resistance coefficient.

2. In contrast to 1. above, the free surface does not influence the total skin friction coefficient of the foil more than two percent when compared with the case of the foil deeply submerged (Figures 16 and 27).

3. The region of breaking waves found by Salvesen was found to be much smaller than he had reported. In particular, the foil can be operated at any depth (even zero depth) if the chord Froude number exceeds about .9.

4. From direct skin-friction measurements using flush-mounted hot-film probes, an average skin friction coefficient was obtained which was somewhat higher but compared reasonably with the calculations and the value obtained from the Schoenherr turbulent friction line.

5. The wave-resistant coefficient was found to be very sensitive to the circulation around the foil. The effect of adding circulation was to decrease the coefficient and move the peak value toward lower Froude numbers (Figure 3). The approximate linear theory in which the body boundary condition

was not satisfied exactly yields wave-resistance coefficients which compare well with the experimental wave resistance as far as the peak values are concerned but the Froude number at which the peak values occur is not predicted correctly.

On the other hand, the consistent linear theory with the Kutta condition satisfied is able to predict the location of the peaks correctly but the peak values are too low (Figure 23).

VI. Suggestions For Further Research

The most obvious area for further work is in hot film techniques for shear stress measurements. The techniques are clearly not well enough developed so that reliable measurements can be made as a routine matter. Probe design and calibration techniques are two areas which merit special attention. It is the author's opinion that there are many questions that could be answered concerning both potential and viscous flows if the flush mounted hot film were widely used.

It is felt that the free surface might have more of an influence on the skin friction coefficient if the chord length of the body were several wave lengths long. This would result in a "wavy" pressure distribution resulting in "wavy" boundary layers.

The extension of this work to three dimensions would naturally be desirable but very difficult due to the dearth of knowledge about three-dimensional boundary layers.

A very simple but useful extension of this work would be to determine the influence of the free surface on the form drag. This could be done merely by considering how the momentum thickness at the trailing edge changes with depth and Froude number.

REFERENCES

1. Welsh, J.E., Harlow, F.H., Shannon, J.P., and Daly, B.J., "The Mac Method," Los Alamos Scientific Laboratory Report No. LA-3425, 1966.

2. Dugan, J.P., "An Integral Representation for Viscous Surface Waves Generated by Steady Disturbances," PhD. Thesis, Northwestern University, August 1967.

3. Couch, R.B., and Moss, J.L., "Application of Large Protruding Bulbs to Ships of High Block Coefficient," SNAME Transactions, 1967.

4. Wu, T.Y., "Interaction Between Ship Waves and Boundary Layer," Proc. International Seminar on Theoretical Wave Making Resistance, Vol. III, University of Michigan, pp. 1263-1287.

5. Salvesen, N., "On Second-Order Wave Theory for Submerged Two-Dimensional Bodies," PhD. Thesis, University of Michigan, April 1966.

6. Giesing, J.P. and Smith, A.M.O., "Potential Flow About Two-Dimensional Hydrofoils", Douglas Aircraft Company, Inc., Report, 1966.

7. Salvesen, N., Unpublished report on higher order wave resistance of a hydrofoil.

8. Kochin, N.E., Kibel, I.A., and Roze, N.V., Theoretical Hydromechanics, Trans. by D. Boganovitch, 1964.

9. Preston, J.H., "The Calculation of Lift Taking Account of the Boundary Layer," A.R.C. R & M 2725, 1953.

10. Schlichting, H., Boundary Layer Theory, McGraw-Hill, 1960.

11. Lin, C.C., "On the Stability of Two-Dimensional Parallel Flows," Quarterly of Applied Mathematics, Vol. 3, 1945-1946.

12. Hahnemann, E., Freeman, J.C., and Finston, M., "Stability of Boundary Layers and of Flow in Entrance Section of Channel," Journal of Aeronautical Science Vol. 15, 1948, pp. 493-496.

REFERENCES (cont.)

13. Head, M.R., "Entrainment in the Turbulent Boundary Layer" A.R.C. R & M 3152, 1960.

14. Schubauer, G.B., and Klebanoff, P.S., "Investigation of Separation of the Turbulent Boundary Layer," N.A.C.A. Tech Note 2133, 1950.

15. Moses, H.L., "The Behavior of Turbulent Boundary Layers in Adverse Pressure Gradients," M.I.T. Gas Turbine Laboratory Report 73, 1964.

16. Bellhouse, B.J. and Schultz, D.L., "Determination of Mean and Dynamic Skin Friction, Separation and Transition in Low-Speed Flow with a Thin-Film Heated Element," J. Fluid Mech. Vol. 24, 1966, pp. 379-400.

17. Brown, G.L., "Theory and Application of Heated Films for Skin Friction Measurements," Proceedings of the 1967 Heat Transfer and Fluid Mechanics Institute.

18. Rasmussen, C.G., "The Air Bubble Problem in Water Flow Hot-Film Anemometry," DISA Information, DISA Corporation.

19. Todd, F.H., "Resistance and Propulsion," Principles of Naval Architecture, ed. John P. Comstock, Society of Naval Architects and Marine Engineers, New York, 1967.

APPENDIX A - THE POHLHAUSEN METHOD

By integrating equations 36 and 37 across the boundary layer the momentum integral equation is obtained:

$$RU\theta\frac{d\theta}{ds} + (2 + \frac{\delta^*}{\theta})\theta^2\frac{dU}{ds} = \frac{RC_f\theta}{2U}, \tag{A1}$$

where

$$\theta = \int_o^\delta [\frac{\bar{u}}{U} - (\frac{\bar{u}}{U})^2]dn, \tag{A2}$$

$$\delta^* = \int_o^\delta (1 - \frac{\bar{u}}{U})dn, \tag{A3}$$

and

$$C_f + \frac{\tau_w}{\frac{1}{2}\rho U_\infty^2}. \tag{A4}$$

Assuming that a one-parameter family of velocity profiles exists of the form

$$\frac{\bar{u}}{v} = f(\eta) = a\eta + b\eta^2 + c\eta^3 + d\eta^4, \tag{A5}$$

where $\eta = n/\delta$ and which satisfies the conditions

$$\bar{u} = 0, \frac{1}{R}\frac{\partial^2\bar{u}}{\partial n^2} = -U\frac{dU}{ds} \text{ at } \eta = 0$$

$$\bar{u} = U, \frac{\partial\bar{u}}{\partial n} = 0, \frac{\partial^2\bar{u}}{\partial n^2} = 0 \text{ at } \eta = 1,$$

the constants a, b, c, and d can be obtained;

$$a = 2 + \frac{\Lambda}{6},\ b = -\frac{\Lambda}{2},\ C = -2 + \frac{\Lambda}{2},\ \text{and}\ d = 1 - \frac{\Lambda}{6},$$

where

$$\Lambda = R\delta^2\frac{dU}{ds}$$

Equation 39 can now be rearranged and written in the form

$$\frac{\bar{u}}{U} = A(\eta) + \Lambda B(\eta), \tag{A6}$$

where

$$\left.\begin{aligned} A(\eta) &= 1 - (1 - \eta)^3(1 + \eta) \\ B(\eta) &= \frac{1}{6}\eta(1 - \eta)^3 \end{aligned}\right\} \tag{A7}$$

Putting the expression A6 into equations A2 and A3, and noting that $C_f = \frac{2}{R}\frac{\partial\bar{u}}{\partial n}|n=0$ expressions for θ, δ^*, and C_f can be written in terms of Λ:

$$\frac{\theta}{\delta} = \frac{37}{315} - \frac{1}{945}\Lambda - \frac{1}{9072}\Lambda^2, \tag{A8}$$

$$\frac{\delta^*}{\delta} = \frac{3}{10} - \frac{1}{120}\Lambda, \tag{A9}$$

and

$$\frac{RC_f\delta}{2U} = 2 + \frac{\Lambda}{6}. \tag{A10}$$

Now, defining a form factor

$$H = \frac{\delta^*}{\theta} = \frac{3/10 - 1/120\ \Lambda}{37/315 - 1/945\ \Lambda - 1/9072\ \Lambda^2} = F_1(K) \tag{A11}$$

and

$$\frac{RC_f\theta}{2U} = (2 + \frac{\Lambda}{6})(\frac{37}{315} - \frac{1}{945}\ \Lambda - \frac{1}{9072}\ \Lambda^2) = F_2(K), \tag{A12}$$

where

$$K = K(\Lambda) = (\frac{37}{315} - \frac{1}{945}\ \Lambda - \frac{1}{9072}\ \Lambda^2)^2\ \Lambda = R\theta^2\frac{dU}{ds}, \tag{A13}$$

the momentum equation 37 becomes:

$$\frac{dZ}{ds} = \frac{F(K)}{U} \tag{A14}$$

with $K = Z\frac{dU}{ds}$, $Z = R\theta^2$, and $F(K) = 2F_2(K) - 4K - 2K\ F_1(K)$. Equation A14 is a nonlinear differential equation for Z as a function of s, the distance from the stagnation point. The function F(K) can be tabulated once and for all since it is independent of the body shape and U(s). Similarly, $F_1(K)$, $F_2(K)$, and $K(\Lambda)$ can be tabulated.

At the upstream stagnation point U = 0 and $\frac{dU}{ds} \neq 0$. Therefore in order that $\frac{dZ}{ds}$ be determinate at the stagnation point F(K) must equal 0. From Figure 5 in the main text, it is apparent that F(K) = 0 at K = .0770, which corresponds to $\Lambda = 7.052$.

The initial slope $\frac{dZ}{ds}|_{s = 0}$ is found by applying L'Hopital's Rule to equation A14 which yields:

$$\frac{dZ}{ds}|_{s = 0} = - .0652\frac{d^2U/ds}{dU/ds}|_{s = 0}$$

However, since $U(s) \propto s$ near $s = 0$ for all flows involving a stagnation point, $d^2U/ds^2 = 0$ at the stagnation point. Therefore $\frac{dZ}{ds} = 0$ at $s = 0$.

APPENDIX 1

The plots of the boundary layer characteristics calculated from the theoretical pressure distributions are included for reference purposes. The symbols on the various curves are not the only computed points, but are for identification only. The characteristics shown were calculated with a step size, $\Delta s = .01$.

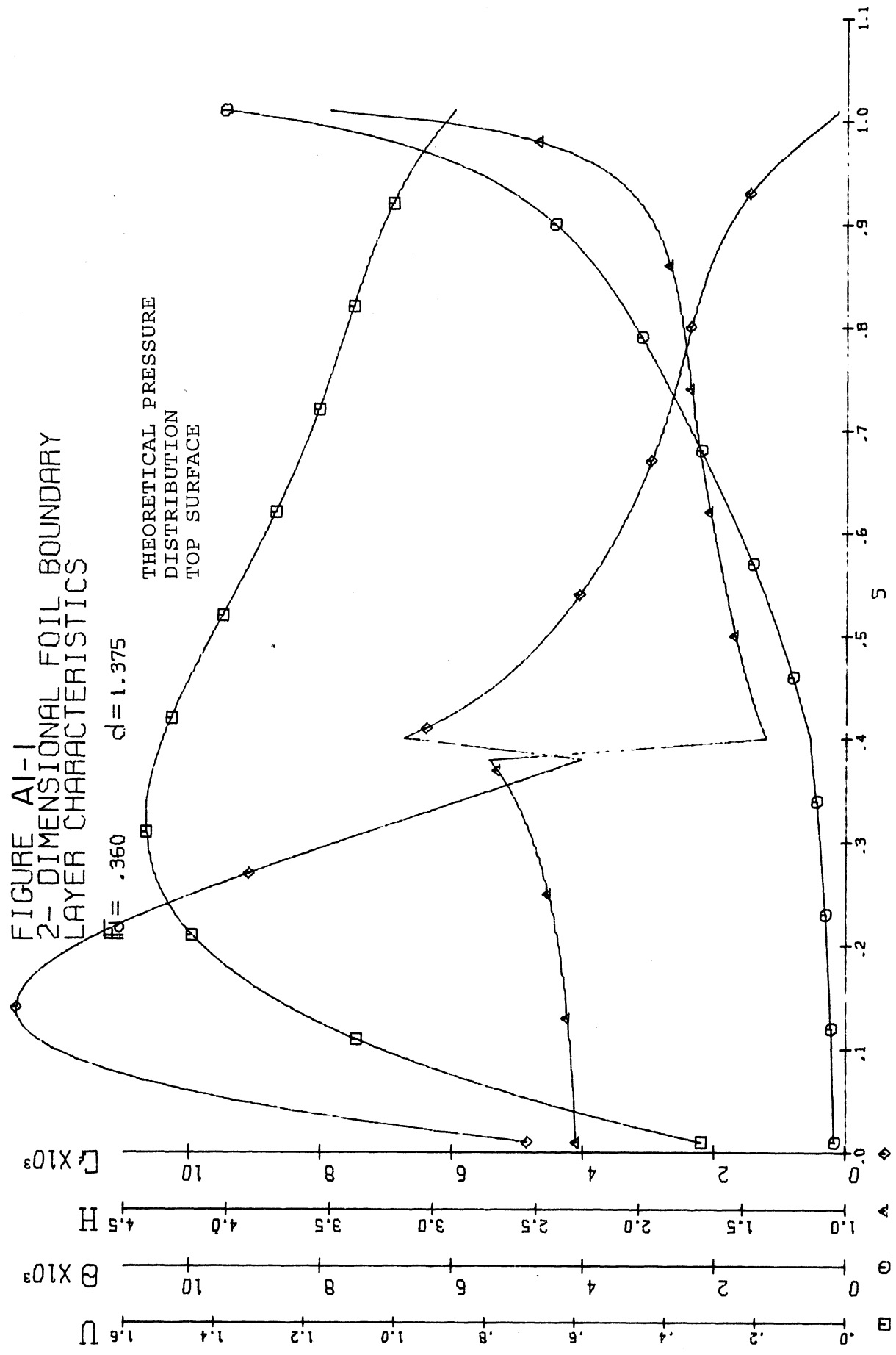
FIGURE AI-1
2- DIMENSIONAL FOIL BOUNDARY
LAYER CHARACTERISTICS
THEORETICAL PRESSURE
DISTRIBUTION
TOP SURFACE
d= 1.375
d= .360
S
U
Θ X10³
H
δ* X10³

FIGURE A1-2
2- DIMENSIONAL FOIL BOUNDARY
LAYER CHARACTERISTICS
$\bar{R}_N$ = .360
d = 1.375
THEORETICAL PRESSURE
DISTRIBUTION
BOTTOM SURFACE
U
H
θ X10³
δ* X10³
S

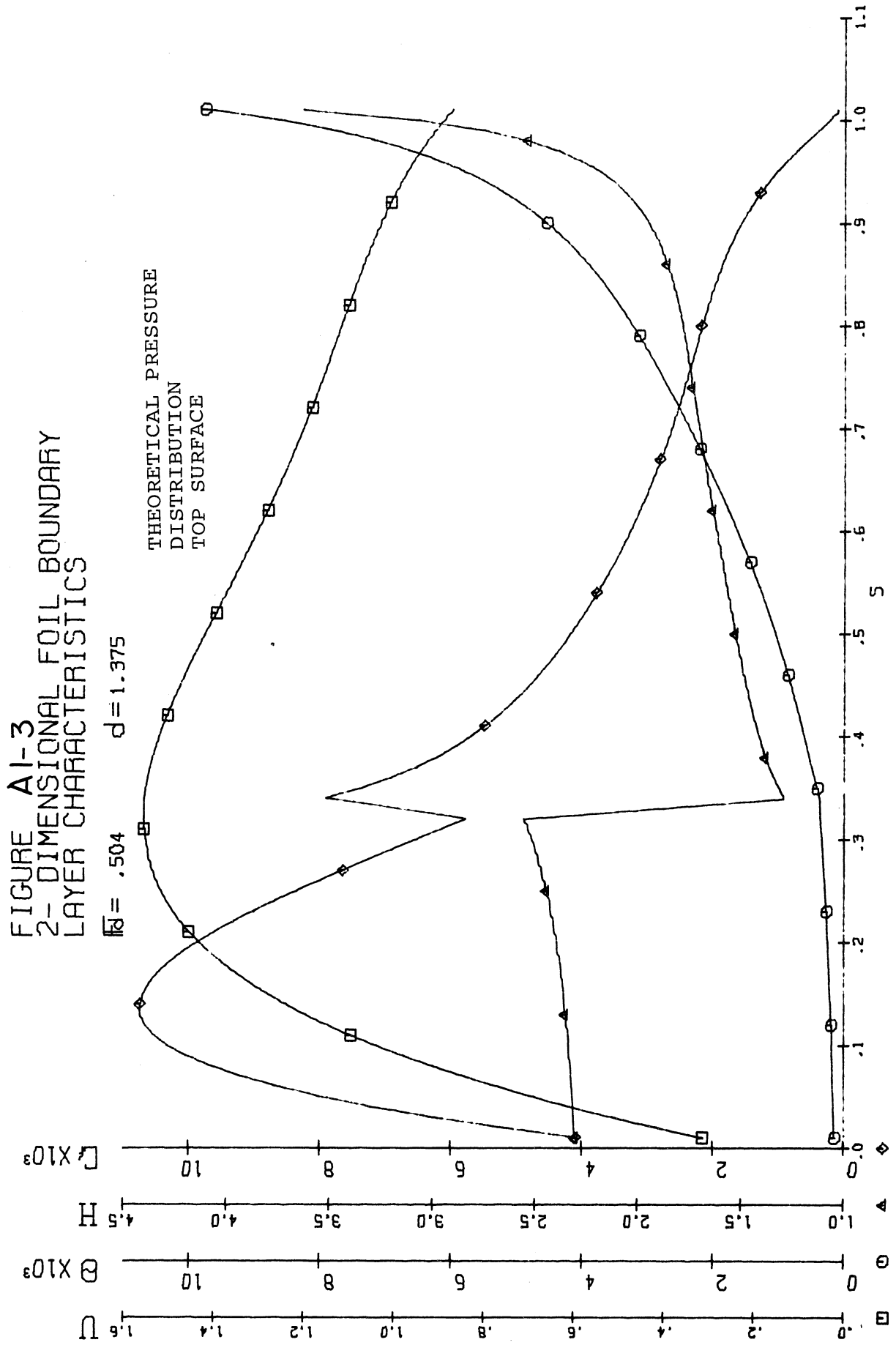
FIGURE A1-3
2- DIMENSIONAL FOIL BOUNDARY
LAYER CHARACTERISTICS
d = 1.375
THEORETICAL PRESSURE
DISTRIBUTION
TOP SURFACE
S
U
Θ X10³
H
Γ X10³

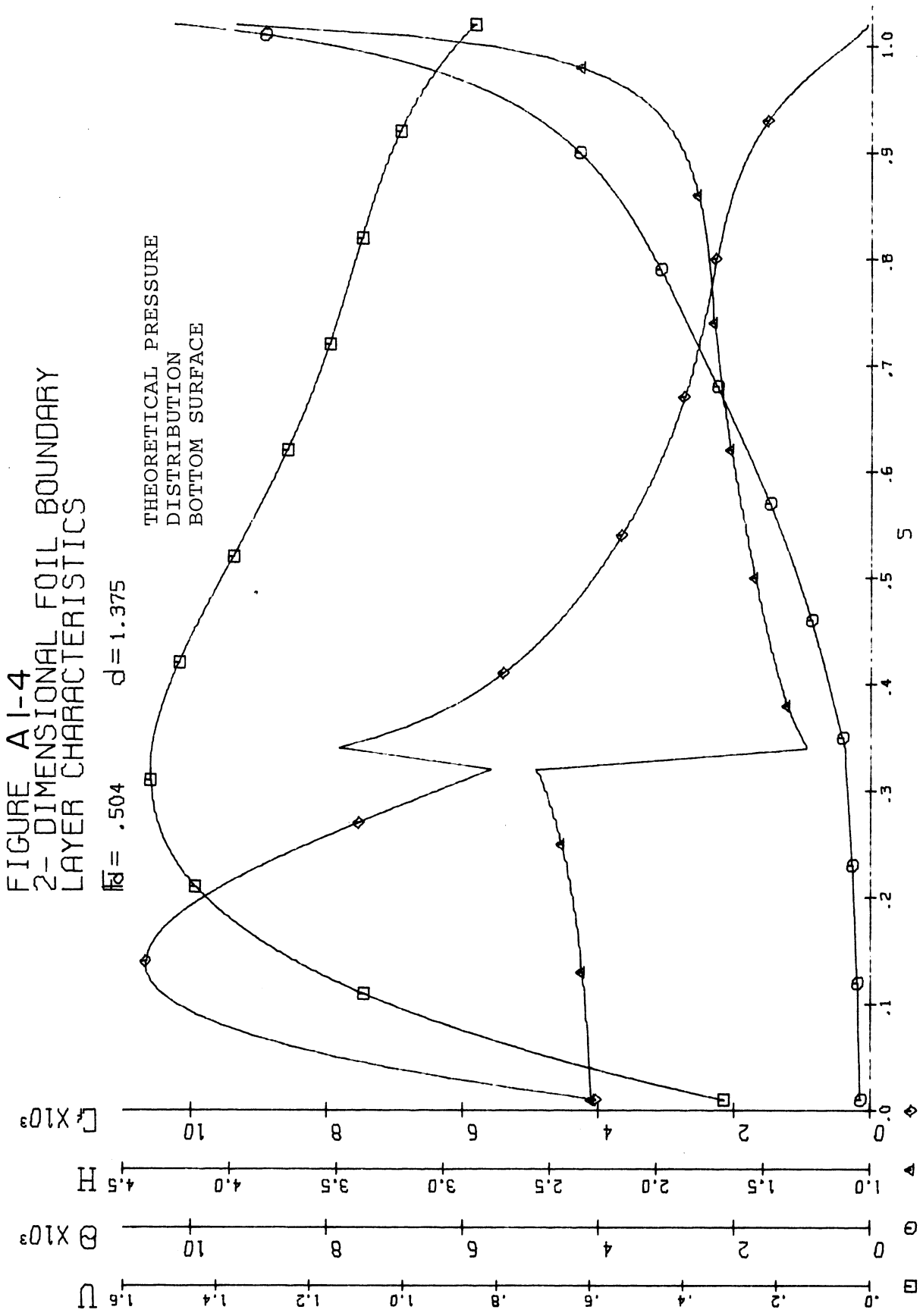
FIGURE A1-4
2- DIMENSIONAL FOIL BOUNDARY
LAYER CHARACTERISTICS
d=1.375
THEORETICAL PRESSURE
DISTRIBUTION
BOTTOM SURFACE
S
U
Θ X10³
H
δ* X10³

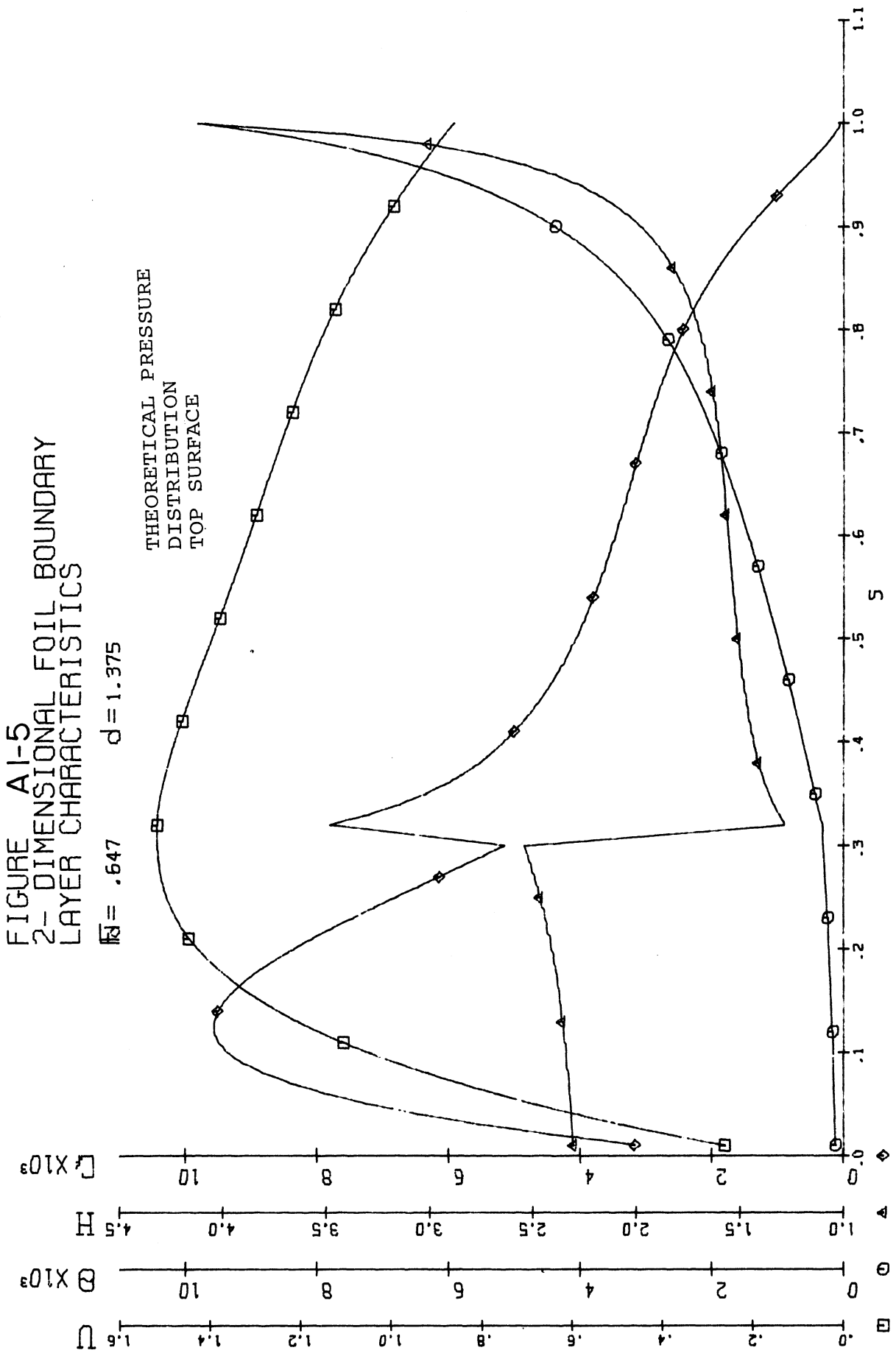
FIGURE A1-5
2- DIMENSIONAL FOIL BOUNDARY
LAYER CHARACTERISTICS
M = .647
d = 1.375
THEORETICAL PRESSURE
DISTRIBUTION
TOP SURFACE
S
U
Θ X10³
H
C_f X10³

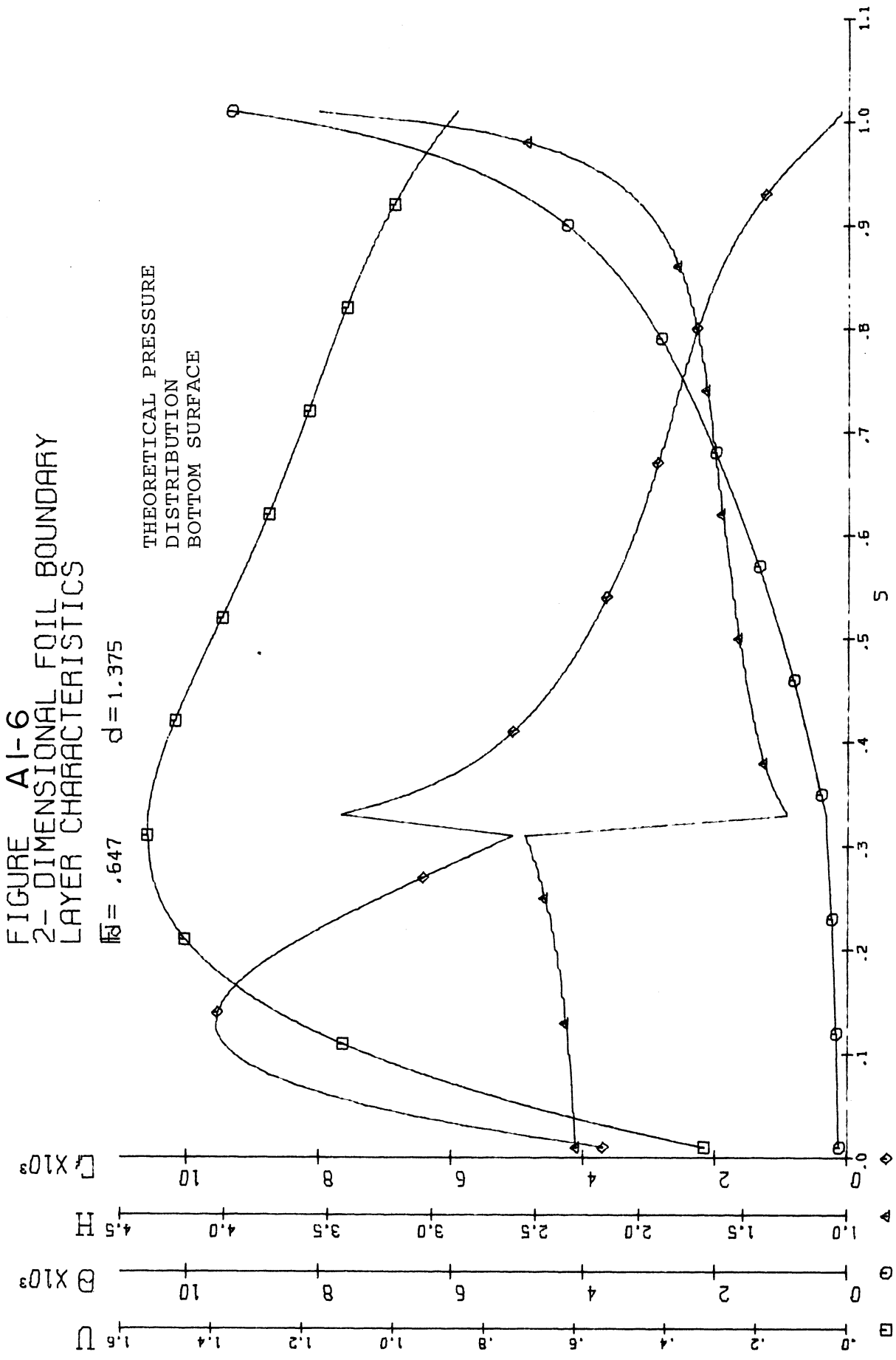
FIGURE A1-6
2- DIMENSIONAL FOIL BOUNDARY
LAYER CHARACTERISTICS
$\overline{R_d}$ = .647 d = 1.375
THEORETICAL PRESSURE
DISTRIBUTION
BOTTOM SURFACE
U
Θ X10³
H
δ* X10³
S

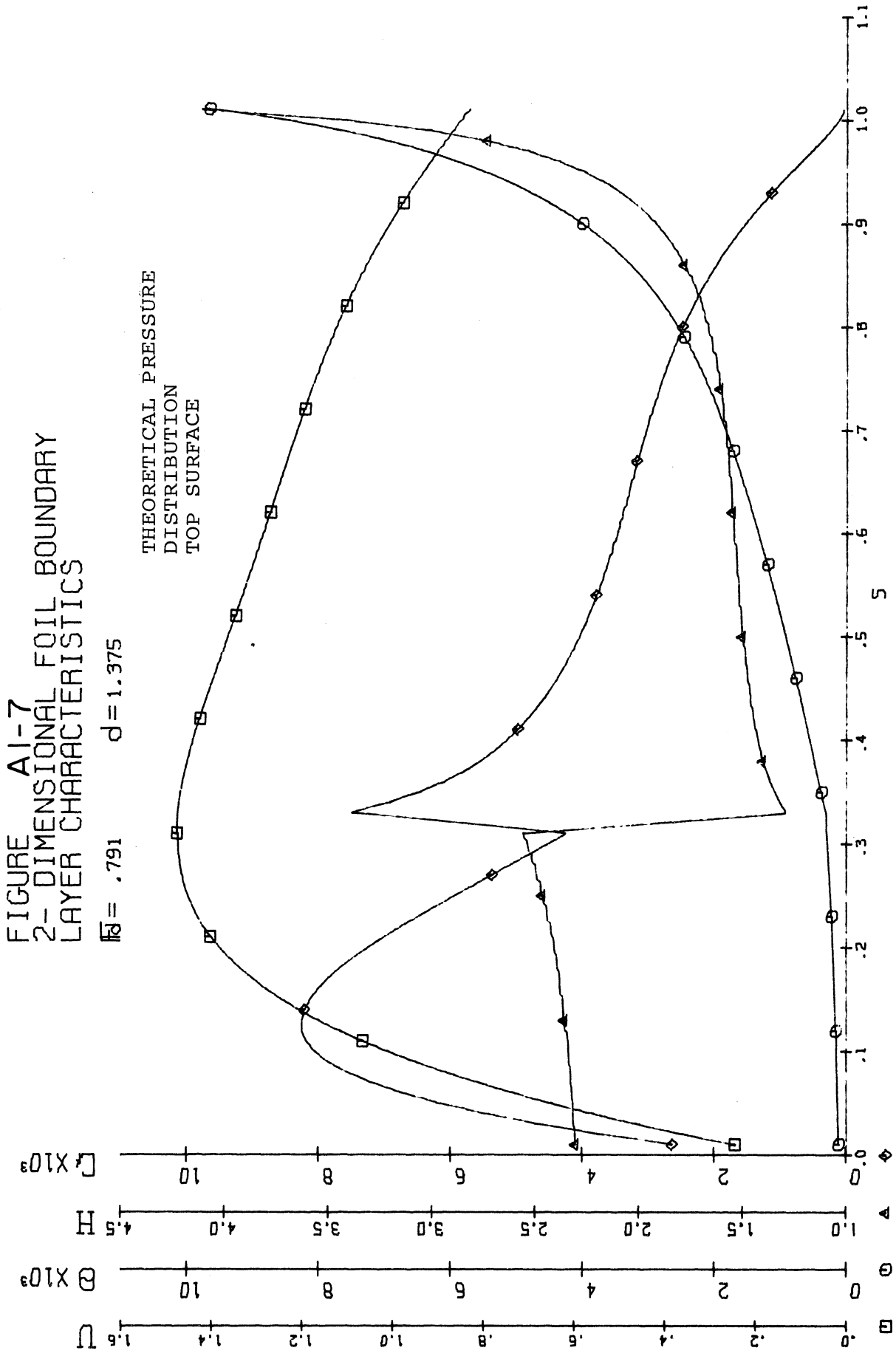
FIGURE A1-7
2- DIMENSIONAL FOIL BOUNDARY
LAYER CHARACTERISTICS
M = .791
d=1.375
THEORETICAL PRESSURE
DISTRIBUTION
TOP SURFACE
S
U
θ X10³
H
C_f X10³

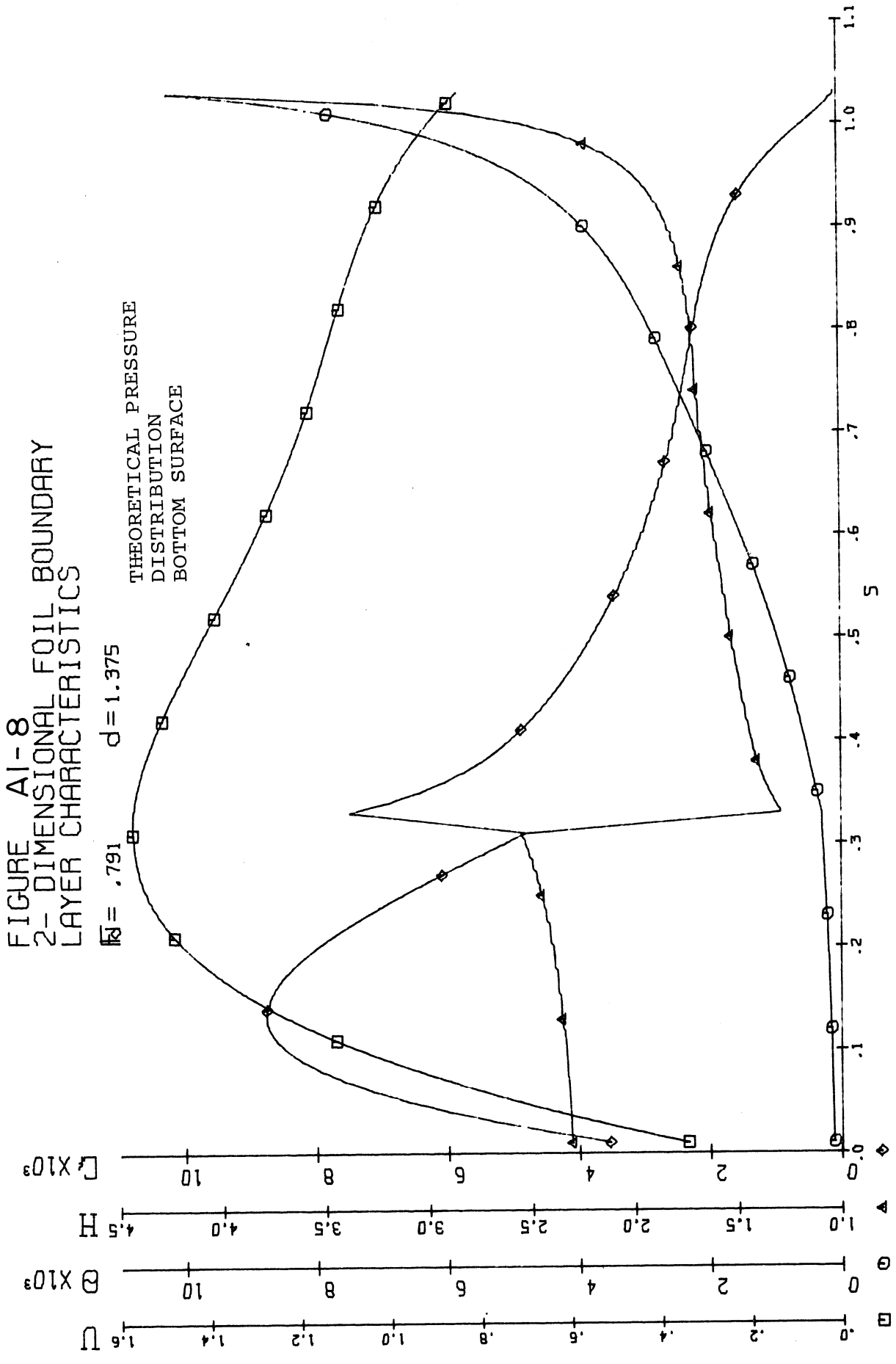
FIGURE A1-8
2- DIMENSIONAL FOIL BOUNDARY
LAYER CHARACTERISTICS
$\overline{R_d}$ = .791
d = 1.375
THEORETICAL PRESSURE
DISTRIBUTION
BOTTOM SURFACE
U
θ X10³
H
δ* X10³
S

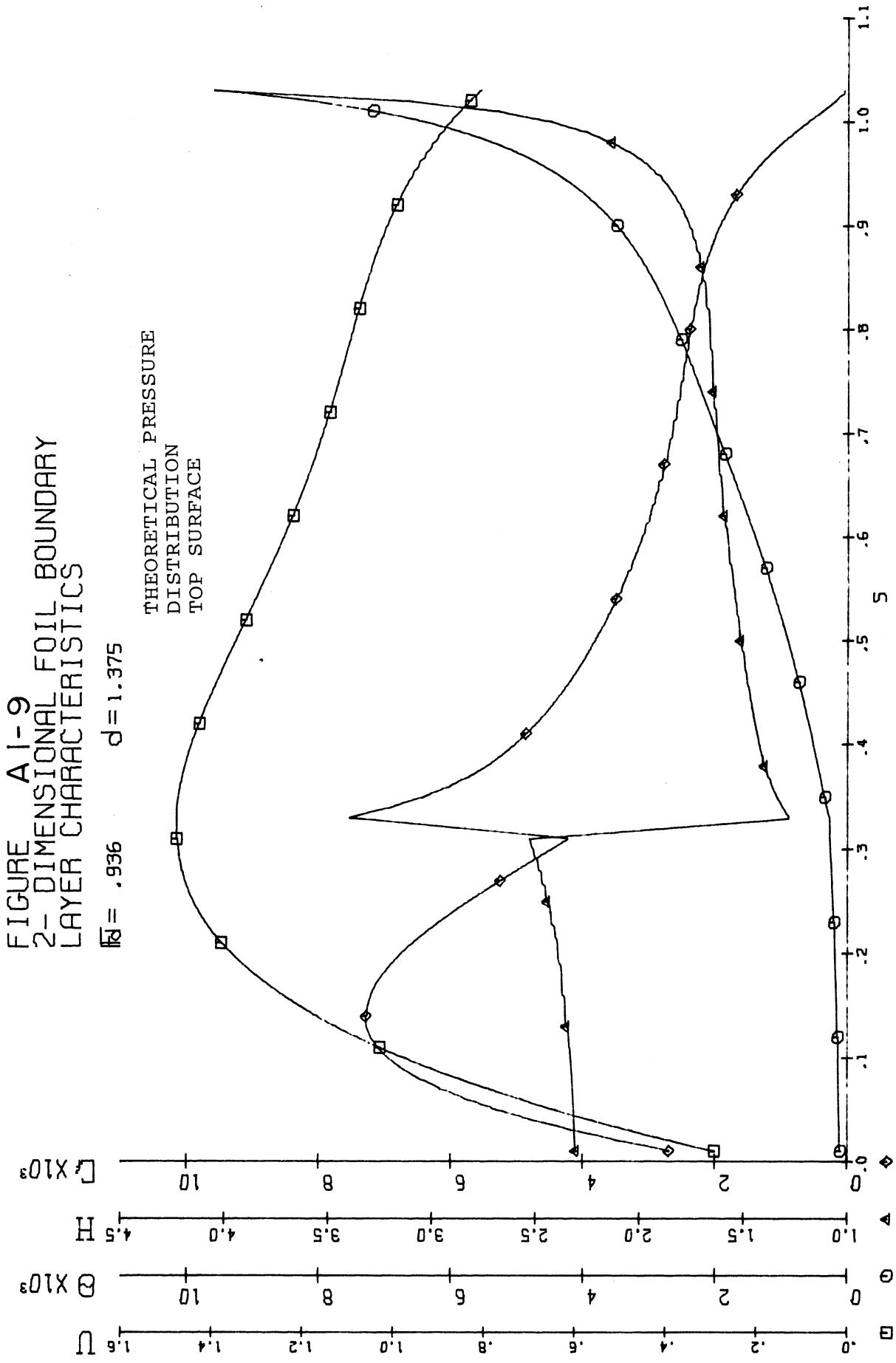
FIGURE A1-9
2- DIMENSIONAL FOIL BOUNDARY
LAYER CHARACTERISTICS
$\bar{M}_d$ = .936 d = 1.375
THEORETICAL PRESSURE
DISTRIBUTION
TOP SURFACE
U
Θ X10³
H
Γ X10³
S

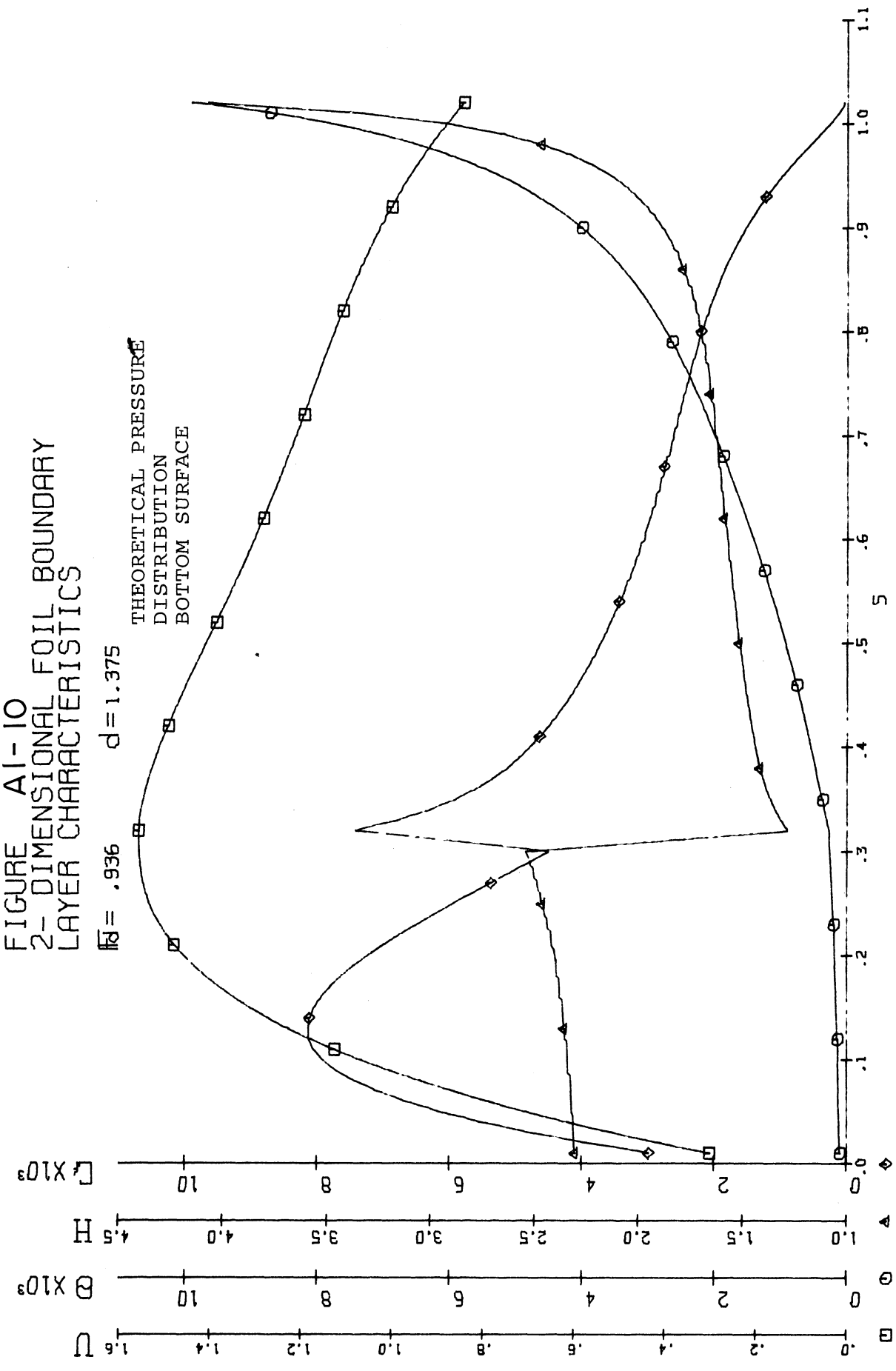
FIGURE A1-10
2-DIMENSIONAL FOIL BOUNDARY
LAYER CHARACTERISTICS
R_d = .936 d=1.375
THEORETICAL PRESSURE
DISTRIBUTION
BOTTOM SURFACE
S
U
Θ X10³
H
δ* X10³

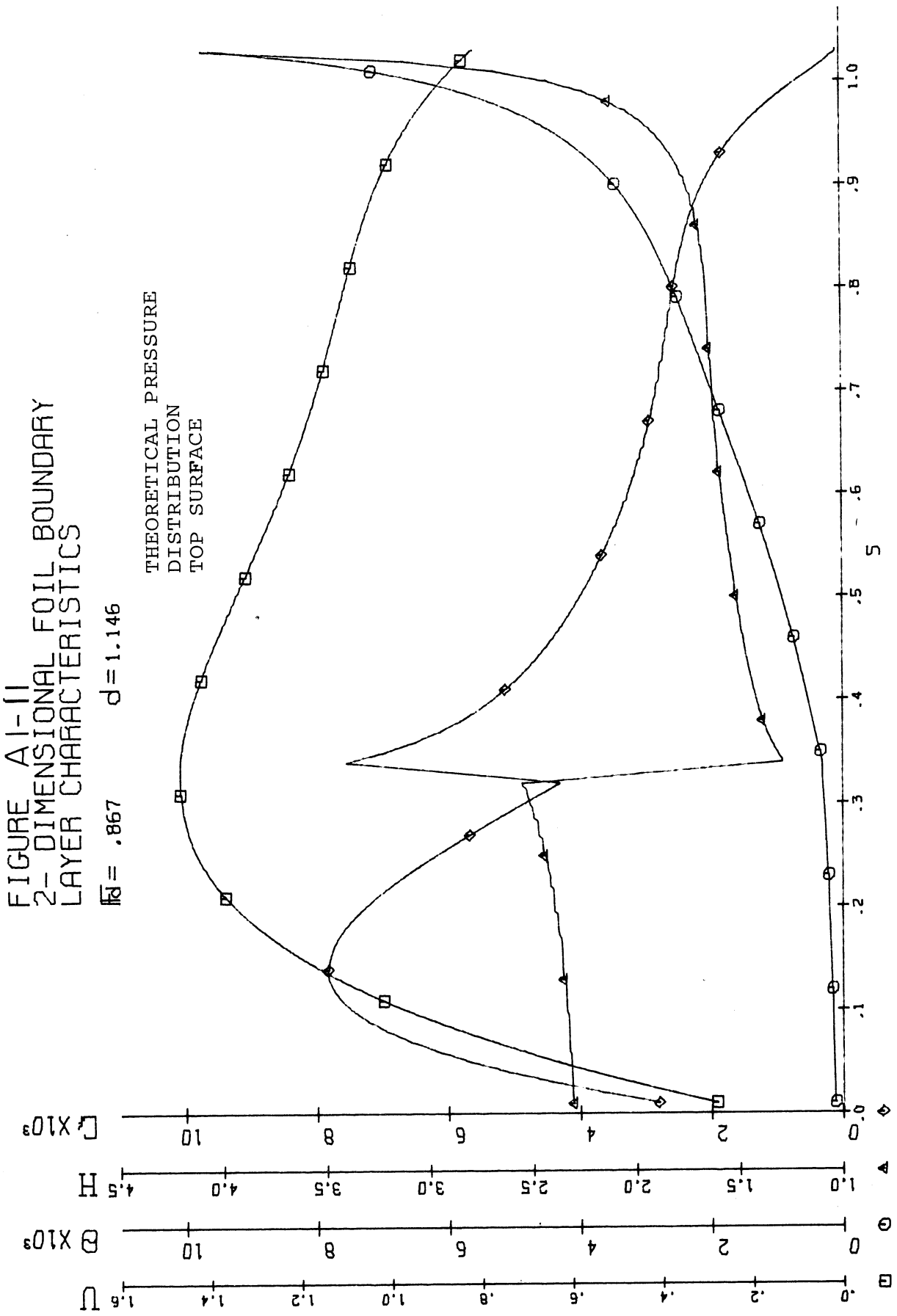
FIGURE A1-11
2- DIMENSIONAL FOIL BOUNDARY
LAYER CHARACTERISTICS
M = .867
d = 1.146
THEORETICAL PRESSURE
DISTRIBUTION
TOP SURFACE
S
U
θ X10³
H
δ* X10³

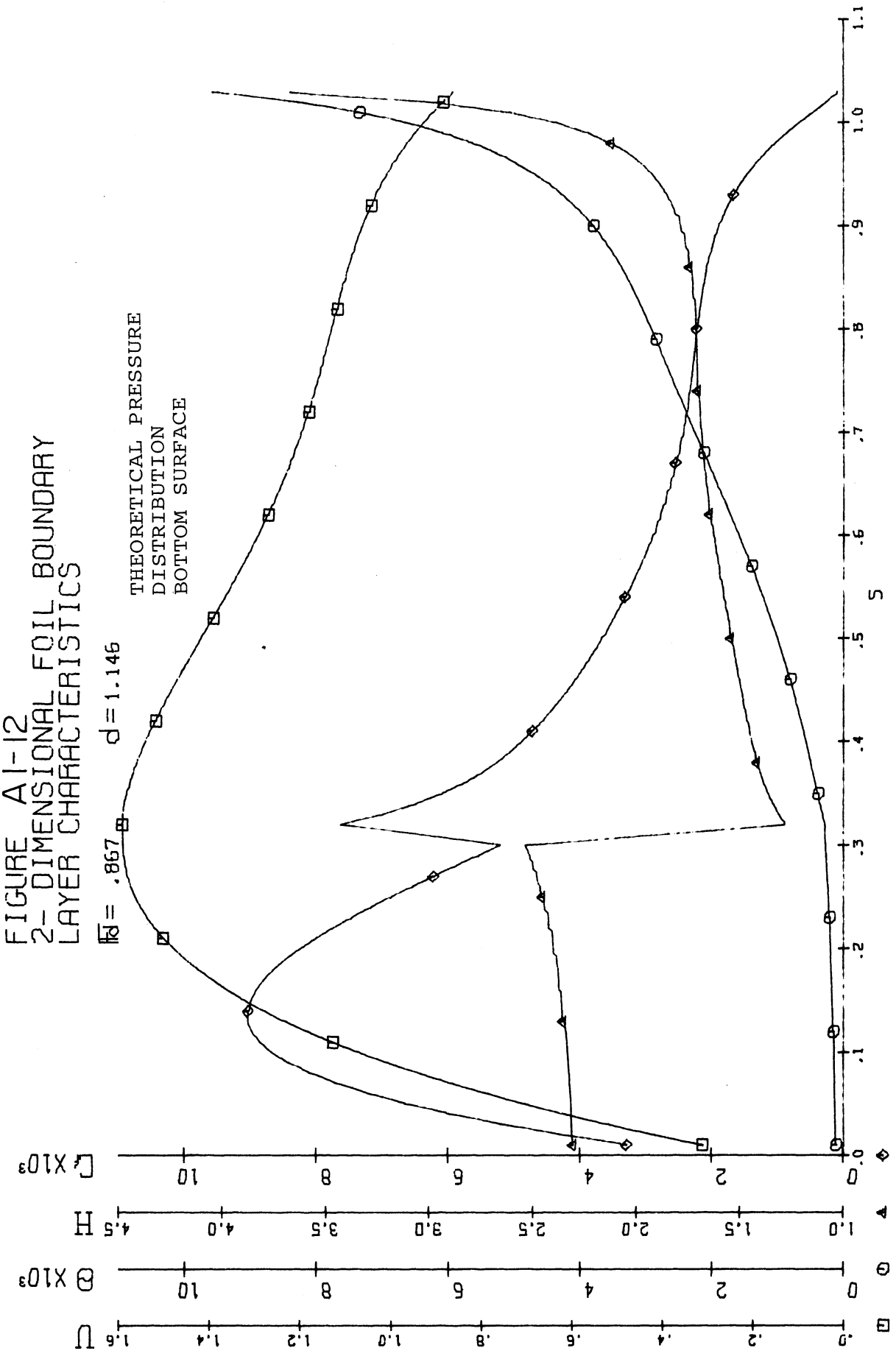
FIGURE A1-12
2- DIMENSIONAL FOIL BOUNDARY
LAYER CHARACTERISTICS
$\overline{R_d}$ = .867
d = 1.146
THEORETICAL PRESSURE
DISTRIBUTION
BOTTOM SURFACE
U
Θ X10³
H
Γ X10³
S

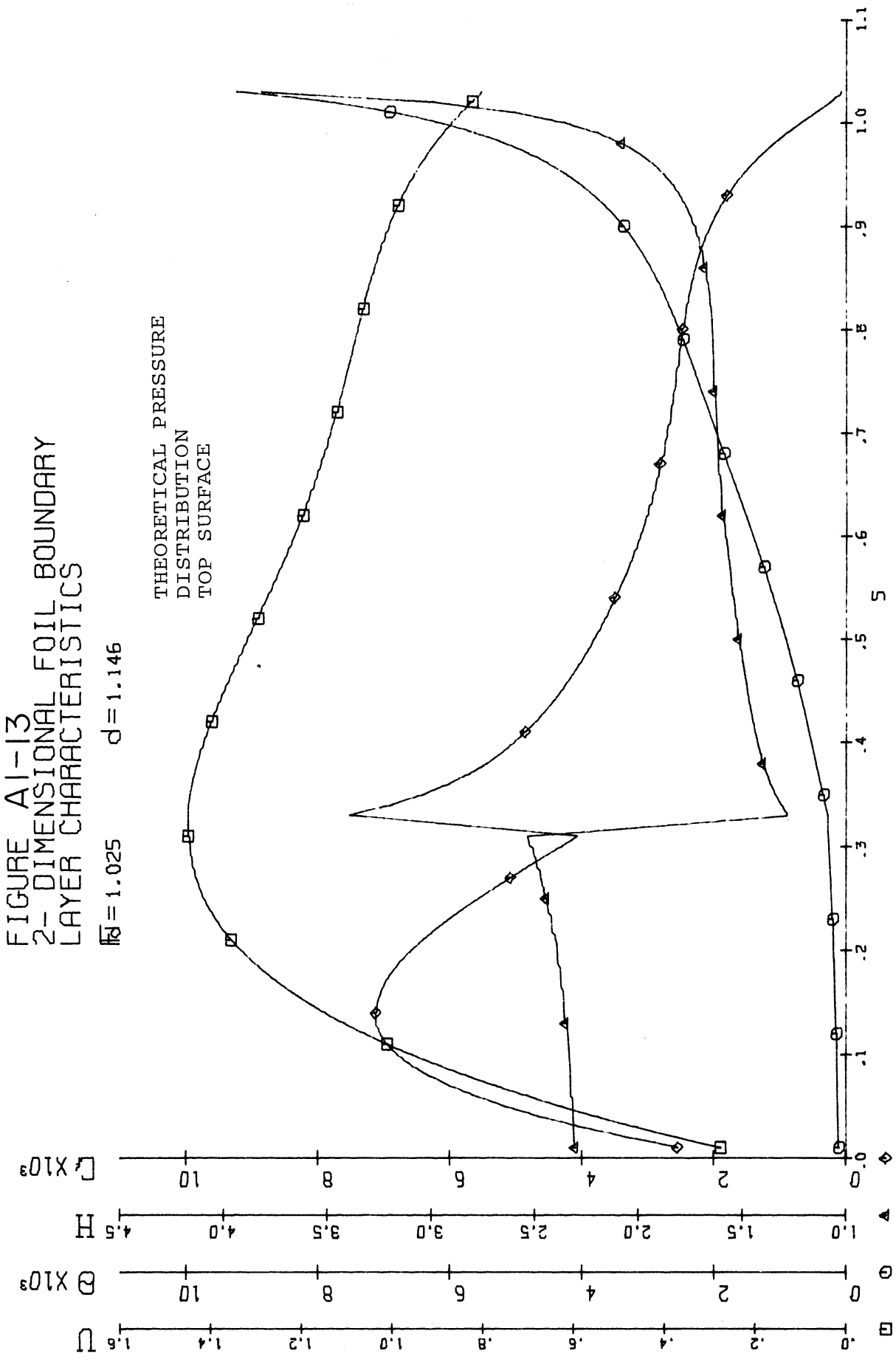
FIGURE A1-13
2- DIMENSIONAL FOIL BOUNDARY
LAYER CHARACTERISTICS
$\overline{M_0}$ = 1.025 d = 1.146
THEORETICAL PRESSURE
DISTRIBUTION
TOP SURFACE
U
Θ X10³
H
δ* X10³
S

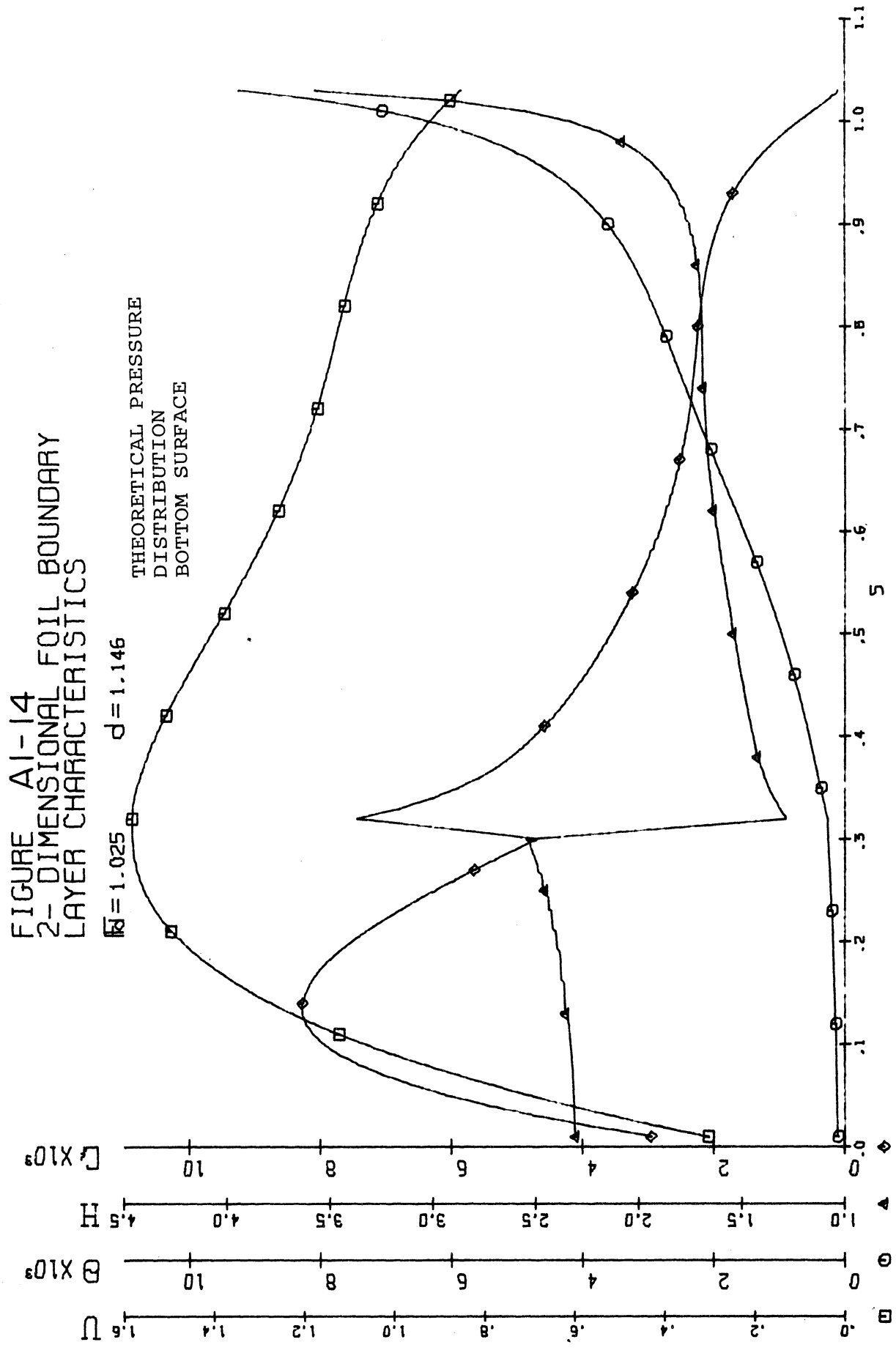
FIGURE A1-14
2- DIMENSIONAL FOIL BOUNDARY
LAYER CHARACTERISTICS
d = 1.146
d = 1.025
THEORETICAL PRESSURE
DISTRIBUTION
BOTTOM SURFACE
S
U
θ X10³
H
δ* X10³

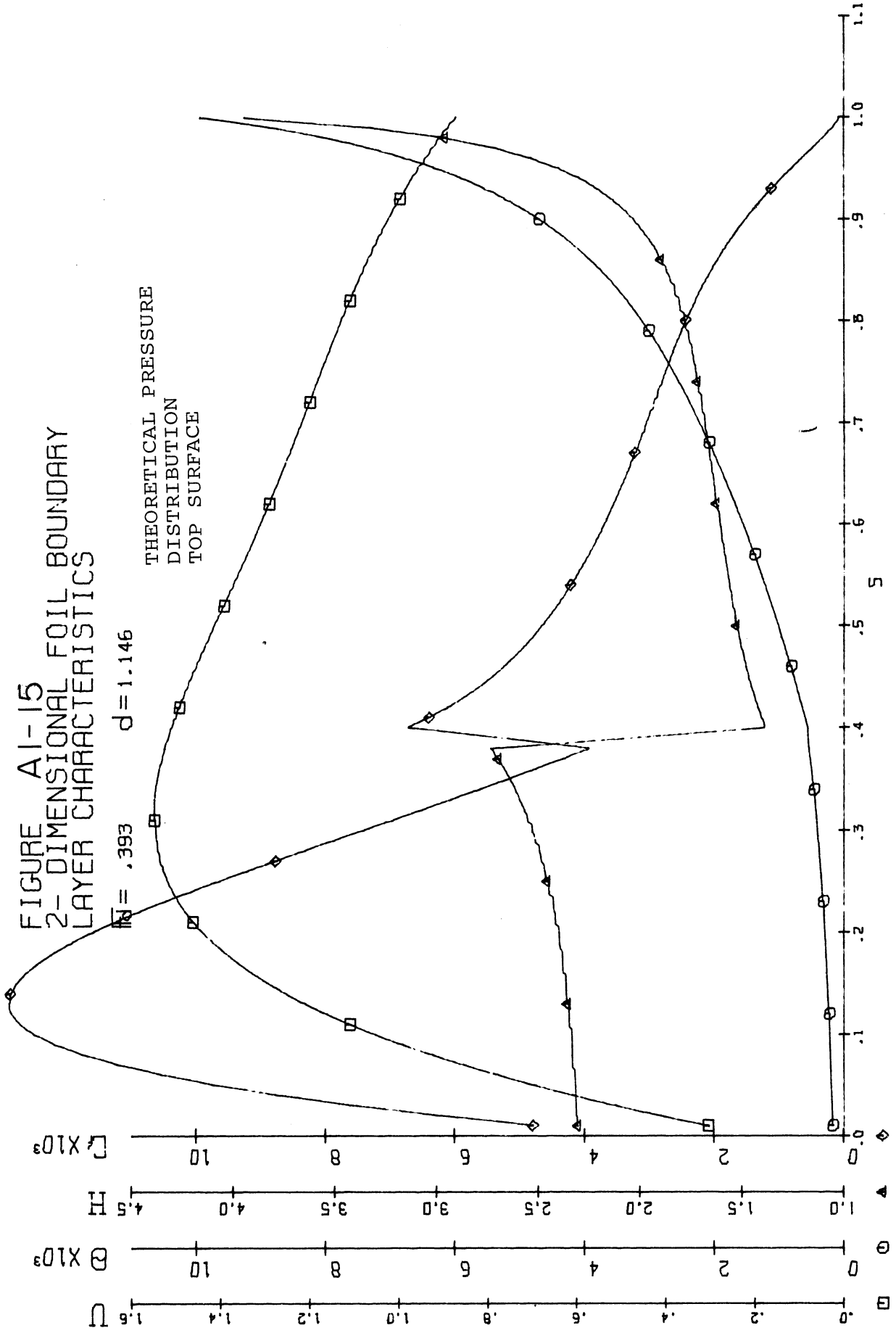
FIGURE A1-15
2- DIMENSIONAL FOIL BOUNDARY
LAYER CHARACTERISTICS
d=1.146
THEORETICAL PRESSURE
DISTRIBUTION
TOP SURFACE
S
U
Θ X10³
H
δ* X10³
C

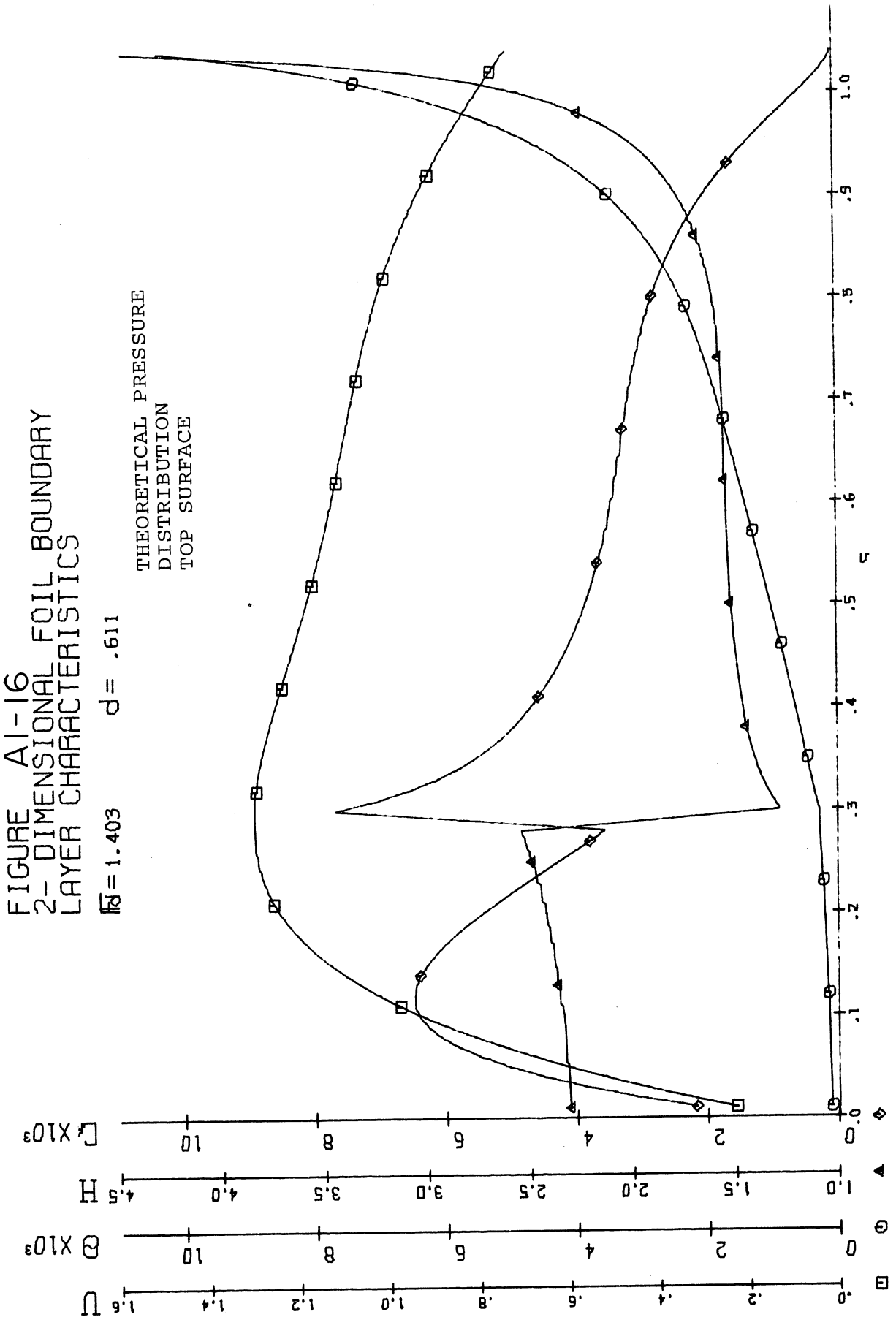
FIGURE A1-16
2- DIMENSIONAL FOIL BOUNDARY
LAYER CHARACTERISTICS
M = 1.403 d = .611
THEORETICAL PRESSURE
DISTRIBUTION
TOP SURFACE
U
θ X10³
H
δ* X10³
η

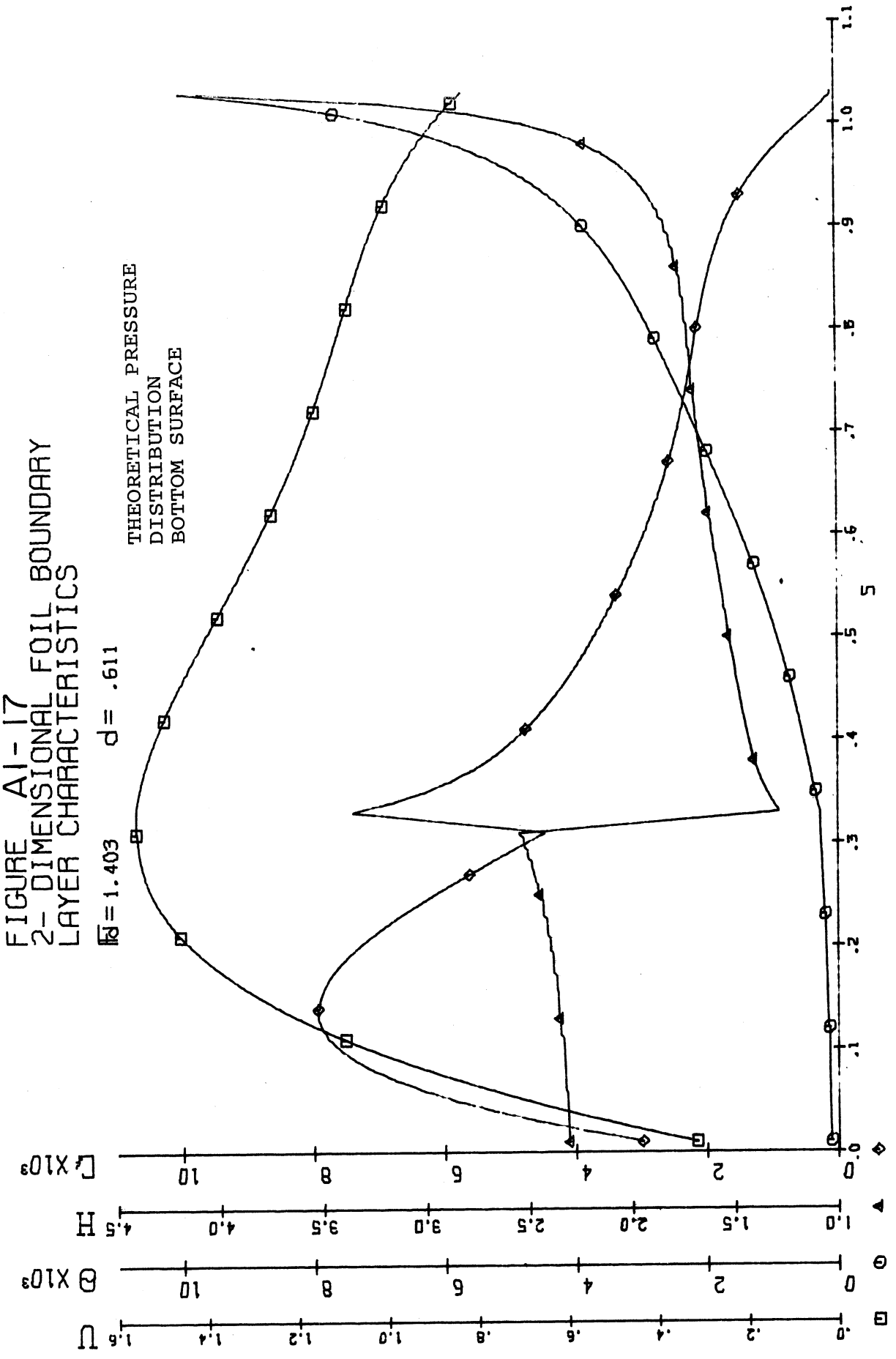
FIGURE A1-17
2- DIMENSIONAL FOIL BOUNDARY
LAYER CHARACTERISTICS
M = 1.403
d = .611
THEORETICAL PRESSURE
DISTRIBUTION
BOTTOM SURFACE
S
U
Θ X10³
H
δ* X10³

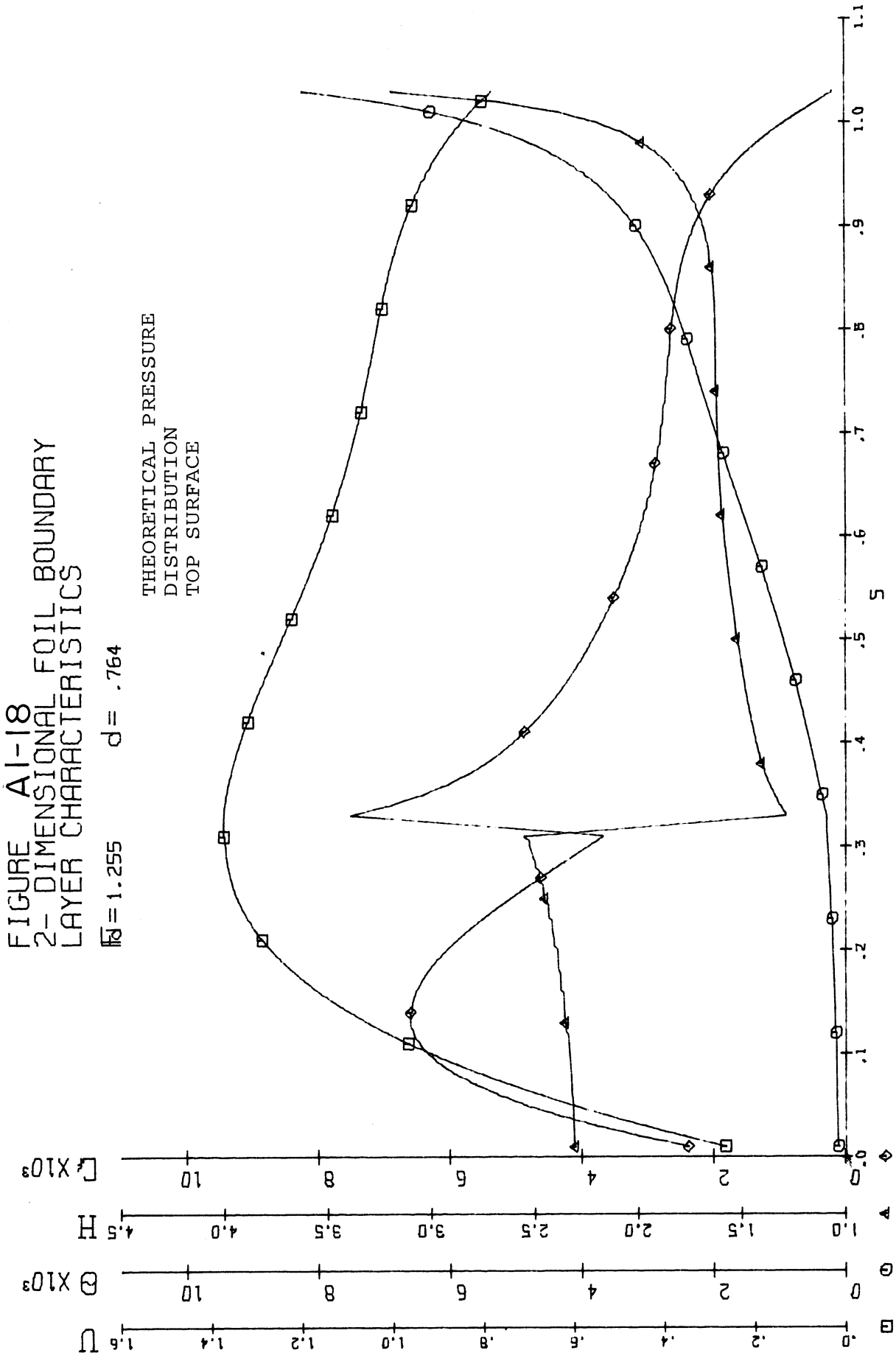
FIGURE A1-18
2- DIMENSIONAL FOIL BOUNDARY
LAYER CHARACTERISTICS
Re = 1.255
d = .764
THEORETICAL PRESSURE
DISTRIBUTION
TOP SURFACE
U
Θ X10³
H
δ* X10³
S

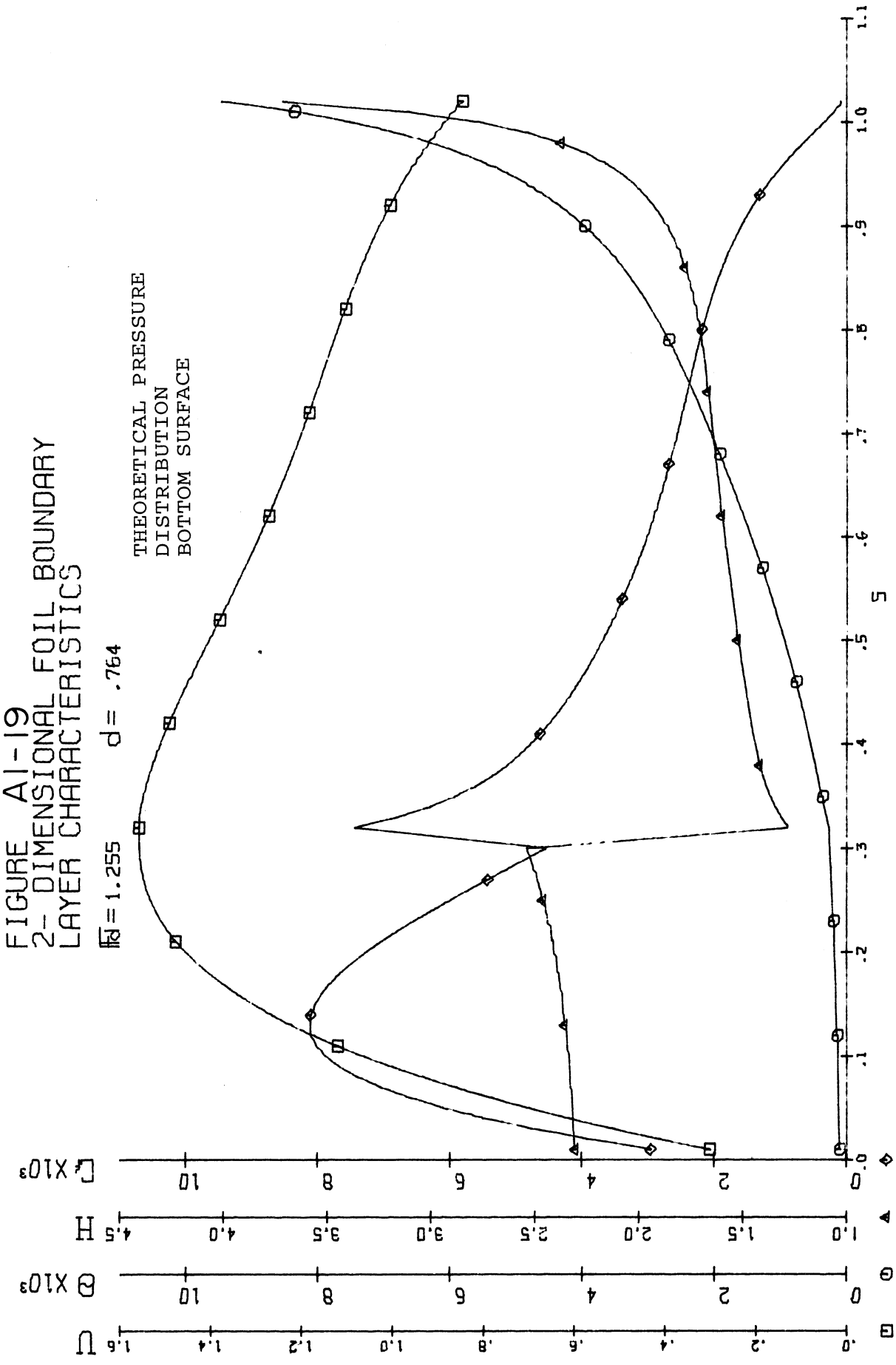
FIGURE A1-19
2- DIMENSIONAL FOIL BOUNDARY
LAYER CHARACTERISTICS
$\overline{R_d}$ = 1.255
d = .764
THEORETICAL PRESSURE
DISTRIBUTION
BOTTOM SURFACE
U
Θ X10³
H
δ* X10³
S

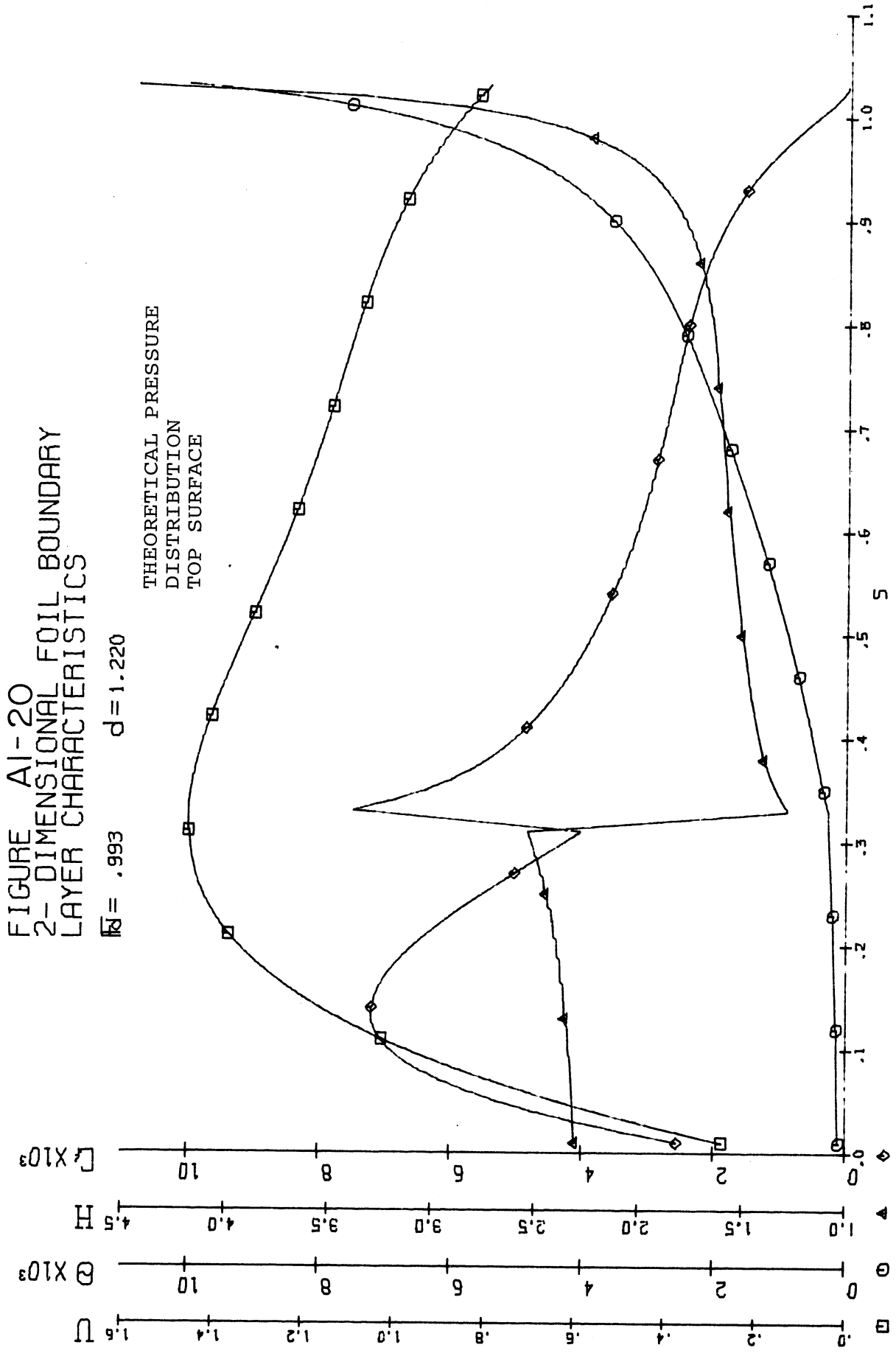
FIGURE A1-20
2- DIMENSIONAL FOIL BOUNDARY
LAYER CHARACTERISTICS
R = .993
d = 1.220
THEORETICAL PRESSURE
DISTRIBUTION
TOP SURFACE
S
U
θ X10³
H
Cf X10³

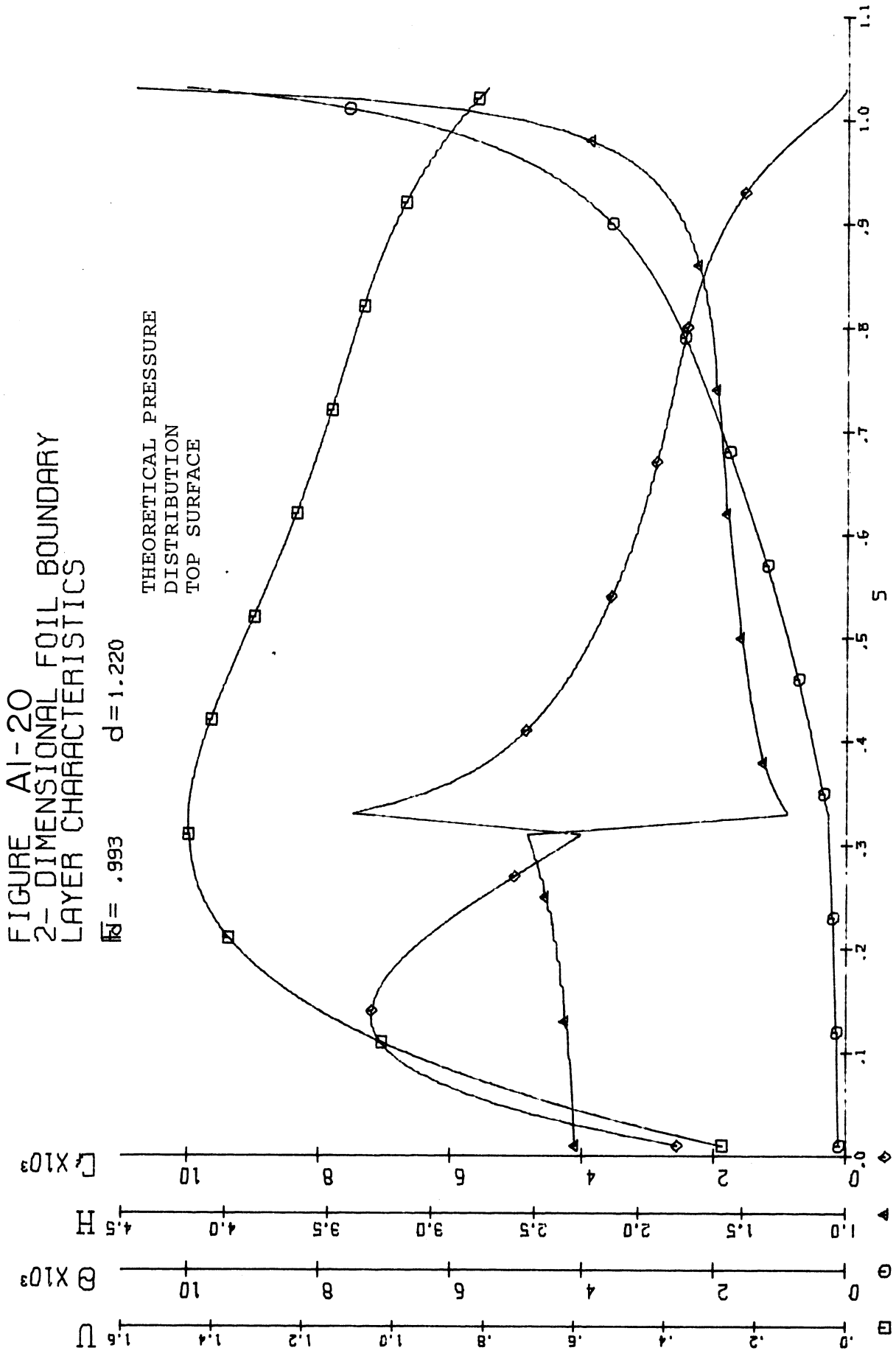
FIGURE A1-20
2- DIMENSIONAL FOIL BOUNDARY
LAYER CHARACTERISTICS
M = .993
d = 1.220
THEORETICAL PRESSURE
DISTRIBUTION
TOP SURFACE
S
Φ
Θ
H
δ* X10³
θ X10³
U

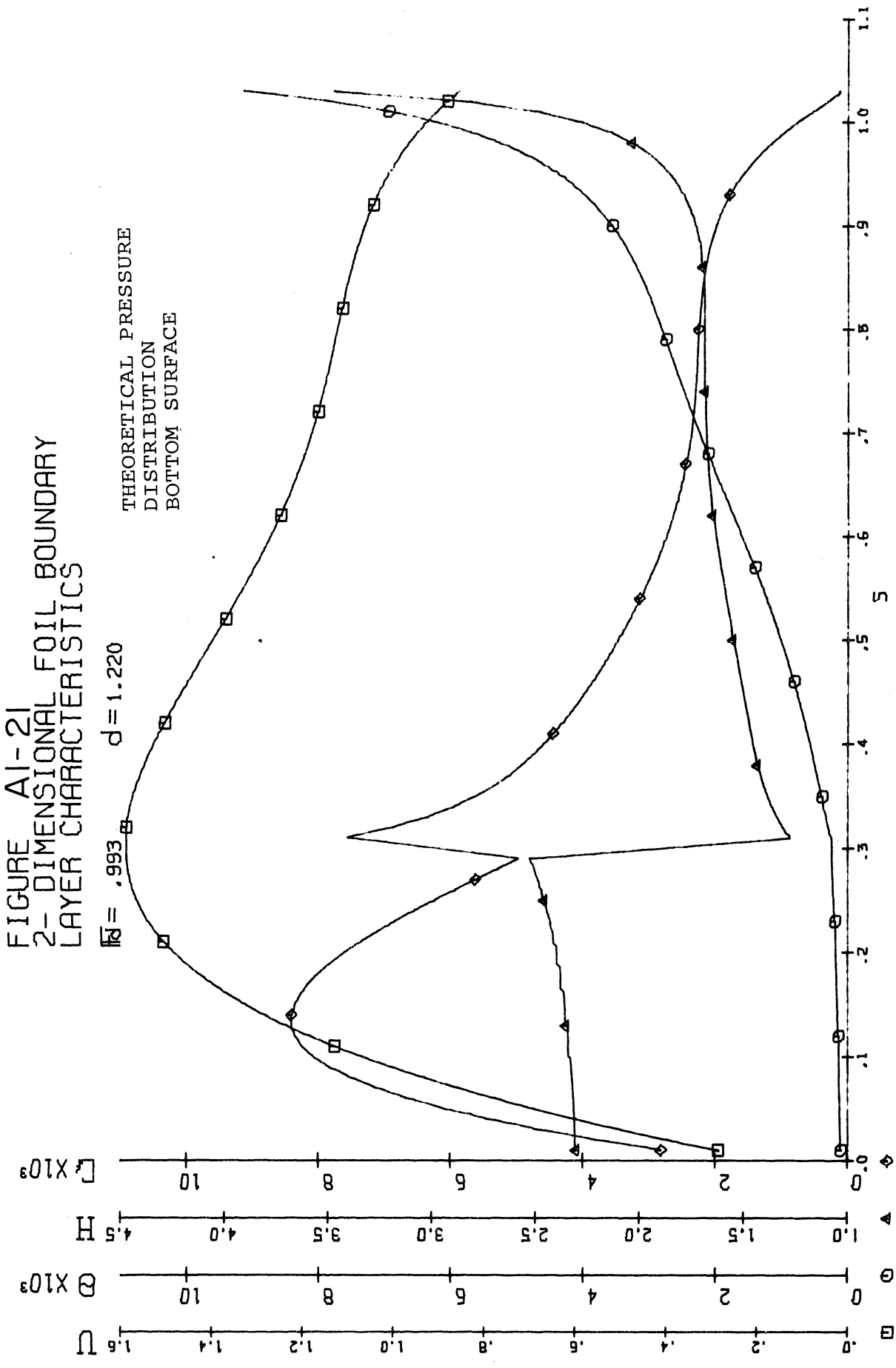
FIGURE A1-21
2- DIMENSIONAL FOIL BOUNDARY
LAYER CHARACTERISTICS
THEORETICAL PRESSURE
DISTRIBUTION
BOTTOM SURFACE
d= 1.220
= .993
U
Θ X10³
H
δ* X10³
δ
S

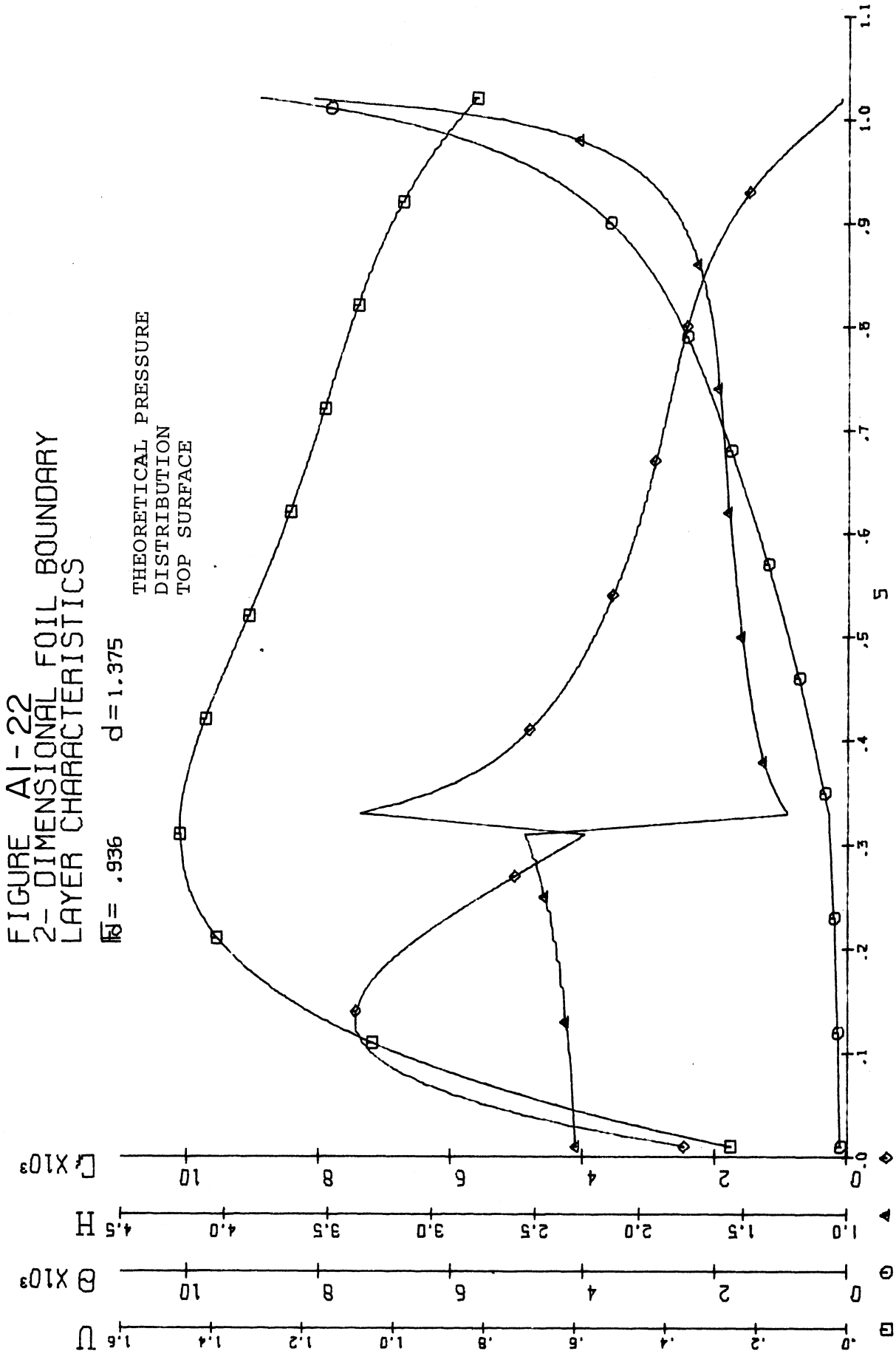
FIGURE A1-22
2- DIMENSIONAL FOIL BOUNDARY
LAYER CHARACTERISTICS
$\bar{M}_\infty$ = .936 d = 1.375
THEORETICAL PRESSURE
DISTRIBUTION
TOP SURFACE
U
Θ X10³
H
δ* X10³
S

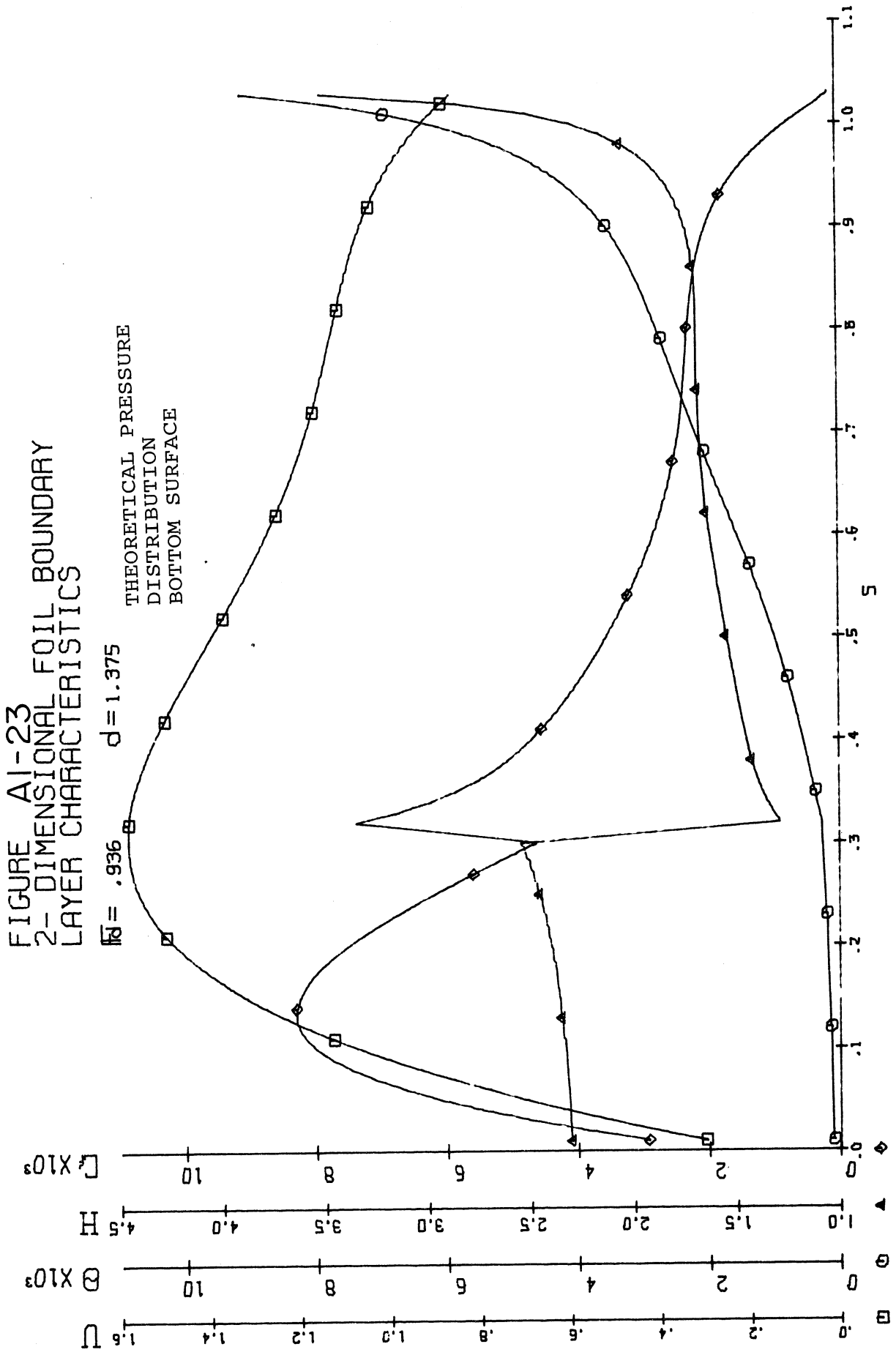
FIGURE A1-23
2- DIMENSIONAL FOIL BOUNDARY
LAYER CHARACTERISTICS
M = .936
d = 1.375
THEORETICAL PRESSURE
DISTRIBUTION
BOTTOM SURFACE
S
U
θ X10³
H
δ* X10³

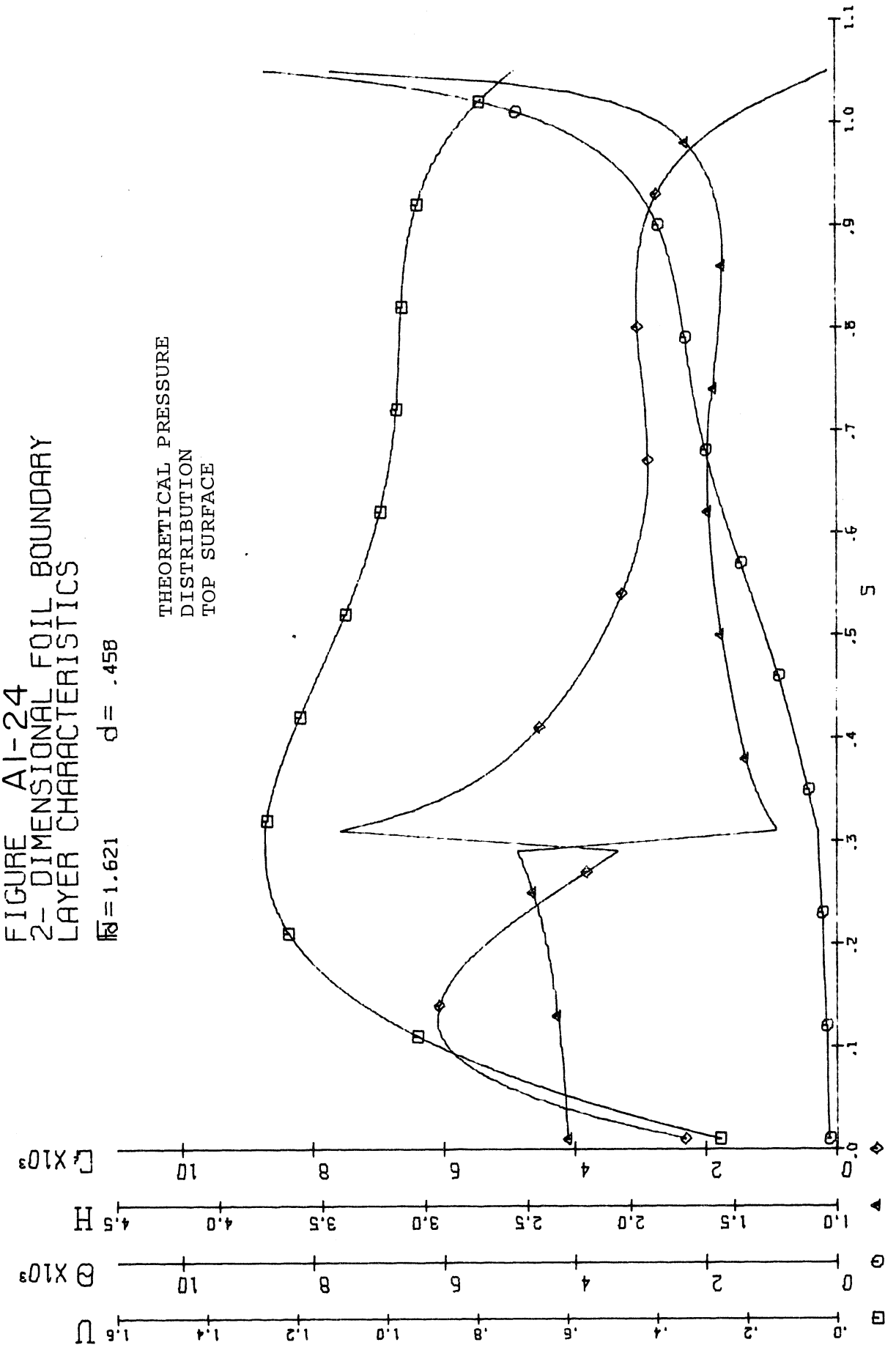
FIGURE A1-24
2- DIMENSIONAL FOIL BOUNDARY
LAYER CHARACTERISTICS
$\overline{k_d}$=1.621 d= .458
THEORETICAL PRESSURE
DISTRIBUTION
TOP SURFACE
U
Θ X10³
H
Cf X10³
S

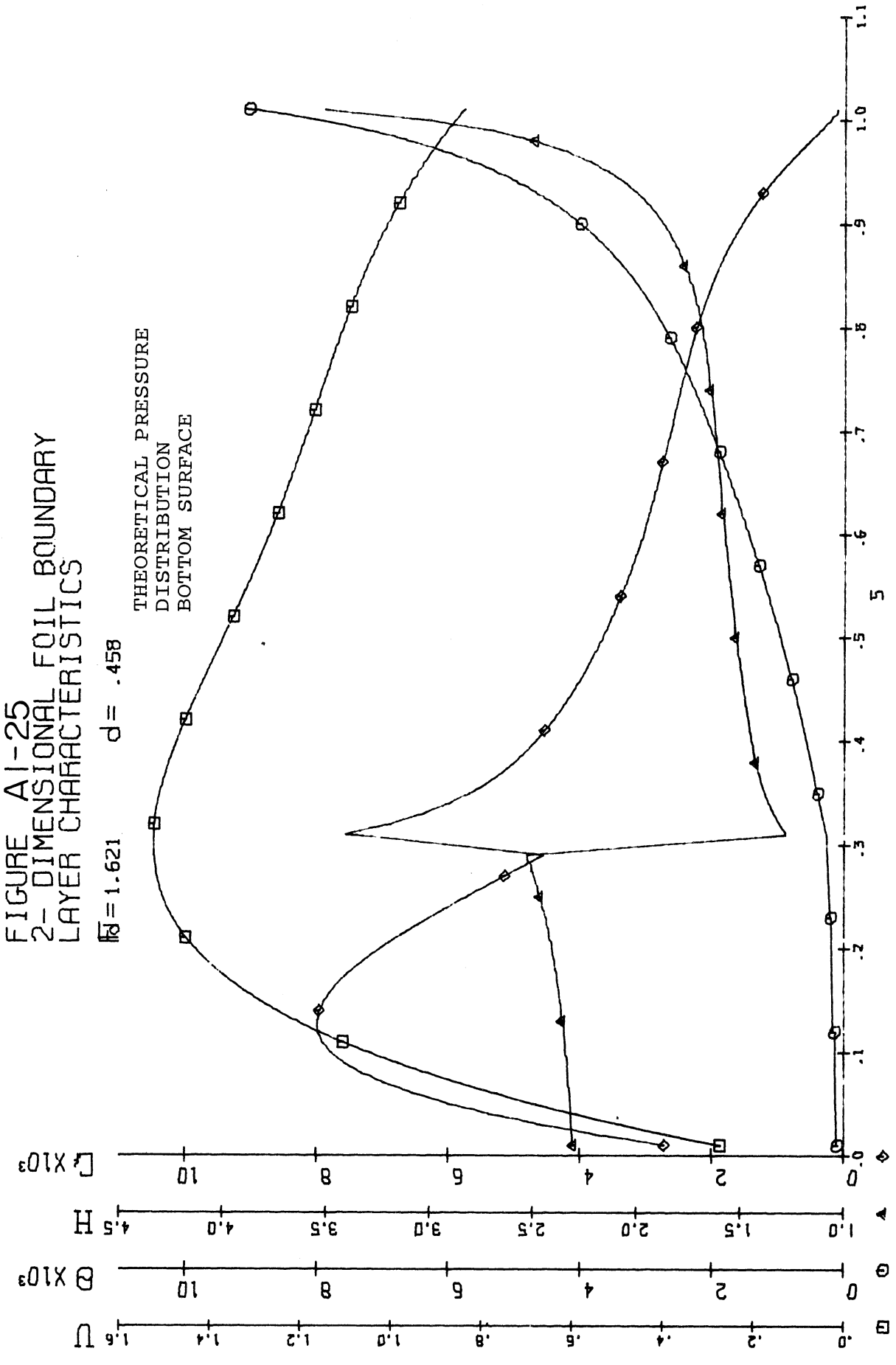
FIGURE A1-25
2- DIMENSIONAL FOIL BOUNDARY
LAYER CHARACTERISTICS
$\overline{M}_\infty$ = 1.621
d = .458
THEORETICAL PRESSURE
DISTRIBUTION
BOTTOM SURFACE
U
Θ X10³
H
δ* X10³
S

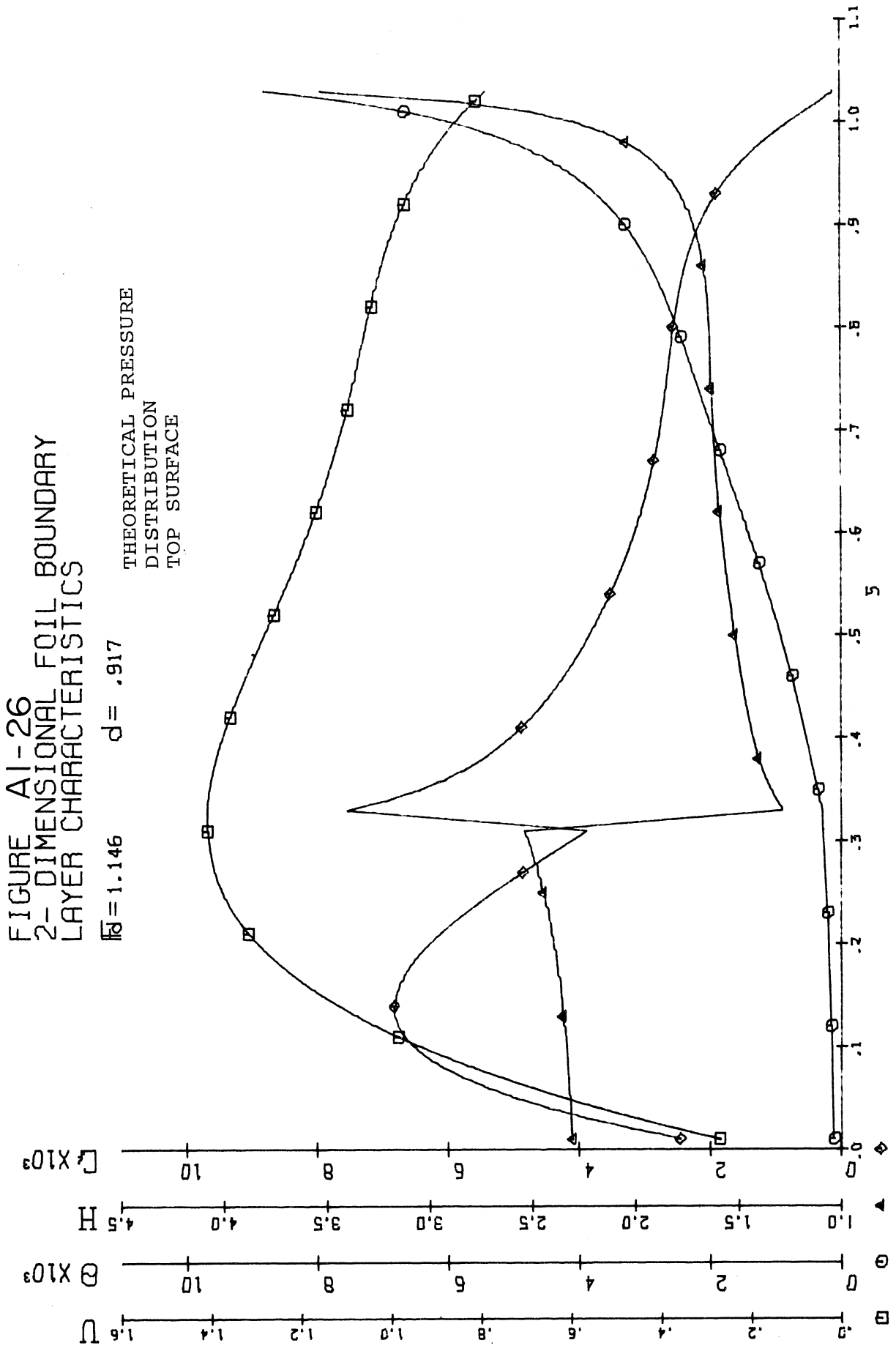
FIGURE A1-26
2- DIMENSIONAL FOIL BOUNDARY
LAYER CHARACTERISTICS
R=1.146
d= .917
THEORETICAL PRESSURE
DISTRIBUTION
TOP SURFACE
U
θ X10³
H
δ* X10³
S

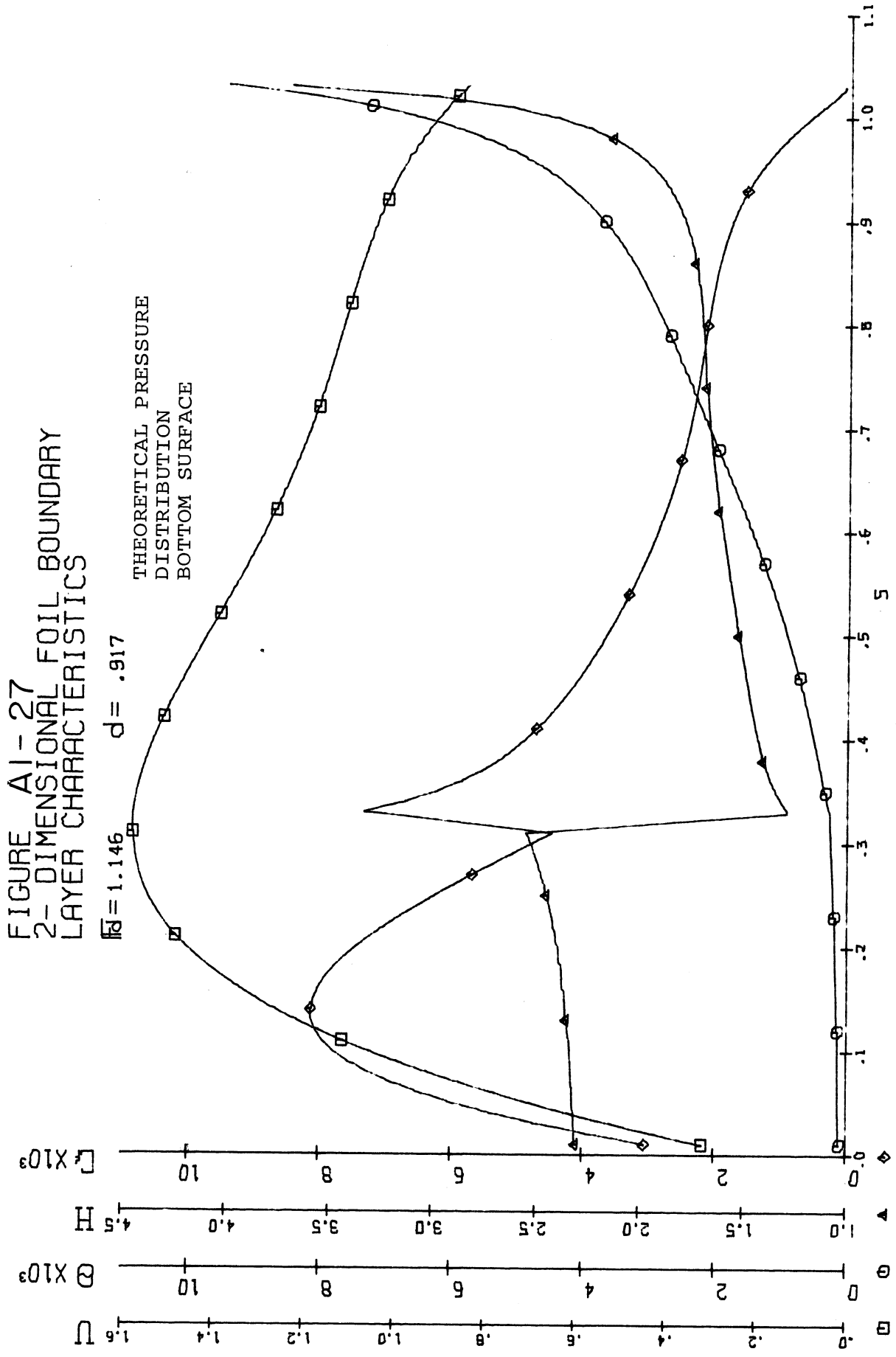
FIGURE AI-27
2- DIMENSIONAL FOIL BOUNDARY
LAYER CHARACTERISTICS
$\overline{R_d}$ = 1.146
d = .917
THEORETICAL PRESSURE
DISTRIBUTION
BOTTOM SURFACE
U
Θ X10³
H
δ* X10³
S

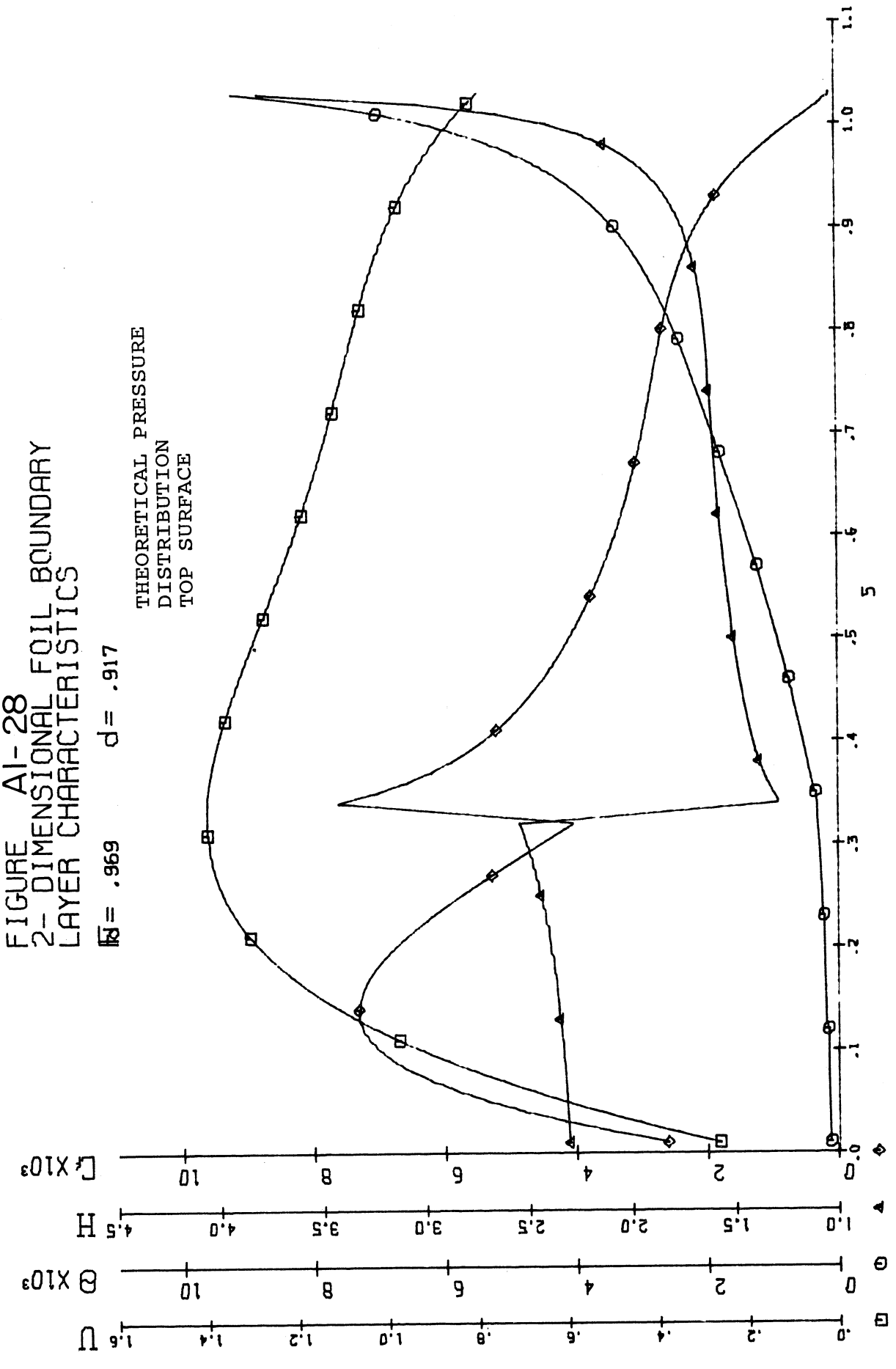
FIGURE A1-28
2- DIMENSIONAL FOIL BOUNDARY
LAYER CHARACTERISTICS
M = .969
d = .917
THEORETICAL PRESSURE
DISTRIBUTION
TOP SURFACE
U
Θ X10³
H
C_f X10³
δ
S

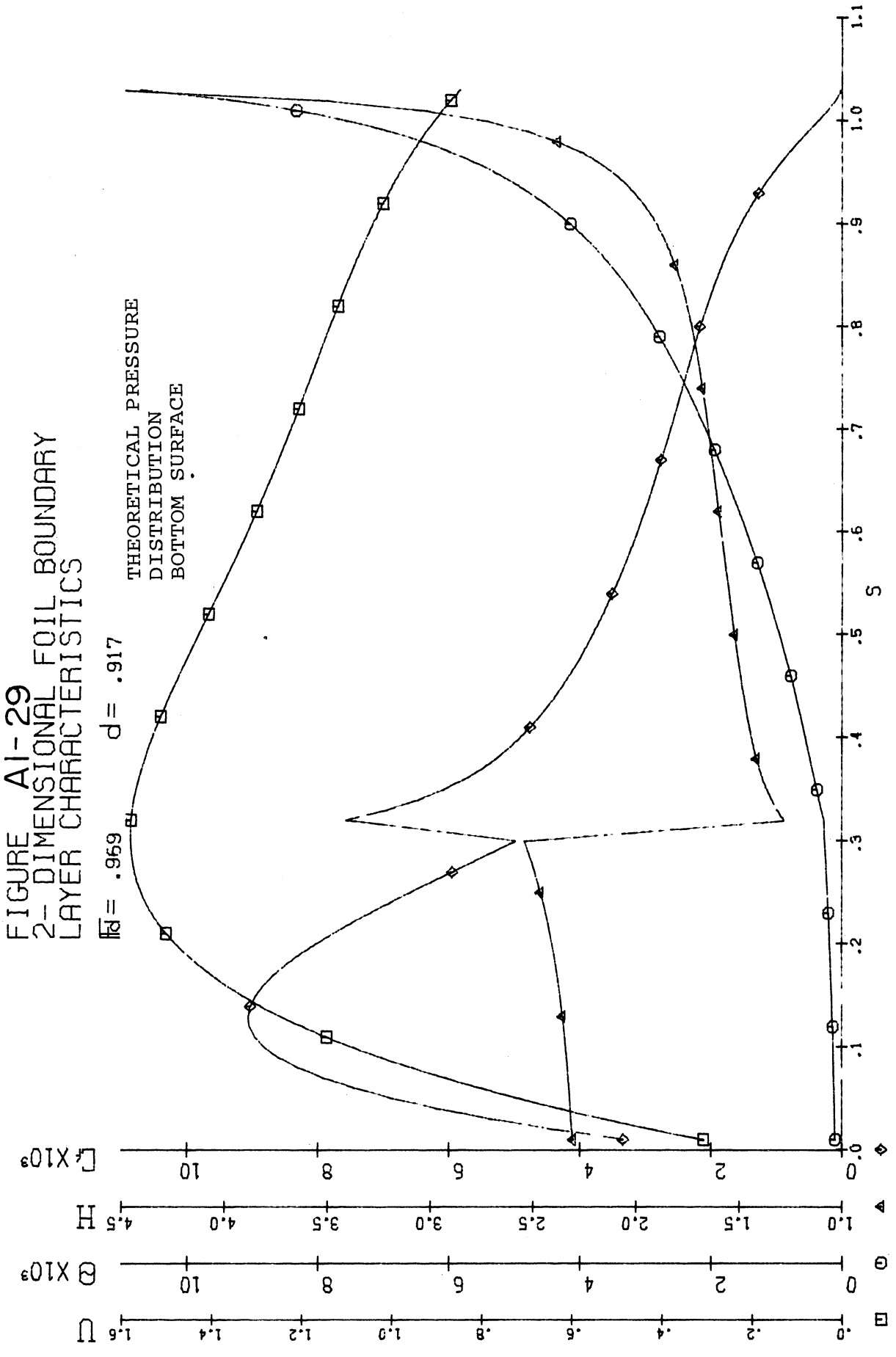
FIGURE A1-29
2- DIMENSIONAL FOIL BOUNDARY
LAYER CHARACTERISTICS
d= .969
d= .917
THEORETICAL PRESSURE
DISTRIBUTION
BOTTOM SURFACE
S
U
Θ X10³
H
δ* X10³

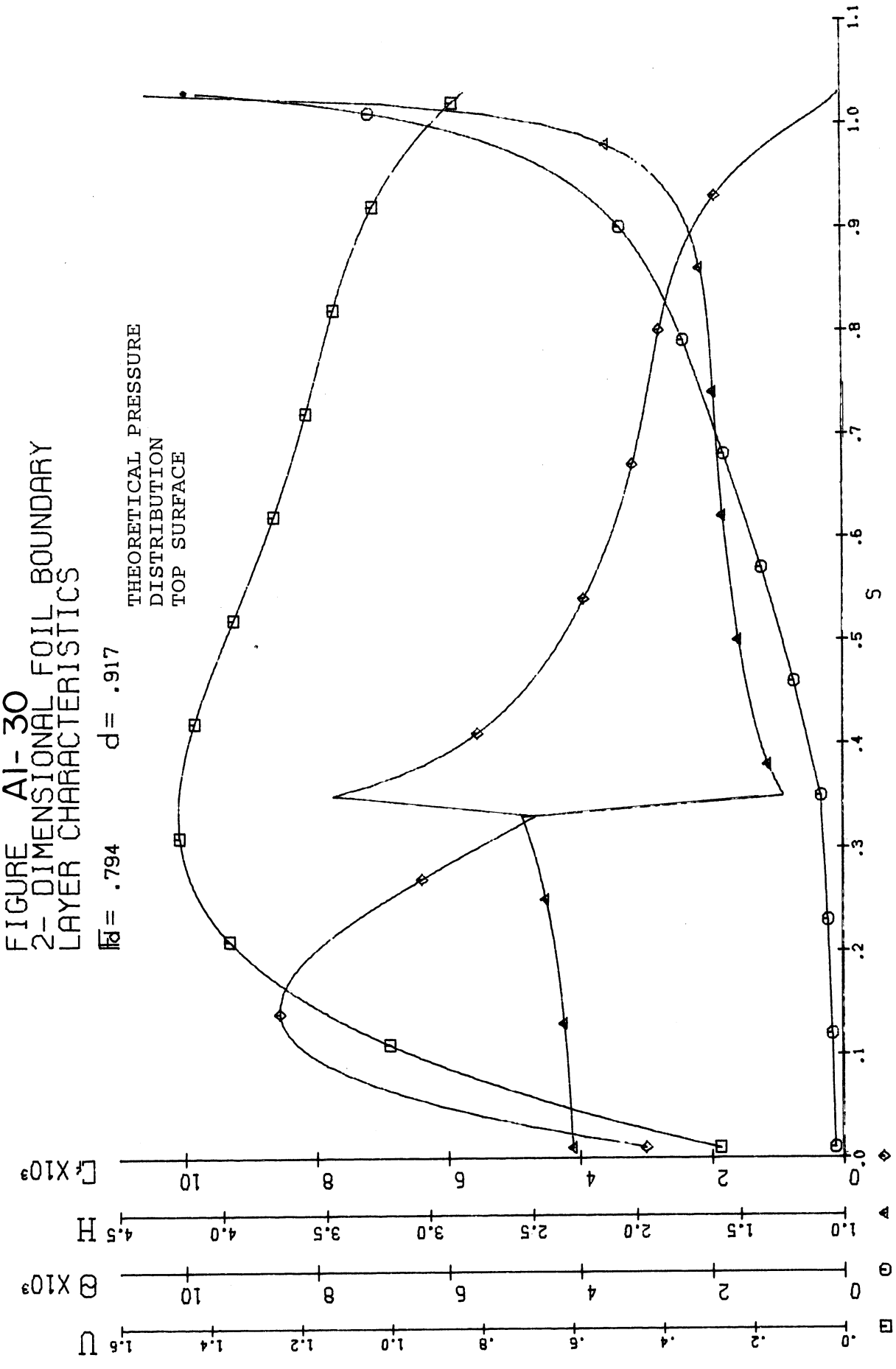
FIGURE A1-30
2- DIMENSIONAL FOIL BOUNDARY
LAYER CHARACTERISTICS
d = .917
THEORETICAL PRESSURE
DISTRIBUTION
TOP SURFACE
S
U
Θ X10³
H
δ* X10³
G

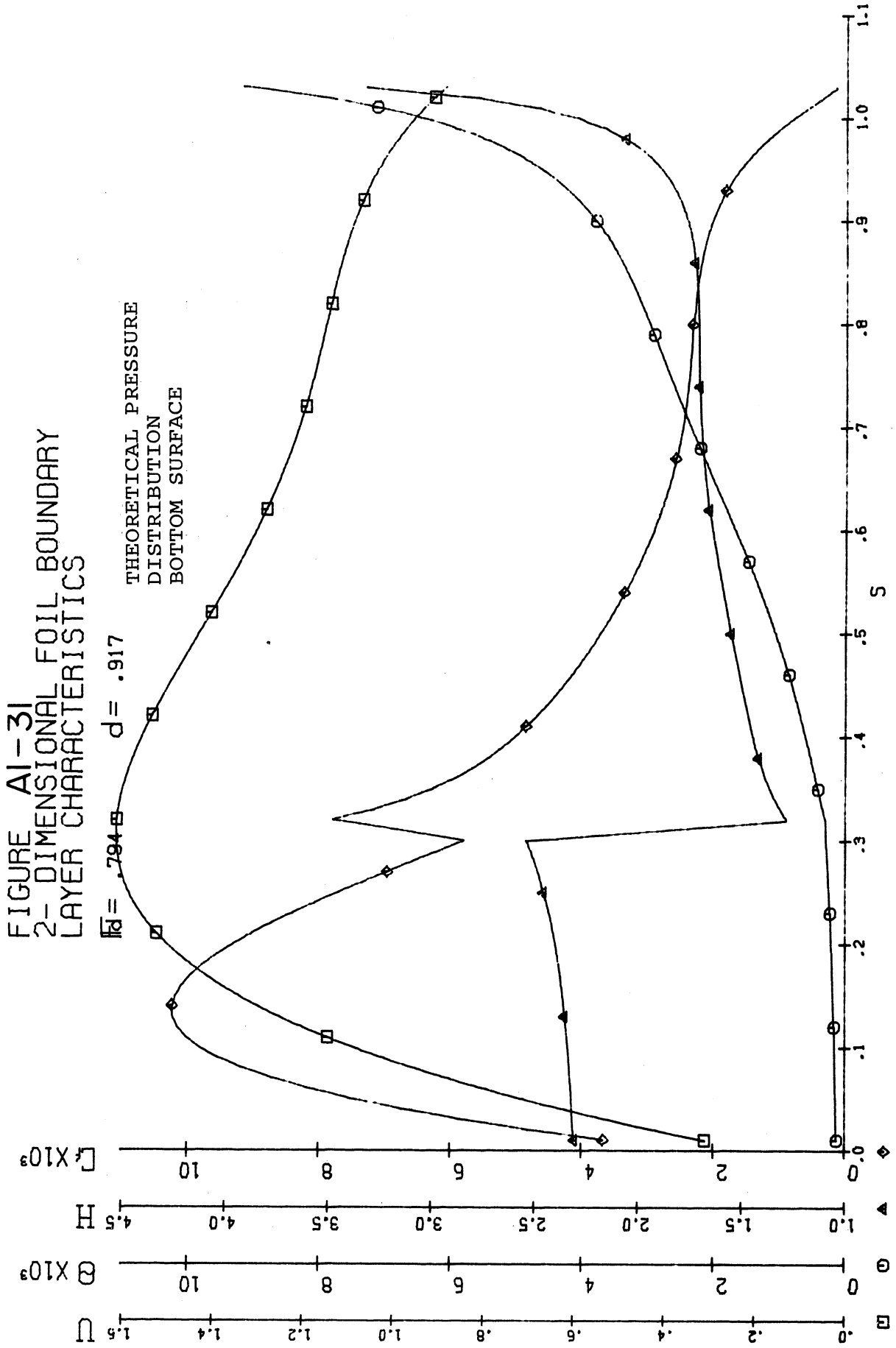
FIGURE A1-31
2- DIMENSIONAL FOIL BOUNDARY
LAYER CHARACTERISTICS
d= .917
d= .794
THEORETICAL PRESSURE
DISTRIBUTION
BOTTOM SURFACE
S
U
θ X10³
H
δ* X10³

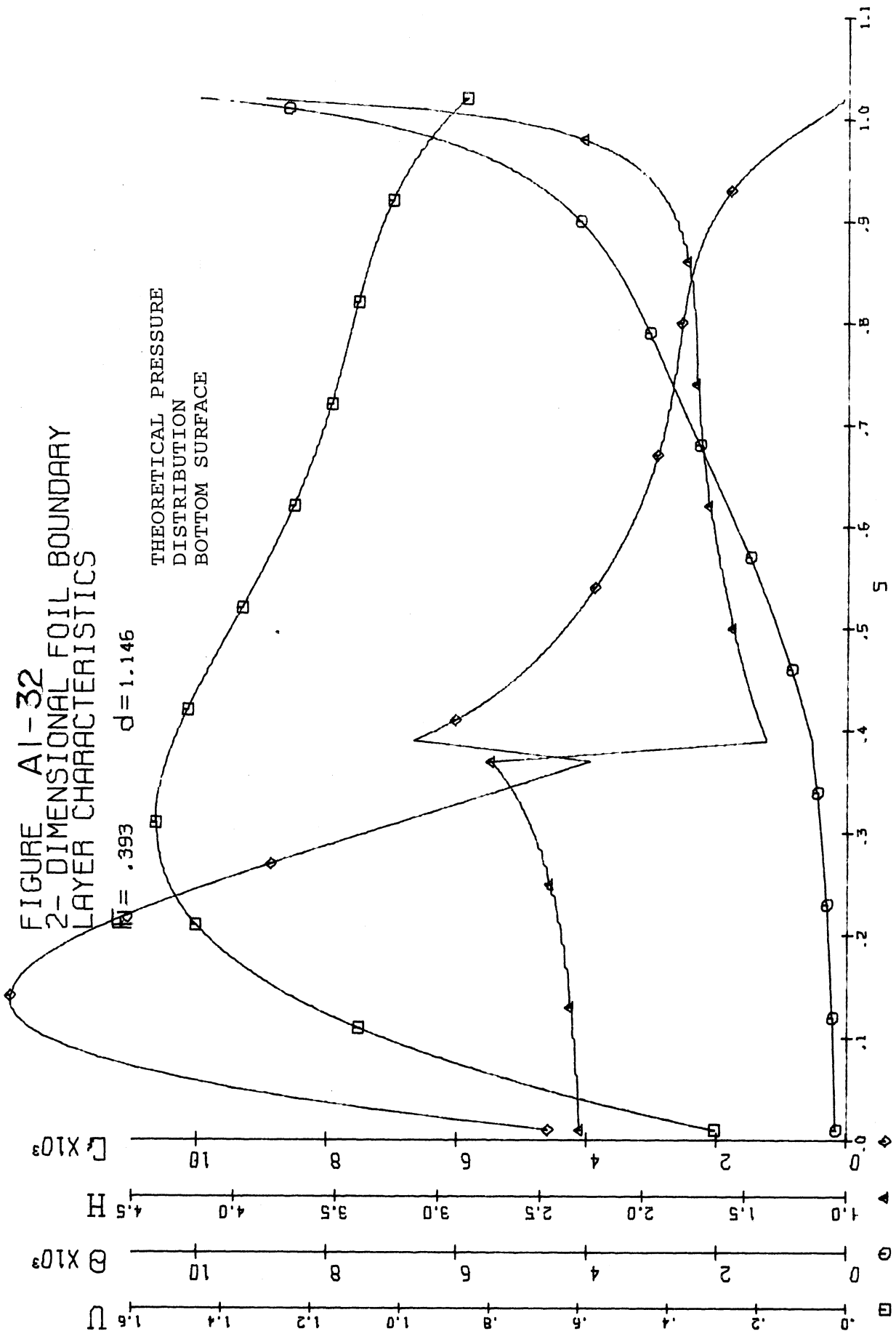
FIGURE A1-32
2- DIMENSIONAL FOIL BOUNDARY
LAYER CHARACTERISTICS
M = .393
d = 1.146
THEORETICAL PRESSURE
DISTRIBUTION
BOTTOM SURFACE
S
U
θ X10³
H
δ* X10³

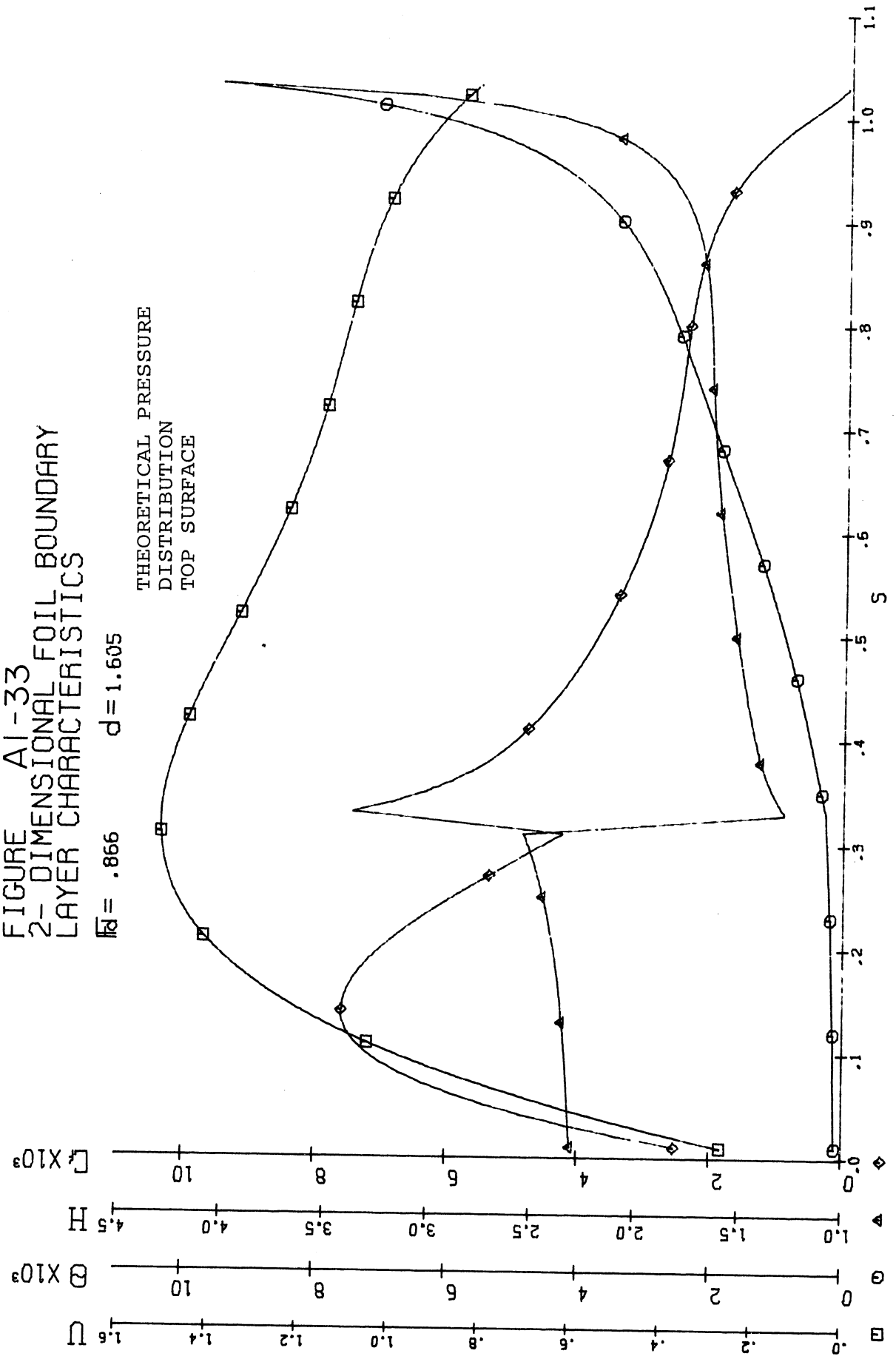
FIGURE A1-33
2- DIMENSIONAL FOIL BOUNDARY
LAYER CHARACTERISTICS
M = .866 d=1.605
THEORETICAL PRESSURE
DISTRIBUTION
TOP SURFACE
S
U
θ X10³
H
δ* X10³

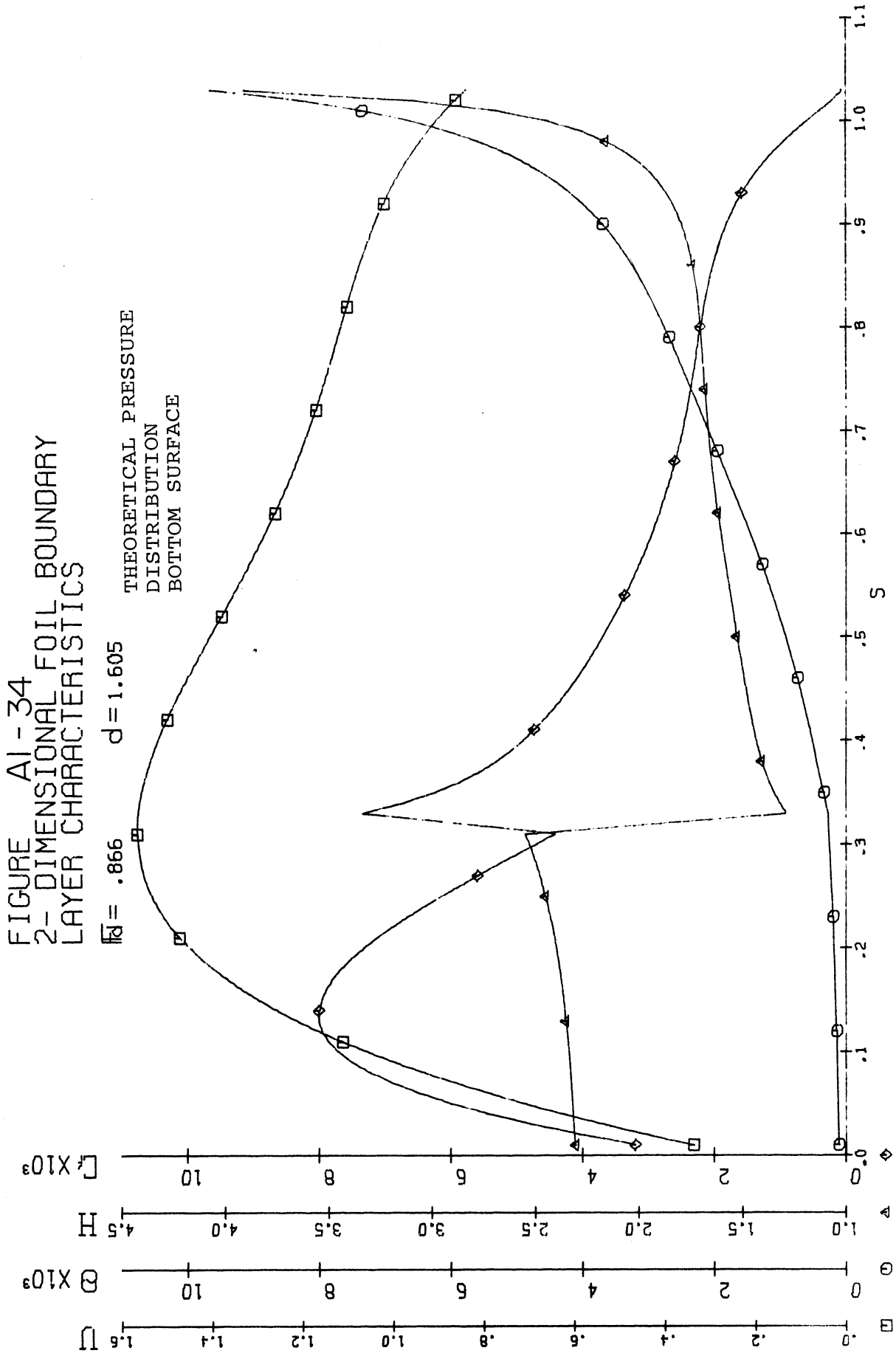
FIGURE A1-34
2-DIMENSIONAL FOIL BOUNDARY
LAYER CHARACTERISTICS
$\bar{x}_d$ = .866
d = 1.605
THEORETICAL PRESSURE
DISTRIBUTION
BOTTOM SURFACE
S
Φ
Θ
H
δ^* X10³
U

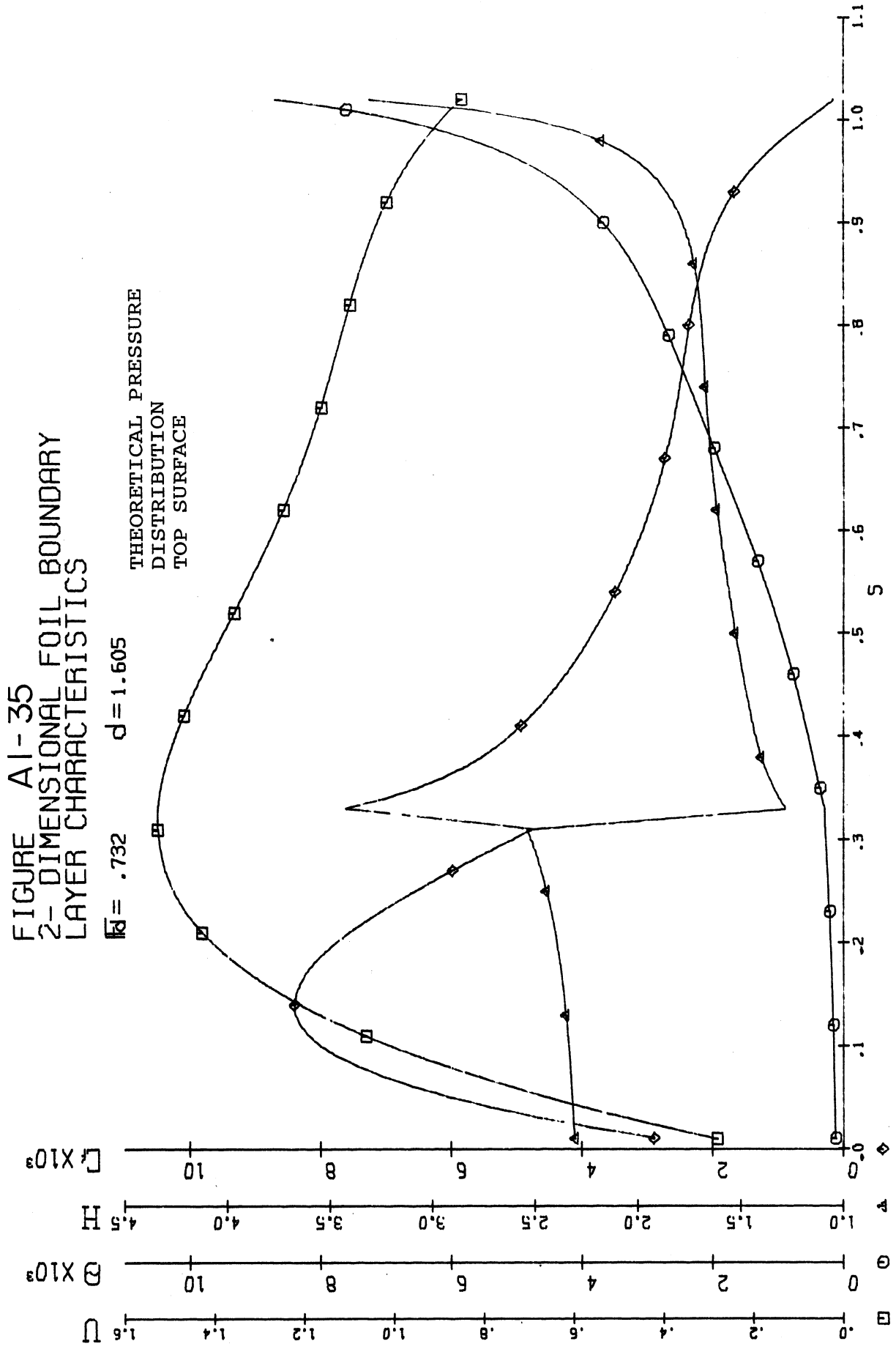
FIGURE A1-35
2- DIMENSIONAL FOIL BOUNDARY
LAYER CHARACTERISTICS
THEORETICAL PRESSURE
DISTRIBUTION
TOP SURFACE
d=1.605
S

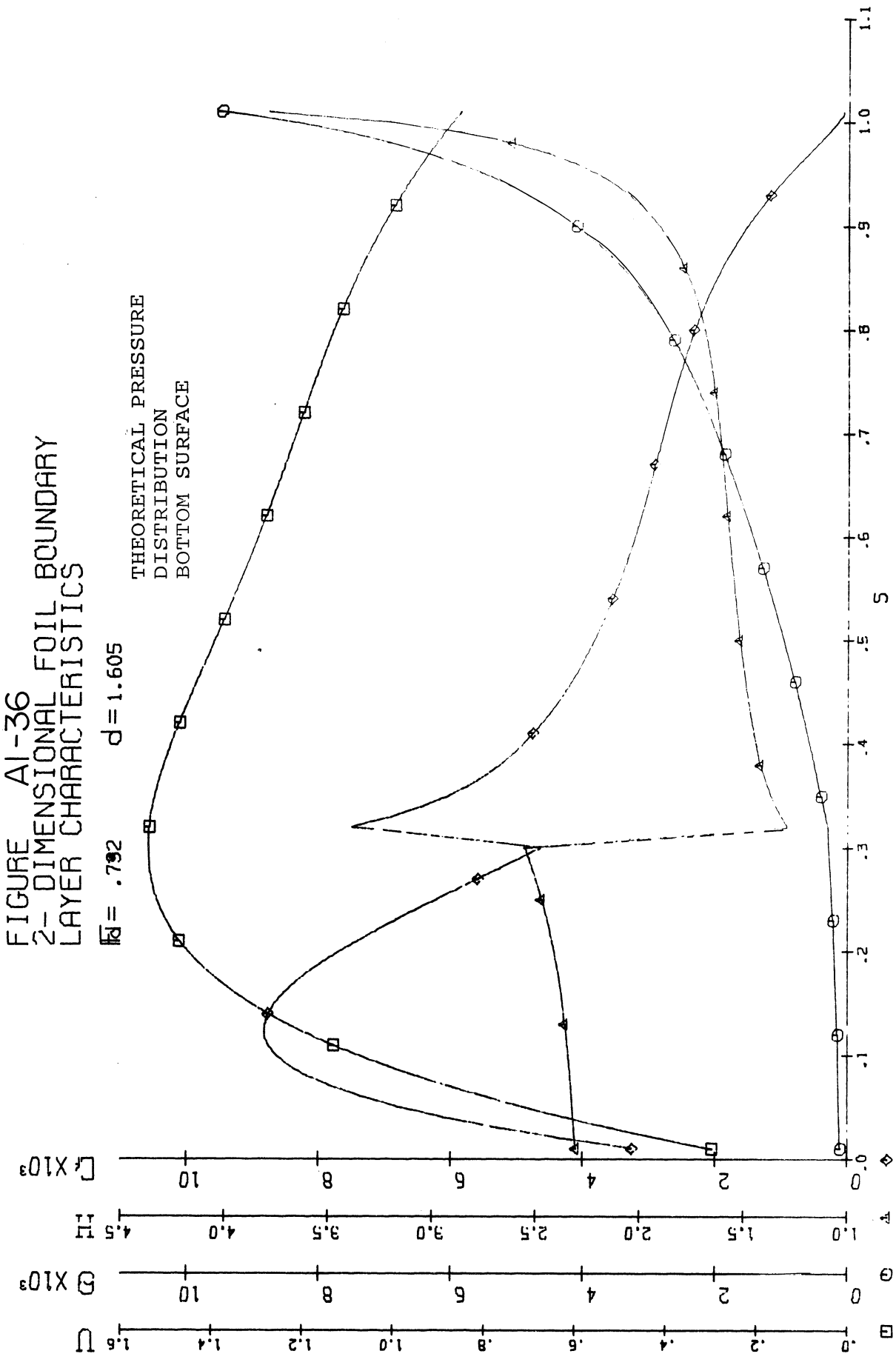
FIGURE A1-36
2- DIMENSIONAL FOIL BOUNDARY
LAYER CHARACTERISTICS
d = 1.605
THEORETICAL PRESSURE
DISTRIBUTION
BOTTOM SURFACE
S
U
δ* X10³
θ X10³
Γ X10³

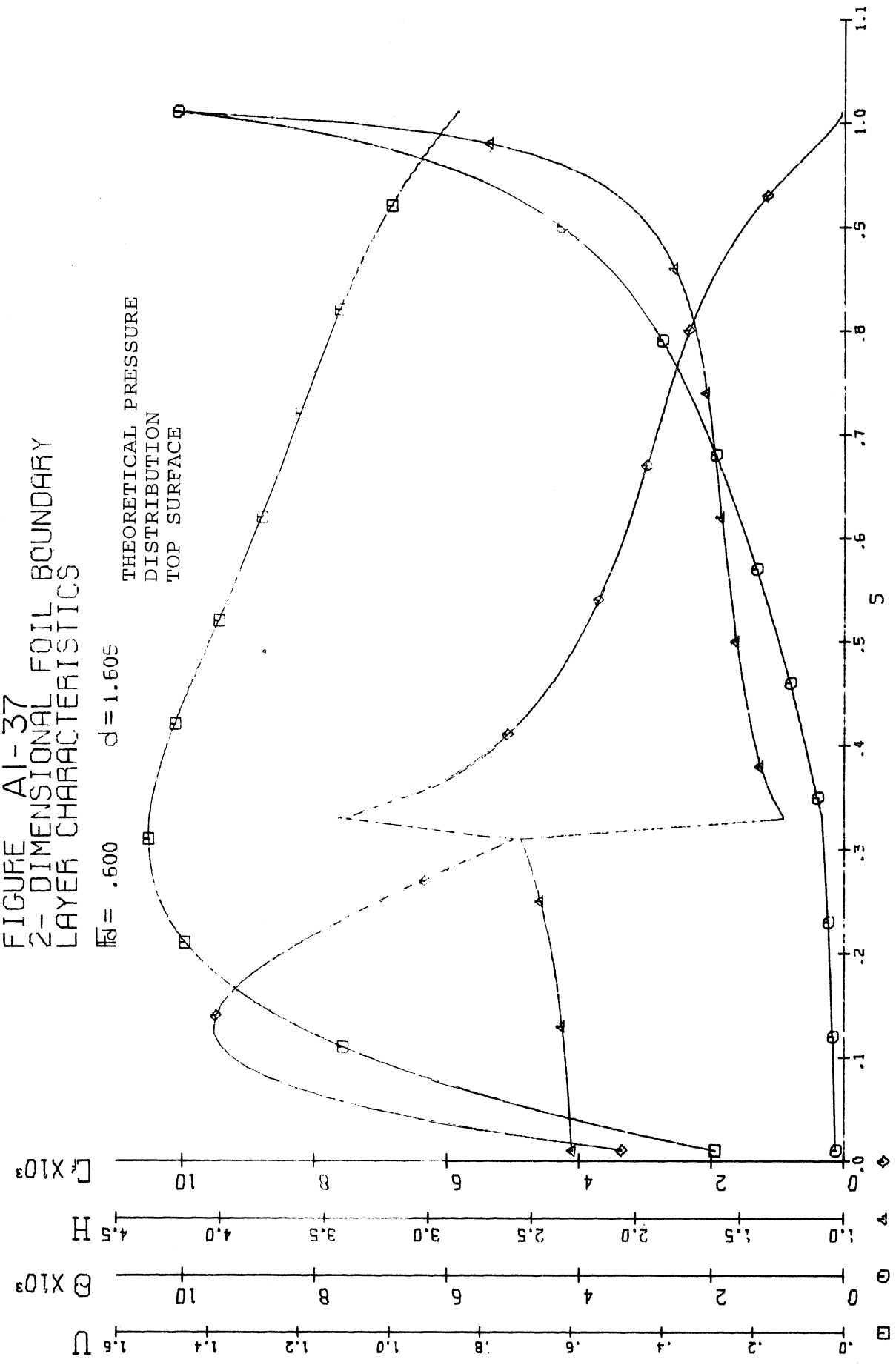
FIGURE A1-37
2- DIMENSIONAL FOIL BOUNDARY
LAYER CHARACTERISTICS
M = .600
d = 1.605
THEORETICAL PRESSURE
DISTRIBUTION
TOP SURFACE
U
Θ X10³
H
δ* X10³
δ
S

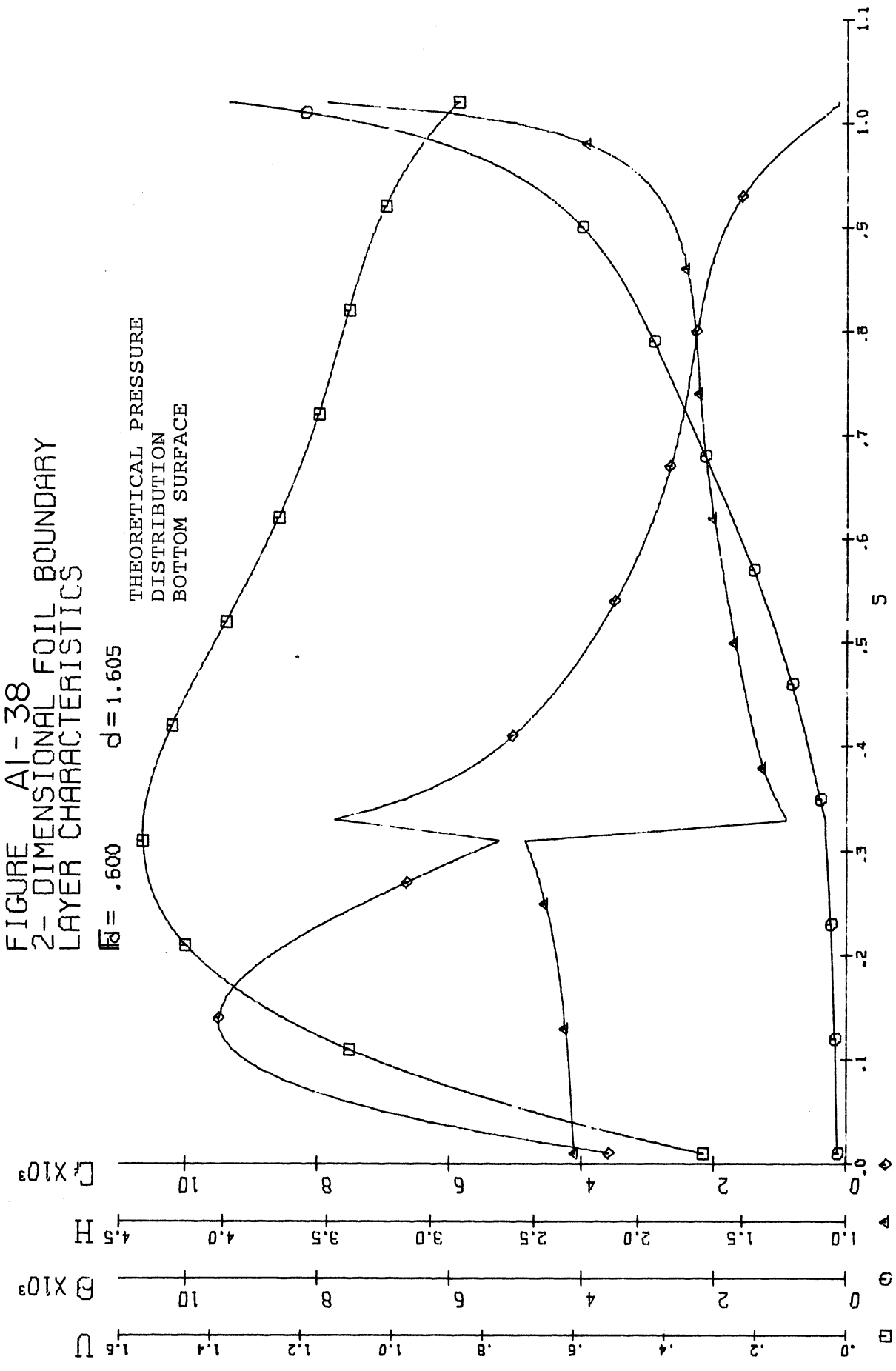
FIGURE A1-38
2-DIMENSIONAL FOIL BOUNDARY
LAYER CHARACTERISTICS
THEORETICAL PRESSURE
DISTRIBUTION
BOTTOM SURFACE
d=1.605
S
U
Θ X10³
H
δ* X10³
δ

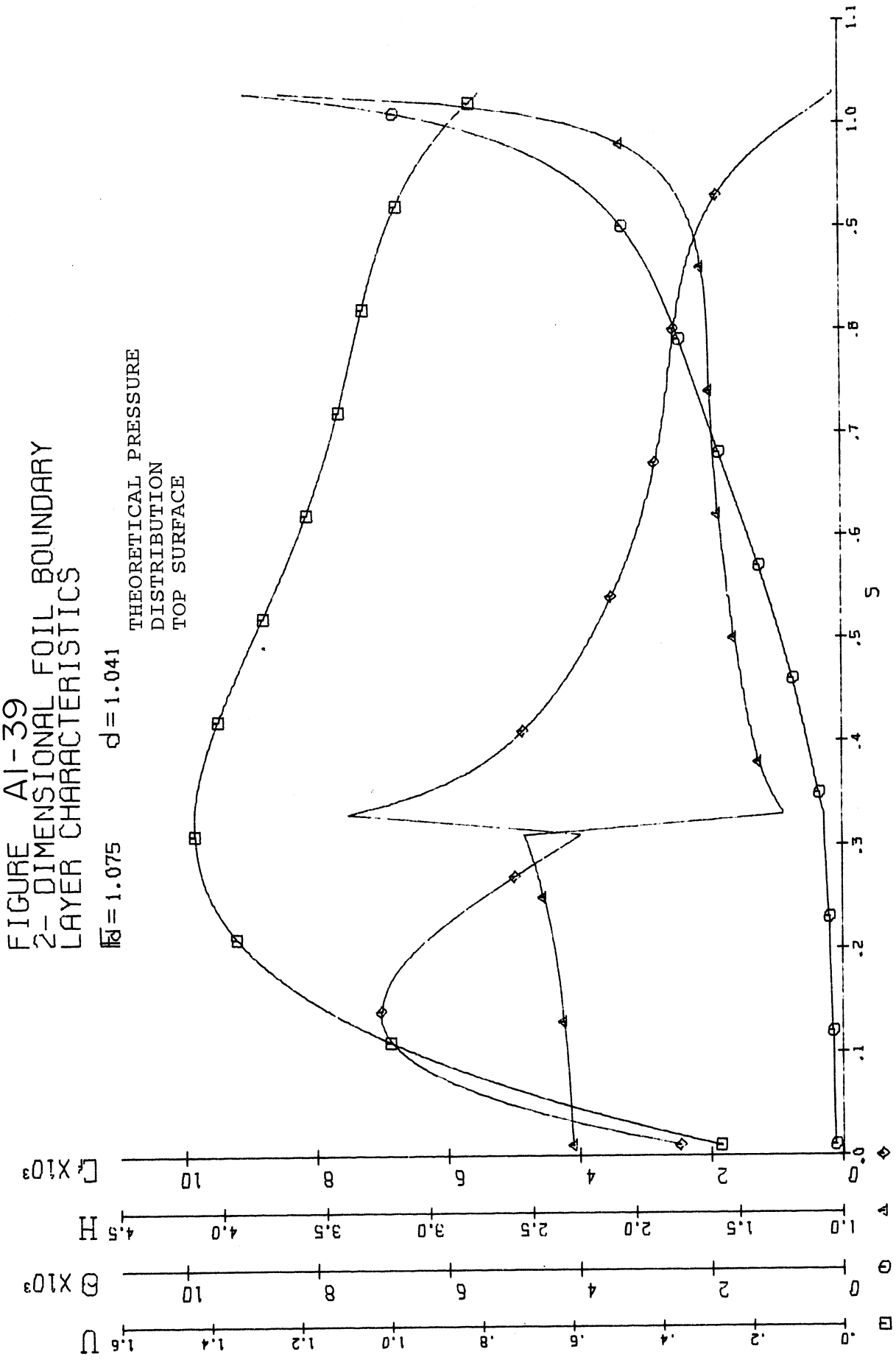
FIGURE A1-39
2- DIMENSIONAL FOIL BOUNDARY
LAYER CHARACTERISTICS
d = 1.041
THEORETICAL PRESSURE
DISTRIBUTION
TOP SURFACE
S
U
Θ X10³
H
Cf X10³

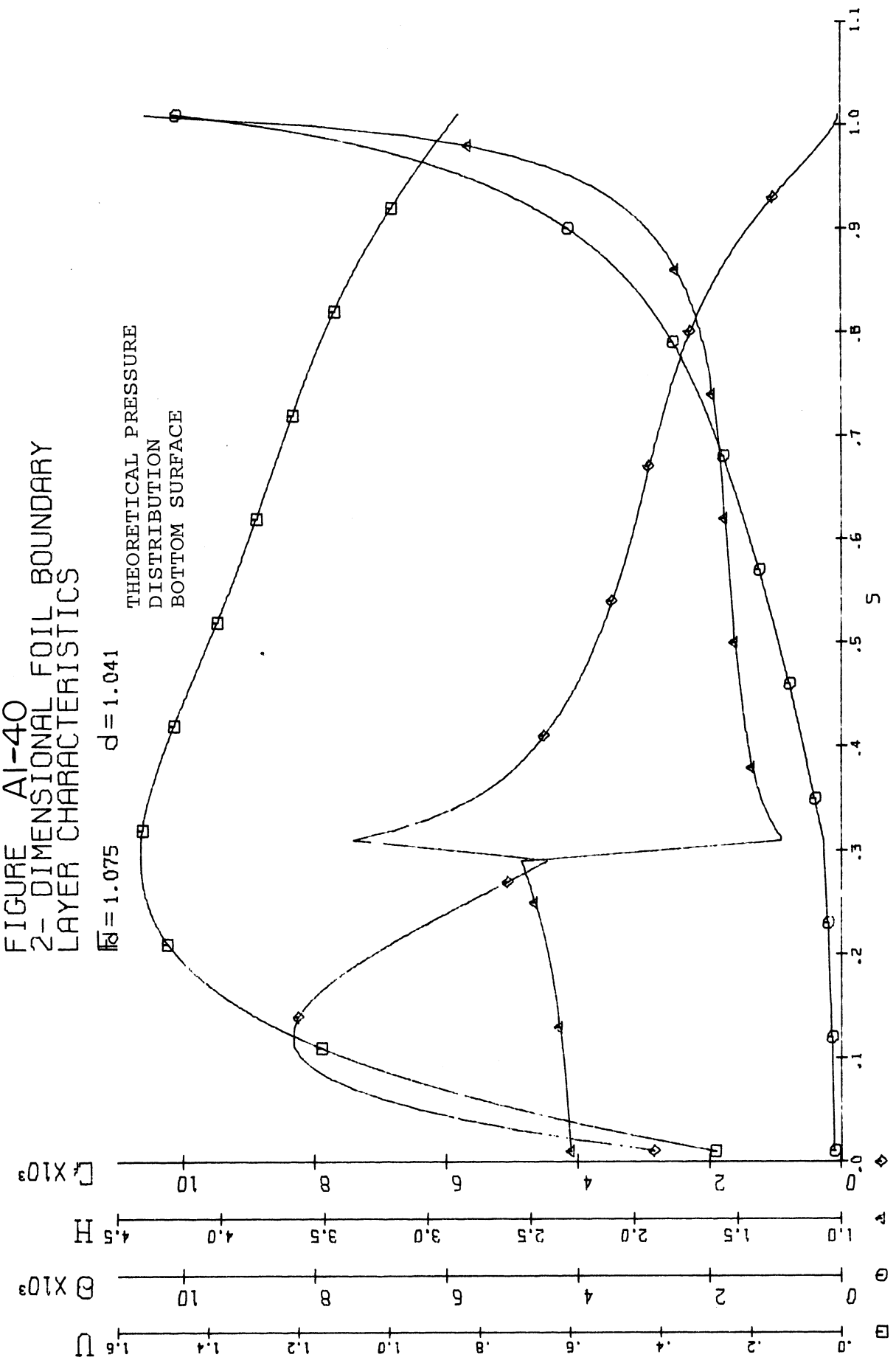
FIGURE A1-40
2- DIMENSIONAL FOIL BOUNDARY
LAYER CHARACTERISTICS
$\overline{M}_d$ = 1.075
d = 1.041
THEORETICAL PRESSURE
DISTRIBUTION
BOTTOM SURFACE
U
Θ X10³
H
δ* X10³
S

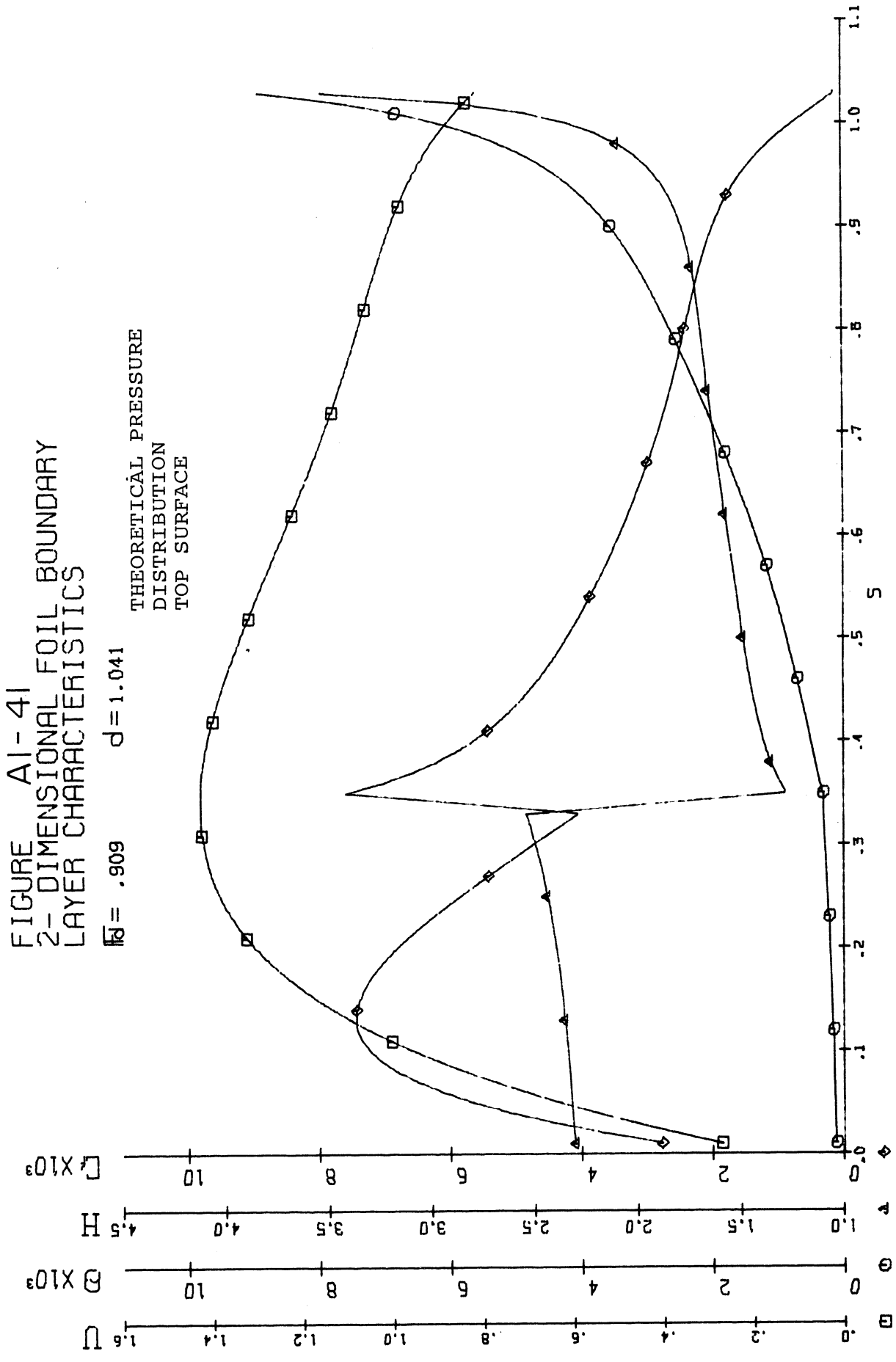
FIGURE A1-41
2- DIMENSIONAL FOIL BOUNDARY
LAYER CHARACTERISTICS
M= .909 d=1.041
THEORETICAL PRESSURE
DISTRIBUTION
TOP SURFACE
S
U
H
δ* X10³
θ X10³
Cf X10³

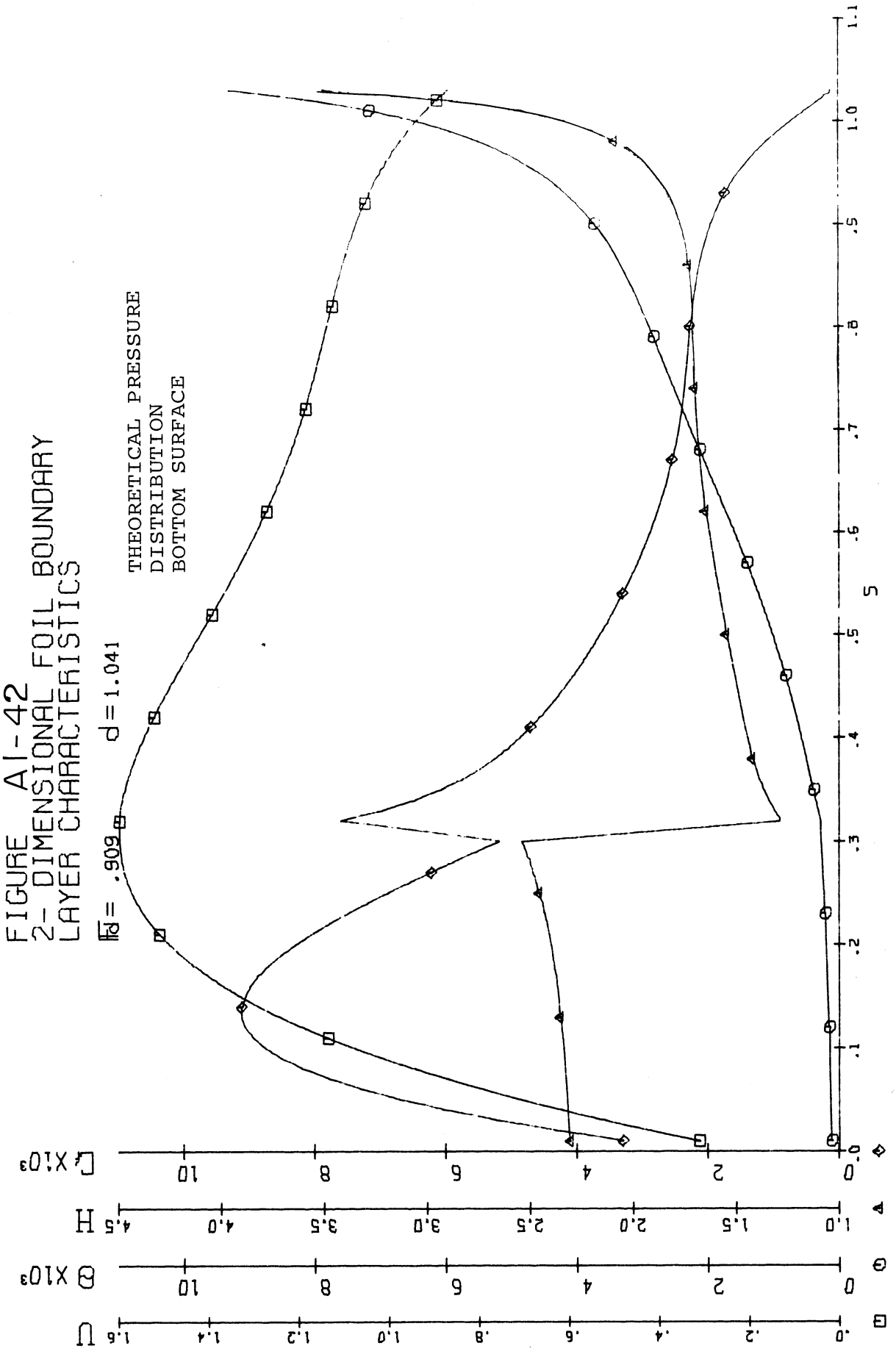
FIGURE A1-42
2- DIMENSIONAL FOIL BOUNDARY
LAYER CHARACTERISTICS
$\bar{R}_d$ = .909
d = 1.041
THEORETICAL PRESSURE
DISTRIBUTION
BOTTOM SURFACE
U
Θ X10³
H
Γ X10³
S

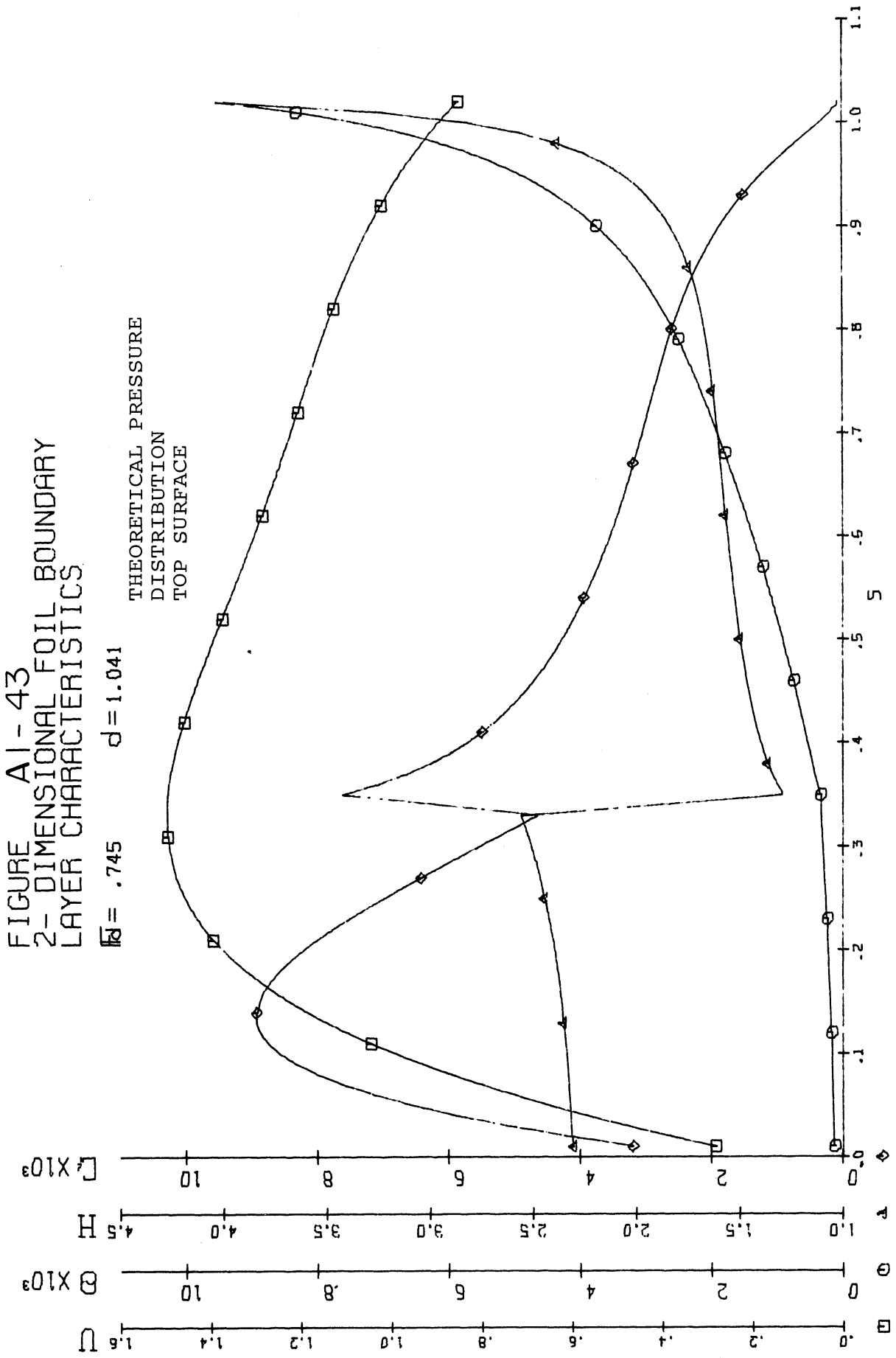
FIGURE A1-43
2- DIMENSIONAL FOIL BOUNDARY
LAYER CHARACTERISTICS
THEORETICAL PRESSURE
DISTRIBUTION
TOP SURFACE
d= 1.041
= .745
S
U
θ X10³
H
δ* X10³

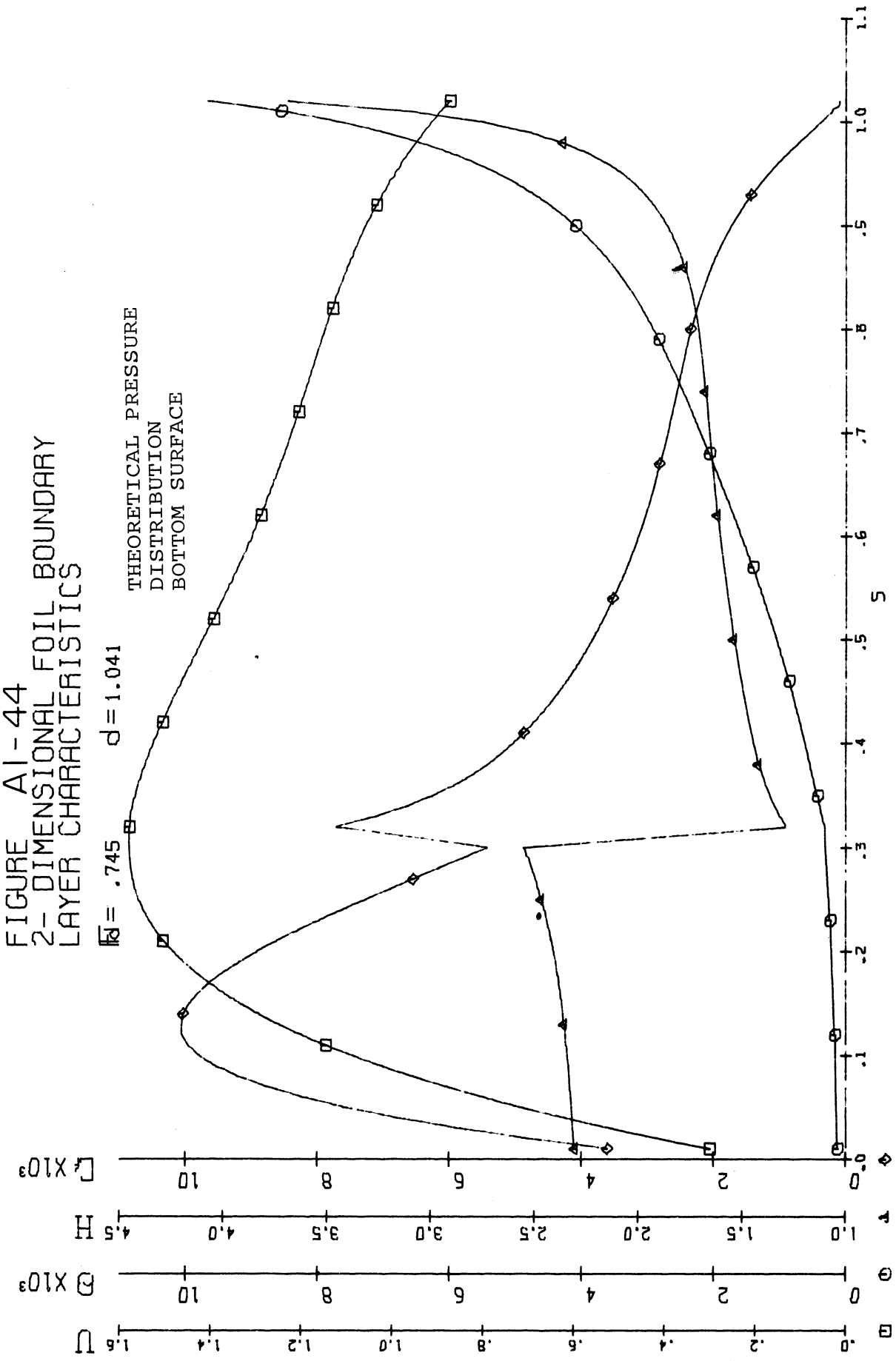
FIGURE A1-44
2- DIMENSIONAL FOIL BOUNDARY
LAYER CHARACTERISTICS
$\bar{k}$ = .745
d = 1.041
THEORETICAL PRESSURE
DISTRIBUTION
BOTTOM SURFACE
U
θ X10³
H
Γ_f X10³
S

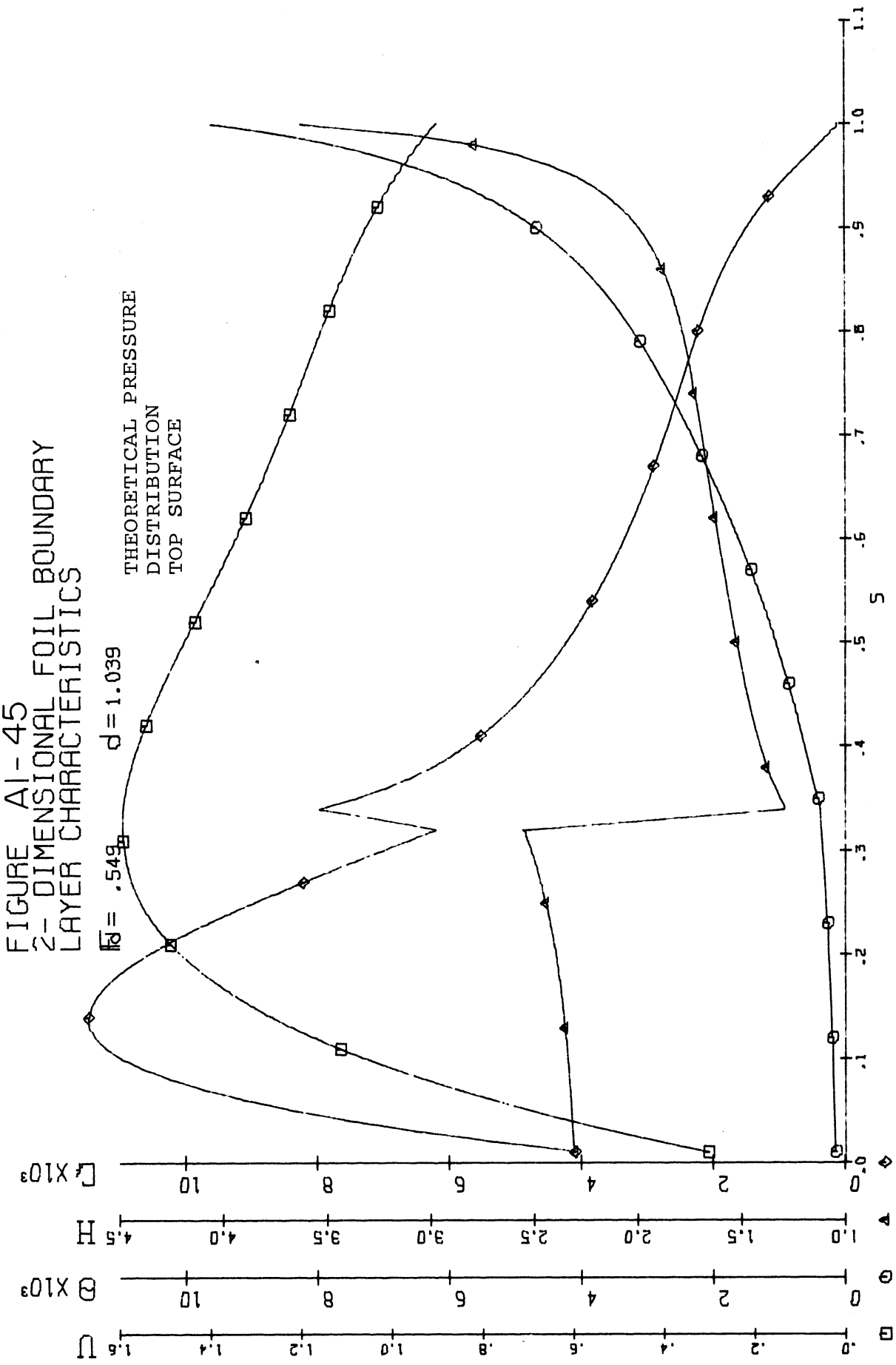
FIGURE AI-45
2- DIMENSIONAL FOIL BOUNDARY
LAYER CHARACTERISTICS
THEORETICAL PRESSURE
DISTRIBUTION
TOP SURFACE
d = 1.039
= .549
S
U
Θ X10³
H
Γ X10³

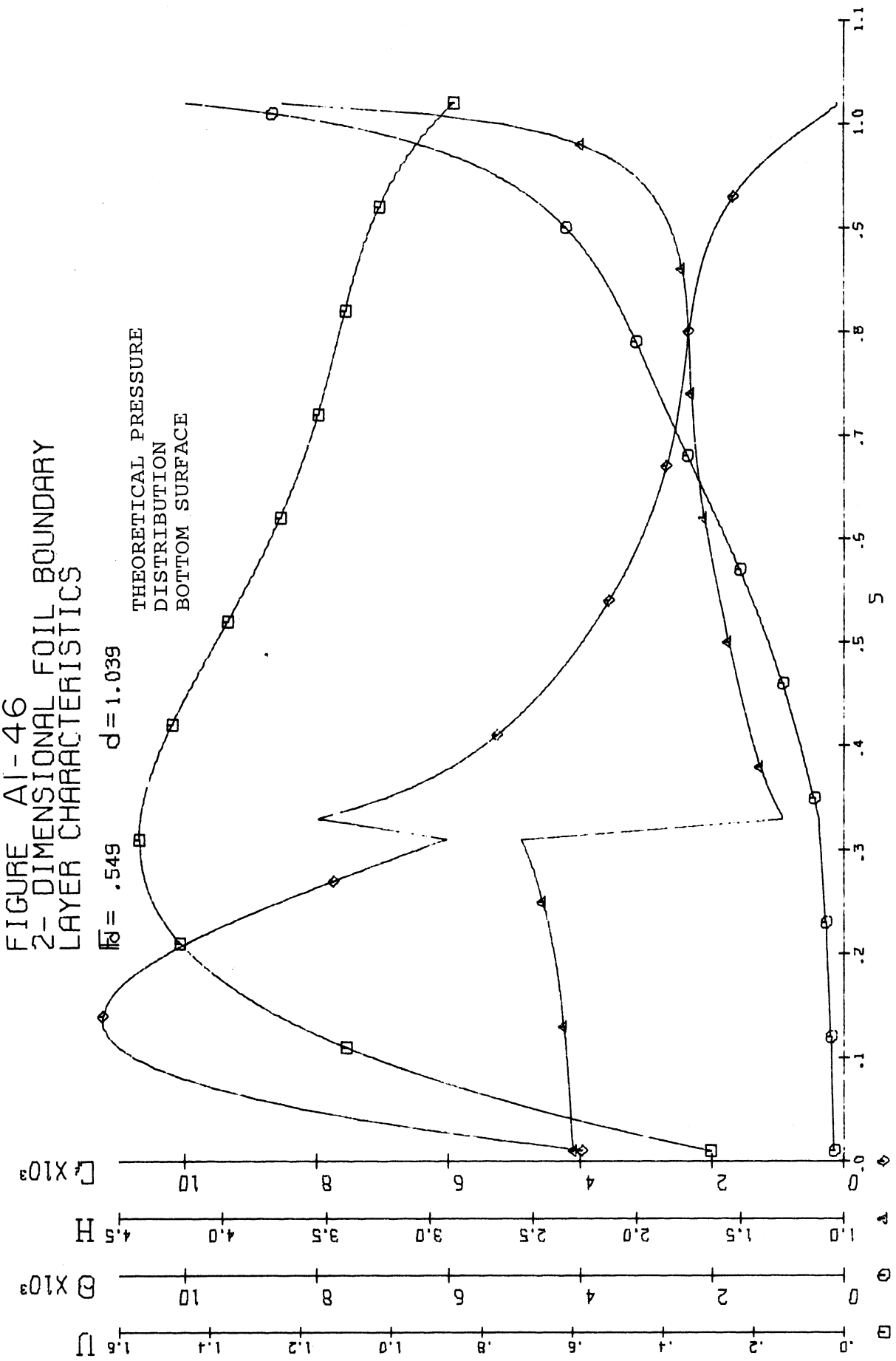
FIGURE AI-46
2- DIMENSIONAL FOIL BOUNDARY
LAYER CHARACTERISTICS
THEORETICAL PRESSURE
DISTRIBUTION
BOTTOM SURFACE
d=1.039
S
H
θ X10³
δ* X10³
U

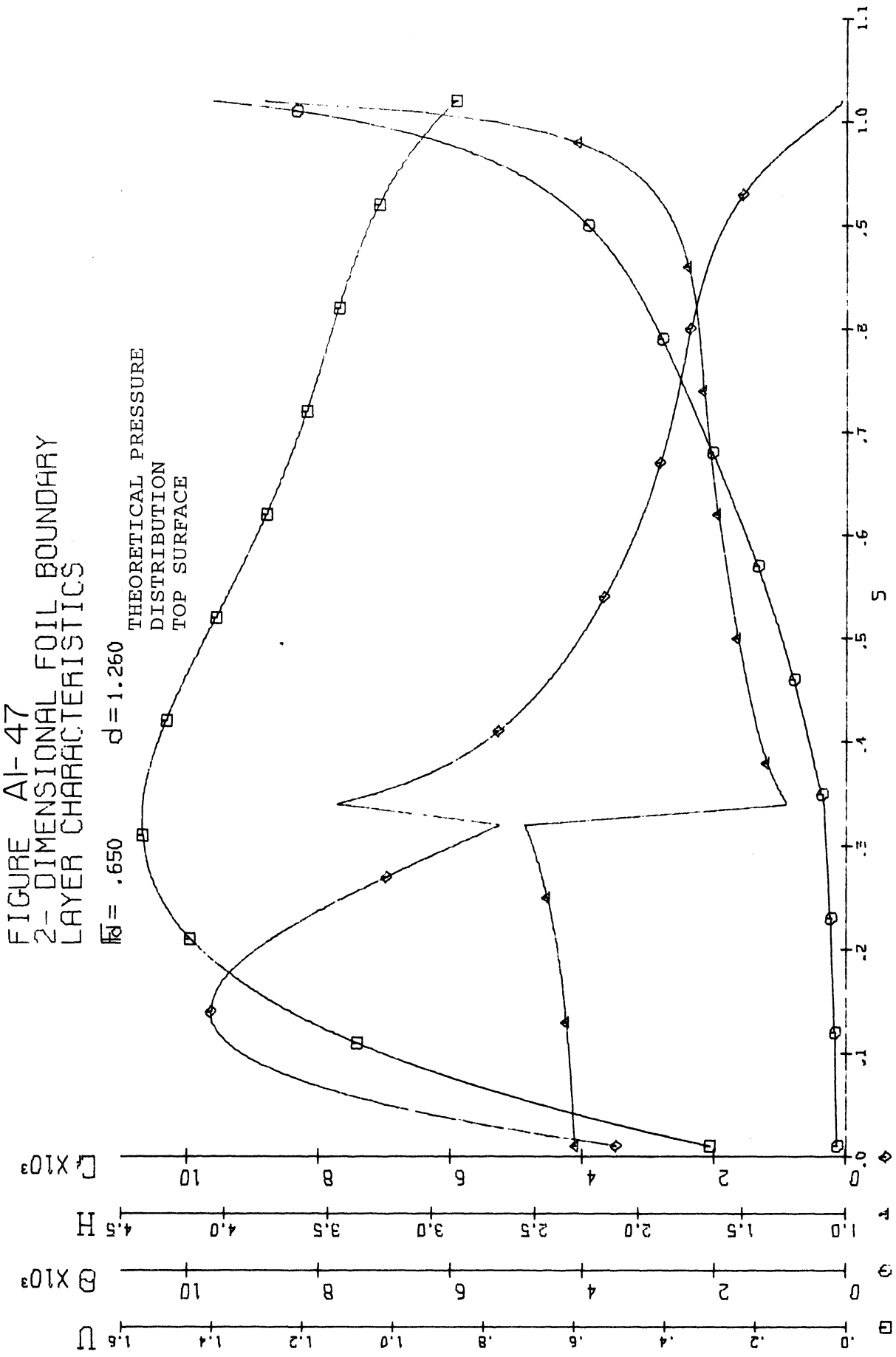
FIGURE A1-47
2- DIMENSIONAL FOIL BOUNDARY
LAYER CHARACTERISTICS
$\overline{k_d}$ = .650
d = 1.260
THEORETICAL PRESSURE
DISTRIBUTION
TOP SURFACE
U
Θ X10³
H
C_f X10³
S

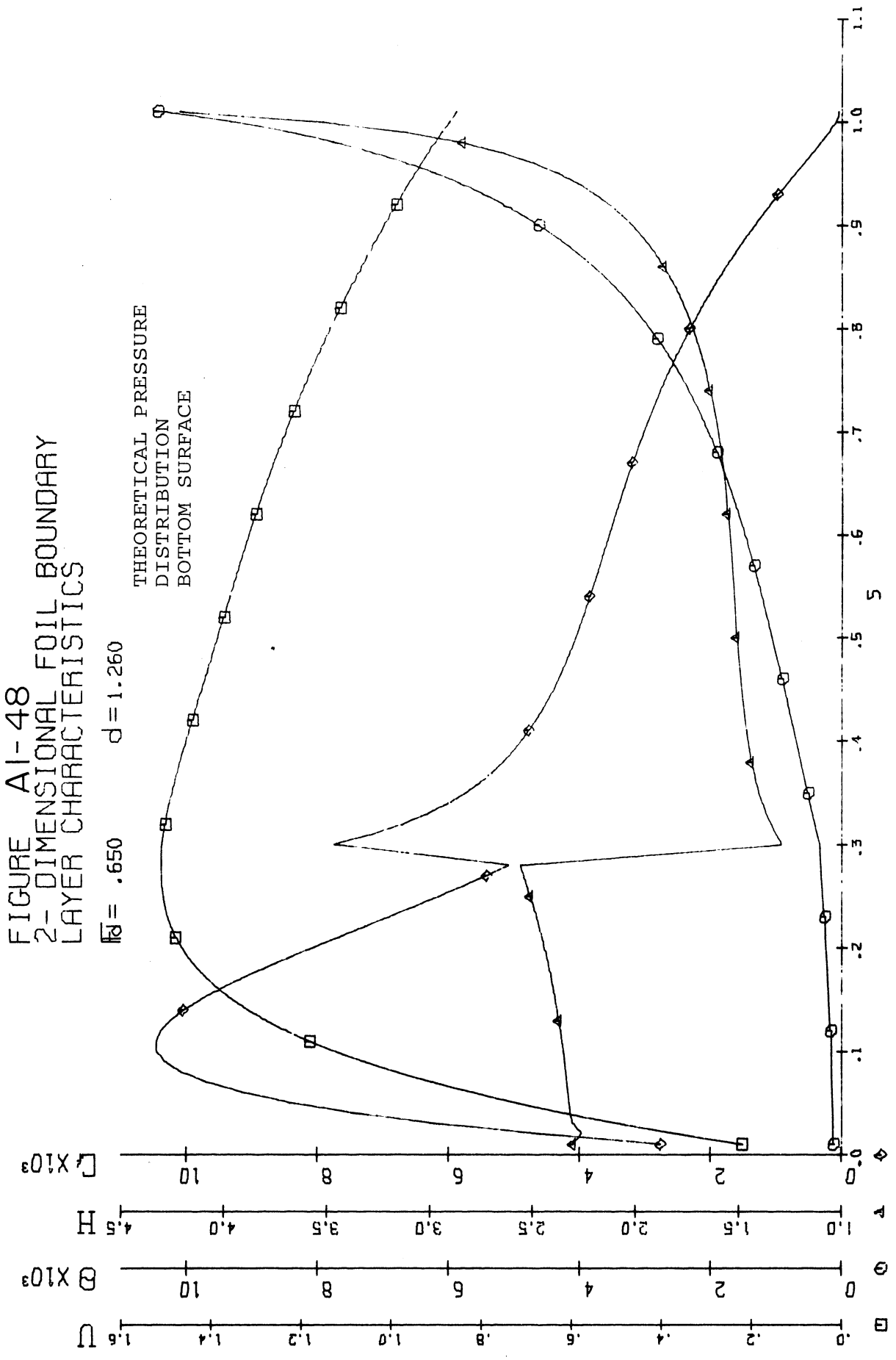
FIGURE A1-48
2- DIMENSIONAL FOIL BOUNDARY
LAYER CHARACTERISTICS
$\overline{R_d}$ = .650
d = 1.260
THEORETICAL PRESSURE
DISTRIBUTION
BOTTOM SURFACE
U
θ X10³
H
Γ X10³
δ
S

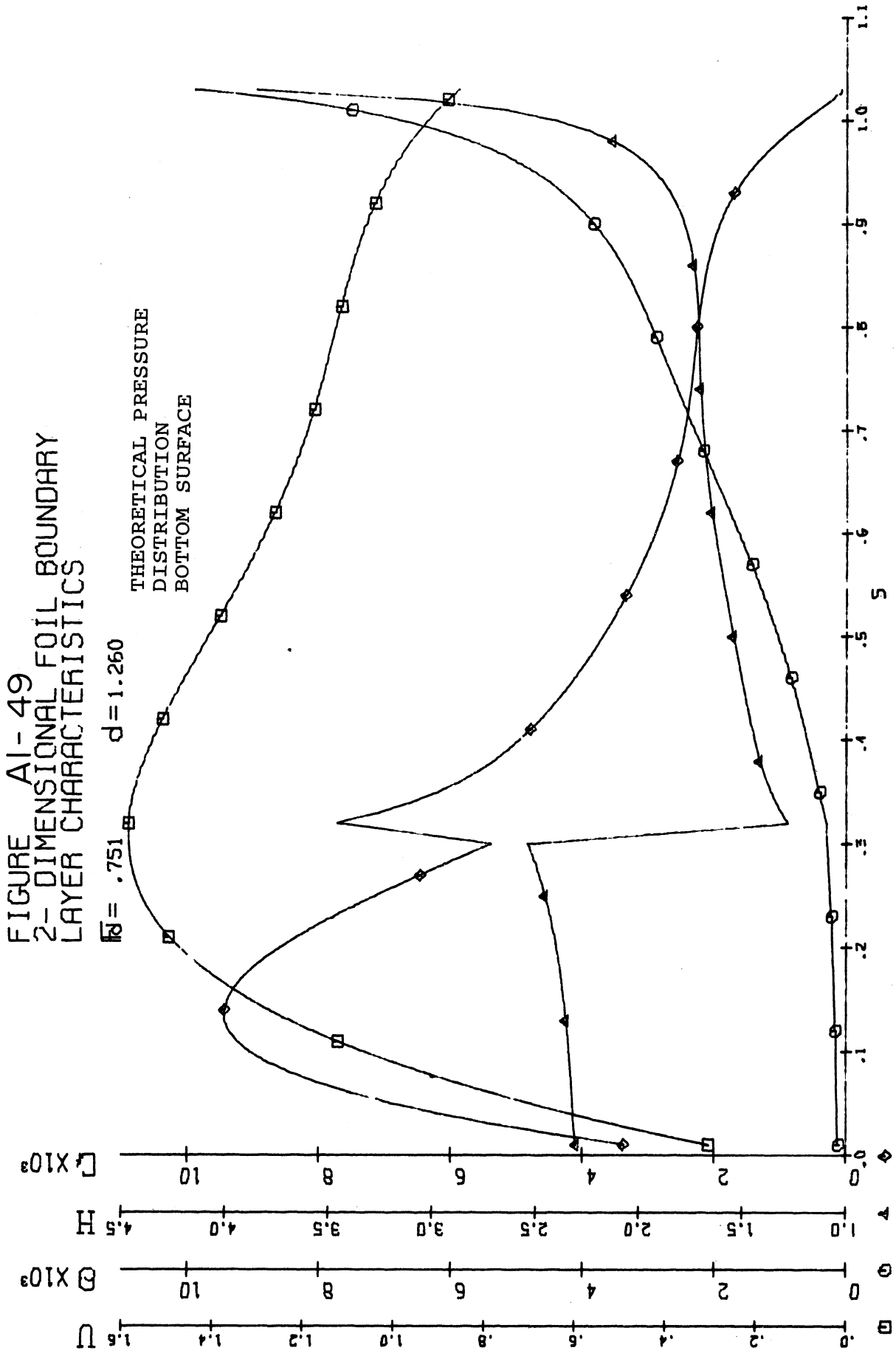
FIGURE A1-49
2- DIMENSIONAL FOIL BOUNDARY
LAYER CHARACTERISTICS
$\bar{\sigma}$ = .751 d=1.260
THEORETICAL PRESSURE
DISTRIBUTION
BOTTOM SURFACE
U
Θ X10³
H
δ^* X10³
S

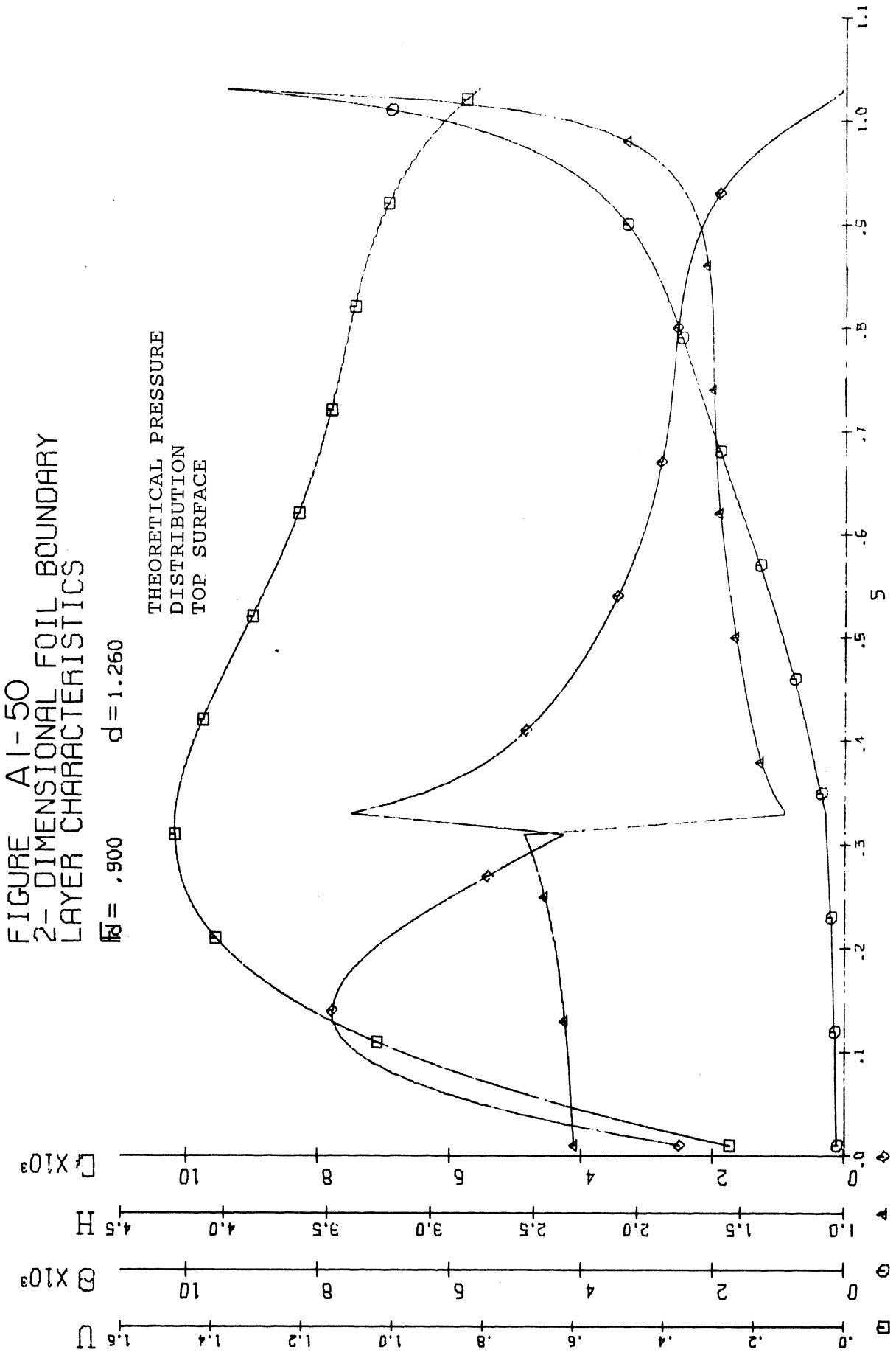
FIGURE A1-50
2-DIMENSIONAL FOIL BOUNDARY
LAYER CHARACTERISTICS
M = .900 d=1.260
THEORETICAL PRESSURE
DISTRIBUTION
TOP SURFACE
S
U
Θ X10³
H
Γ X10³
δ

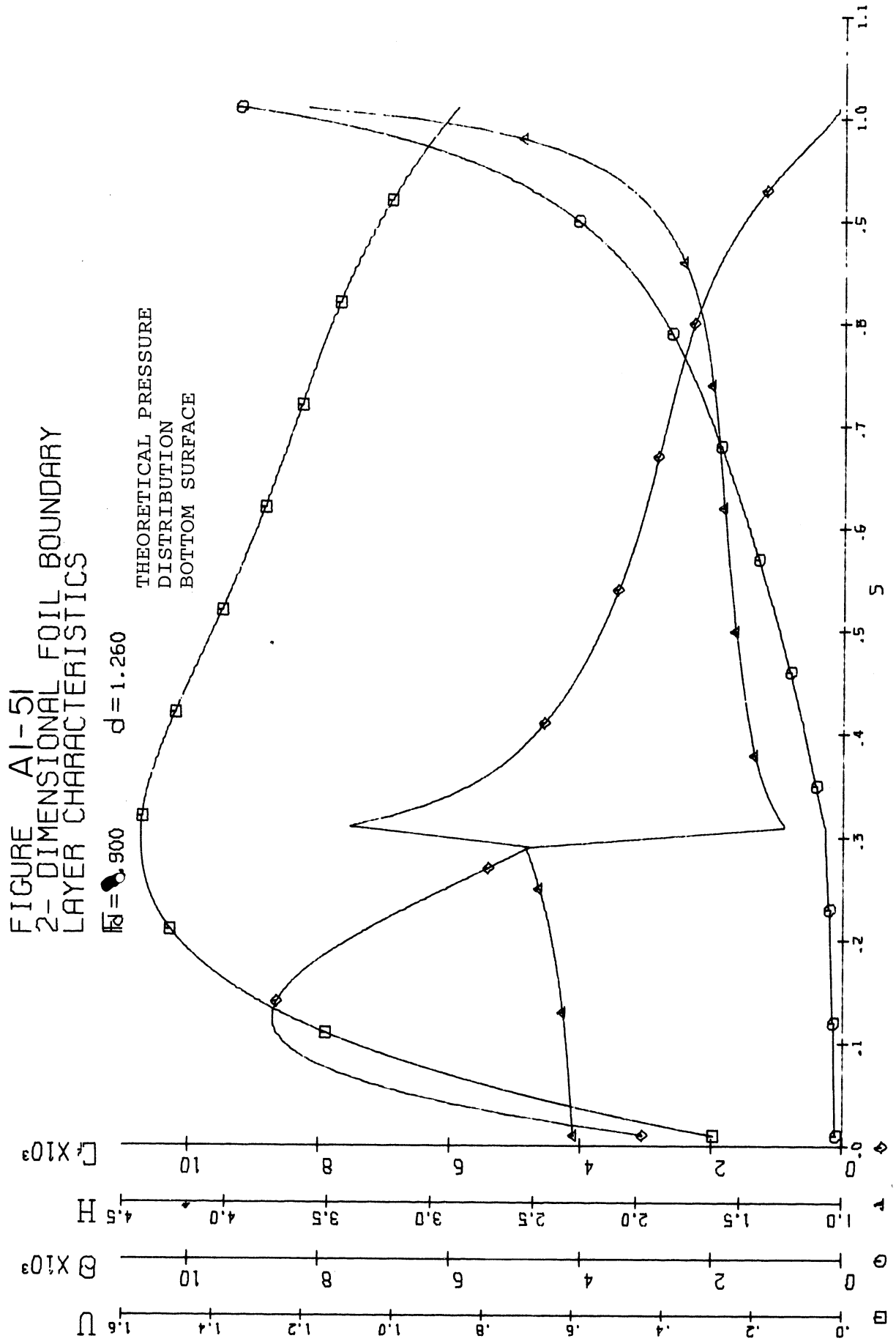
FIGURE A1-5I
2- DIMENSIONAL FOIL BOUNDARY
LAYER CHARACTERISTICS
α = 9.900 d = 1.260
THEORETICAL PRESSURE
DISTRIBUTION
BOTTOM SURFACE
U
Θ X10³
H
δ* X10³
S

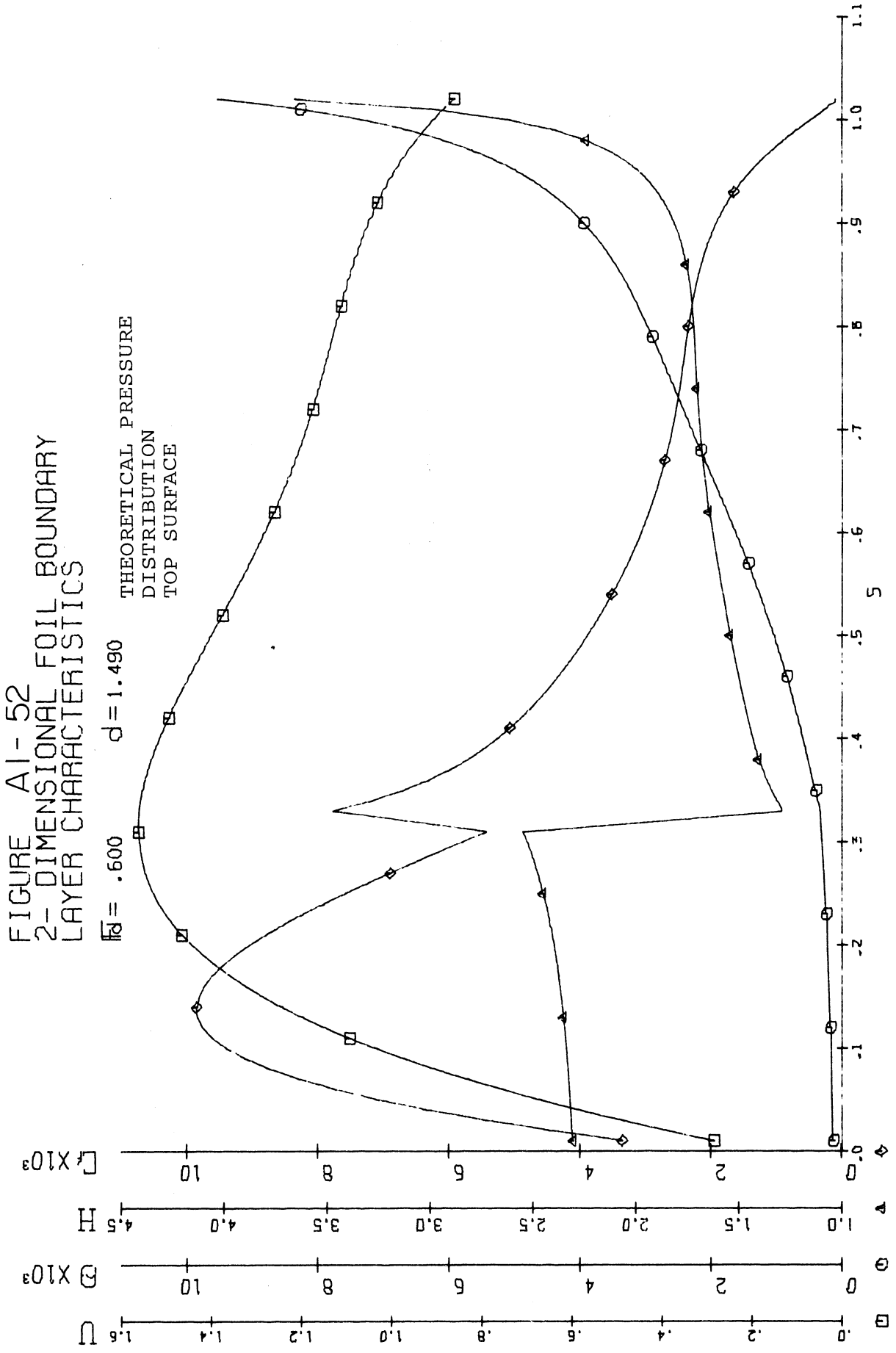
FIGURE A1-52
2-DIMENSIONAL FOIL BOUNDARY
LAYER CHARACTERISTICS
THEORETICAL PRESSURE
DISTRIBUTION
TOP SURFACE
d = 1.490
= .600
S
U
θ X10³
H
δ* X10³

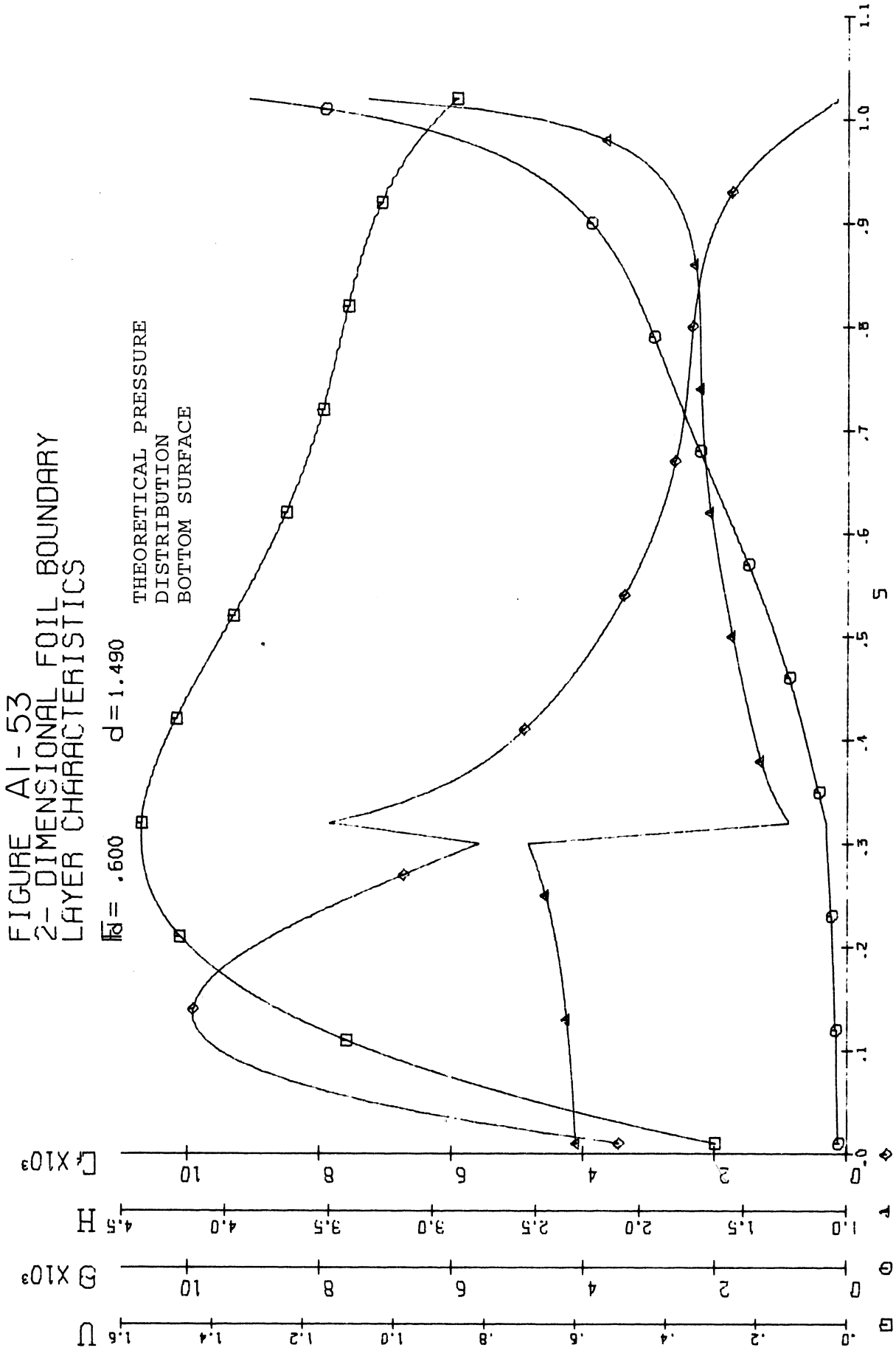
FIGURE A1-53
2- DIMENSIONAL FOIL BOUNDARY
LAYER CHARACTERISTICS
$\bar{R}_d$ = .600 d = 1.490
THEORETICAL PRESSURE
DISTRIBUTION
BOTTOM SURFACE
U
D X10³
H
Γ X10³
S

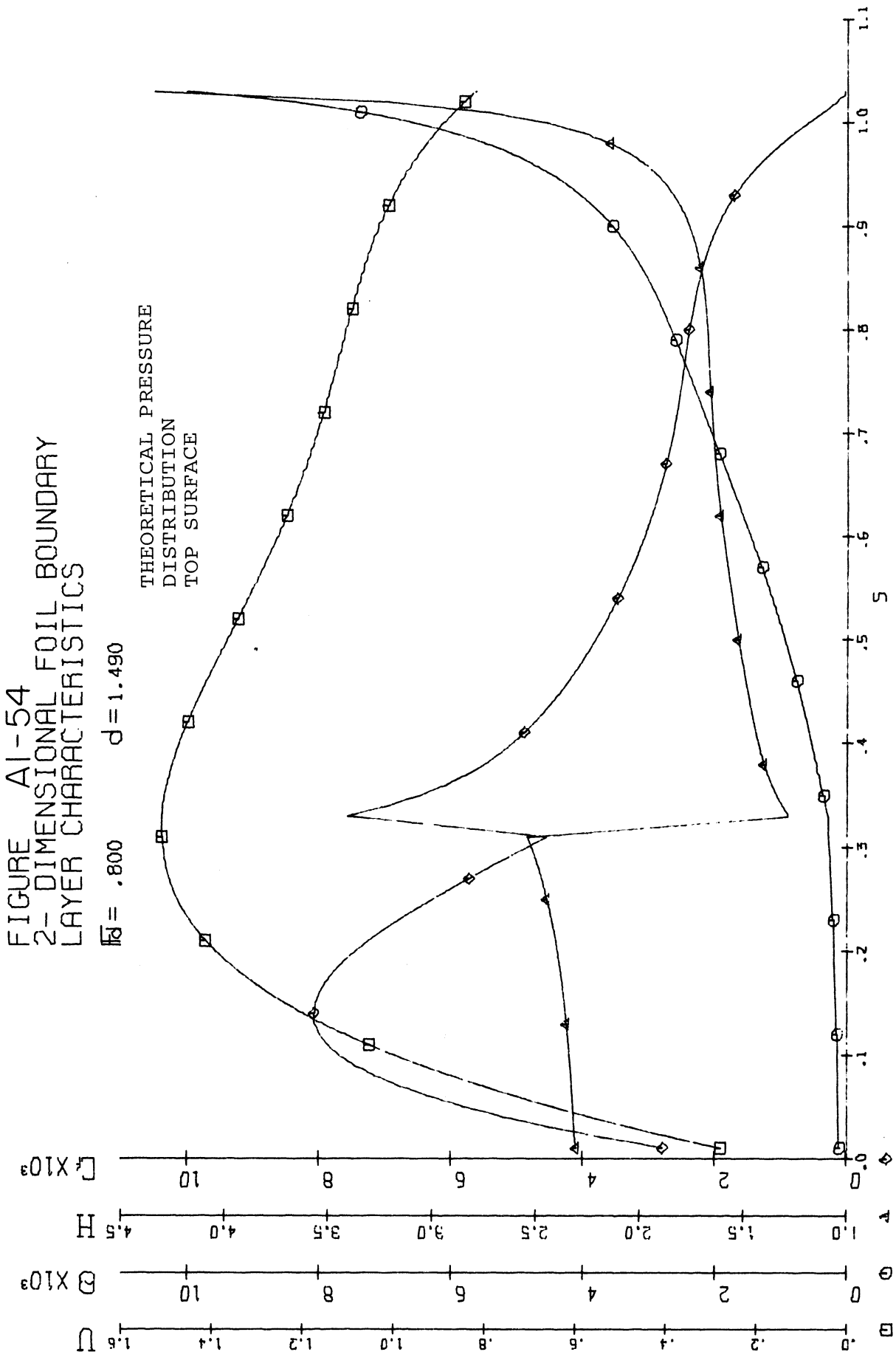
FIGURE A1-54
2- DIMENSIONAL FOIL BOUNDARY
LAYER CHARACTERISTICS
M = .800 d = 1.490
THEORETICAL PRESSURE
DISTRIBUTION
TOP SURFACE
U
Θ X10³
H
δ* X10³
δ
Θ
V
S

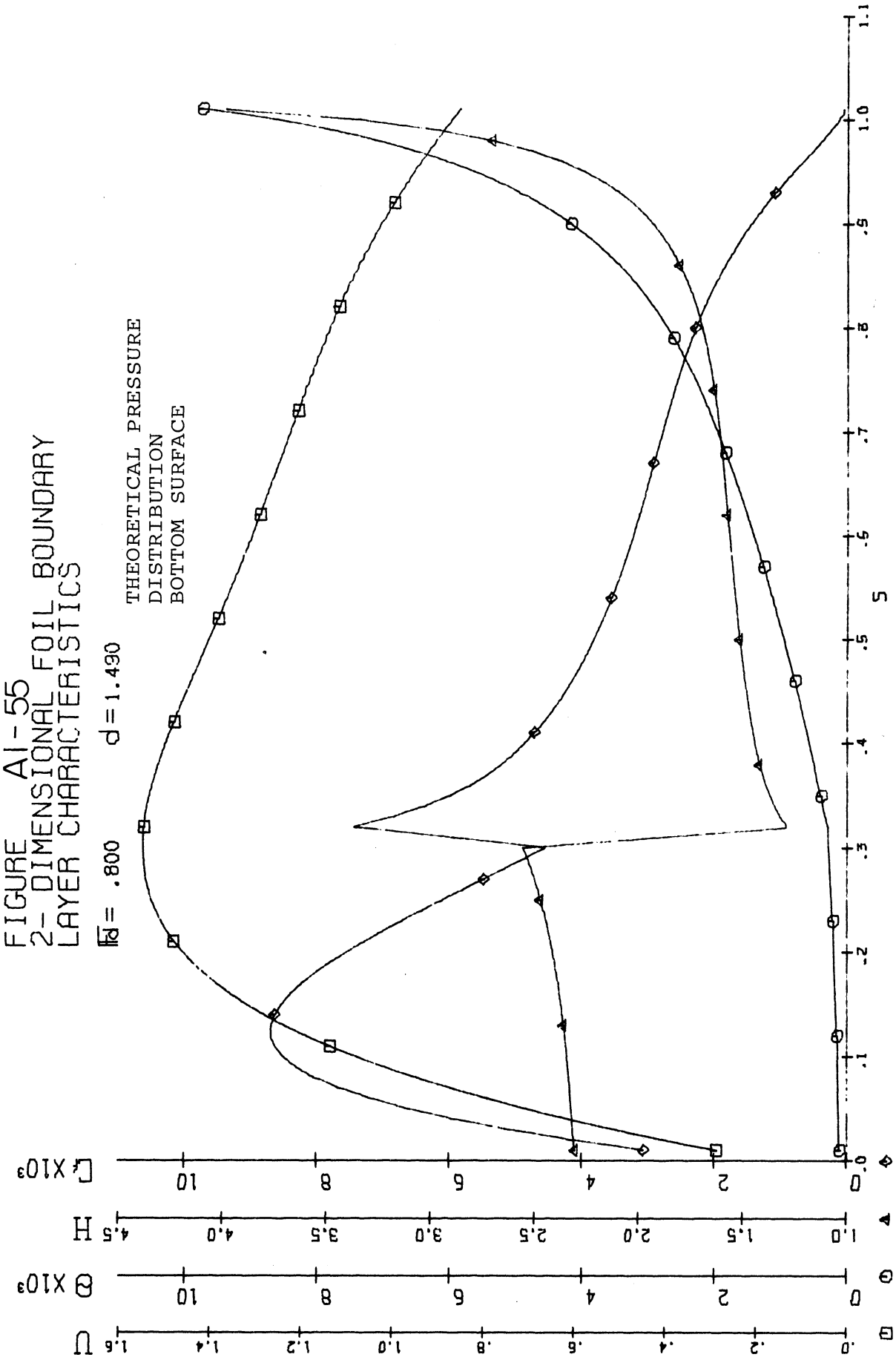
FIGURE A1-55
2- DIMENSIONAL FOIL BOUNDARY
LAYER CHARACTERISTICS
M = .800
d = 1.430
THEORETICAL PRESSURE
DISTRIBUTION
BOTTOM SURFACE
S
U
θ X10³
H
δ* X10³

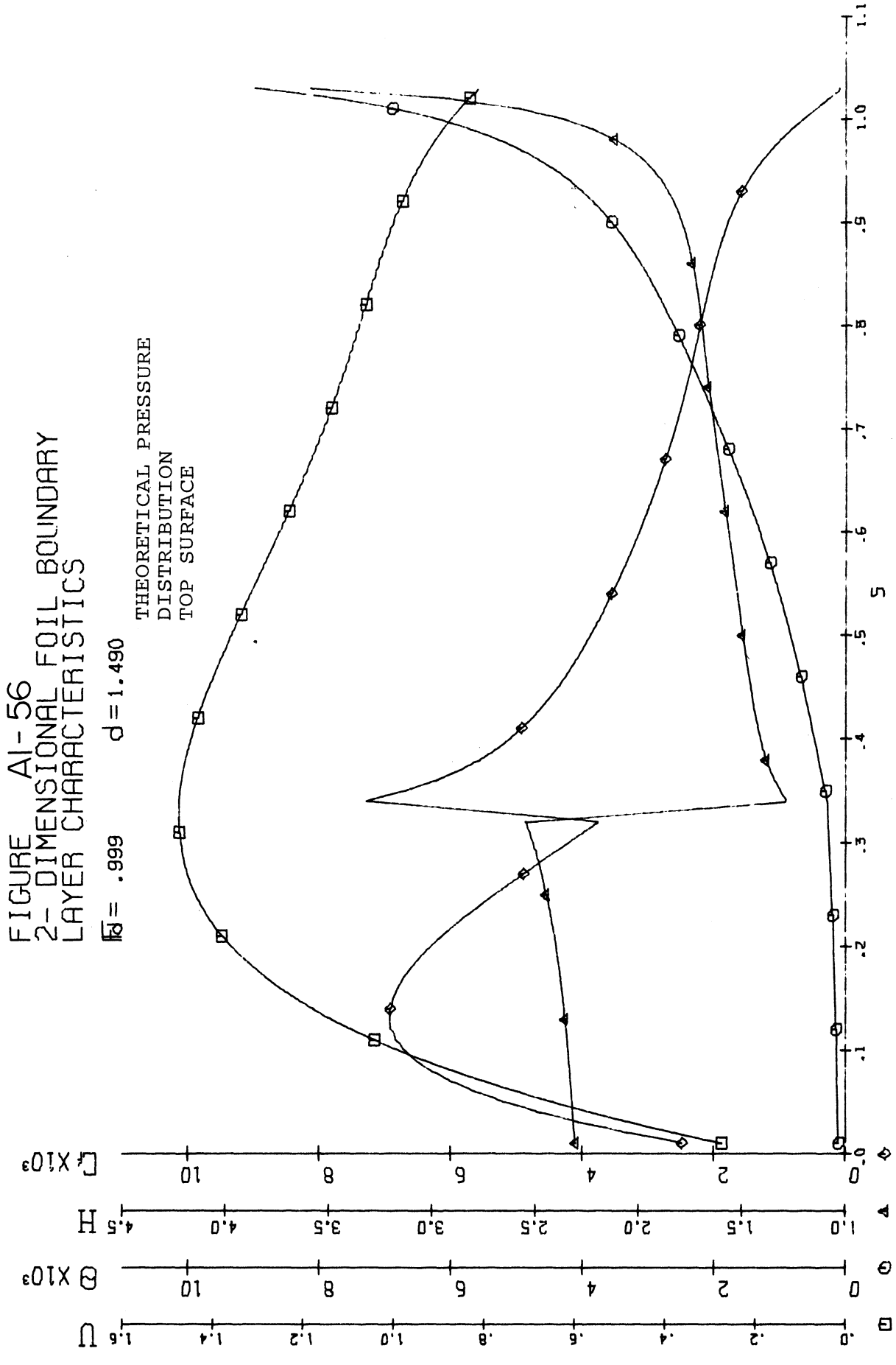
FIGURE A1-56
2- DIMENSIONAL FOIL BOUNDARY
LAYER CHARACTERISTICS
THEORETICAL PRESSURE
DISTRIBUTION
TOP SURFACE
d = 1.490
S
U
θ X10³
H
δ* X10³
Cp

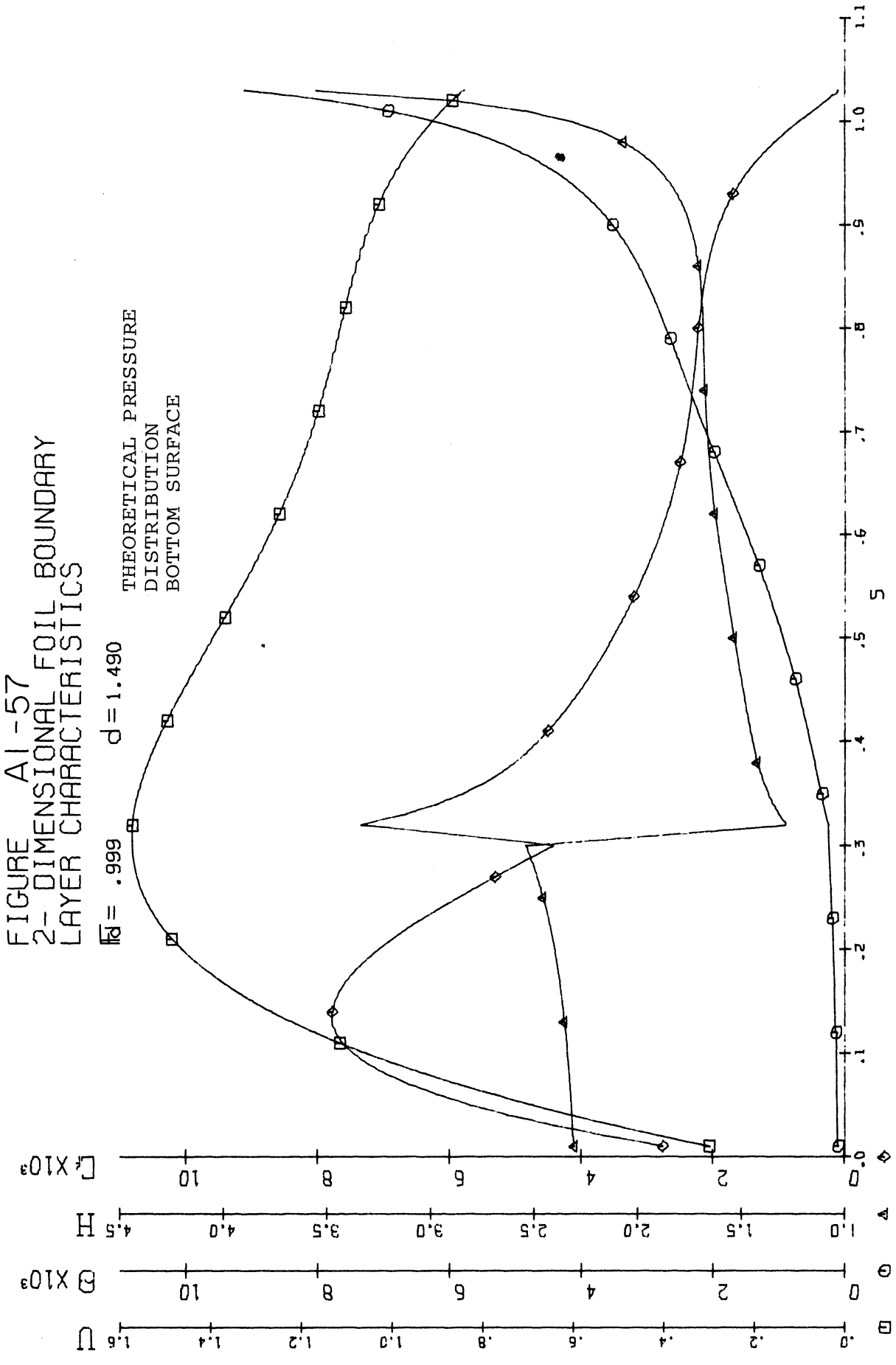
FIGURE A1-57
2- DIMENSIONAL FOIL BOUNDARY
LAYER CHARACTERISTICS
Rd = .999
d = 1.490
THEORETICAL PRESSURE
DISTRIBUTION
BOTTOM SURFACE
U
Θ X10³
H
Γ X10³
δ
S

APPENDIX 2

The plots on the following pages are the same as those in Appendix 1 except that the measured pressure distributions were used in the calculations. The same comments apply to these plots as apply for those in Appendix 1.

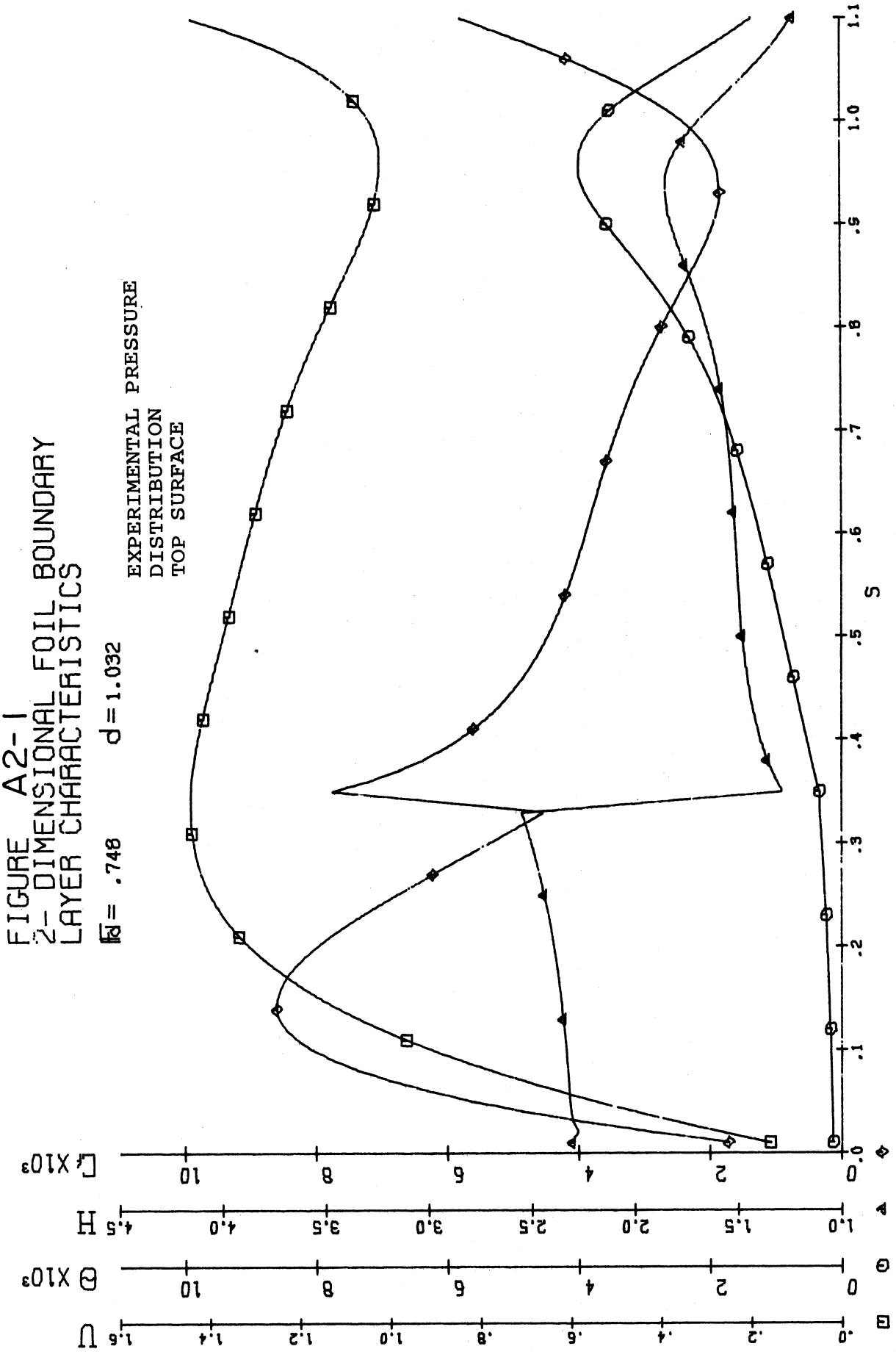
FIGURE A2-1
2- DIMENSIONAL FOIL BOUNDARY
LAYER CHARACTERISTICS
EXPERIMENTAL PRESSURE
DISTRIBUTION
TOP SURFACE
d=1.032
S
U
Θ X10³
H
δ* X10³
δ

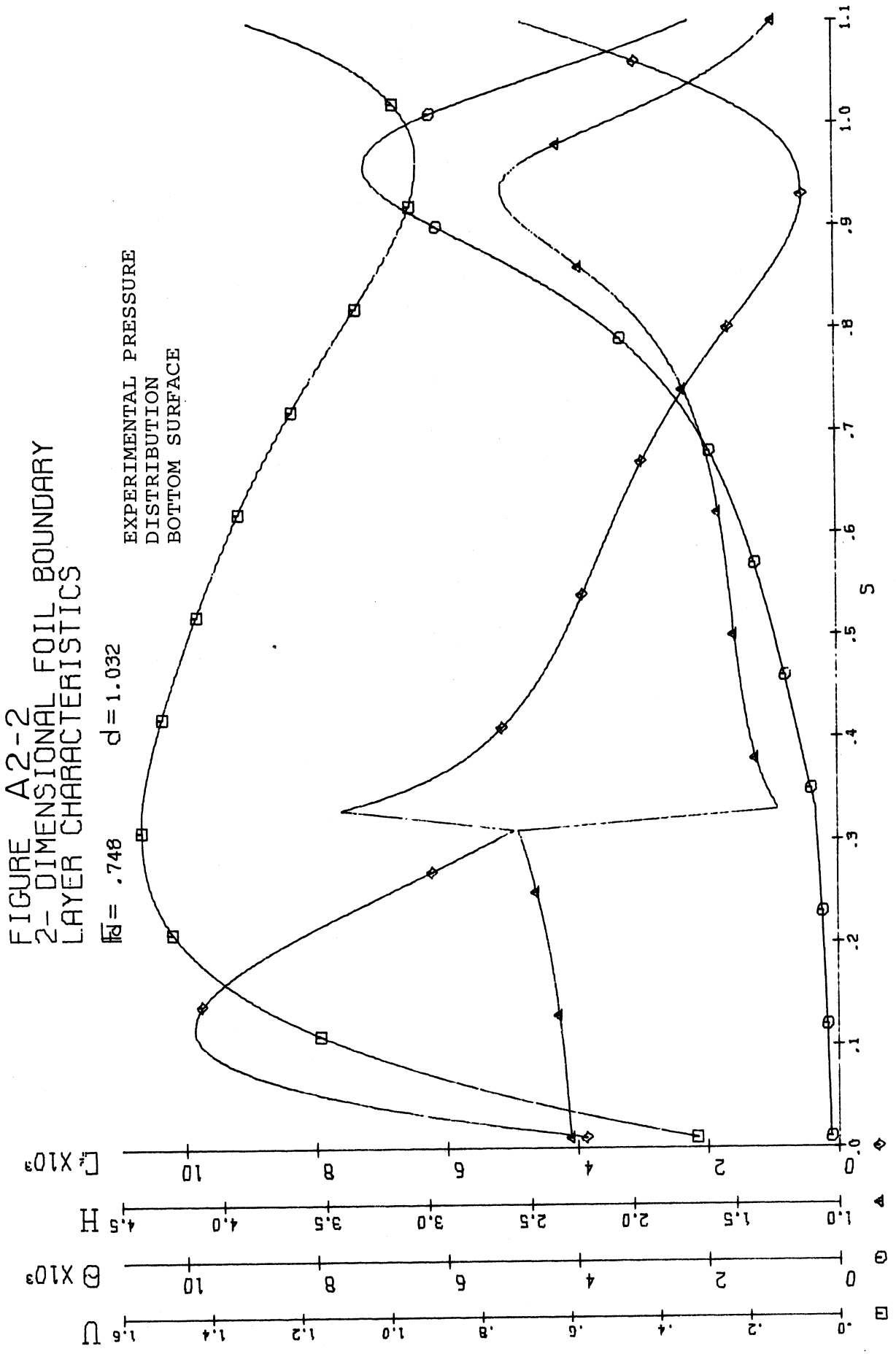
FIGURE A2-2
2- DIMENSIONAL FOIL BOUNDARY
LAYER CHARACTERISTICS
EXPERIMENTAL PRESSURE
DISTRIBUTION
BOTTOM SURFACE
d = 1.032
S

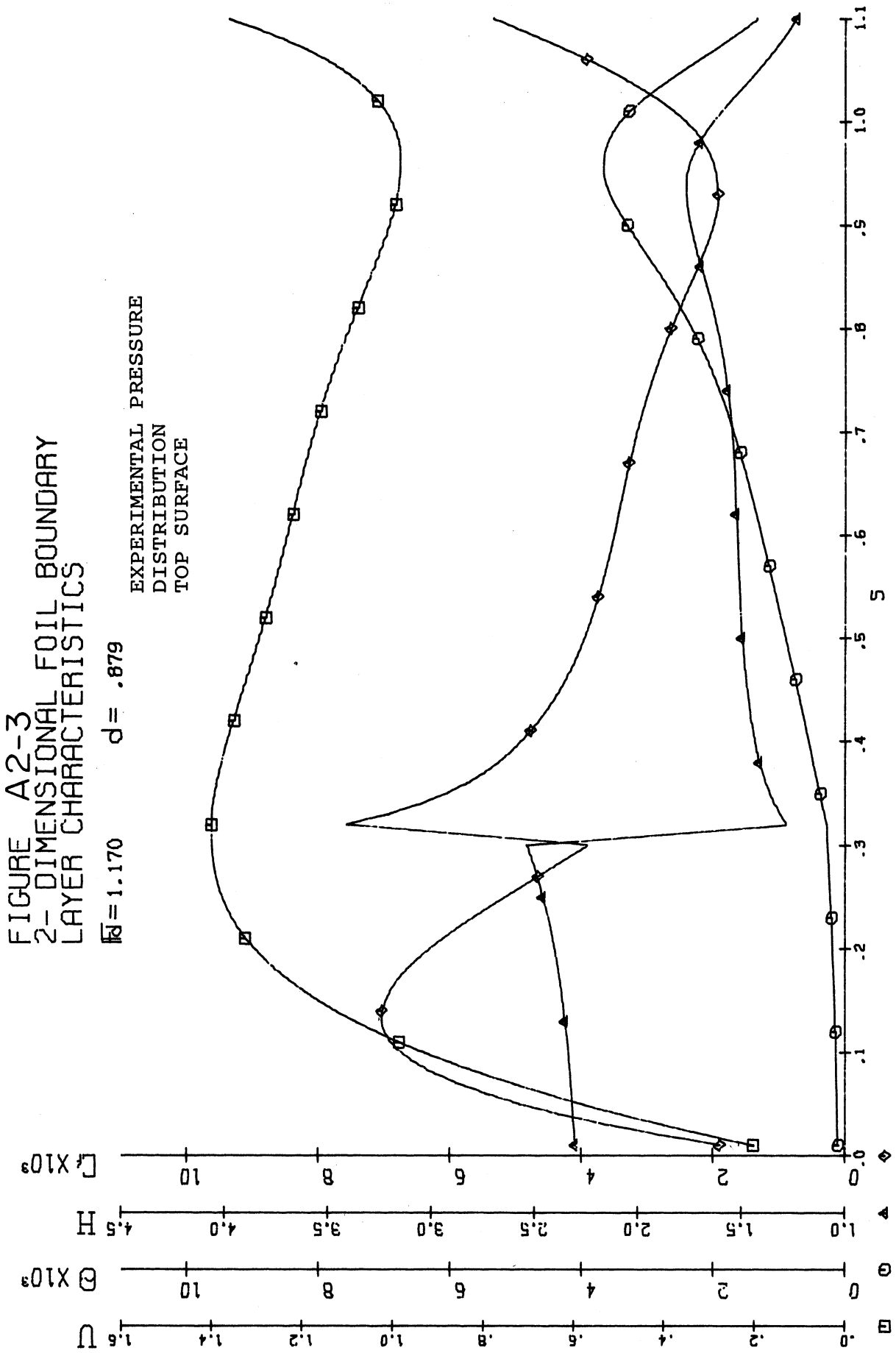
FIGURE A2-3
2- DIMENSIONAL FOIL BOUNDARY
LAYER CHARACTERISTICS
EXPERIMENTAL PRESSURE
DISTRIBUTION
TOP SURFACE
d= .879
S
U
Θ X10³
H
δ* X10³

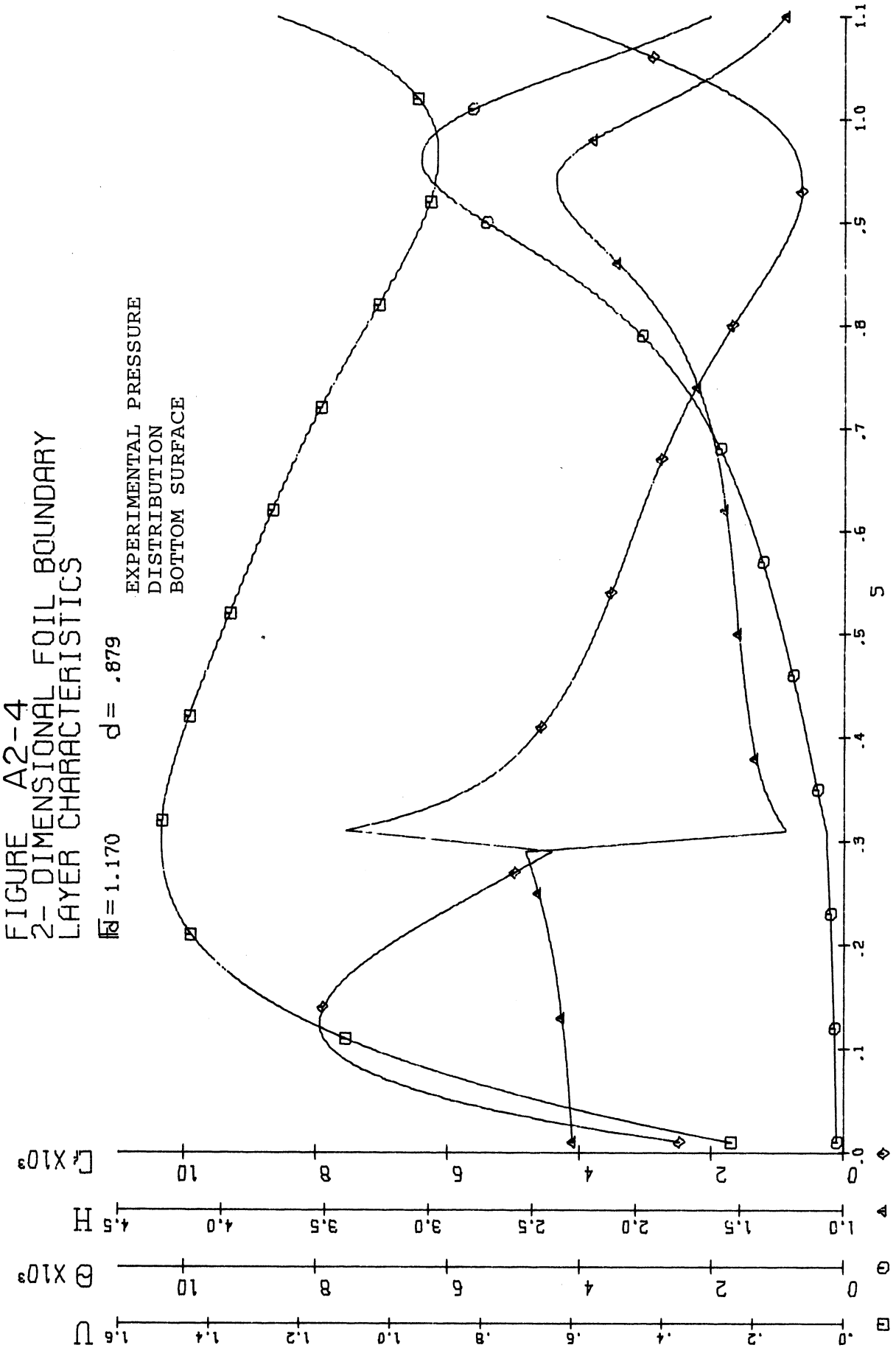
FIGURE A2-4
2- DIMENSIONAL FOIL BOUNDARY
LAYER CHARACTERISTICS
$\overline{R_d}$ = 1.170 d = .879
EXPERIMENTAL PRESSURE
DISTRIBUTION
BOTTOM SURFACE
U
θ X10³
H
δ* X10³
S

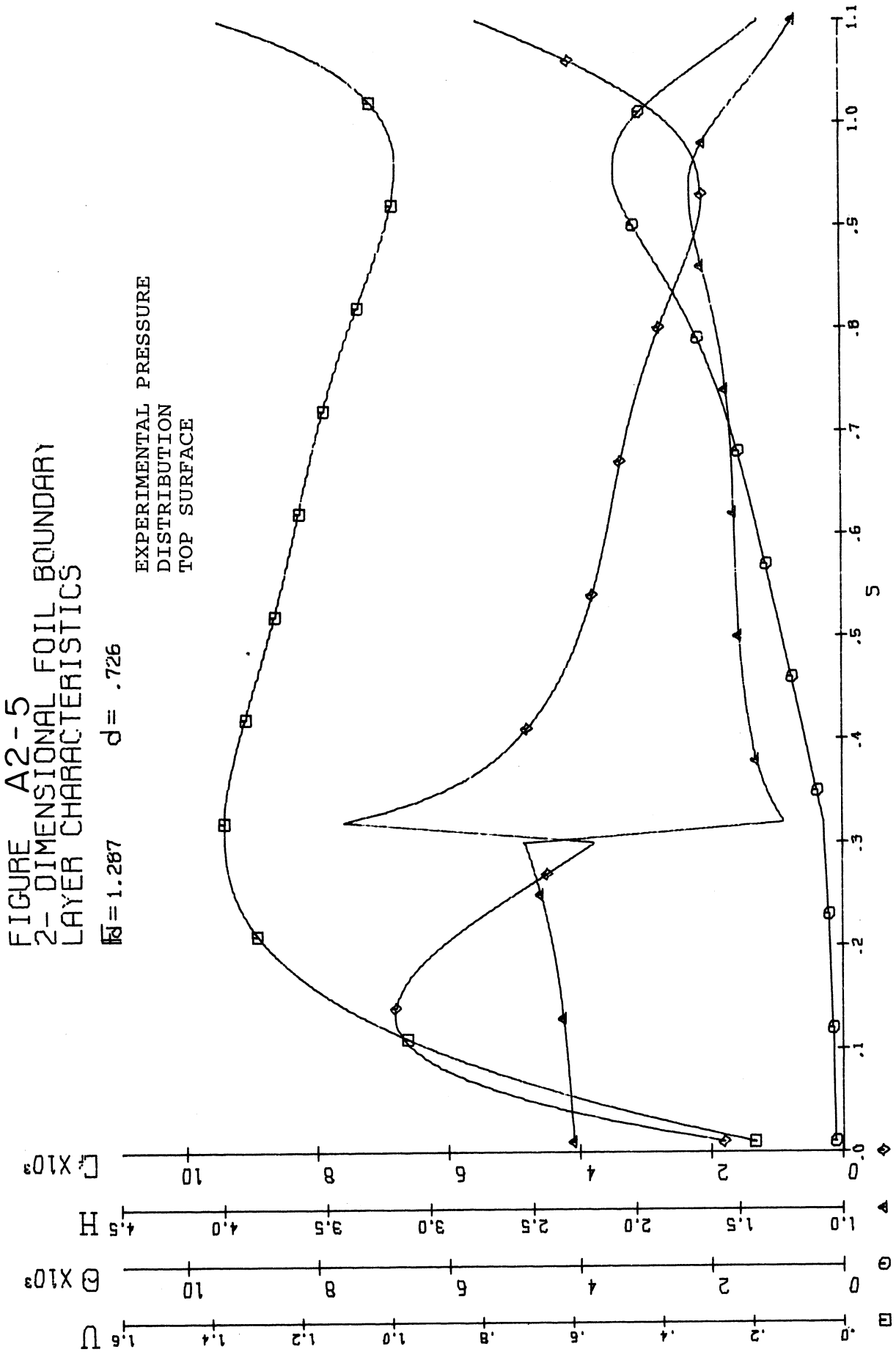
FIGURE A2-5
2- DIMENSIONAL FOIL BOUNDARY
LAYER CHARACTERISTICS
EXPERIMENTAL PRESSURE
DISTRIBUTION
TOP SURFACE
d= .726
S
U
H

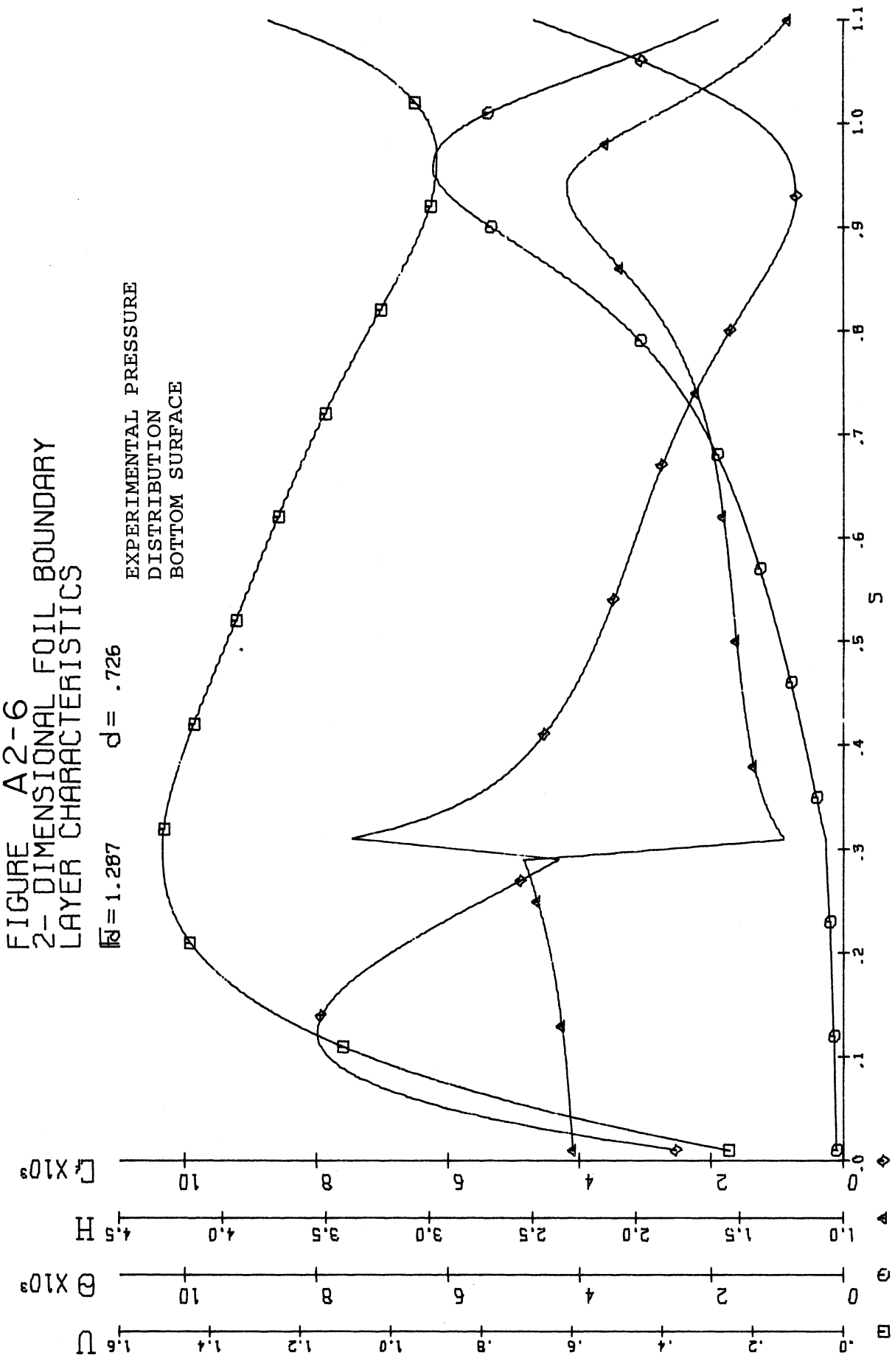
FIGURE A2-6
2- DIMENSIONAL FOIL BOUNDARY
LAYER CHARACTERISTICS
$\bar{R}_d$ = 1.287
d = .726
EXPERIMENTAL PRESSURE
DISTRIBUTION
BOTTOM SURFACE
U
θ X10³
H
C_f X10³
S

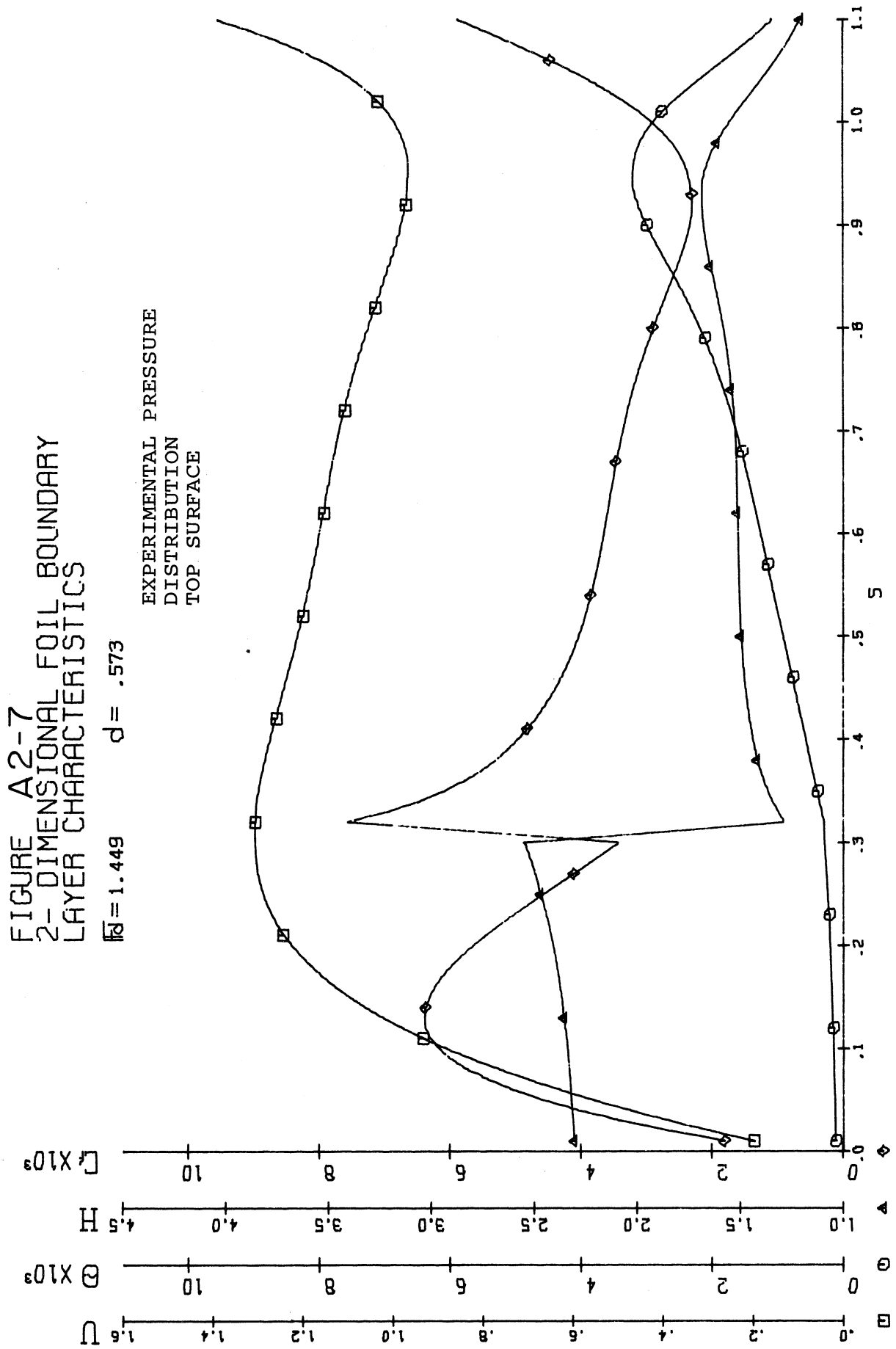
FIGURE A2-7
2- DIMENSIONAL FOIL BOUNDARY
LAYER CHARACTERISTICS
$\bar{M}_\infty$=1.449 d= .573
EXPERIMENTAL PRESSURE
DISTRIBUTION
TOP SURFACE
U
Θ X10³
H
δ* X10³
δ
S

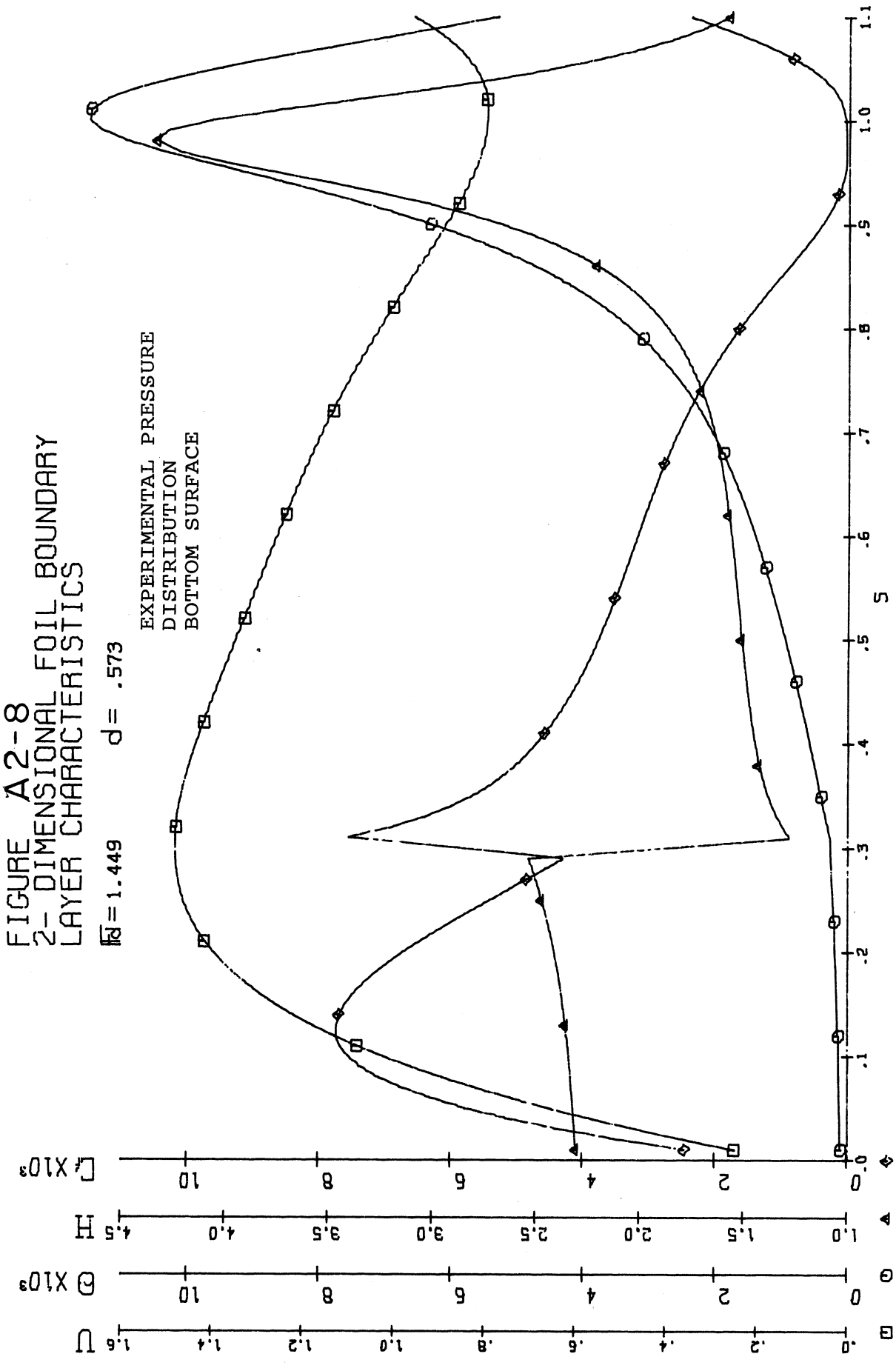
FIGURE A2-8
2- DIMENSIONAL FOIL BOUNDARY
LAYER CHARACTERISTICS
M = 1.449 d = .573
EXPERIMENTAL PRESSURE
DISTRIBUTION
BOTTOM SURFACE
U
Θ X10³
H
δ* X10³
δ
S

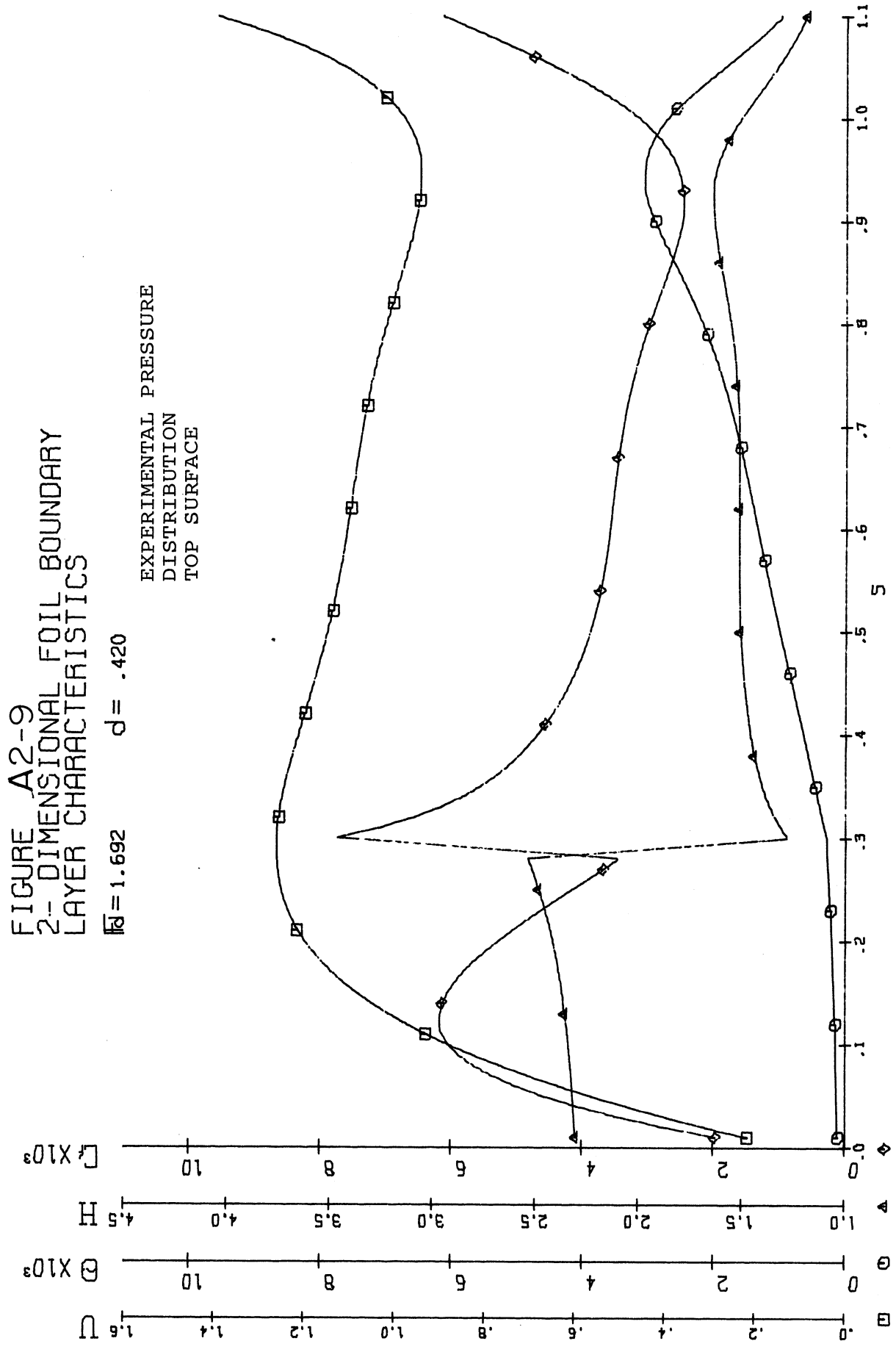
FIGURE A2-9
2- DIMENSIONAL FOIL BOUNDARY
LAYER CHARACTERISTICS
$\overline{C_d}$ = 1.692 d = .420
EXPERIMENTAL PRESSURE
DISTRIBUTION
TOP SURFACE
U
Θ X10³
H
C_f X10³
S

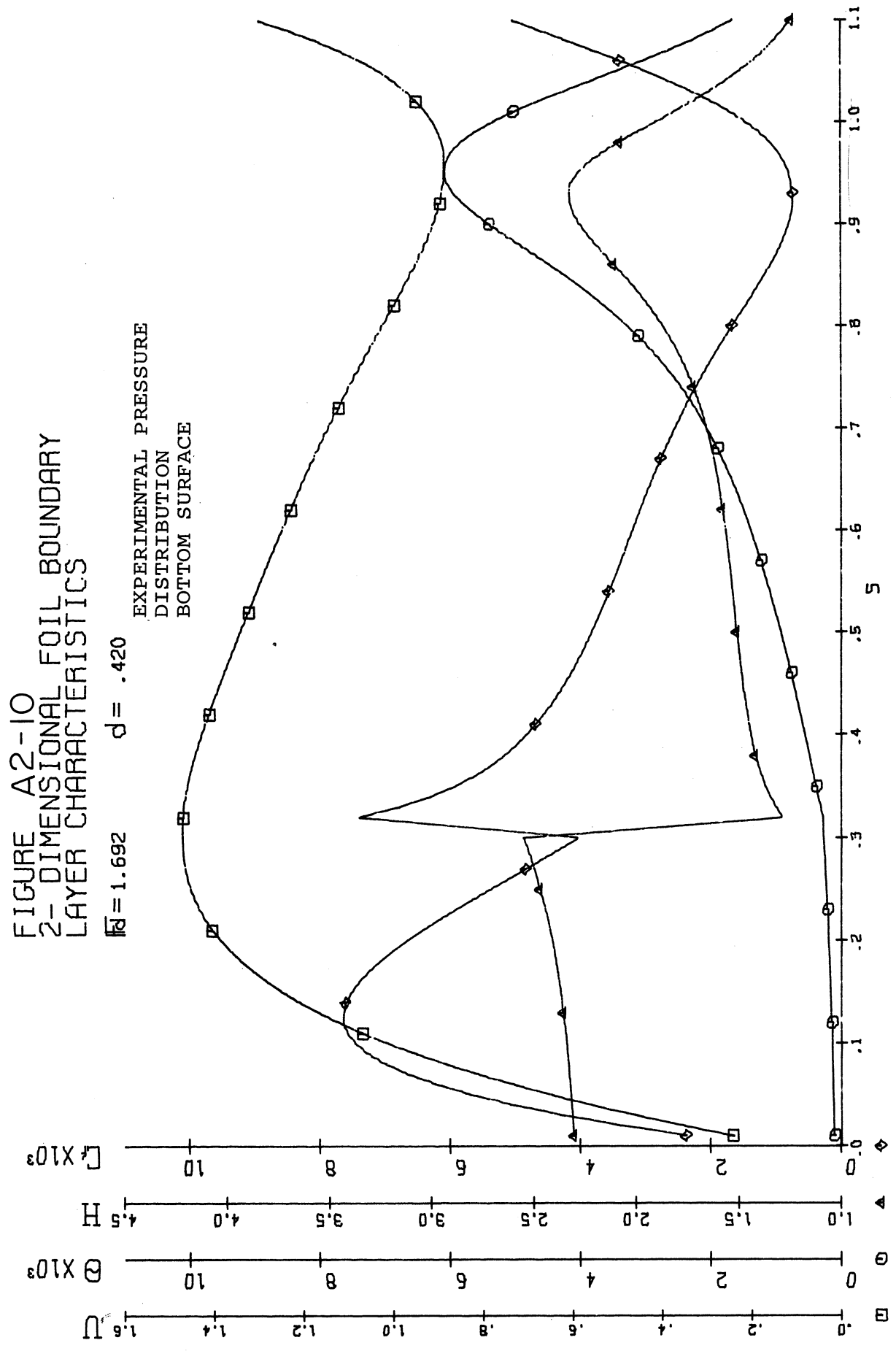
FIGURE A2-10
2- DIMENSIONAL FOIL BOUNDARY
LAYER CHARACTERISTICS
$\overline{R_d}$ = 1.692
d = .420
EXPERIMENTAL PRESSURE
DISTRIBUTION
BOTTOM SURFACE
U
Θ X10³
H
δ* X10³
δ
s

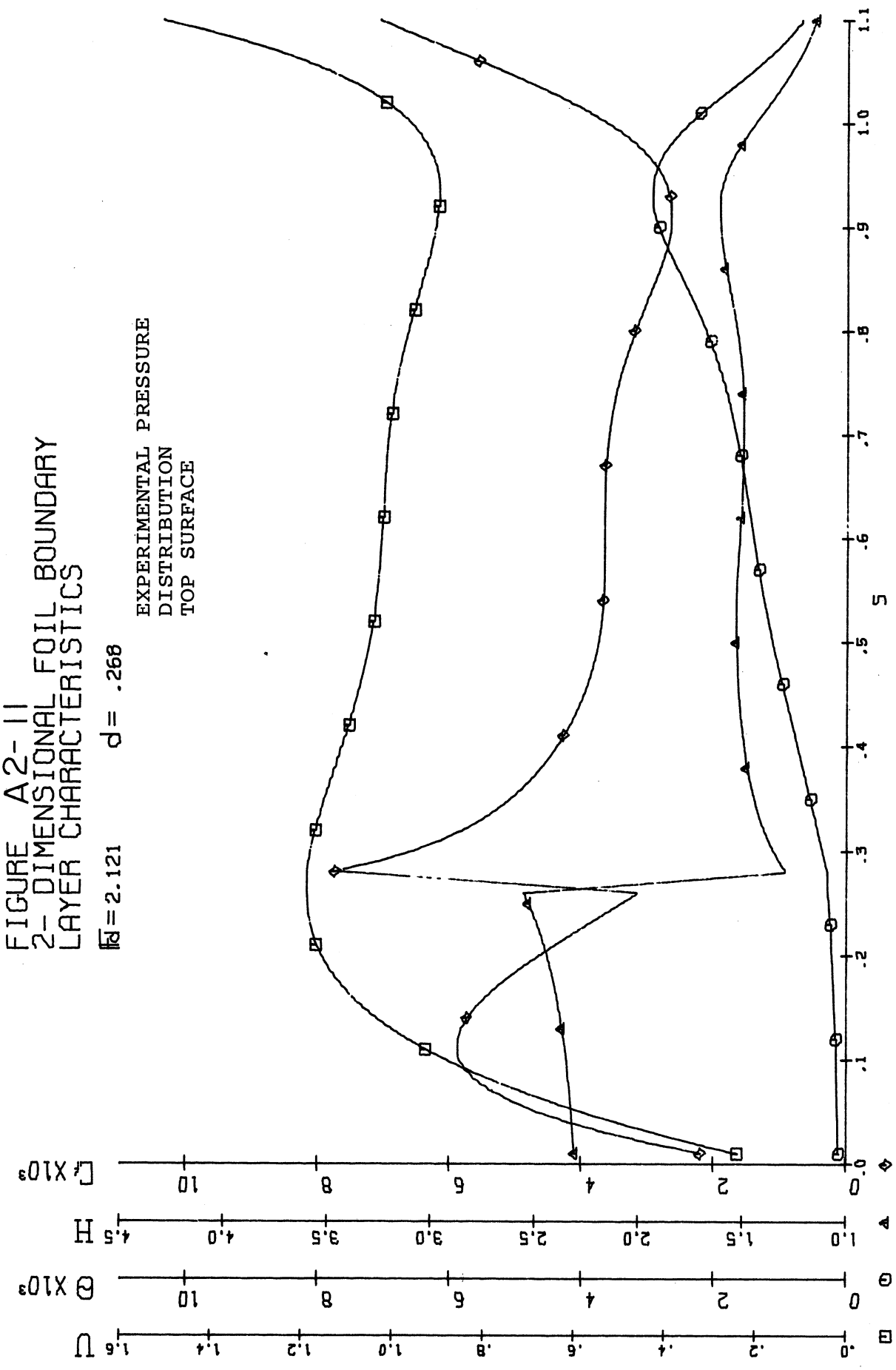
FIGURE A2-11
2-DIMENSIONAL FOIL BOUNDARY
LAYER CHARACTERISTICS
$\overline{R_d}$=2.121 d= .268
EXPERIMENTAL PRESSURE
DISTRIBUTION
TOP SURFACE
U
Θ X10³
H
Cf X10³
S

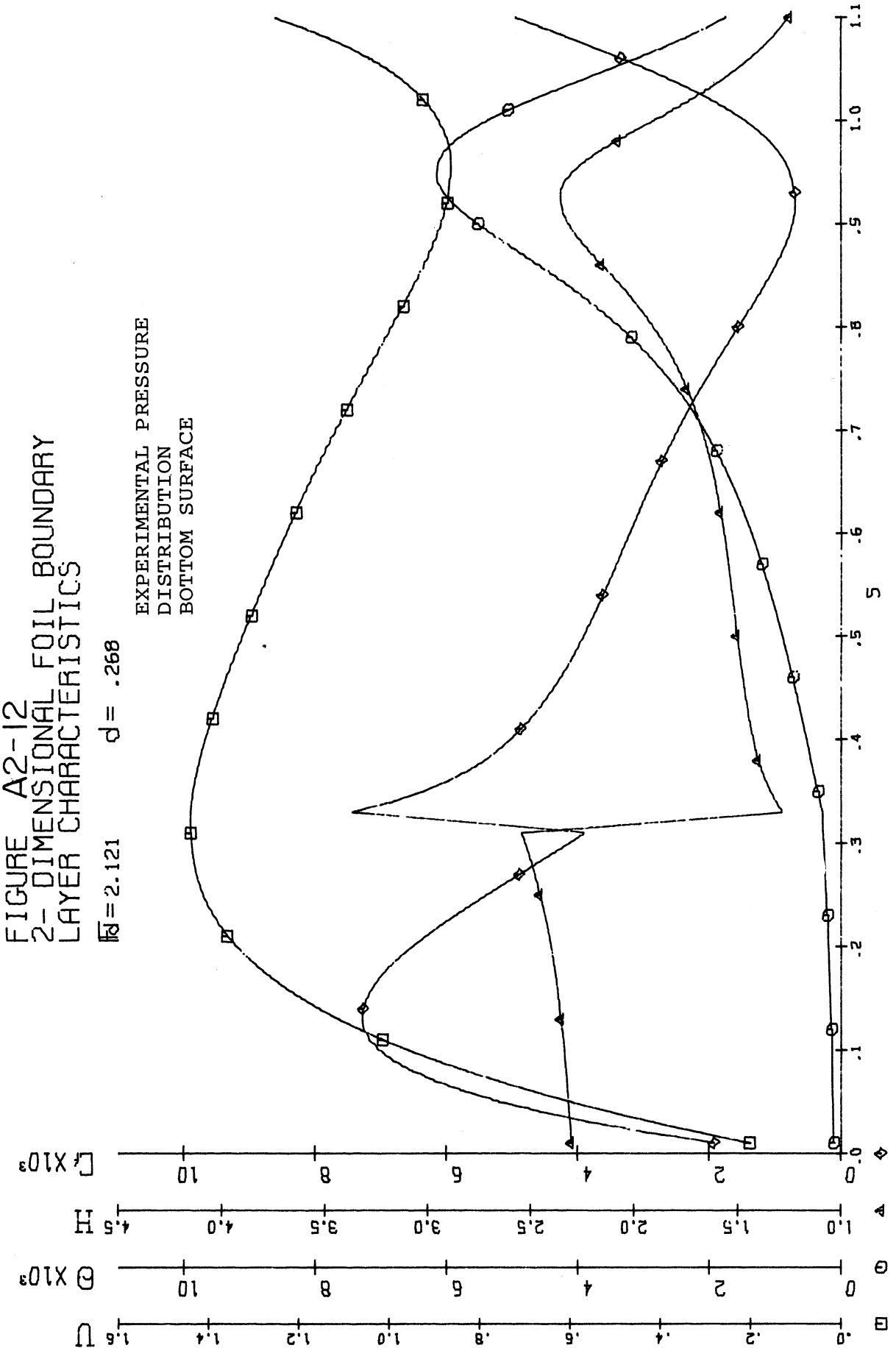
FIGURE A2-12
2- DIMENSIONAL FOIL BOUNDARY
LAYER CHARACTERISTICS
$\overline{R_d}$ = 2.121
d = .268
EXPERIMENTAL PRESSURE
DISTRIBUTION
BOTTOM SURFACE
U
Θ X10³
H
Γ X10³
S

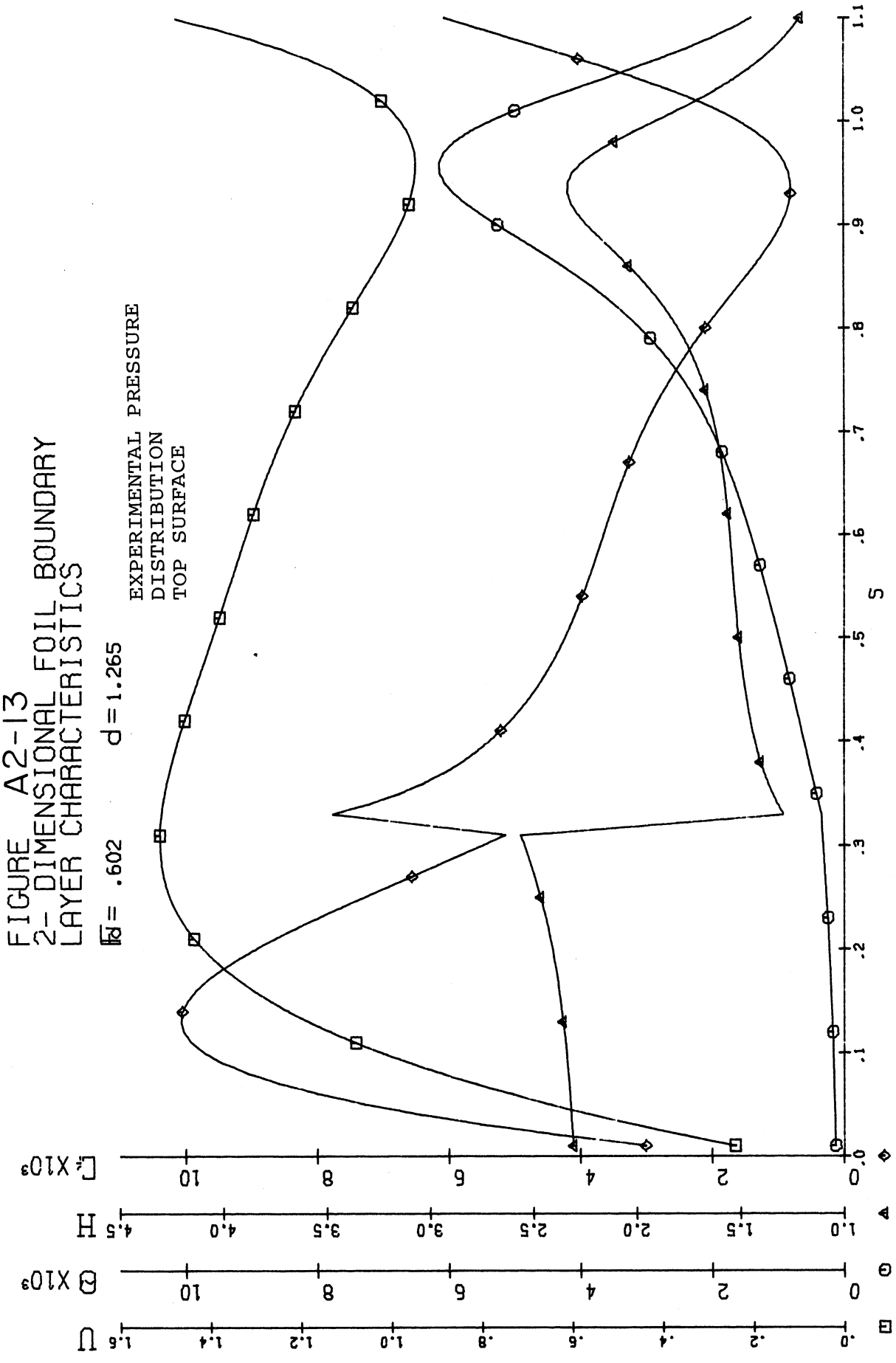
FIGURE A2-13
2- DIMENSIONAL FOIL BOUNDARY
LAYER CHARACTERISTICS
EXPERIMENTAL PRESSURE
DISTRIBUTION
TOP SURFACE
d=1.265
S
U
Θ X10³
H
δ* X10³

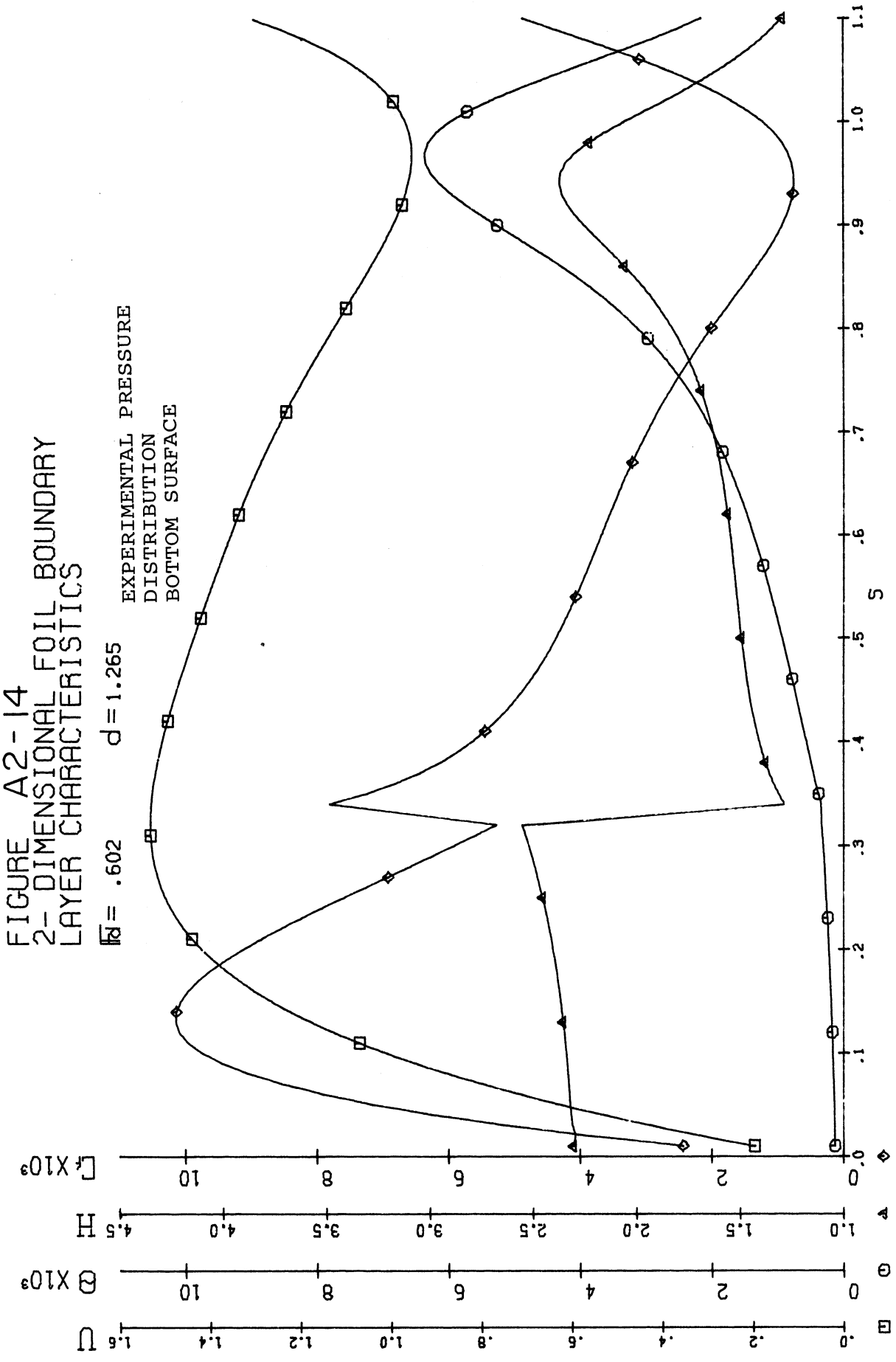
FIGURE A2-14
2-DIMENSIONAL FOIL BOUNDARY
LAYER CHARACTERISTICS
EXPERIMENTAL PRESSURE
DISTRIBUTION
BOTTOM SURFACE
d=1.265
= .602
U
Θ X10³
H
δ* X10³
S

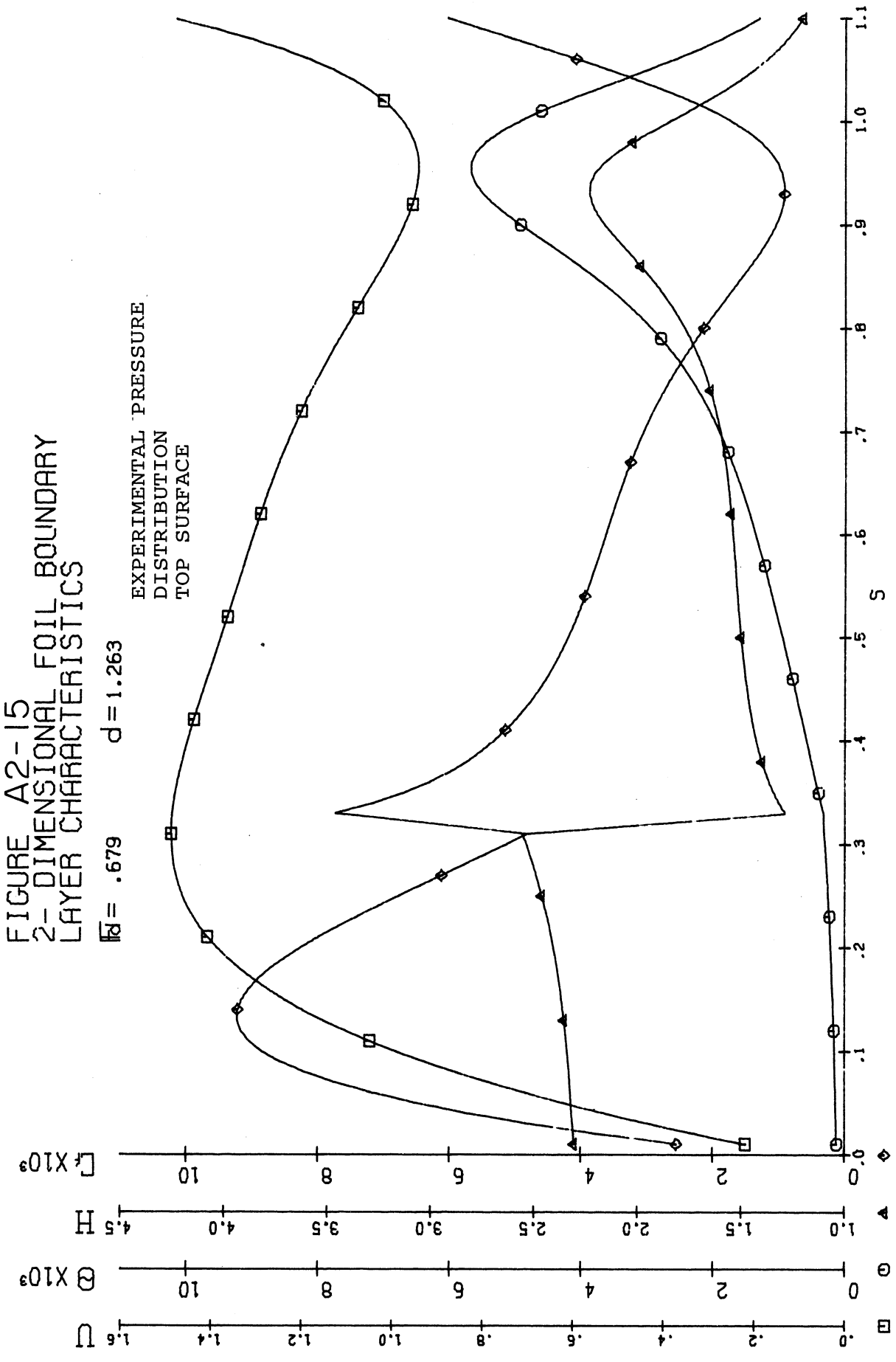
FIGURE A2-15
2- DIMENSIONAL FOIL BOUNDARY
LAYER CHARACTERISTICS
Rd = .679
d = 1.263
EXPERIMENTAL PRESSURE
DISTRIBUTION
TOP SURFACE
U
Θ X10³
H
Γ X10³
S

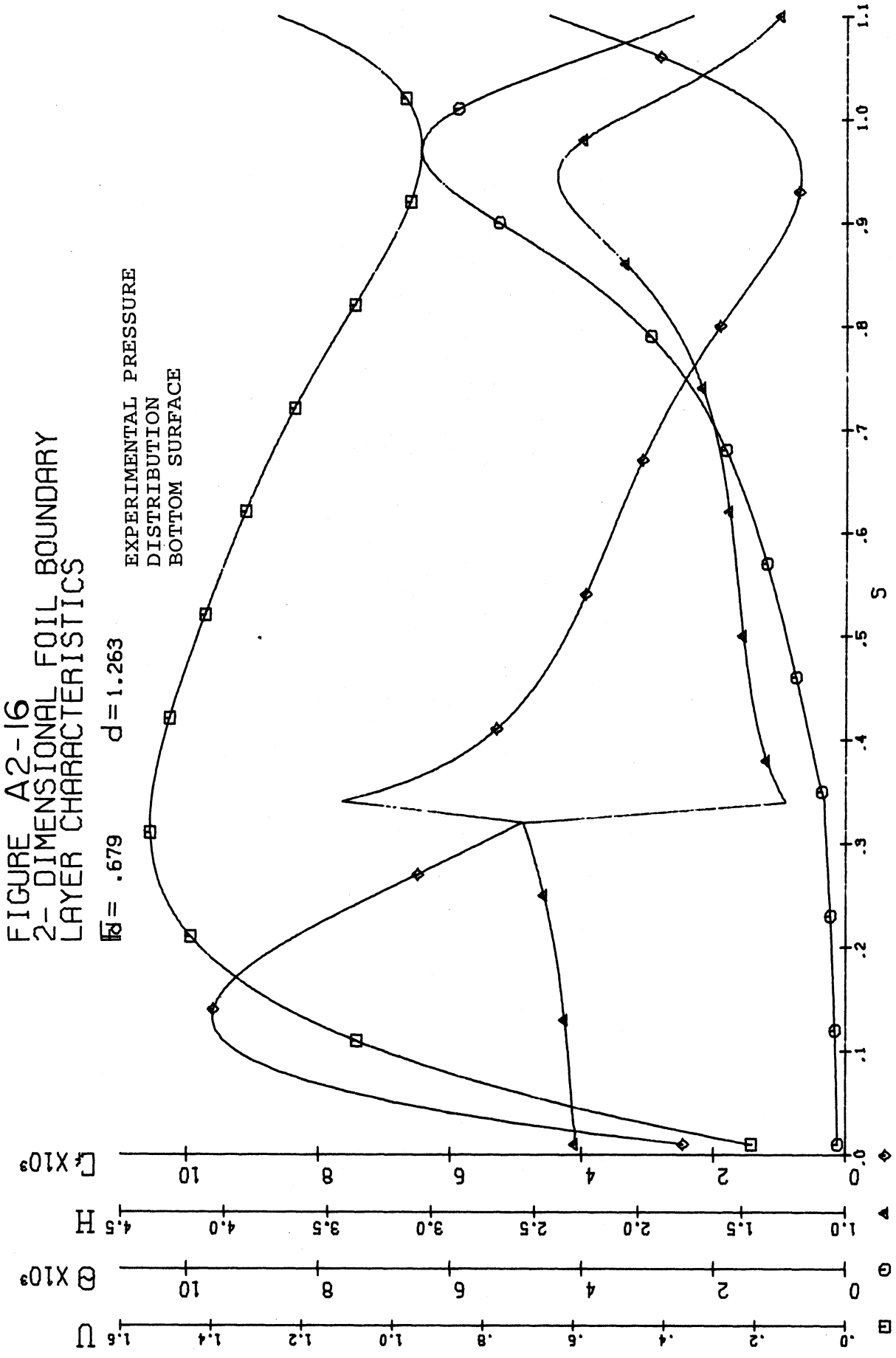
FIGURE A2-16
2- DIMENSIONAL FOIL BOUNDARY
LAYER CHARACTERISTICS
EXPERIMENTAL PRESSURE
DISTRIBUTION
BOTTOM SURFACE
d=1.263
= .679
S
U
Θ X10³
H
δ* X10³

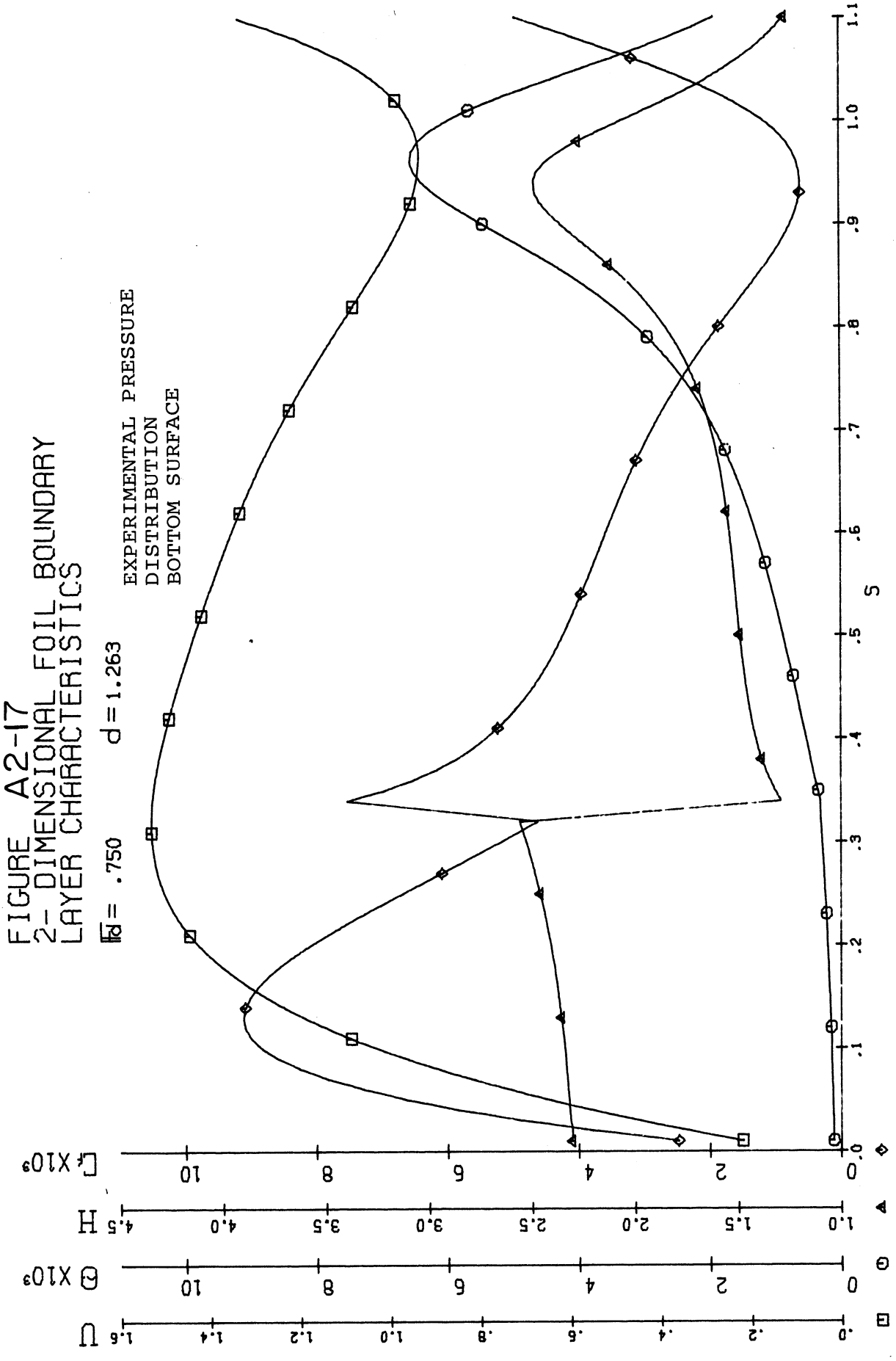
FIGURE A2-17
2- DIMENSIONAL FOIL BOUNDARY
LAYER CHARACTERISTICS
EXPERIMENTAL PRESSURE
DISTRIBUTION
BOTTOM SURFACE
d = 1.263
= .750
U
Θ X10³
H
δ* X10³
S

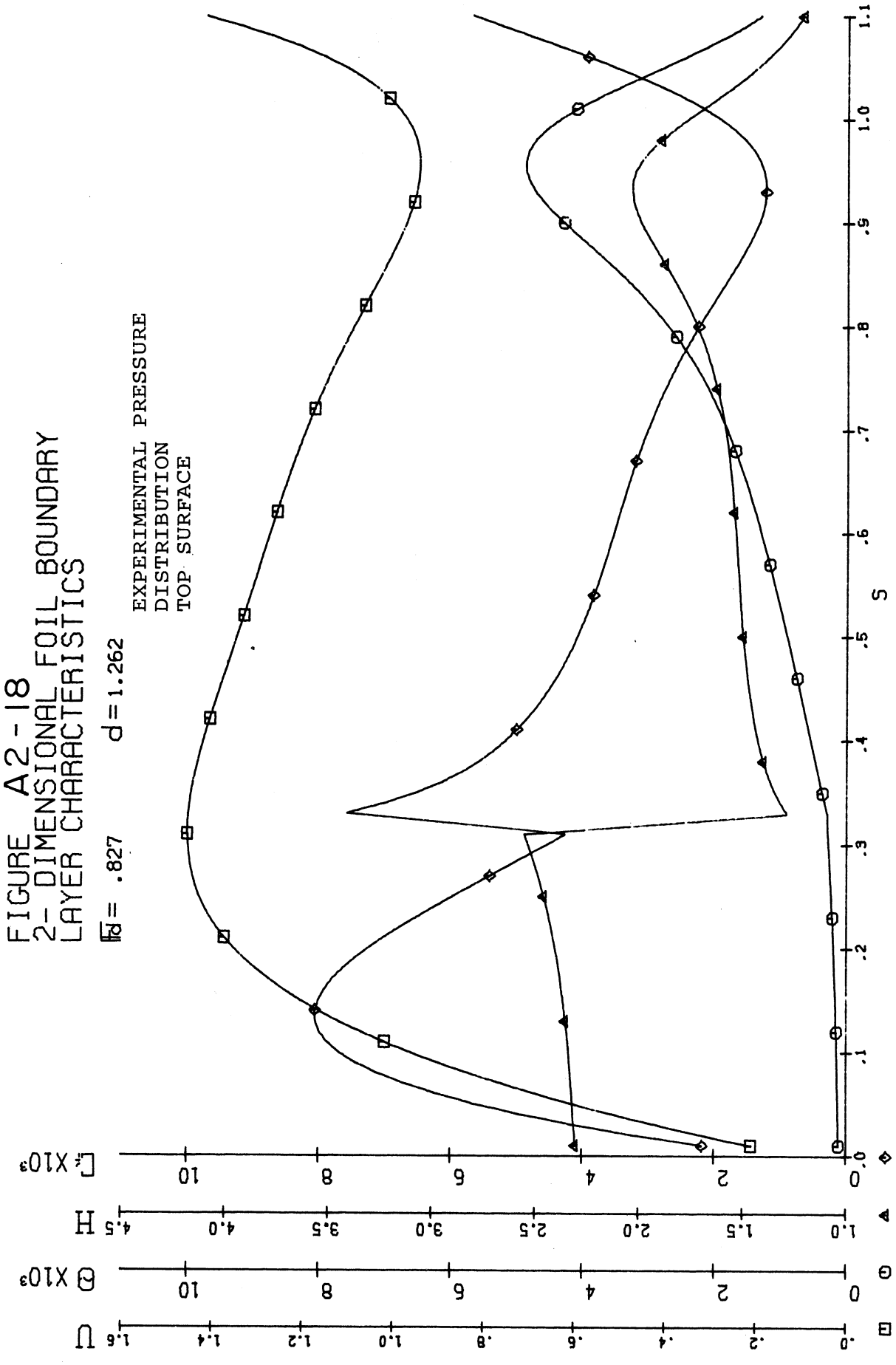
FIGURE A2-18
2- DIMENSIONAL FOIL BOUNDARY
LAYER CHARACTERISTICS
Rd = .827
d = 1.262
EXPERIMENTAL PRESSURE
DISTRIBUTION
TOP SURFACE
U
Θ X10³
H
δ* X10³
S

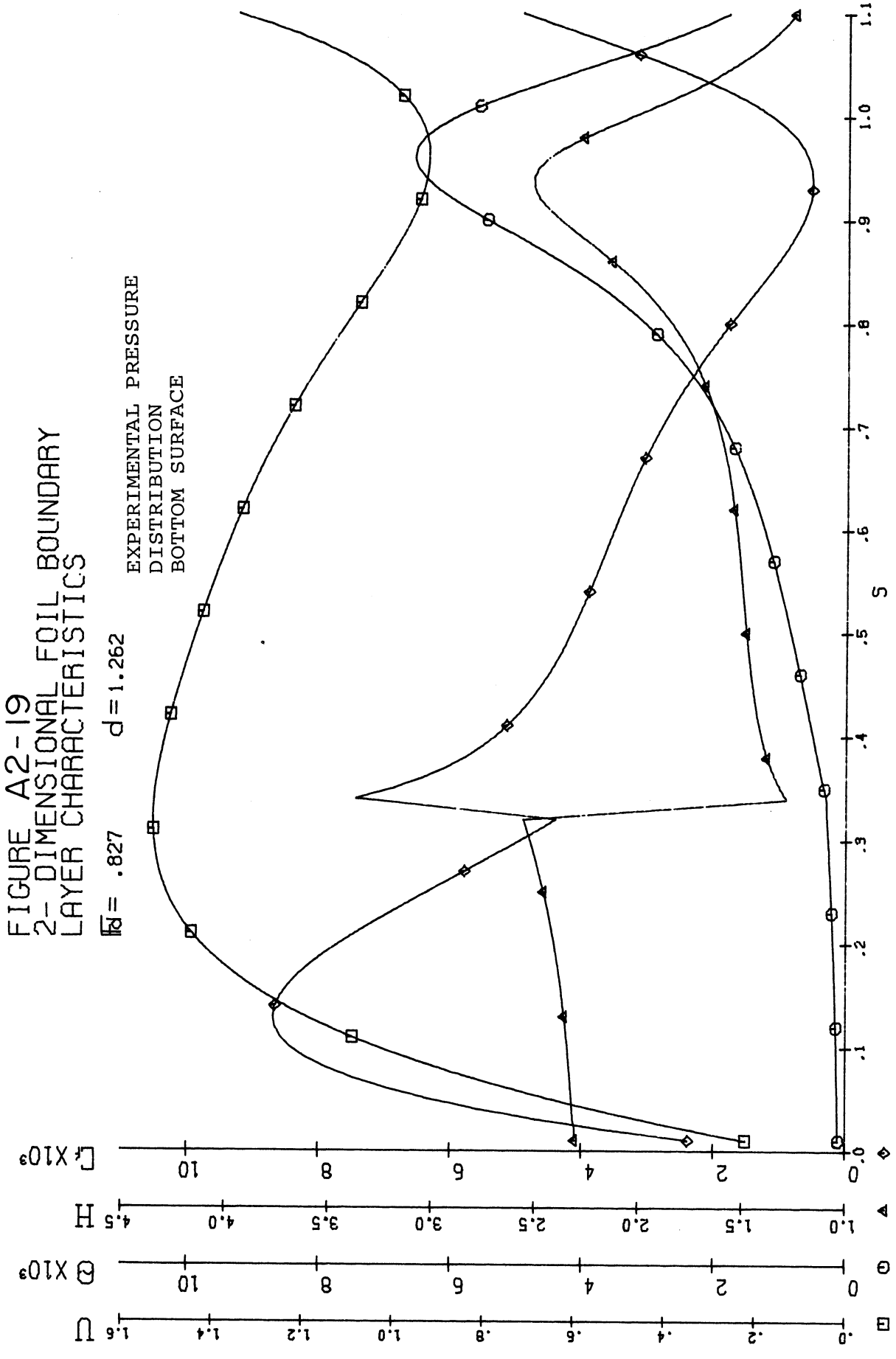
FIGURE A2-19
2- DIMENSIONAL FOIL BOUNDARY
LAYER CHARACTERISTICS
M = .827
d = 1.262
EXPERIMENTAL PRESSURE
DISTRIBUTION
BOTTOM SURFACE
U
Θ X10³
H
δ* X10³
S

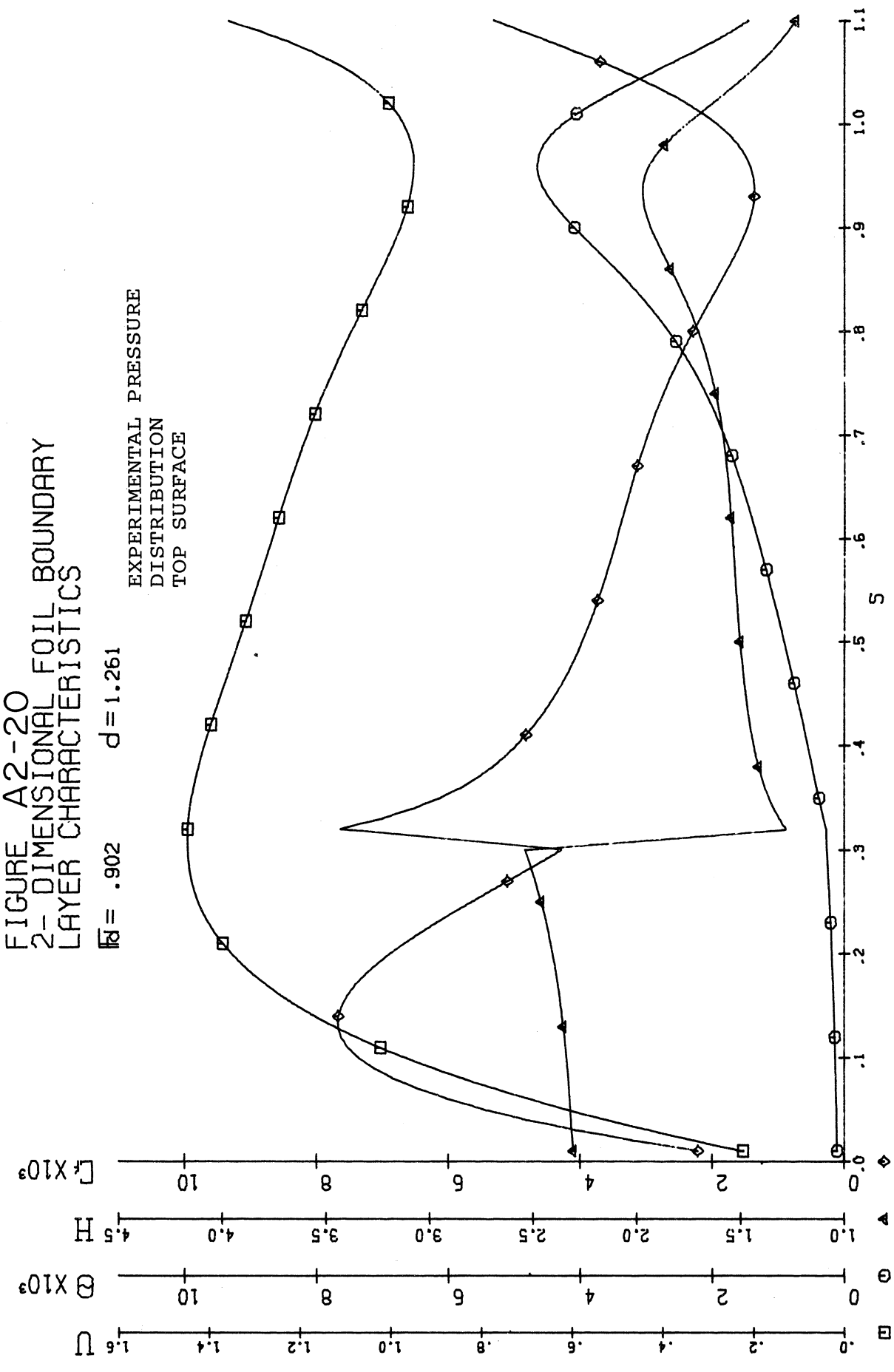
FIGURE A2-20
2-DIMENSIONAL FOIL BOUNDARY
LAYER CHARACTERISTICS
R_d = .902 d=1.261
EXPERIMENTAL PRESSURE
DISTRIBUTION
TOP SURFACE
U
Θ X10³
H
δ* X10³
S

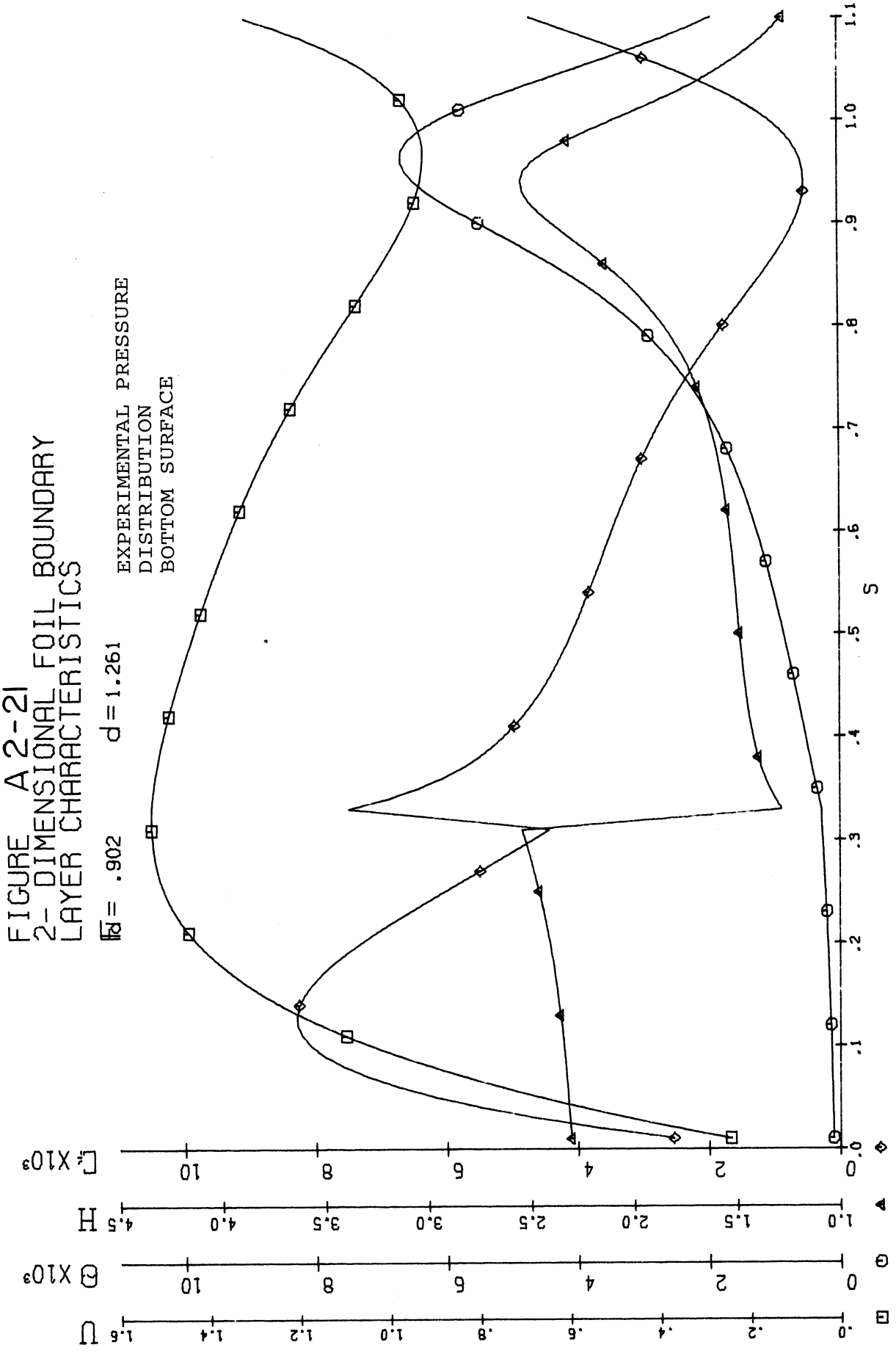
FIGURE A 2-21
2- DIMENSIONAL FOIL BOUNDARY
LAYER CHARACTERISTICS
EXPERIMENTAL PRESSURE
DISTRIBUTION
BOTTOM SURFACE
d=1.261
S
U
Θ X10³
H
Γ X10³

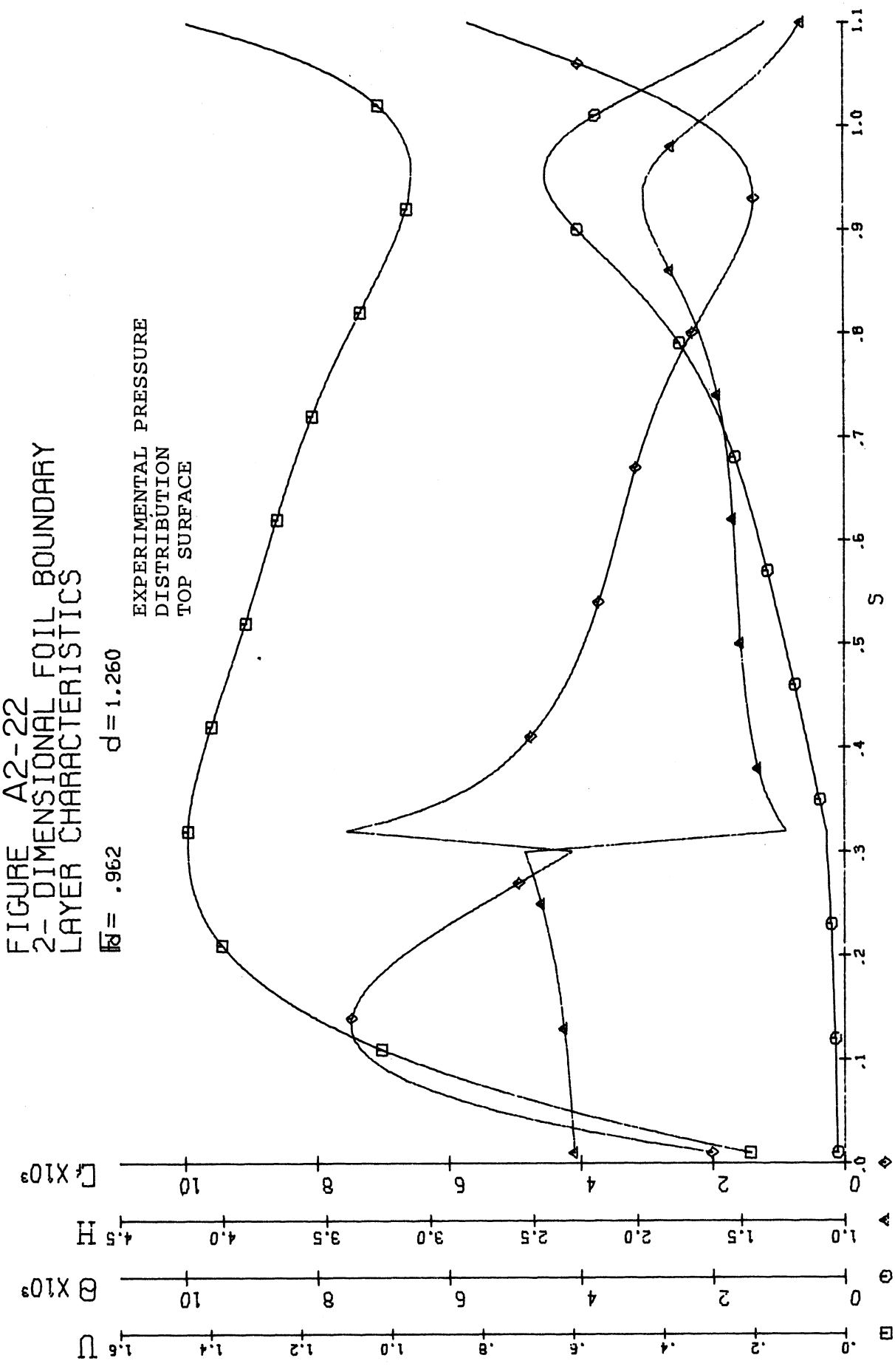
FIGURE A2-22
2-DIMENSIONAL FOIL BOUNDARY
LAYER CHARACTERISTICS
M = .962 d = 1.260
EXPERIMENTAL PRESSURE
DISTRIBUTION
TOP SURFACE
U
θ X10³
H
C_f X10³
S

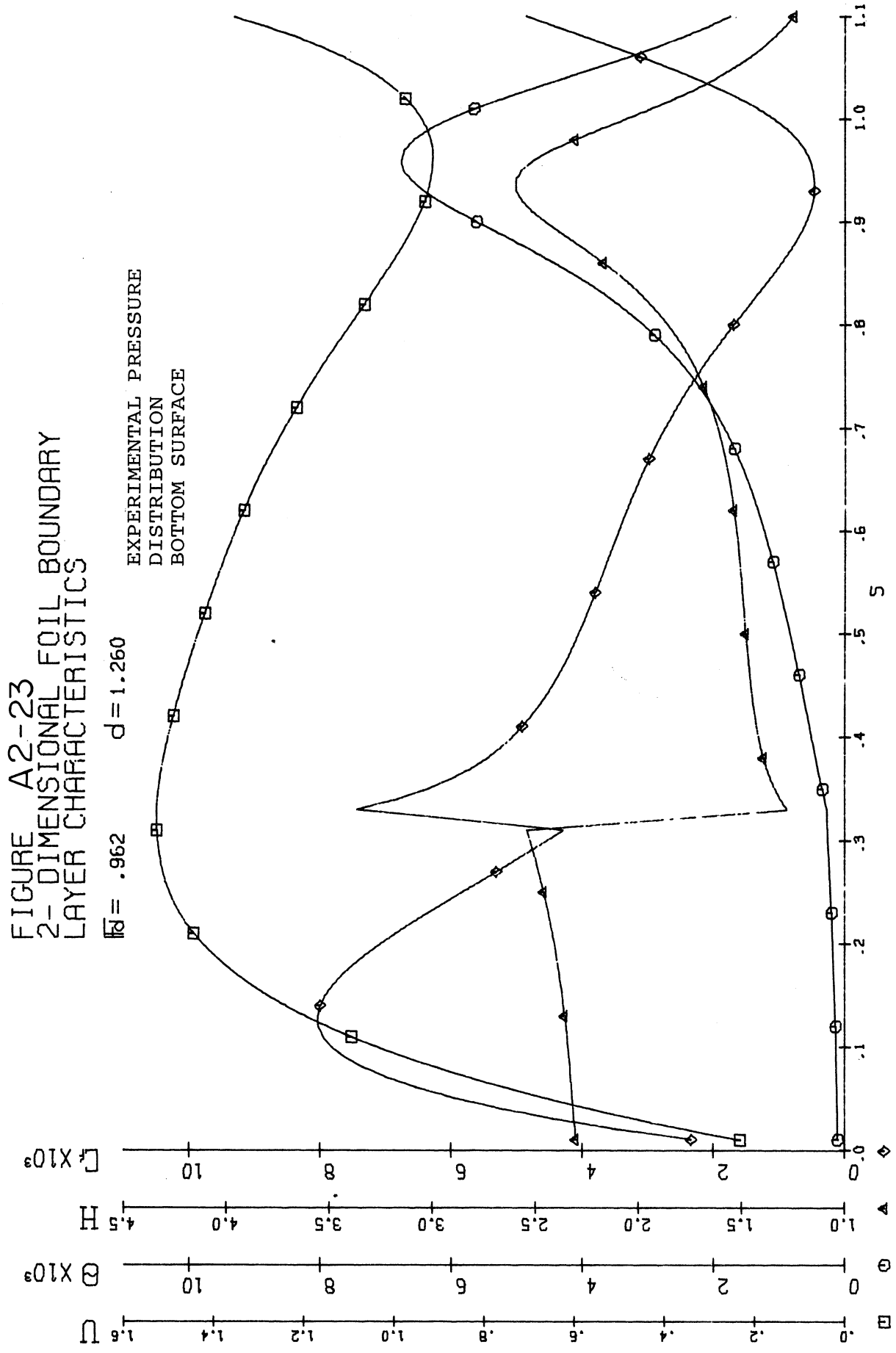
FIGURE A2-23
2- DIMENSIONAL FOIL BOUNDARY
LAYER CHARACTERISTICS
$\overline{M_d}$ = .962 d = 1.260
EXPERIMENTAL PRESSURE
DISTRIBUTION
BOTTOM SURFACE
U
Θ X10³
H
Γ X10³
S

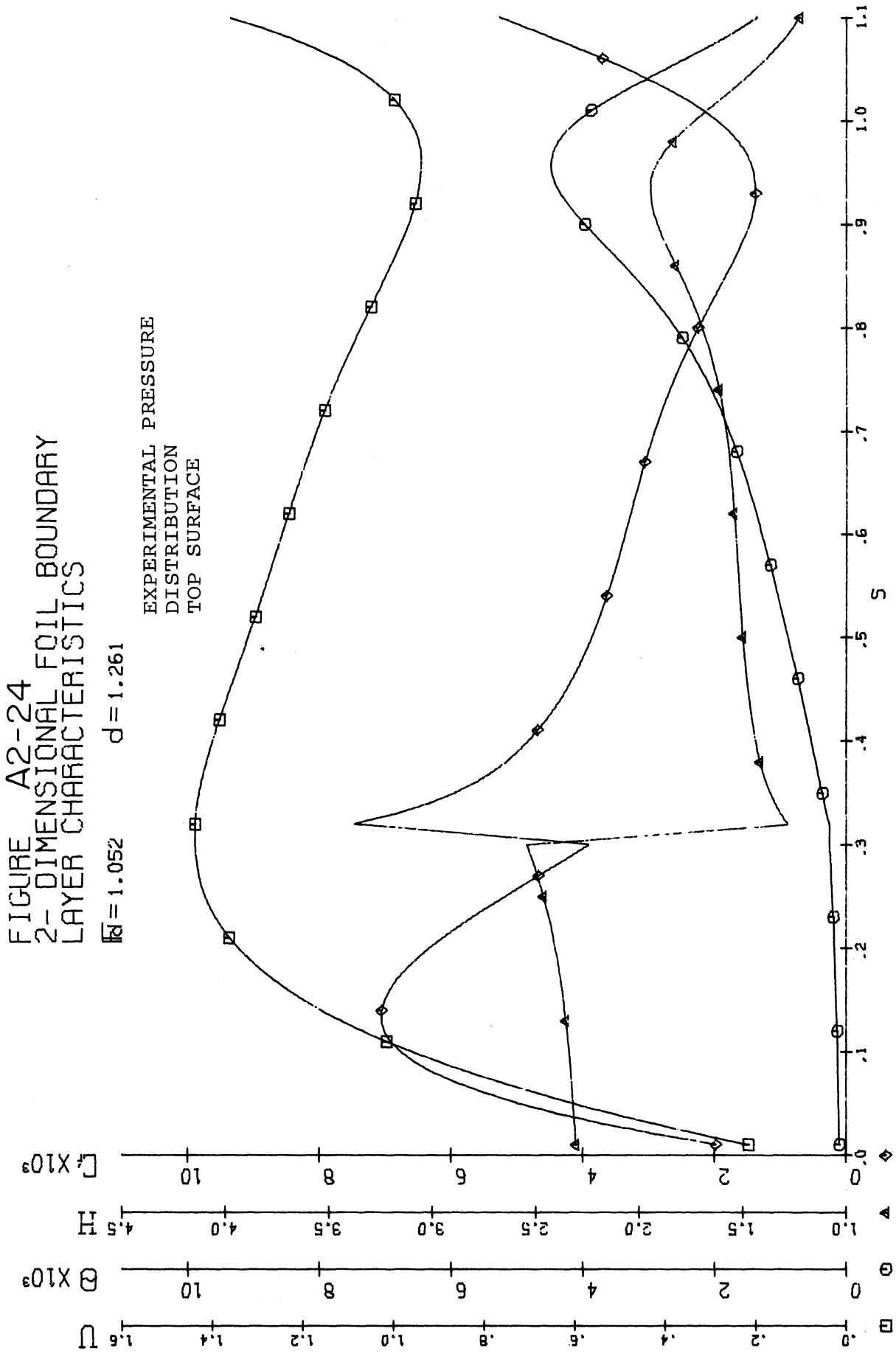
FIGURE A2-24
2- DIMENSIONAL FOIL BOUNDARY
LAYER CHARACTERISTICS
d = 1.261
EXPERIMENTAL PRESSURE
DISTRIBUTION
TOP SURFACE
S

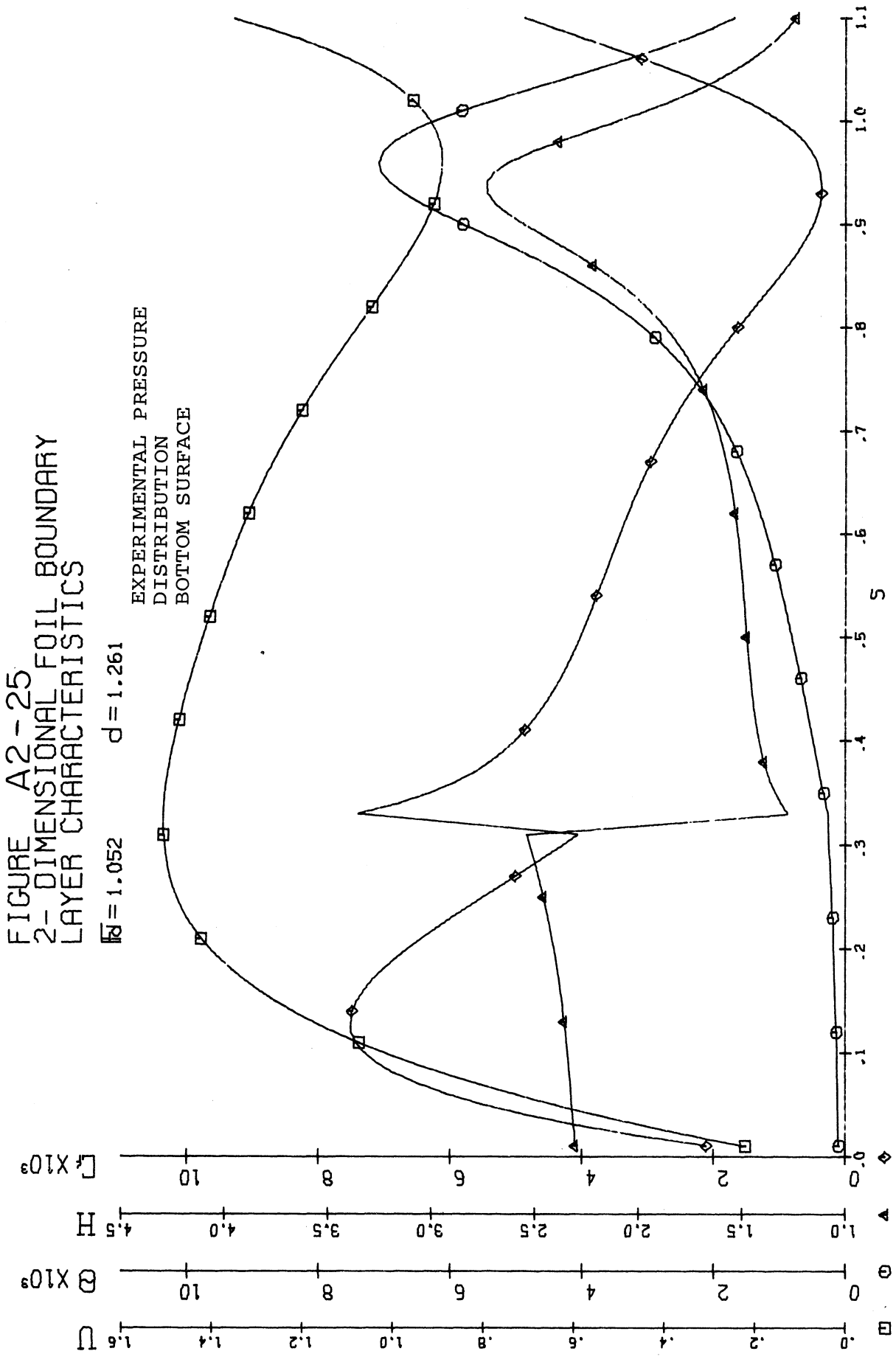
FIGURE A2-25
2-DIMENSIONAL FOIL BOUNDARY
LAYER CHARACTERISTICS
Re = 1.052
d = 1.261
EXPERIMENTAL PRESSURE
DISTRIBUTION
BOTTOM SURFACE
U
Θ X10³
H
δ* X10³
S

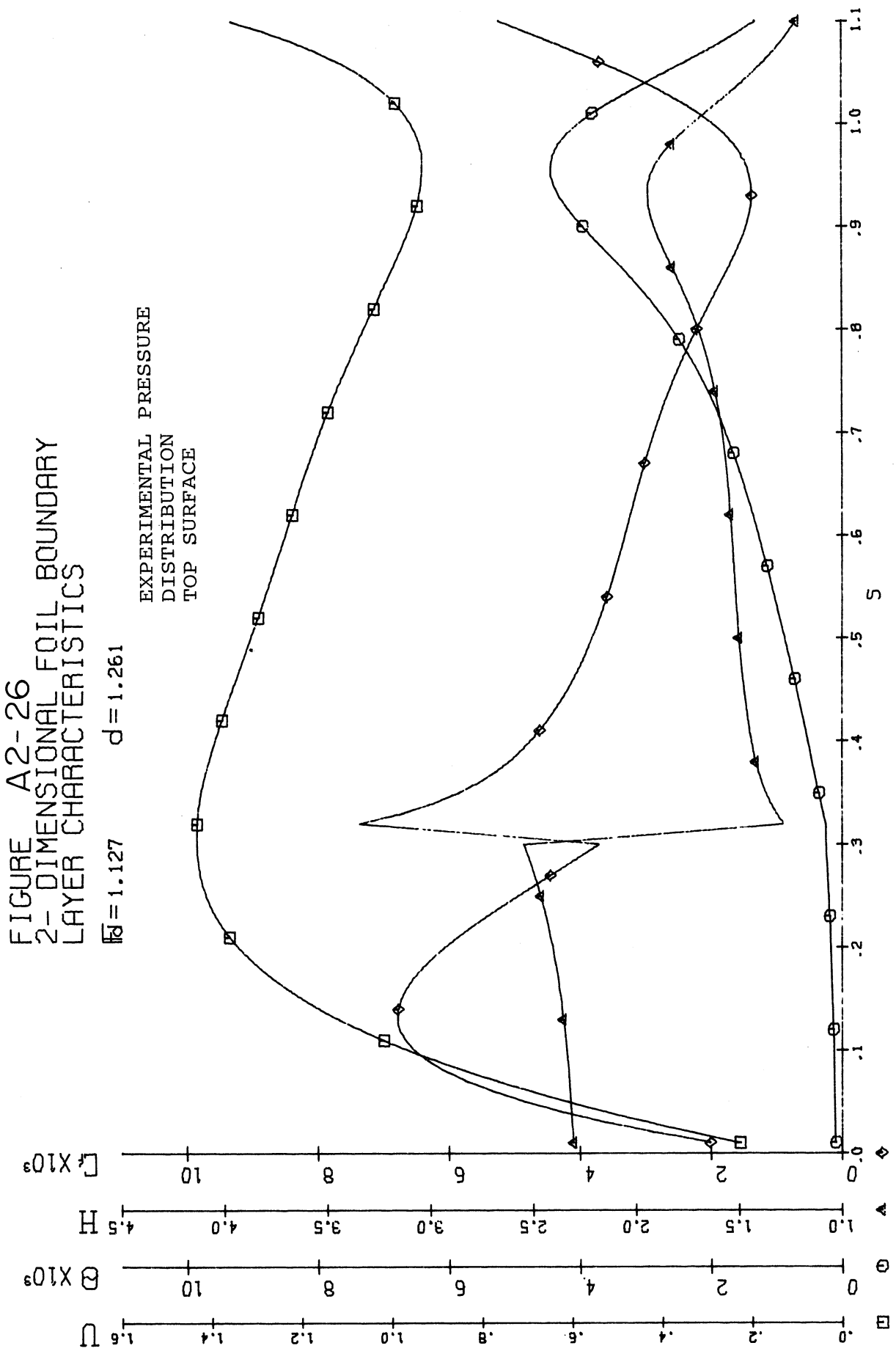
FIGURE A2-26
2- DIMENSIONAL FOIL BOUNDARY
LAYER CHARACTERISTICS
d = 1.261
d = 1.127
EXPERIMENTAL PRESSURE
DISTRIBUTION
TOP SURFACE
S
H
θ X10³
δ* X10³
U

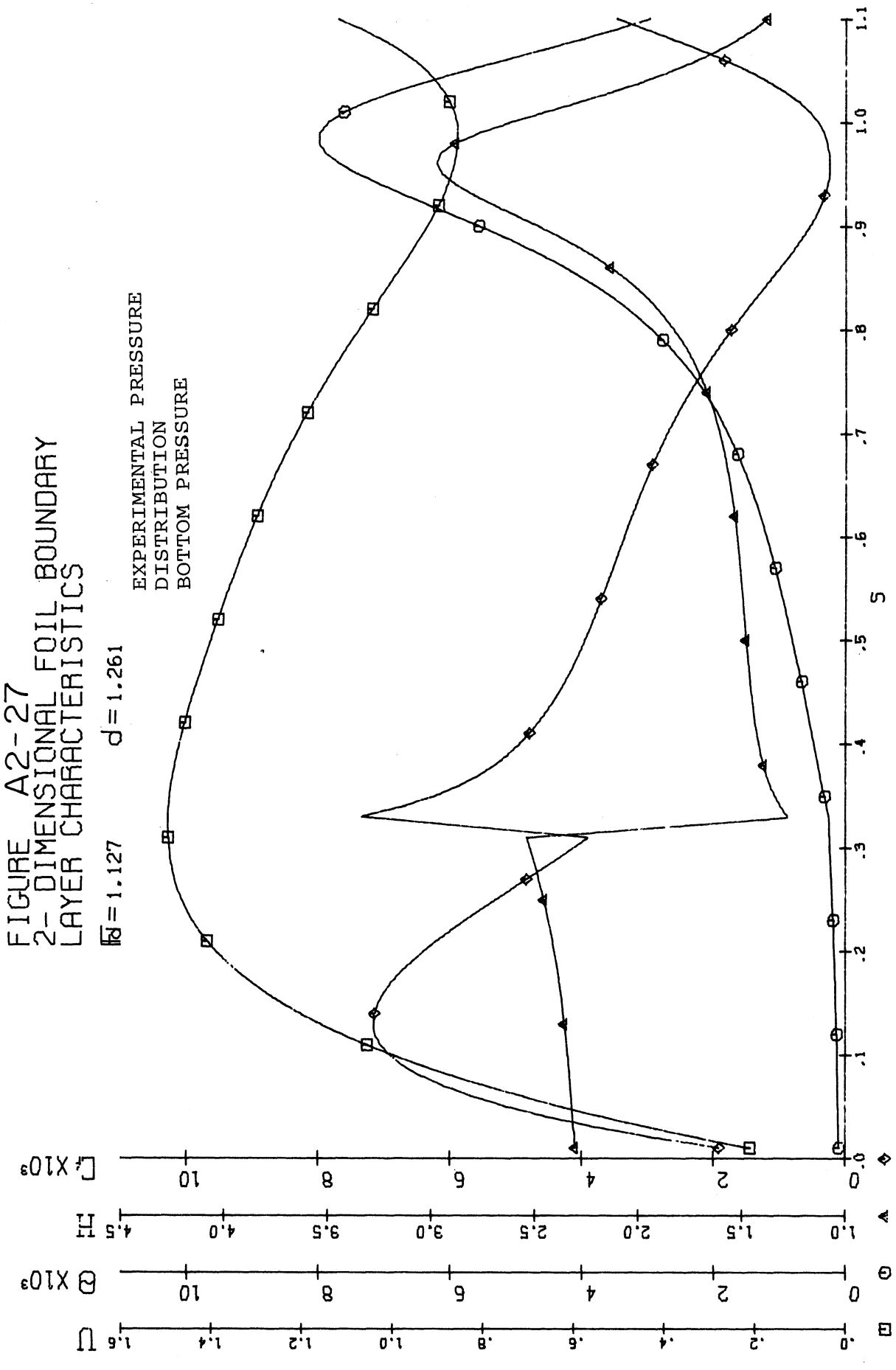
FIGURE A2-27
2- DIMENSIONAL FOIL BOUNDARY
LAYER CHARACTERISTICS
$\bar{R}_d = 1.127$ d = 1.261
EXPERIMENTAL PRESSURE
DISTRIBUTION
BOTTOM PRESSURE
S
U
Θ X10³
H
δ* X10³

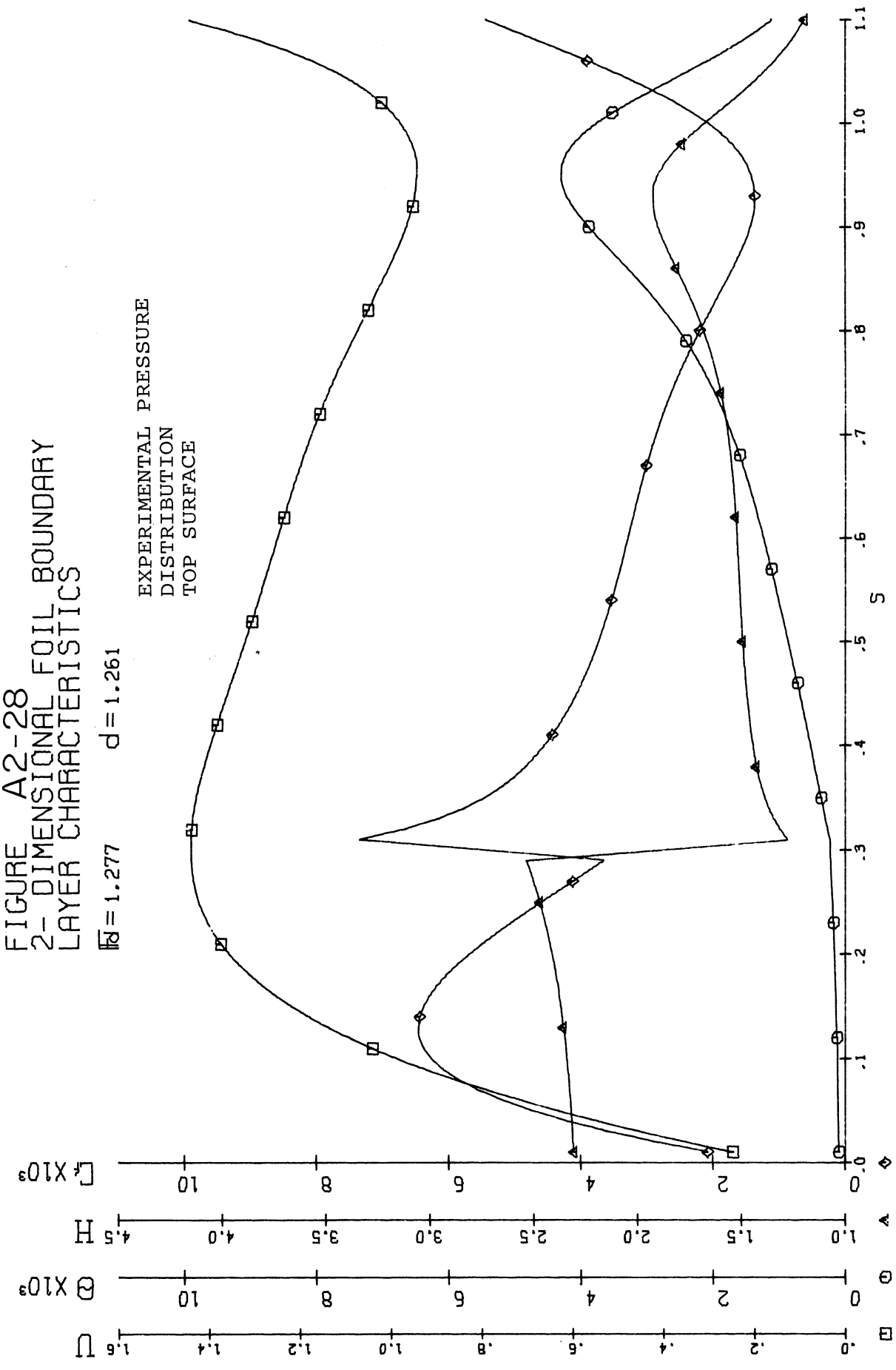
FIGURE A2-28
2- DIMENSIONAL FOIL BOUNDARY
LAYER CHARACTERISTICS
$\overline{R_d}$ = 1.277 d = 1.261
EXPERIMENTAL PRESSURE
DISTRIBUTION
TOP SURFACE
U
Θ X10³
H
C_f X10³
S

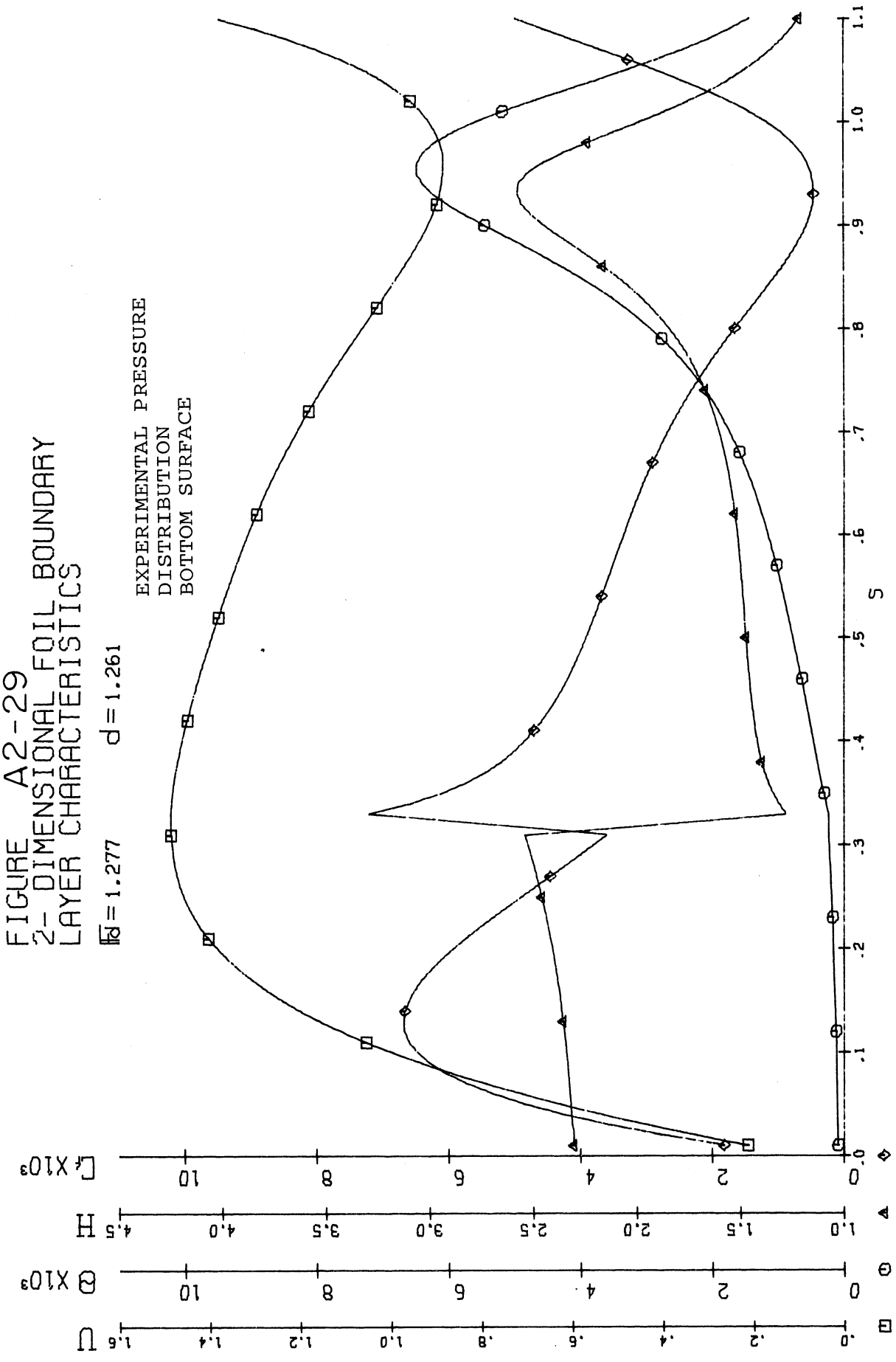
FIGURE A2-29
2- DIMENSIONAL FOIL BOUNDARY
LAYER CHARACTERISTICS
Re = 1.277
d = 1.261
EXPERIMENTAL PRESSURE
DISTRIBUTION
BOTTOM SURFACE
U
Θ X10³
H
δ* X10³
S

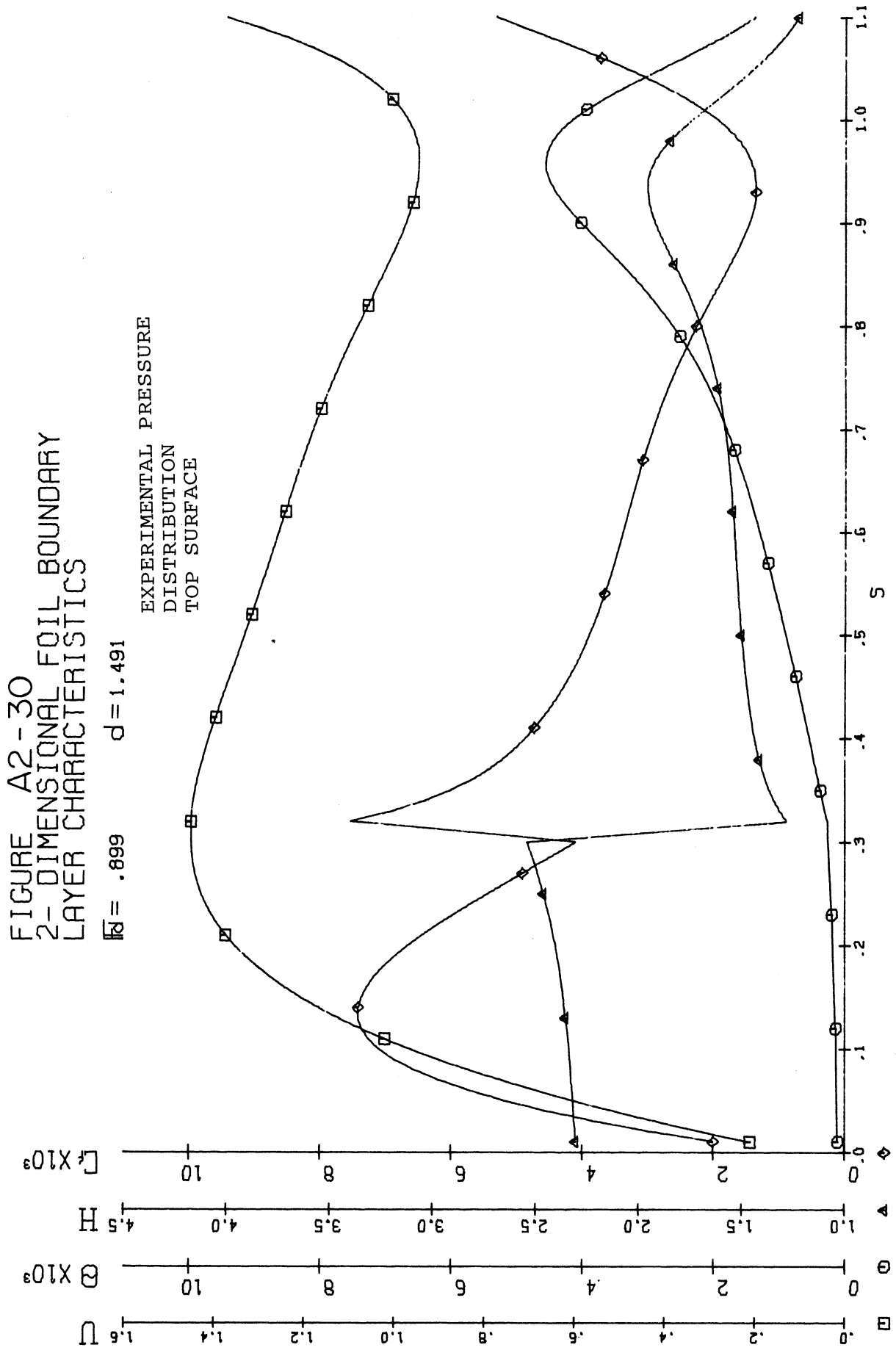
FIGURE A2-30
2-DIMENSIONAL FOIL BOUNDARY
LAYER CHARACTERISTICS
M = .899 d = 1.491
EXPERIMENTAL PRESSURE
DISTRIBUTION
TOP SURFACE
U
Θ X10³
H
δ* X10³
S

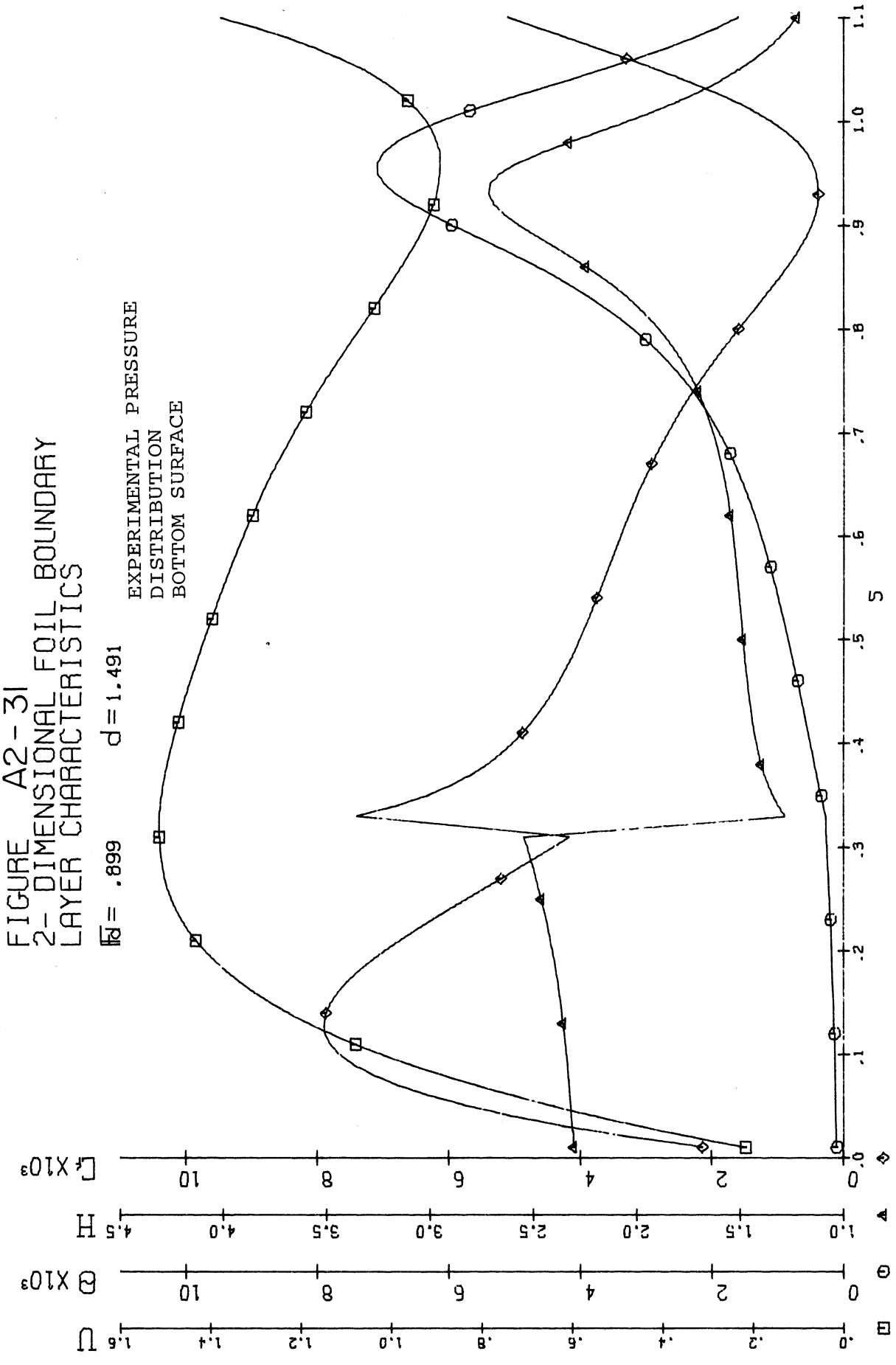
FIGURE A2-31
2-DIMENSIONAL FOIL BOUNDARY
LAYER CHARACTERISTICS
$\overline{Re}$ = .899 d=1.491
EXPERIMENTAL PRESSURE
DISTRIBUTION
BOTTOM SURFACE
U
Θ X10³
H
δ* X10³
S

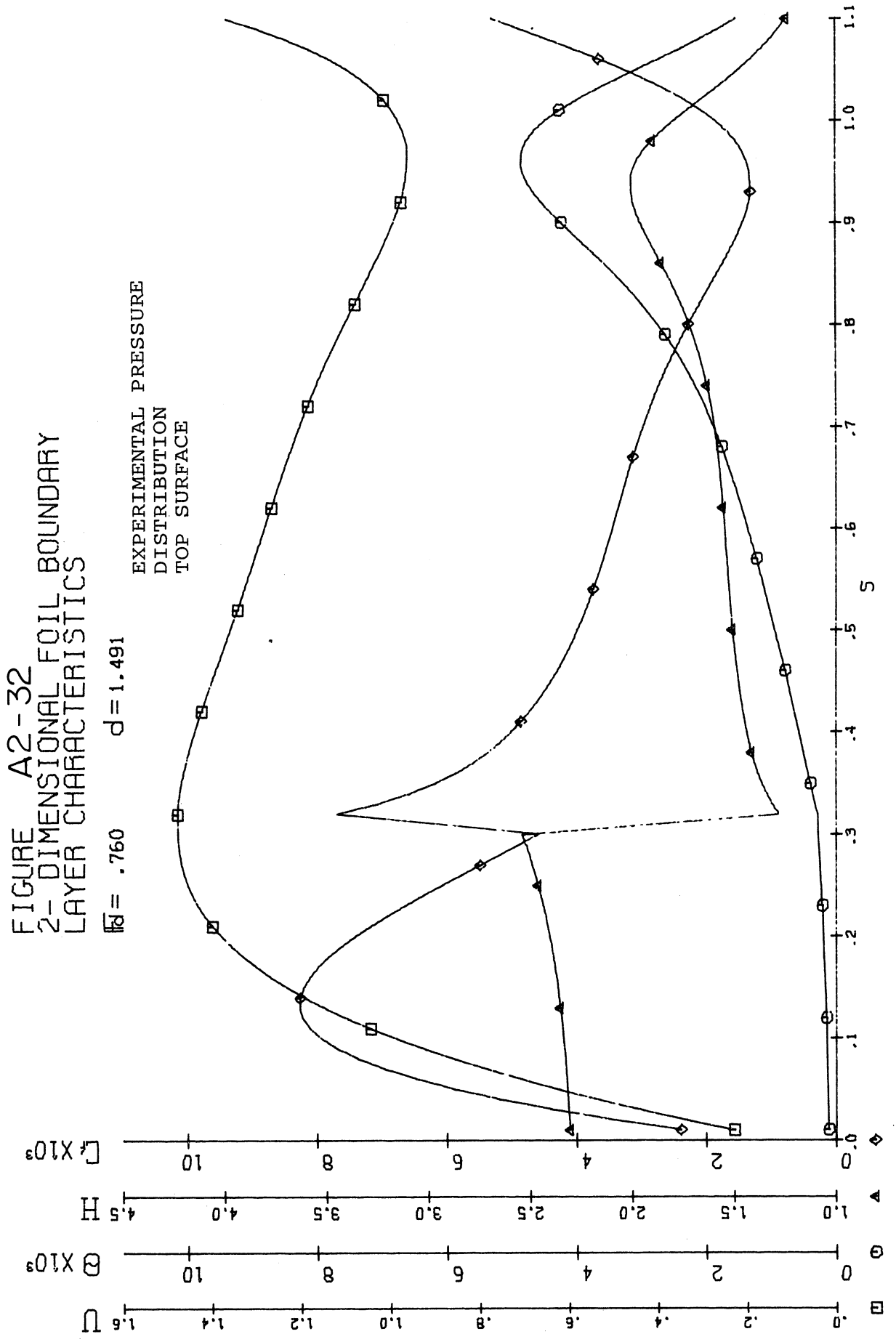
FIGURE A2-32
2-DIMENSIONAL FOIL BOUNDARY
LAYER CHARACTERISTICS
d = 1.491
EXPERIMENTAL PRESSURE
DISTRIBUTION
TOP SURFACE
S
U
Θ X10³
H
δ* X10³

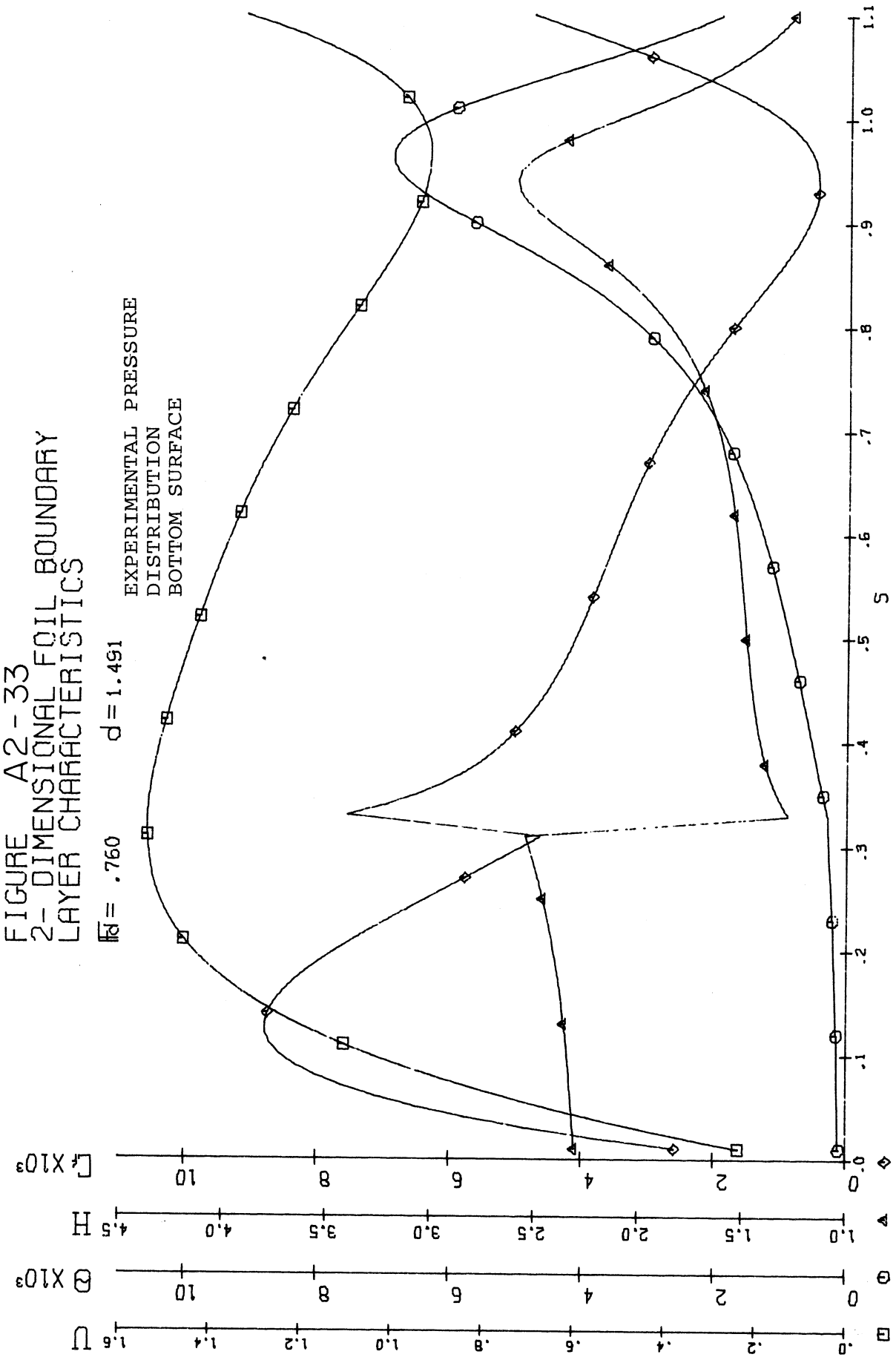
FIGURE A2-33
2- DIMENSIONAL FOIL BOUNDARY
LAYER CHARACTERISTICS
R_d = .760
d = 1.491
EXPERIMENTAL PRESSURE
DISTRIBUTION
BOTTOM SURFACE
U
Θ X10^3
H
δ^* X10^3
S

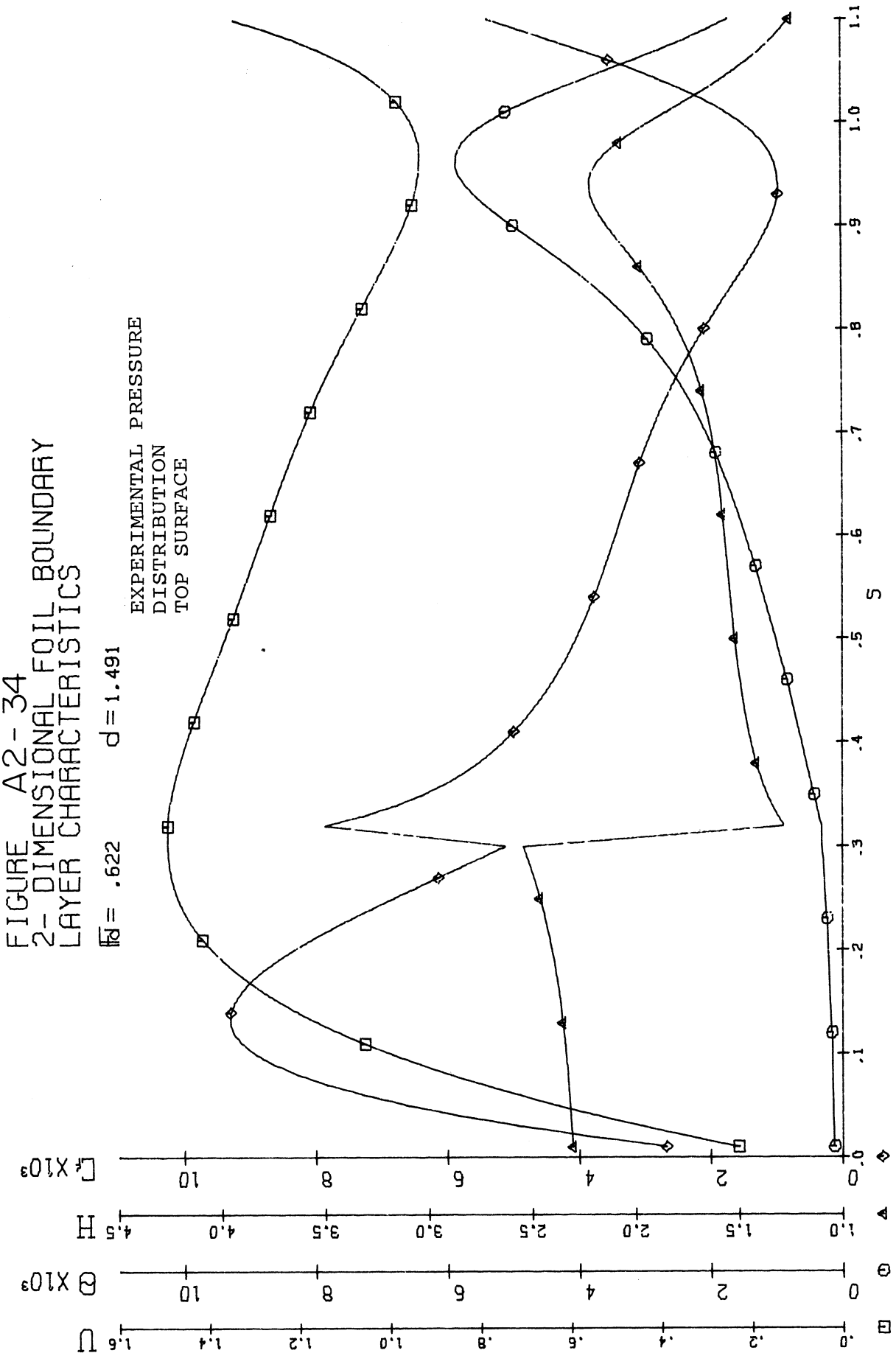
FIGURE A2-34
2-DIMENSIONAL FOIL BOUNDARY
LAYER CHARACTERISTICS
Re = .622
d = 1.491
EXPERIMENTAL PRESSURE
DISTRIBUTION
TOP SURFACE
U
θ X10³
H
Cf X10³
S

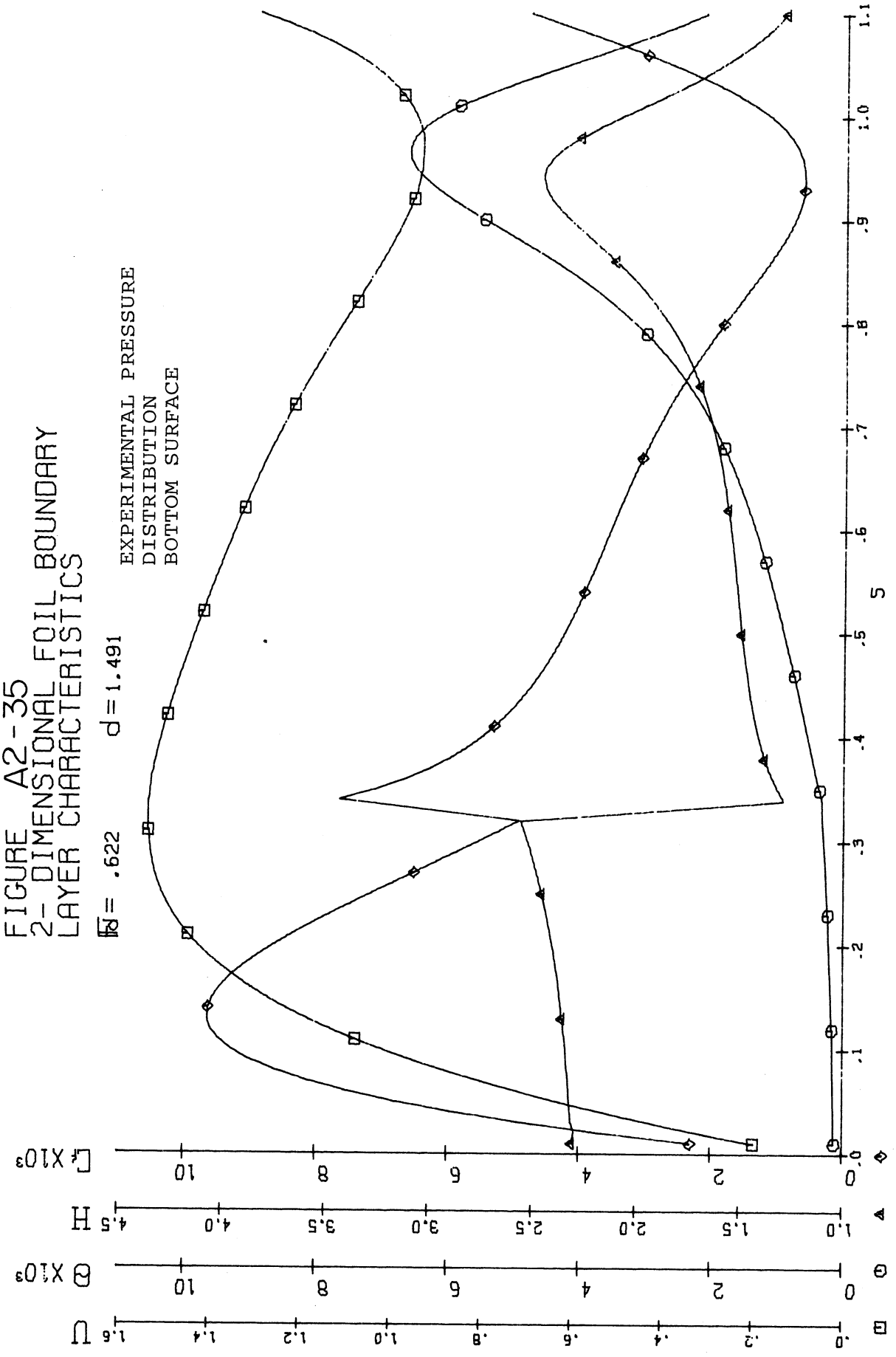
FIGURE A2-35
2-DIMENSIONAL FOIL BOUNDARY
LAYER CHARACTERISTICS
EXPERIMENTAL PRESSURE
DISTRIBUTION
BOTTOM SURFACE
d = 1.491
= .622
S
U
θ X10³
H
δ* X10³

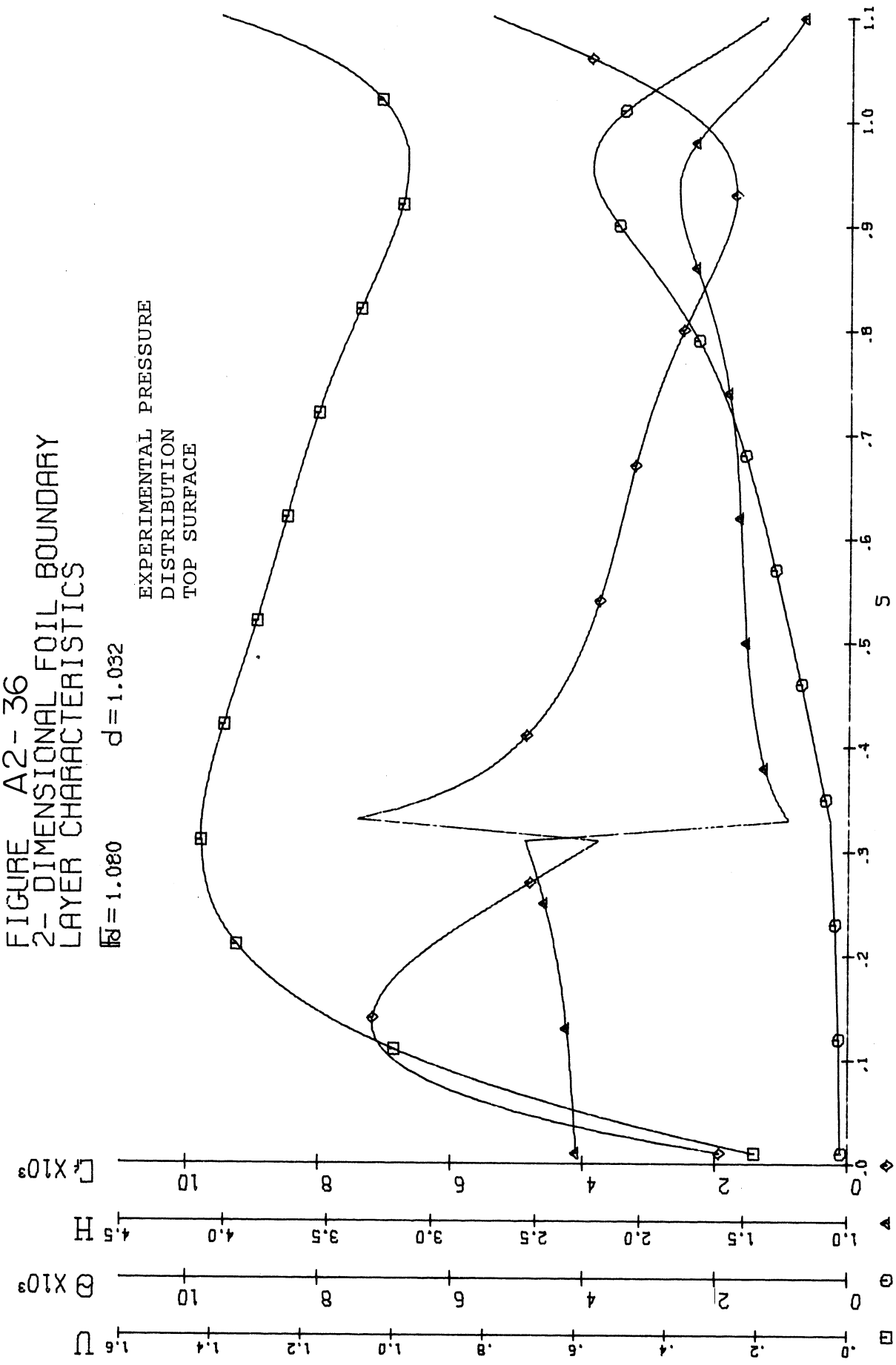
FIGURE A2- 36
2- DIMENSIONAL FOIL BOUNDARY
LAYER CHARACTERISTICS
M = 1.080 d = 1.032
EXPERIMENTAL PRESSURE
DISTRIBUTION
TOP SURFACE
U
Θ X10³
H
δ* X10³
S

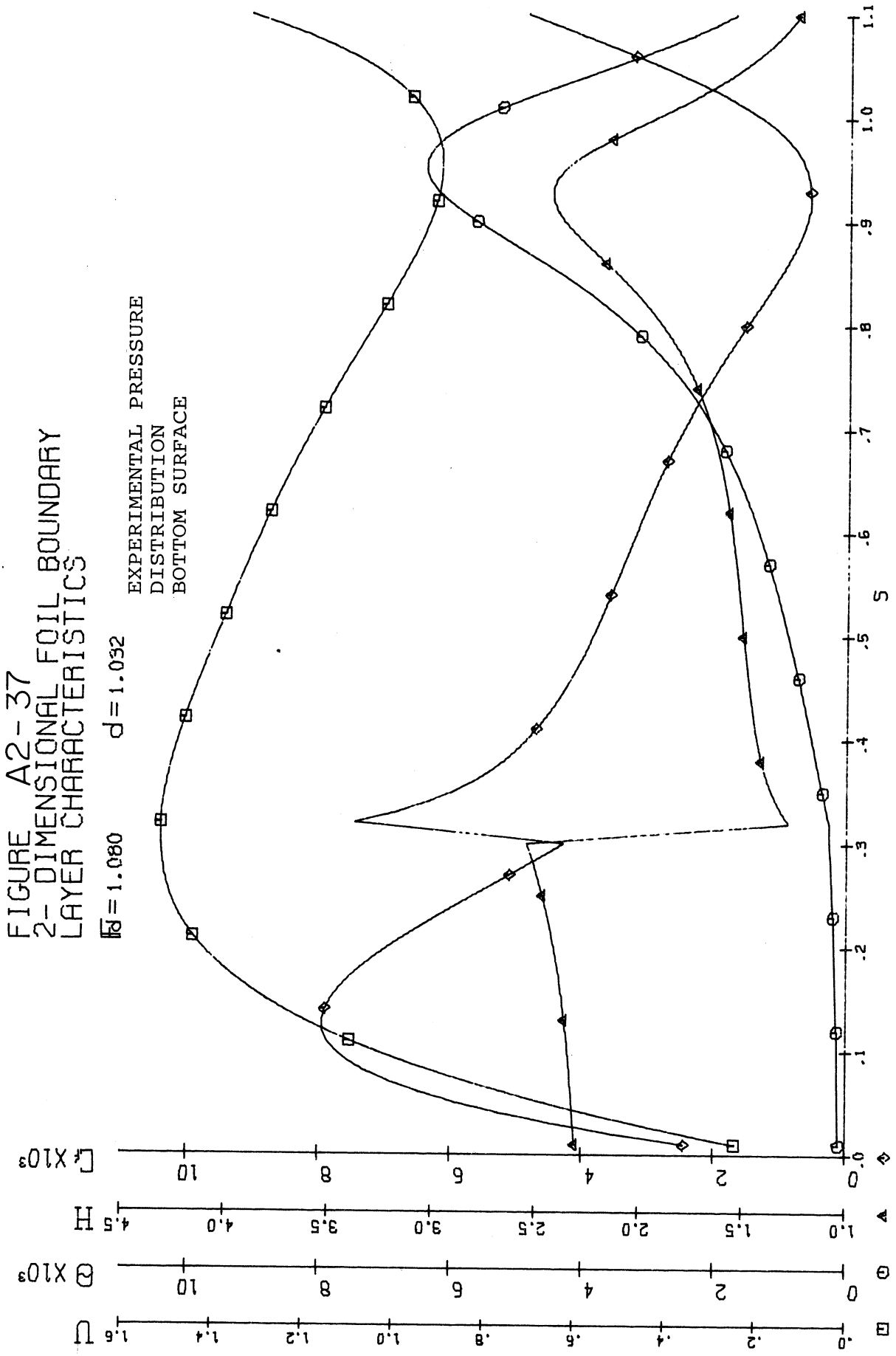
FIGURE A2-37
2- DIMENSIONAL FOIL BOUNDARY
LAYER CHARACTERISTICS
$\bar{M}_d$ = 1.080 d = 1.032
EXPERIMENTAL PRESSURE
DISTRIBUTION
BOTTOM SURFACE
S
U
Θ X10³
H
δ* X10³

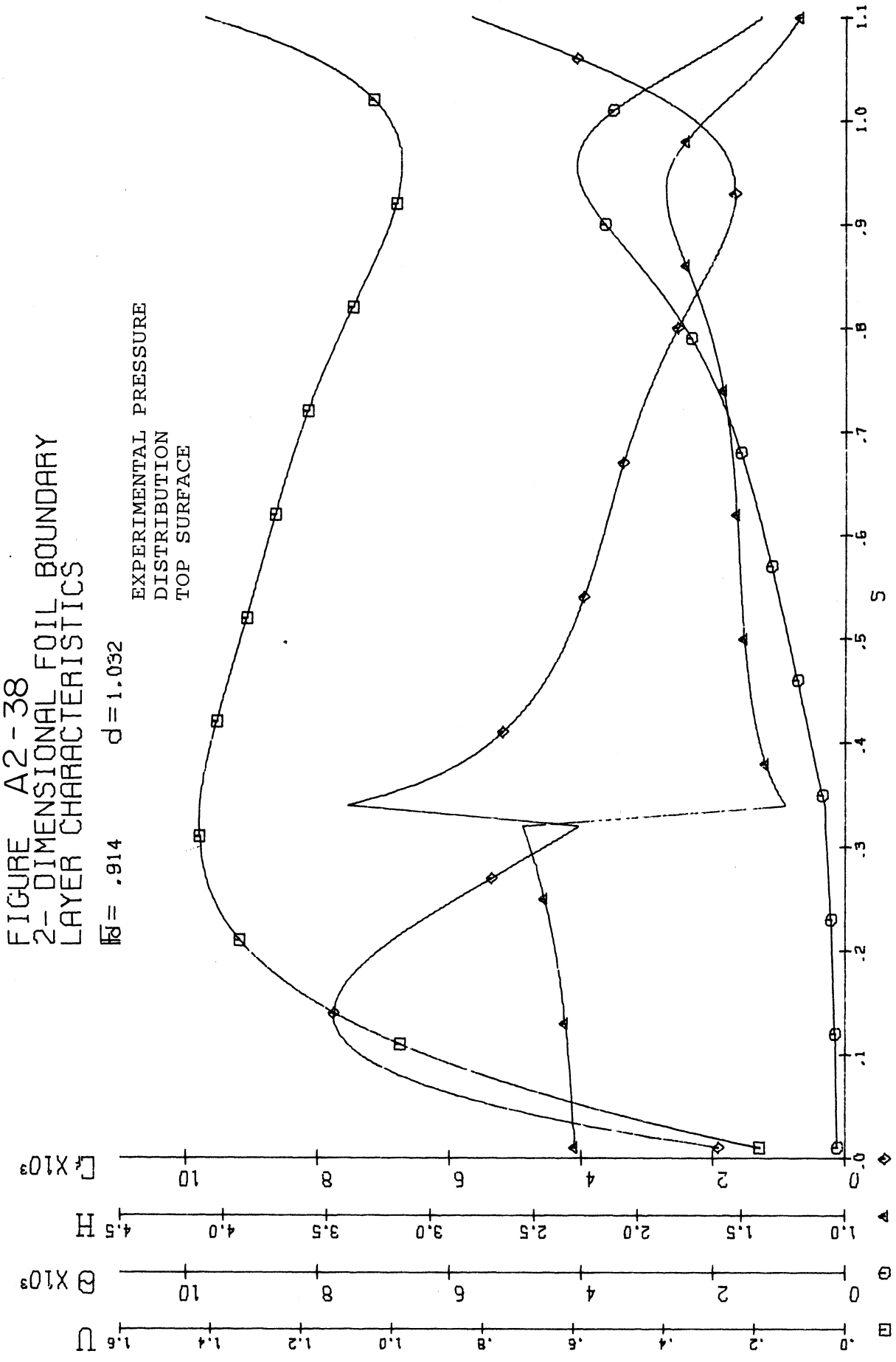
FIGURE A2-38
2- DIMENSIONAL FOIL BOUNDARY
LAYER CHARACTERISTICS
M = .914 d=1.032
EXPERIMENTAL PRESSURE
DISTRIBUTION
TOP SURFACE
S
H
θ X10³
δ* X10³
U

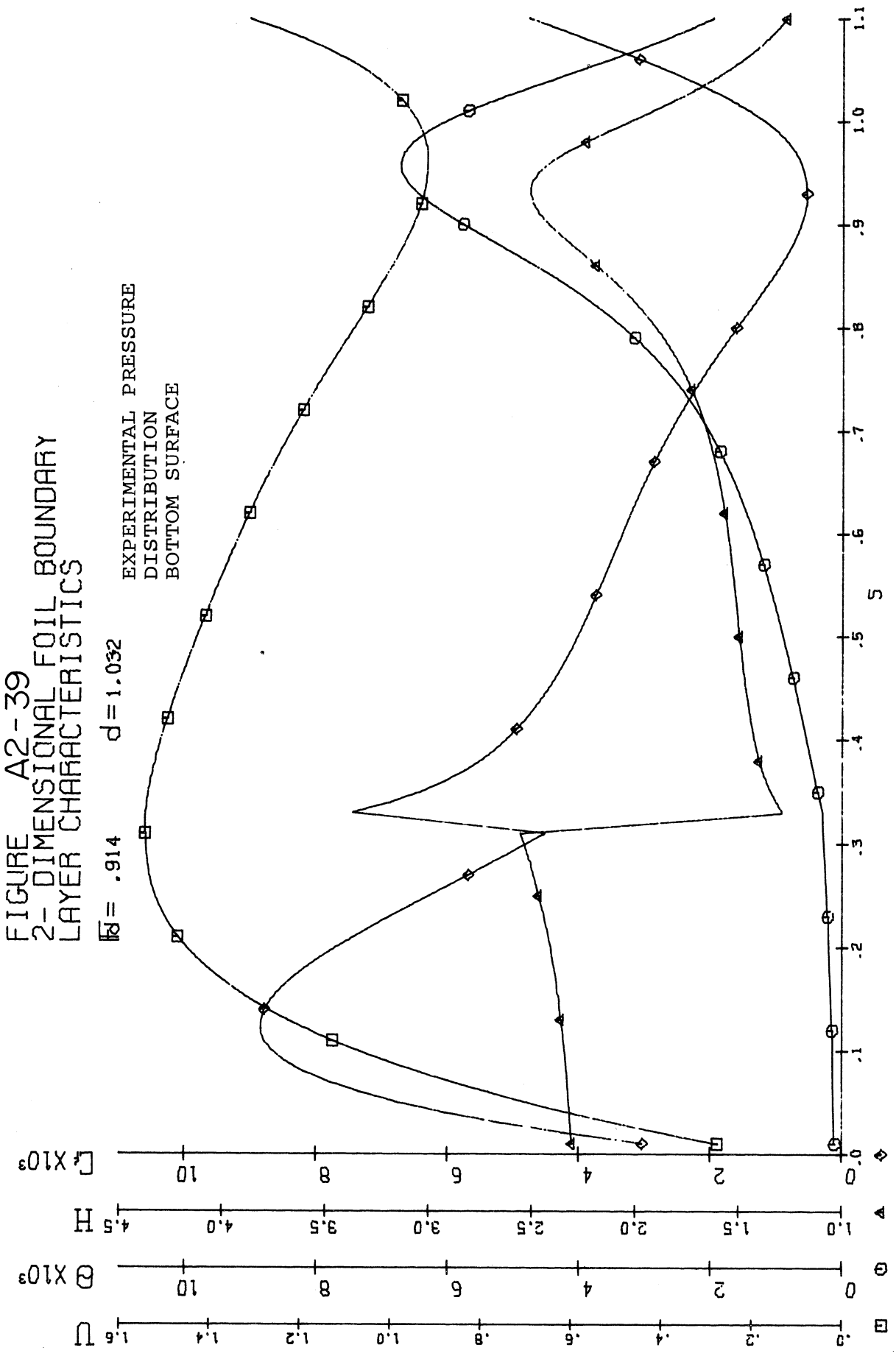
FIGURE A2-39
2- DIMENSIONAL FOIL BOUNDARY
LAYER CHARACTERISTICS
EXPERIMENTAL PRESSURE
DISTRIBUTION
BOTTOM SURFACE
d = 1.032
= .914
S
U
θ X10³
H
δ* X10³

FIGURE A2-40
2-DIMENSIONAL FOIL BOUNDARY
LAYER CHARACTERISTICS
EXPERIMENTAL PRESSURE
DISTRIBUTION
TOP SURFACE
d = 1.032
S
U
Θ X10³
H
δ* X10³
δ

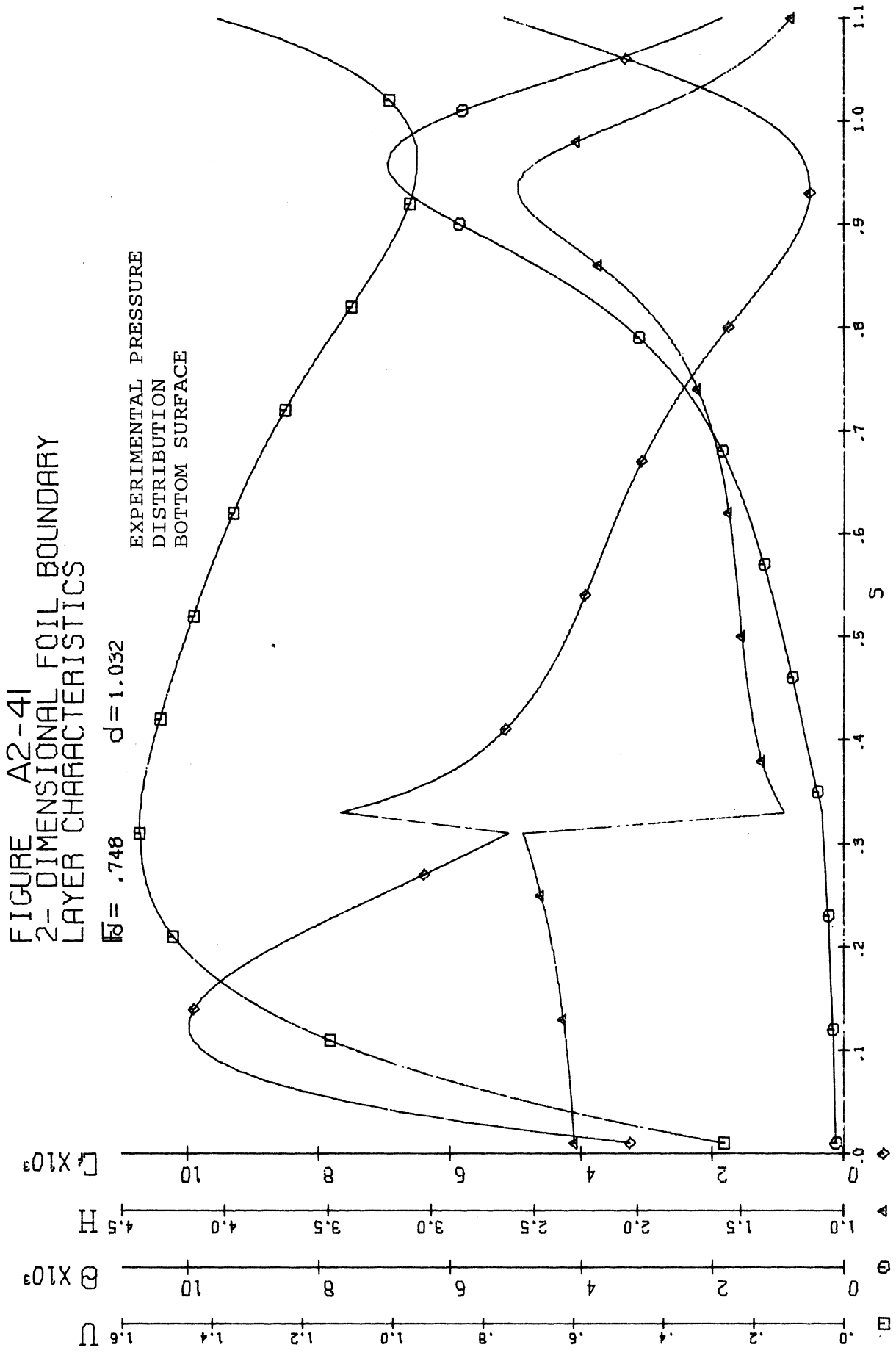
FIGURE A2-41
2- DIMENSIONAL FOIL BOUNDARY
LAYER CHARACTERISTICS
$\bar{R}_d$ = .748 d = 1.032
EXPERIMENTAL PRESSURE
DISTRIBUTION
BOTTOM SURFACE
U
Θ X10³
H
δ* X10³
S

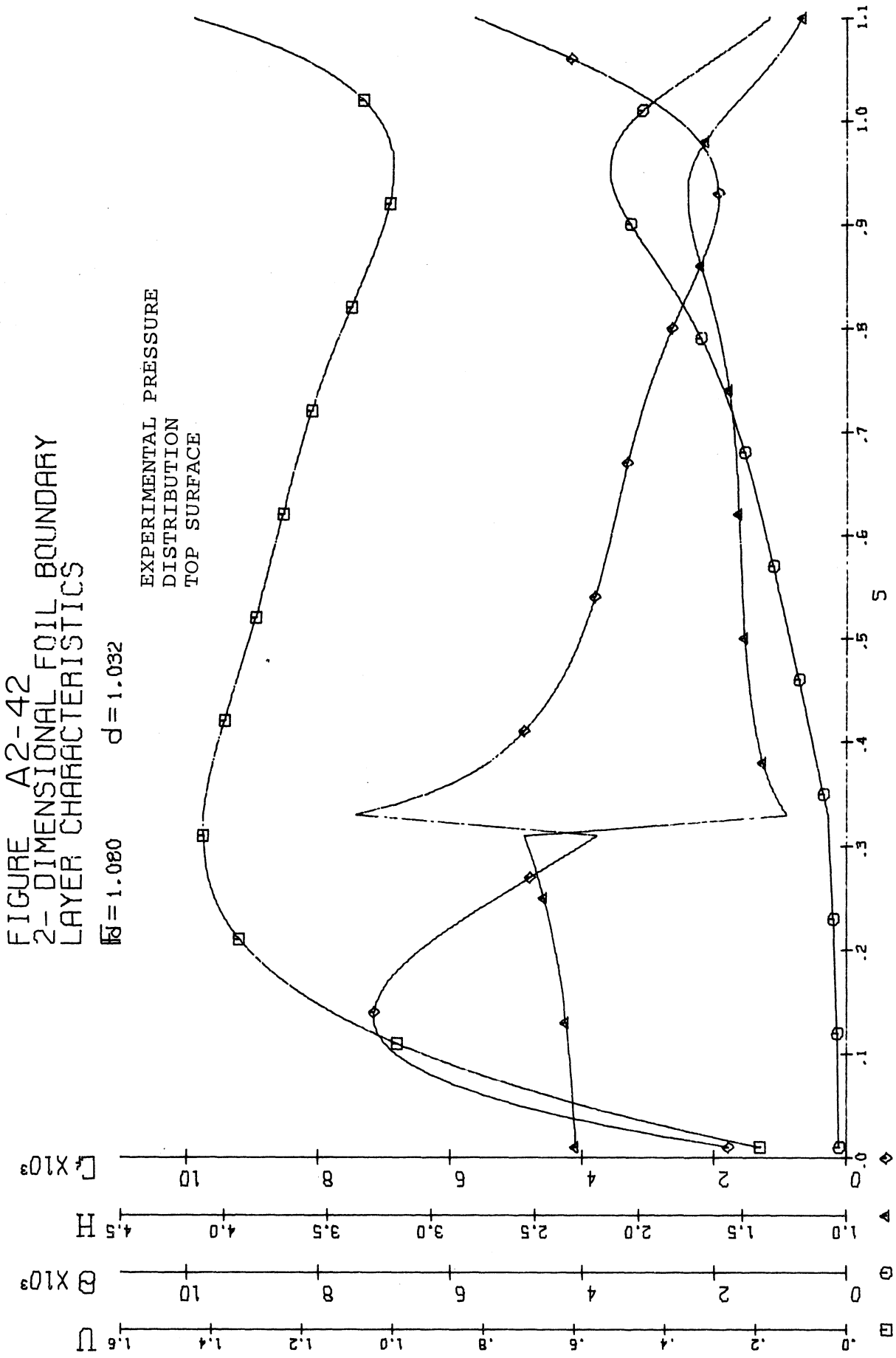
FIGURE A2-42
2- DIMENSIONAL FOIL BOUNDARY
LAYER CHARACTERISTICS
EXPERIMENTAL PRESSURE
DISTRIBUTION
TOP SURFACE
d = 1.032
S
U
Θ X10³
H
δ* X10³